

ABSTRACT

Title of Dissertation: ENGINEERING HIERARCHICAL MESO-
/MICROPOROUS LAMELLAR ZEOLITES
WITH VARIABLE TEXTURAL AND
CATALYTIC PROPERTIES

Laleh Emdadi, Doctor of Philosophy, 2016

Dissertation directed by: Professor Dongxia Liu, Department of Chemical
& Biomolecular Engineering

Meso-/microporous zeolites combine the characteristics of well-defined micropores of zeolite with efficient mass transfer consequences of mesopores to increase the efficiency of the catalysts in reactions involving bulky molecules. Different methods such as demetallation and templating have been explored for the synthesis of meso-/microporous zeolites. However, they all have limitations in production of meso-/microporous zeolites with tunable textural and catalytic properties using few synthesis steps. To address this challenge, a simple one-step dual template synthesis approach has been developed in this work to engineer lamellar meso-/microporous zeolites structures with tunable textural and catalytic properties.

First, one-step dual template synthesis of meso-/microporous mordenite framework inverted (MFI) zeolite structures was investigated. Tetrapropyl ammonium hydroxide (TPAOH) and diquatary ammonium surfactant ($[\text{C}_{22}\text{H}_{45}\text{-N}^+(\text{CH}_3)_2\text{-C}_6\text{H}_{12}\text{-N}^+(\text{CH}_3)_2\text{-C}_6\text{H}_{13}]\text{Br}_2$, C₂₂₋₆₋₆) were used as templates to produce

micropores and mesopores, respectively. The variation in concentration ratios of dual templates and hydrothermal synthesis conditions resulted in production of multi-lamellar MFI and the hybrid lamellar-bulk MFI (HLBM) zeolite structures. The relationship between the morphology, porosity, acidity, and catalytic properties of these catalysts was systematically studied. Then, the validity of the proposed synthesis approach for production of other types of zeolites composites was examined by creating a meso-/microporous bulk polymorph A (BEA)-lamellar MFI (BBLM) composite. The resulted composite samples showed higher catalytic stability compared to their single component zeolites. The studies demonstrated the high potential of the one-step dual template synthesis procedure for engineering the textural and catalytic properties of the synthesized zeolites.

ENGINEERING HIERARCHICAL MESO-/MICROPOROUS LAMELLAR
ZEOLITES WITH VARIABLE TEXTURAL AND CATALYTIC PROPERTIES

by

Laleh Emdadi

Dissertation submitted to the Faculty of the Graduate School of the
University of Maryland, College Park, in partial fulfillment
of the requirements for the degree of
Doctor of Philosophy
2016

Advisory Committee:
Professor Dongxia Liu, Chair
Professor Michael Zachariah
Professor Chunsheng Wang
Professor Yu-Huang Wang
Professor Dat T. Tran

© Copyright by
Laleh Emdadi
2016

Dedication

To my lovely family

Acknowledgements

I like to thank my advisor Prof. Dongxia Liu for providing me the opportunity to work in her research laboratory. Without her guidance and mentoring, this dissertation would not have reached anywhere. Prof. Liu's strategic approach towards conducting research aided me in advancing my research in the right direction. She helped me to achieve a lot more than what I could have managed otherwise. Her systematic approach to problem solving has always been a source of inspiration and her feedback on research and on the way of conducting research helped me to become a better scientist. I want to extend my appreciation to Prof. Michael Zachariah, Prof. Chunsheng Wang, Prof. Yu-Huang Wang, and Prof. Dat T. Tran for agreeing to serve on my committee.

I am very grateful to the members in Dr. Liu's laboratory with whom I had many beneficial discussions. I especially want to thank Yiqing Wu, Su Cheun Oh, Guanghui Zhu, Mann Sakbodin, and Wei Wu who helped me a lot in running my experiments and sample characterizations.

I would also like to acknowledge and thank our collaborators in US Army Research Lab, Dr. Ivan Lee and Dr. Dat Tran whose help and valuable feedback was instrumental in achieving the objectives of my research and I have enjoyed working with them.

I wish to express my sincere gratitude to my best friend Karthik Sridhara who was always there for me and helped me both professionally and personally.

I would like to thank my parents Shoreh Emdadi and Mahmoud Emdadi and my sister Golsa Emdadi for their blessings. This journey would not have been possible without their encouragement and motivation during the difficult times.

Last but definitely not the least, I want to thank my lovely uncle and aunt Ali Niak and Shideh Emdadi for their never-ending love and support.

Table of Contents

Dedication	ii
Acknowledgements	iii
Table of Contents	v
List of Tables	vii
List of Figures	ix
Chapter 1: Introduction	1
1.1. Zeolites	1
1.2. Zeolite synthesis, crystallization, and growth	3
1.3. Different applications of zeolites	5
1.4. Meso-/microporous zeolites	8
1.5. Template synthesis of meso-/microporous zeolites	11
1.5.1. Dual template synthesis of meso-/microporous lamellar zeolites	13
1.5.2. Tuning the catalytic performance of meso-/microporous lamellar zeolites	16
1.6. Dual template synthesis of meso-/microporous composite zeolites	17
1.7. Research objectives	19
1.8. Thesis outline	19
Chapter 2: Dual template synthesis of meso-/microporous MFI zeolite nanosheet assemblies with tailored activity in catalytic reactions	23
2.1. Introduction	23
2.2. Experimental section	27
2.2.1. Materials for catalyst synthesis and reactions	27
2.2.2. Dual template synthesis of MFI zeolites	29
2.2.3. Ion-exchange of zeolite catalysts	30
2.2.4. Catalyst characterization	31
2.2.5. Determination of acid sites	32
2.2.6. Ethanol dehydration reactions	33
2.2.7. Catalytic conversion of benzyl alcohol in mesitylene	34
2.3. Results and discussion	36
2.3.1. Textural properties of zeolite catalysts	36
2.3.2. Acidity of zeolite catalysts	46
2.3.3. Ethanol dehydration reactions	51
2.3.4. Benzyl alcohol reactions over zeolite catalysts	52
2.3.5. Effect of pH changes due to the presence of TPAOH in the synthesis recipe on catalyst morphology	61
2.4. Concluding remarks	62
Chapter 3: One-step dual template synthesis of hybrid lamellar-bulk MFI zeolite	64
3.1. Introduction	64
3.2. Experimental section	67
3.2.1. Materials for zeolite synthesis	67
3.2.2. Dual template synthesis of HLBZM zeolite	67
3.2.3. Materials characterization	68

3.3. Results and discussion	69
3.3.1. HLBM structure formation assisted by dual templates.....	69
3.3.2. Scheme for the formation of the HLBM structure.....	73
3.3.3. Domain sizes of the lamellar shell tuned by C ₂₂₋₆₋₆ concentration	78
3.3.4. Domain sizes of the bulk core tuned by ageing temperature or time.....	83
3.4. Concluding remarks	86
Chapter 4: The role of external acidity of meso-/microporous zeolites in determining selectivity for acid-catalyzed reactions of benzyl alcohol	88
4.1. Introduction.....	88
4.2. Experimental section.....	90
4.2.1. Synthesis of HLBM zeolite catalysts.....	90
4.2.2. Characterization of HLBM zeolite catalysts.....	92
4.2.3. Determination of external surface, pore mouth, and internal Brønsted acid sites.....	93
4.2.4. Catalytic conversion of benzyl alcohol in mesitylene	94
4.3. Results and discussion	95
4.3.1. Structural properties of HLBM zeolite catalysts	95
4.3.2. Textural properties of HLBM zeolite catalysts.....	101
4.3.3. Acidity properties of HLBM zeolite catalysts	104
4.3.4. Catalytic performance of HLBM zeolite catalysts.....	110
4.4. Concluding remarks	130
Chapter 5: BEA nanosponge@ultra-thin lamellar MFI prepared in one-step: Integration of 3D and 2D zeolites into core-shell composite for efficient alkylation reactions	132
5.1. Introduction.....	132
5.2. Experimental section.....	135
5.2.1. Materials for catalyst synthesis and reactions.....	135
5.2.2. Zeolite composite synthesis	135
5.2.3. Materials characterization.....	137
5.2.4. Determination of external and internal Brønsted acid sites	138
5.2.5. Catalytic conversion of benzyl alcohol in mesitylene	139
5.3. Results and discussion	140
5.3.1. BBLM structure formation assisted by dual templates.....	140
5.3.2. Scheme for formation of BBLM zeolite composite.....	144
5.3.3. Textural properties of BBLM zeolite composites.....	149
5.3.4. Acidity of BBLM zeolite composites	152
5.3.5. Catalytic performance of BBLM zeolite composites.....	156
5.4. Concluding remarks	160
Chapter 6: Conclusions and future work	161
6.1. Conclusions.....	161
6.2. Future work.....	166
References.....	171

List of Tables

Table 2.1. Compositions for crystallization of zeolite nanosheet assemblies by dual template synthesis method.....	30
Table 2.2. Textural properties of zeolite catalysts determined from N ₂ adsorption-desorption data.....	43
Table 2.3. Textural property of zeolite catalyst measured by Ar adsorption-desorption isotherm.....	45
Table 2.4. Acidity of the zeolite catalyst measured by elemental analysis and chemical titrations; Rate constants (k_{meas}) of DEE production at 383 K, measured activation energies of DEE synthesis (ΔE_{meas}) and entropies of MFI zeolite catalysts (ΔS_{meas}).....	47
Table 2.5. Concentration of Brønsted and Lewis acid sites of selected zeolite catalysts measured by FTIR spectra of adsorbed pyridine at 393 K.....	49
Table 2.6. Rate constants of mesitylene alkylation, benzyl alcohol self-etherification and selectivity for alkylation and self-etherification reactions.....	56
Table 3.1. Compositions for synthesis of HLBM zeolites by dual template method.....	68
Table 3.2. Textural properties of HLBM zeolites synthesized using different C ₂₂₋₆₋₆ content in the recipe measured by N ₂ adsorption-desorption method.....	82
Table 3.3. Textural properties of MFI-5/36 zeolite synthesized at different ageing temperatures measured by N ₂ adsorption-desorption method.....	85
Table 3.4. Textural properties of MFI-3/36 zeolite synthesized using different ageing times measured by N ₂ adsorption-desorption method.....	86
Table 4.1. Textural properties of the HLBM zeolite catalysts determined from Ar isotherms.....	103
Table 4.2. Textural properties of HLBM-3/36 zeolite catalysts with different Si/Al molar ratios.....	103
Table 4.3. Si/Al ratio and acidity of HLBM zeolite catalysts.....	104
Table 4.4. External acidity (external surface and in the pore mouth region) of HLBM zeolite catalysts.....	106

Table 4.5. Rate constants of mesitylene alkylation and benzyl alcohol etherification and selectivity for alkylation and etherification reactions.....	112
Table 4.6. Effectiveness factor analysis of internal etherification reaction in HLBM zeolite catalysts.....	118
Table 4.7. Rate constants of etherification and alkylation on external acid sites and selectivity of external acid sites in HLBM zeolite catalysts.....	122
Table 4.8. Rate constants of etherification and alkylation reactions on remaining active external acid sites in HLBM zeolite catalysts when the external acid sites were cumulatively poisoned by DTBP.....	129
Table 5.1. Textural properties of the BBLM-3/36 zeolite composite at different synthesis times determined from Ar isotherms.....	148
Table 5.2. Textural properties of the BEA and BBLM zeolite composites determined from Ar isotherms.....	151
Table 5.3. Acidity, acid site distribution and fraction of BEA content in the BBLM zeolite composites.....	152
Table 6.1. Examples of the different proposed dual template structures can be used for synthesis of lamellar zeolite nanosheet assemblies. The general synthesis recipe is $30\text{Na}_2\text{O}/1\text{Al}_2\text{O}_3/100\text{SiO}_2/10\text{mesoporogen}/x\text{microporogen}/4000\text{H}_2\text{O}/18\text{H}_2\text{SO}_4$, where x equals to 1, 2, 3, 5, 8, 12, and 20, respectively.....	168

List of Figures

- Figure 1.1. Schematic diagram of an example for zeolite building unit development from primary to secondary and to tertiary, respectively. Yellow circles show the T atoms (T: Si, Al, etc.) and blue lines indicate the oxygen bridges between T atoms....3
- Figure 1.2. Representation of the crystal structure and schematic drawing of the three-dimensional (3D) channel system of (A and B) BEA, (C and D) MOR, (E and F) FAU, and (G and H) MFI zeolites, respectively. The intersection points in figures (A), (C), (E), and (G) represent sites for tetrahedral atoms (termed T-atoms) like silicon. The oxygen would reside near the midpoint of any line.....6
- Figure 1.3. Schematic representation of different synthesis routes for formation of meso-/microporous zeolites. Exfoliation/pillaring of layered zeolites (A), demetallation (desilication/dealumination) of microporous zeolites (B), Templating synthesis method using hard templates (C) or soft templates (D).....9
- Figure 2.1. Production of MFI zeolite lamellae using diquatery ammonium surfactant as mesoporegen by single template method.....24
- Figure 2.2. Production of supported zeolite lamellae by dual template method (hypothesized scheme).....25
- Figure 2.3. Experimental setup for catalytic conversion of benzyl alcohol in mesitylene.....35
- Figure 2.4. SEM images of MFI zeolites obtained with C₂₂₋₆₋₆/TPAOH molar ratio of (A) 10/0, (B) 10/1, (C) 10/2, (D) 10/3, (E) 10/5, (F) 10/8, (G) 10/12, and (H) 10/20, respectively, in the dual template synthesis. (I) Commercial MFI with Si/Al ratio of ~ 40 was used for comparison.....37
- Figure 2.5. TEM images of MFI zeolites obtained with C₂₂₋₆₋₆/TPAOH molar ratio of (A) 10/0, (B) 10/1, (C) 10/2, (D) 10/3, (E) 10/5, (F) 10/8, (G) 10/12, and (H) 10/20, respectively, in the dual template synthesis. (I) Commercial MFI with Si/Al ratio of ~ 40 was used for comparison.....38
- Figure 2.6. Wide angle (A) and low angle (B) XRD patterns of MFI zeolites synthesized with C₂₂₋₆₋₆/TPAOH molar ratio of (a) 10/0, (b) 10/1, (c) 10/2, (d) 10/3, (e) 10/5, (f) 10/8, (g) 10/12, and (h) 10/20, respectively.....40
- Figure 2.7. N₂ adsorption-desorption isotherms (A) and the corresponding pore size distributions (B) as derived from N₂ sorption (NLDFT on the adsorption branch) of MFI zeolite obtained with C₂₂₋₆₋₆/TPAOH molar ratio of (a) 10/0, (b) 10/1, (c) 10/2, (d) 10/3, (e) 10/5, (f) 10/8, (g) 10/12, and (h) 10/20, respectively. (i) Commercial MFI with Si/Al ratio of ~ 40 was used for comparison.....41

Figure 2.8. Ar adsorption-desorption isotherms (A) and the corresponding pore size distributions (B) as derived from Ar sorption (NLDFT on the adsorption branch) of MFI zeolite obtained with C₂₂₋₆₋₆/TPAOH molar ratio of (a) 10/0, (b) 10/1, (c) 10/2, (d) 10/3, (e) 10/5, (f) 10/8, (g) 10/12, and (h) 10/20, respectively. (i) Commercial MFI with Si/Al ratio of ~ 40 was used for comparison.....44

Figure 2.9. FTIR spectra of adsorbed pyridine on selected MFI zeolites obtained with C₂₂₋₆₋₆/TPAOH molar ratio of (a) 10/12, (b) 10/5, (c) 10/2, and (d) 10/0, respectively. (e) Commercial MFI with Si/Al ratio of ~ 40 was used for comparison.....48

Figure 2.10. Multinuclear solid state NMR spectra of MFI zeolites obtained with C₂₂₋₆₋₆/TPAOH molar ratio of 10/2, 10/5, and 10/12: (A) ²⁹Si MAS NMR, (B) ²⁹Si CP MAS NMR, and (C) ²⁷Al MAS NMR.....50

Figure 2.11. Measured rate constants of DEE production over MFI zeolite catalysts synthesized by the dual template method.....52

Figure 2.12. Scheme for mesitylene alkylation (k_{alk}) and benzyl alcohol self-etherification (k_{eth}) reactions over MFI zeolite catalysts.....53

Figure 2.13. Plots for determination of rate constants of benzyl alcohol conversion in the absence of DTBP (A) and in the presence of DTBP (B), respectively. (C)-(D) are rate constants of dibenzyl ether and 1,3,5-trimethyl-2-benzylbenzene formation, respectively, in the absence of DTBP. (E) is the rate constant of dibenzyl ether formation in the presence of DTBP. (F) is the rate constant of 1,3,5-trimethyl-2-benzylbenzene formation in the absence of DTBP versus fraction of external surface area.....58

Figure 2.14. S_{ext}/S_{BET} (extracted from N₂ isotherms) versus MFI catalysts synthesized with C₂₂₋₆₋₆/TPAOH molar ratio of 10/0, 10/1, 10/2, 10/3, 10/5, 10/8, 10/12, and 10/20, respectively. Commercial MFI was used for comparison.....59

Figure 2.15. SEM images of MFI zeolites obtained with C₂₂₋₆₋₆/TPABr molar ratio of (A) 10/2, (B) 10/5, (C) 10/12, and (D) 10/20, respectively, in the dual template synthesis.....61

Figure 3.1. Schematic illustration of HLBM zeolite synthesis.....66

Figure 3.2. Low-angle (A) and wide-angle (B) XRD patterns of MFI-0/36, MFI-3/36, and MFI-3/0 after 120 h of hydrothermal synthesis.....70

Figure 3.3. SEM and TEM images of HLBM zeolites after 120 h of hydrothermal synthesis. (SEM: (A) MFI-0/36, (C) MFI-3/36, and (E) MFI-3/0. TEM: (B) MFI-0/36, (D) MFI-3/36, and (F) MFI-3/0. Inset picture in (C) shows the side view of the MFI-3/36 particles and inset picture in (D) shows the HRTEM image for MFI-3/36.).....71

Figure 3.4. Ar adsorption-desorption isotherm and the corresponding NLDFT pore size distribution (inset image) of MFI-0/36 and MFI-3/36 zeolite samples.....	72
Figure 3.5. Low-angle (A) and wide-angle (B) XRD patterns of MFI-3/36 after 0 h, 3 h, 6 h, 12 h, 24 h, and 72 h hydrothermal synthesis, respectively.....	74
Figure 3.6. SEM images of MFI-3/36 after (A) 0 h, (B) 3 h, (C) 6 h, (D) 12 h, (E) 24 h, and (F) 72 h of hydrothermal synthesis, respectively.....	75
Figure 3.7. N ₂ adsorption-desorption isotherms (A) and the corresponding NLDFT pore size distributions (B) of MFI-3/36 after 0 h, 3 h, 6 h, 12 h, 24 h, 72 h, and 120 h hydrothermal synthesis, respectively.....	77
Figure 3.8. SEM and TEM images of HLBM zeolite after 120 h of hydrothermal synthesis. (SEM: (A) MFI-1/36, (C) MFI-5/36, and (E) MFI-7/36. TEM: (B) MFI-1/36, and (D), (F) MFI-5/36. Inset picture in (B) show the TEM of MFI-1/36 at high magnification and inset picture in (D) shows HRTEM image for MFI-5/36.).....	79
Figure 3.9. TGA curves of HLBM zeolite synthesized using different C ₂₂₋₆₋₆ concentration in the recipe.....	81
Figure 3.10. Low-angle (A) and wide-angle (B) XRD patterns of MFI-1/36, MFI-5/36, and MFI-7/36 after 120 h of hydrothermal synthesis.....	81
Figure 3.11. SEM images and particle size distributions (inset) of MFI-5/36 sample synthesized at ageing temperature of (A) 298 K, (B) 323 K, (C) 353 K, and (D) 373 K, respectively. The SEM image of MFI-5/36 at 298 K is represented here for comparison purpose. (E) shows XRD patterns of these samples.....	84
Figure 3.12. SEM images and particle size distributions (inset) of MFI-3/36 synthesized at ageing time of (A) 2 h, (B) 8 h, and (C) 16 h, respectively. The SEM image of MFI-3/36 at 8 h is represented here for comparison purpose. (D) shows XRD patterns of these samples.....	85
Figure 4.1. XRD patterns of synthesized HLBM-0/36, HLBM-1/36, HLBM-3/36, and HLBM-5/36 zeolite catalysts.....	96
Figure 4.2. SEM and TEM images of HLBM zeolite with Si/Al=300 after 5 days of hydrothermal synthesis. (SEM: (A) HLBM-0/36, (C) HLBM-1/36, (E) HLBM-3/36, and (G) HLBM-5/36. TEM: (B) HLBM-0/36, (D) HLBM-1/36, (F) HLBM-3/36, and (H) HLBM-5/36.).....	98
Figure 4.3. High resolution TEM images of HLBM zeolite with Si/Al=300 after 5 days of hydrothermal synthesis. ((A)-(C): HLBM-1/36; (D)-(F): HLBM-3/36, and (G)-(H): HLBM-5/36, respectively.).....	99

Figure 4.4. SEM images of synthesized HLBM-3/36 zeolite samples, which were obtained using Si/Al molar ratio of (A) 500, (B) 300, (C) 150, (D) 100, and (E) 75, respectively. (HLBM-3/36 with Si/Al ratio=300 has been represented here for comparison purpose.).....100

Figure 4.5. Ar adsorption-desorption isotherms (A) and the corresponding NLDFT pore size distributions (B) derived from Ar adsorption branch of the HLBM zeolite catalysts.....102

Figure 4.6. Solid state ^{29}Si SP MAS NMR (A) and ^{27}Al MAS NMR (B) spectra of HLBM zeolite catalysts.....107

Figure 4.7. (A) FTIR spectra of adsorbed pyridine ((a) HLBM-0/36, (b) HLBM-1/36, (c) HLBM-3/36, and (d) HLBM-5/36, respectively) on HLBM zeolite catalysts and (B) B/L acid site ratio versus relative external surface area of HLBM zeolite catalysts.....109

Figure 4.8. Plots for rate constant and selectivity determination for mesitylene alkylation reactions over HLBM zeolite catalysts. The slope of each plot is the apparent rate constant, $k_{\text{alk,app}}$113

Figure 4.9. Plots for rate constant determination for benzyl alcohol etherification over HLBM zeolite catalysts. (A) HLBM-0/36, (B) HLBM-1/36, (C) HLBM-3/36, and (D) HLBM-5/36. (Slope of the linear plot is $k_{\text{eth,app,int}} C_{\text{H}^+} V_{\text{cat}} \overline{K} C_{\text{A}}^{\text{max}} / V_{\text{sol}}$, from which $k_{\text{eth,app,int}}$ can be evaluated given that other parameters have been determined as shown in Table 4.6, section 4.3.4.3, and inset information in each plot.).....118

Figure 4.10. Measured alkylation and etherification rate constants of benzyl alcohol with mesitylene reaction in absence of DTBP (A) and in presence of DTBP (B), rate constants of alkylation on external surface acid sites (C) and etherification on external acid sites (D), and selectivity (E) versus relative external surface area of HLBM zeolite catalysts.....125

Figure 4.11. Rate constants of etherification on external acid sites (A) and alkylation on external surface acid sites (B) of HLBM-3/36 and HLBM-5/36, respectively, with accumulative addition of DTBP to poison the external acid sites. (x (%) is the percentage of active external acid sites (A) and the percentage of active external surface acid sites (B) that were poisoned by DTBP.).....130

Figure 5.1. Schematic representation of 3D bulk BEA- 2D lamellar MFI composite.....134

Figure 5.2. XRD patterns of BEA and BBLM zeolite composites after 14 days of hydrothermal synthesis. XRD pattern of lamellar MFI catalyst has been presented for comparison purpose.....	141
Figure 5.3. SEM images of BEA (A), BBLM-1/36 (B), BBLM-3/36 (C), and BBLM-9/36 (D), respectively, after 14 days of hydrothermal synthesis.....	142
Figure 5.4. TEM images of BEA (A), (B), and (C), BBLM-1/36 (D), (E), and (F), BBLM-3/36 (G), (H), and (I), and BBLM-9/36 (J), (K), and (L) zeolite composite catalysts with Si/Al=50 after 14 days of hydrothermal synthesis.....	143
Figure 5.5. XRD patterns of BBLM-3/36 zeolite composite after 1 day, 3 days, 7 days, and 14 days hydrothermal synthesis, respectively.....	145
Figure 5.6. SEM images of BBLM-3/36 zeolite composite after (A) 1 day, (B) 3 days, (C) 7 days, and (D) 14 days hydrothermal synthesis, respectively.....	146
Figure 5.7. Ar adsorption-desorption isotherms (A) and the corresponding NLDFT pore size distributions (B) derived from Ar adsorption branch of isotherms for the BBLM-3/36 zeolite composite after 1 day, 3 days, 7 days, and 14 days hydrothermal synthesis, respectively. The inset image in Figure 6(B) shows the NLDFT micro pore size distribution of BBLM-3/36 zeolite composite.....	147
Figure 5.8. Ar adsorption-desorption isotherms (A), the corresponding NLDFT pore size distributions (B)-(C) derived from Ar adsorption branch of isotherms, and cumulative pore volume versus pore size (D) of the BEA, lamellar MFI, and BBLM zeolite composites.....	150
Figure 5.9. Solid-state ^{29}Si SP MAS NMR (A) and ^{27}Al MAS NMR (B) spectra of the BEA and BBLM zeolite composites.....	154
Figure 5.10. NH_3 -TPD profiles of the BEA, lamellar MFI and BBLM zeolite composites.....	155
Figure 5.11. Conversion of benzyl alcohol in mesitylene versus reaction time of 7 h (A) and 2 h (B) over BBLM zeolite composite catalysts. BEA and physical mixture of BEA/lamellar MFI zeolites were included for comparison.....	158
Figure 6.1. Schematic representation of one-pot synthesis of EMF from glucose over Sn-BEA/MFI zeolite composite fabricated by one-step dual template synthesis method. Red circles and blue sheets depict the Sn-BEA zeolite and lamellar MFI zeolite structures, respectively.....	170

Chapter 1: Introduction

1.1. Zeolites

Zeolites are crystalline microporous aluminosilicates comprising a network of SiO_2 and Al_2O_3 tetrahedra (with pore sizes typically less than 1 nm).^{1,2} Many of them occur as natural minerals and the others are synthesized. The distribution of sizes, shapes, and volumes of the pores in zeolites directly affect their performance in different applications. The correlation between the zeolite pore structure and its textural properties has been widely studied since the discovery of zeolite by Axel Fredrick Cronstedt, a Swedish mineralogist, in 1756. Cronstedt chose the term zeolite based on the Greek words *zein* and *lithos* meaning ‘boiling stones’. Since then, many naturally occurring zeolites have been discovered and zeolites gradually found application in water treatment, ion-exchange processes, and adsorption of organic molecules. The first synthetic zeolite ‘mordenite’ was reported by Barrer in 1948.¹ Later on, many other synthetic zeolites have been reported such as natrolite, chabazite, and ferrierite. The synthesis of new families of zeolite structures with new pore size/shape or modification and fine-tuning of the properties of the available zeolite structures for different applications in separation and catalysis have always been an active research area and by advanced progress in nanotechnology in recent years, novel applications of zeolites have also been emerged such as fabrication of optical devices, selective sensors, and antibacterial and medical compounds.³

Solid porous materials such as zeolites are usually categorized to three different groups based on the size of their pores. Microporous materials have pore

sizes less than 2 nm, while mesoporous ones have pore sizes in the range of 2-50 nm, and the pore size of macroporous solids is larger than 50 nm.² Zeolites are usually classified as microporous materials since their pore sizes are usually smaller than 2 nm, but if a synthesized zeolite contains at least two different pore size systems such as meso-/micropores or meso-/macropores, it is called hierarchical zeolite structure.⁴

5

The chemistry of zeolites is based on tetrahedron (TO_4), where, T: tetrahedrally coordinated atom is usually silicon (Si) or aluminum (Al). The tetrahedral units, also called primary building units, are connected to each other by shared oxygen atoms as bridges to form rings with different number of T atoms as secondary building units.⁶ The most common rings are 4-T, 6-T, 8-T, 10-T, and 12-T, respectively and T-O-T angles vary mostly in the range of 130-180°. The secondary building units are further interconnected to form the tertiary building units, as illustrated in Figure 1.1, and finally the tertiary building units connect to each other to build the three-dimensional (3D) structure of zeolites.⁷ Substitution of Si and Al atoms in zeolite frameworks with other elements such as vanadium (V), titanium (Ti), gallium (Ga), germanium (Ge), boron (B), and etc. enables the synthesized zeolites to have different compositions and crystal structures and makes them proper for specific applications.⁸ Zeolites are usually categorized based on different pore size/shape and interconnection of their channel systems (one-, two-, or three-dimensional) which result in a unique zeolite framework topology. A three capital letter code is assigned to each zeolite family by the Structural Commission of the International Zeolite Association (IZA) based on the zeolite framework type. For example, LTA refers to

the Linde type A zeolite framework structures. Even though, the number of possible zeolite frameworks is (theoretically) unlimited, but until now only 213 different zeolite framework structures have been accepted by the Structural Commission of IZA.⁹

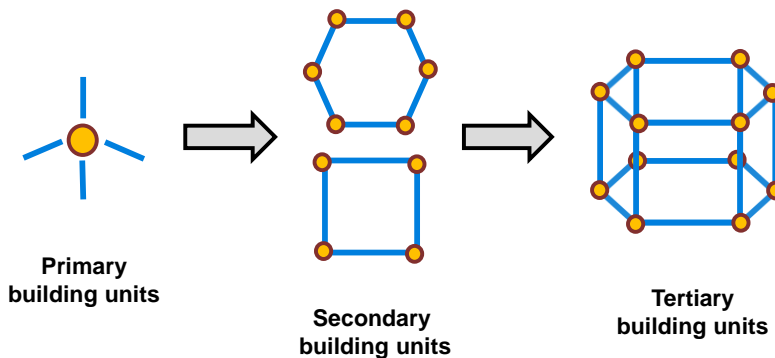


Figure 1.1. Schematic diagram of an example for zeolite building unit development from primary to secondary and to tertiary, respectively. Yellow circles show the T atoms (T: Si, Al, etc.) and blue lines indicate the oxygen bridges between T atoms.^{7, 10}

1.2. Zeolite synthesis, crystallization, and growth

Synthesis of zeolites is usually carried out by heating the aqueous zeolite synthesis gel at relatively high temperatures (above 100°C) in closed systems under autogenous pressure for selected periods of time which is called hydrothermal synthesis.^{1, 11} Hydrothermal synthesis of zeolites involves the conversion of amorphous Si and Al precursors to microporous crystalline structures using structure directing agents (SDAs), mineralizing agents such as fluoride ions, and water via an alkaline supersaturated solution. The SDAs could be alkali metal cations such as Na⁺, K⁺, Li⁺, and etc. or positively charged organic molecules such as amines or quaternary ammonium ions. The SDA has a crucial role in zeolite crystallization by

leading the Si and Al precursors to form a specific zeolite type and topology based on its geometry using both electronic and steric effects.¹¹ After crystallization, the SDAs remained in the zeolite pores are removed by heating the zeolite at high temperatures (500-600°C) which is called calcination process. Mineralizing agents control the solubility and mobility of the zeolite precursors in the synthesis gel during zeolite formation.¹¹ Zeolite synthesis is usually carried out under basic conditions in water media since water can promote the mixing and transport of materials and facilitates the crystallization process. Moreover, the zeolite precursors can be dissolved better in the synthesis media under alkaline conditions and also the nucleation and growth of the zeolite crystals are highly dependent on the alkalinity of the synthetic solution. Changing the pH of the zeolite synthesis gel influences the supersaturation, kinetics, morphology, shape, size, crystallinity, and crystal type of the produced structures.¹ After mixing the zeolite precursors for a certain time at a proper temperature which is called ageing process, the zeolite synthesis can be carried out by heating the synthesis gel in a Teflon-lined autoclave using a heating source such as oven under controlled temperature conditions.¹

The mechanism of zeolite crystallization, including the zeolite nucleation and growth is very complex and has not been fully understood yet. Davis and Lobo (1992)¹² have proposed two different mechanisms for zeolite crystallization. First one is the solution-mediated transport mechanism and the second one is the solid-phase transformation mechanism. In solution-mediated transport mechanism, the aluminate, silicate, and/or aluminosilicate species diffuse from the liquid phase to the nucleation sites for crystal growth in a clear homogeneous solution media. On the other hand, in

solid-phase transformation mechanism, the nuclei are formed close to the surface of the solid gel and then the amorphous gel diffuses to the nucleation sites and the nuclei grow and form the zeolite crystals. In some cases zeolites are formed by a combination of these two mechanisms. Different parameters such as sequence of mixing, ageing time and temperature of the zeolite synthesis gel, stirring, hydrothermal synthesis time and temperature, molar composition of the zeolite synthetic gel, type of initial sources, additives, and solvents, and alkalinity (pH) of the synthetic gel can also affect the zeolite crystallization process and as a result the type, phase, morphology, and shape/size of the zeolite structures that are formed. Therefore, for rational design of new zeolite structures with controlled structural and textural properties, these factors should be carefully adjusted.¹³

1.3. Different applications of zeolites

The pore diameter of zeolites are in molecular scale, so these nanoporous zeolite structures have the ability to discriminate between different molecules based on their size and molecular shapes. Zeolites have been widely used as heterogeneous catalysts, adsorbents, and ion-exchange materials for oil refining, petrochemical processing, and fine chemical synthesis mainly because of their well-defined structure, composition, and angstrom-size micropores that are responsible for shape selectivity.¹⁴⁻¹⁹ In catalysis, zeolites occupy more than 40% of the entire solid catalysts in the current chemical industry.²⁰ The most widely commercialized zeolite catalysts are beta polymorph A (BEA), mordenite (MOR), faujasite (FAU), and mordenite framework inverted (MFI) zeolites.²¹ Figure 1.2 shows the representative

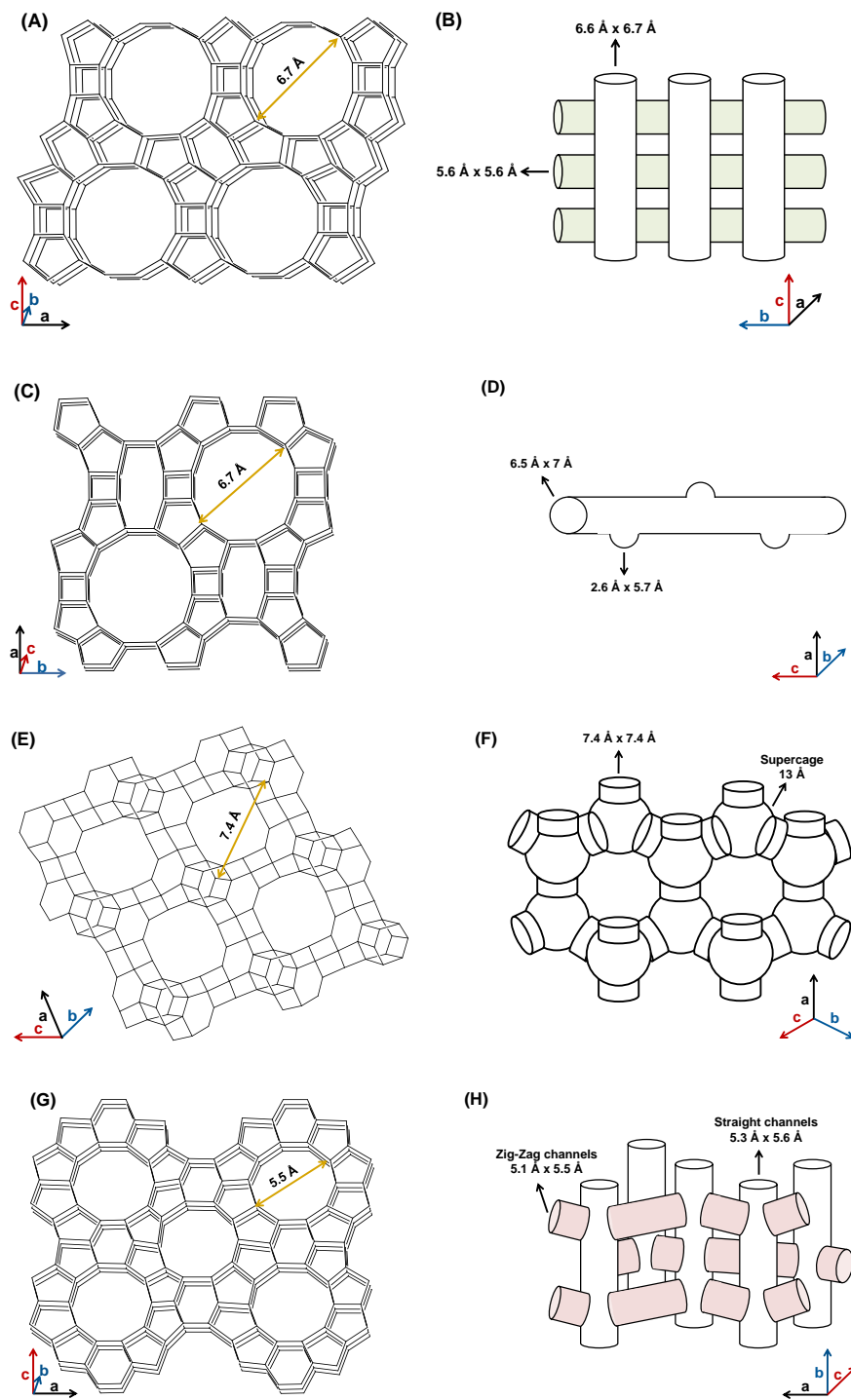


Figure 1.2. Representation of the crystal structure and schematic drawing of the three-dimensional (3D) channel system of (A and B) BEA, (C and D) MOR, (E and F) FAU, and (G and H) MFI zeolites, respectively. The intersection points in figures (A), (C), (E), and (G) represent sites for tetrahedral atoms (termed T-atoms) like silicon. The oxygen would reside near the midpoint of any line.

structures of these four zeolites and their 3D channel systems together with micropore sizes. Isomerization (e.g. paraffin isomerization), alkylation (e.g. isobutane-butene alkylation), cracking, hydrocracking, reforming, dewaxing, methanol to gasoline conversion, NO_x reduction, and epoxidation reactions are just a few examples of important catalytic applications of zeolites.^{19, 22}

Separation is another important application of zeolite structures. Zeolite membranes provide a sustainable, energy efficient route to separate chemicals. The chemical and thermal stability of zeolites and also their separation performance (permeance and separation efficiency) are better than those of the polymer membranes due to the stiff crystalline microporous structure of zeolites.²³ In the past two decades, a number of studies have demonstrated and discussed the purification of gases (e.g. H₂ from CO₂²⁴), organic vapors (xylene isomers²⁵), and alcohols (ethanol from water²⁶) using zeolite membranes.²³

In addition to traditional applications of zeolites in separation, catalysis, and ion-exchange, there are other emerging applications of these porous materials in areas such as optoelectronic and microelectronic devices, sensors, medicine, and green chemistry.^{2, 27-29} For example, the stabilization of metals such as silver (Ag) within the zeolite matrix produces highly active antifungal and antibacterial compounds and immobilization of biomolecules and drugs on the surface of porous nanocrystal zeolite materials can be used for controlled drug delivery applications.²⁹

1.4. Meso-/microporous zeolites

As discussed before, microporous crystalline zeolites are used in numerous commercial applications such as catalysis, separation, and ion-exchange processes due to their unique properties such as large specific surface area, high adsorption capacity, uniform and intricate channels, and well-defined micropores. However, the processing of heavy feedstocks over zeolites is limited by mass transport due to their restricted pore access and slow transport to or from the active sites in the relatively small micropores.³⁰⁻³² These diffusion limitations provoke the low catalyst utilization. In addition, polymerization of by-products or reaction intermediates covering catalytic active sites may occur within the microporous channels of zeolite structures due to the slow diffusion. This can cause catalytic deactivation.²⁰ Vigorous research works have been conducted to make zeolites with more open structures. The meso-/microporous zeolites, coupling the structural feature of microporosity and the fast mass transport consequences of mesoporosity in a single material, can overcome the above mentioned disadvantages of microporous zeolites and thereby enable beneficial effects on the activity, selectivity, and stability of the zeolite catalyst in a wide range of catalytic reactions.^{8, 31, 33-35}

Meso-/microporous zeolites have been studied as catalysts for many catalytic reactions involving bulky molecules such as aromatization of 1-hexane over alkali-treated MFI zeolites³⁶, isomerizations of 1-hexane and 1,2,4-trimethylbenzene over MFI zeolites^{36, 37}, alkylation of benzene over MFI and MOR zeolites^{17, 31, 38}, cracking of cumene and branched polyethylene over MFI zeolites^{37, 39}, and pyrolysis of low density polyethylene over BEA zeolites.¹⁷

Different methods have been explored for the synthesis of meso-/microporous zeolites, mainly including post-synthesis modifications (exfoliation/pillaring of layered zeolites^{21, 40-43} and demetallation (desilication/dealumination) of microporous zeolites^{17, 44-47}) and templating synthesis.²⁰ Figure 1.3 shows the schematic representation of these different synthesis routes for the formation of meso-/microporous zeolites.

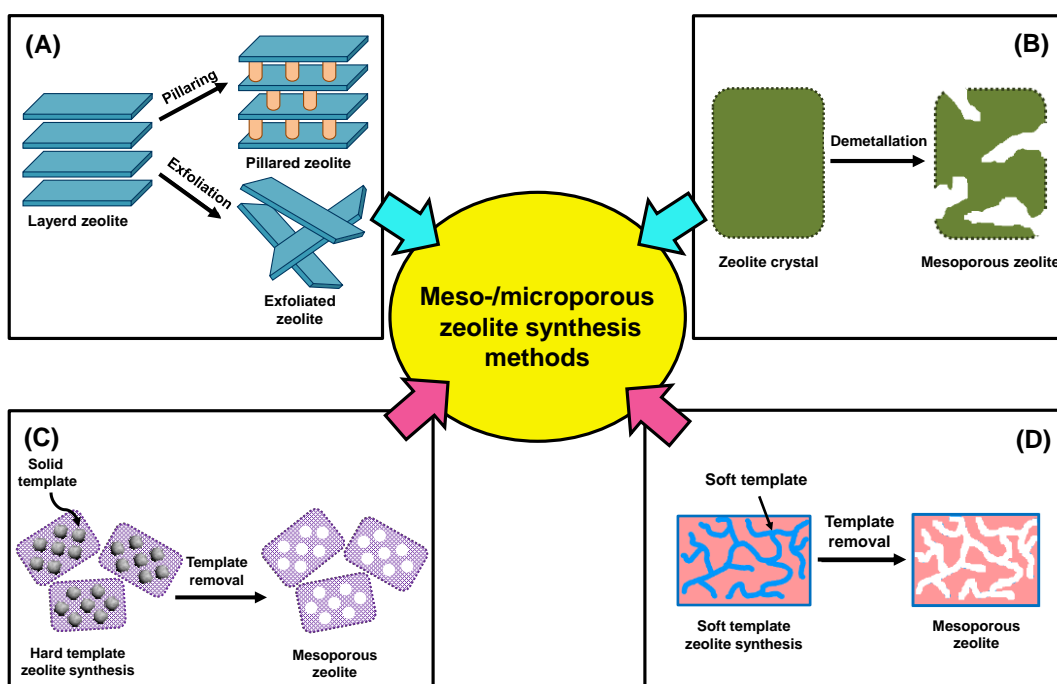


Figure 1.3. Schematic representation of different synthesis routes for formation of meso-/microporous zeolites. Exfoliation/pillaring of layered zeolites (A), demetallation (desilication/dealumination) of microporous zeolites (B), Templating synthesis method using hard templates (C) or soft templates (D).

In exfoliation/pillaring of layered zeolites, the zeolite layers are separated to produce thin layers of zeolite (exfoliation) with high surface area and active site accessibility for large reactant molecules or the layered zeolite precursor is treated with tetraethyl orthosilicate (TEOS) which creates silica pillars between zeolite layers

(pillaring) to preserve the ordered structure and mesoporosity of the zeolite structure after removing the zeolite template by calcination.^{40, 43} The exfoliation/pillaring methods are multi-step methods and are not simple to carry out. Moreover, they are only applicable to a few types of zeolites having layered precursor structures.⁹

In desilication/dealumination of microporous zeolites, silicon/aluminium are partially extracted from the pre-synthesized zeolite framework through chemical degradation in alkali/acidic solutions, giving rise to appearance of mesoporosity. The major drawbacks of these demetallization methods is that they can drastically deteriorate both the framework crystallinity and the morphology of the zeolite and it is also not easy to control the mesopore sizes to be uniform.⁴⁸

The direct generation of intracrystalline mesopores in meso-/microporous zeolites can be achieved by adding templates of a mesopore diameter such as carbon nanoparticles and polymers as hard templates or surfactant micelles as soft templates.⁴⁹ Different templating procedures have been developed to synthesize meso-/microporous zeolites until now, but they are usually multi-step and tedious to carry out.

There is only a limited capability of tuning the meso-/microporosity of the synthesized zeolites and controlling their pore size and active site distributions for most of the above mentioned meso-/microporous synthesis methods. Furthermore, understanding the correlations between the meso-/microporosity of the zeolites and their catalytic performances in different catalytic reactions, has not been systematically investigated. Therefore, it is necessary to create a simple one-step synthesis approach to produce meso-/microporous zeolites with tunable textural and

catalytic properties in order to overcome these above mentioned disadvantages of the available methods for meso-/microporous zeolite synthesis.

1.5. Template synthesis of meso-/microporous zeolites

Synthesis of zeolites using templates have been studied for creating different zeolite structures. Traditionally, the small molecular zeolite templates such as alkali metal ions or organic amine or ammonium cations whose sizes are similar to or smaller than the zeolite micropore dimensions are used to assist zeolite micropore formation (microporogen). The reason is the special role of this molecular zeolite template in stabilizing the microporous zeolite structure which is due to the combination of several factors. Charge, hydrophobicity, and geometry of the template are among these factors, which all lead to energetically favorable associations between aluminosilicate or silicate anions and the template and promote the zeolite nuclei formation. Altering the length of the alkyl chain or simple substitution of the chemical groups of the molecular template can change the nucleation of the zeolite structure.⁵⁰

The combination of different molecular zeolite templates have also been used to direct the formation of zeolites with different properties. For example, microporous ferrierite (FER) zeolite structures have been produced using different combination of templates such as quinuclidine/1-benzyl-1-methylpyrrolidinium (bmp)⁵¹, tetramethylammonium (TMA)/pyrrolidine⁵², and TMA/bmp⁵³. The results showed that the active site location in these microporous FER zeolite structures is different from those synthesized using one molecular template and a good correlation between

active sites locations/accessibility and catalytic activity of the synthesized zeolites was found.⁵²

On the other hand, the large organic assemblies such as polymers or objects such as carbon beads or fibers are usually used as hard templates to create mesopores in zeolites (mesoporegen).⁵⁴ The most important drawbacks of these methods are the damage to the zeolite microporous structure using high combustion temperatures needed for removal of carbon templates and limitation that the low melting point of polymer templates induces for hydrothermal synthesis of zeolites which is usually needed to be carried out at high temperatures. Using soft templates such as surfactant molecules is another strategy to produce meso-/microporous zeolites. Surfactants are molecules with two important distinct chemistries: a hydrophilic head group, which is often charged and a hydrophobic tail.⁹ These surfactant molecules can successfully produce ordered mesoporous materials as reported by Mobil Oil researchers in 1992⁵⁵, but the resulted mesoporous structures cannot be considered as truly zeolitic materials because their pore walls are completely amorphous. Different authors realized soon that the use of mixed template systems (dual templates) such as a small organic molecular zeolite template and a large organic surfactant might be a proper strategy to generate the crystalline meso-/microporous zeolite structures.

The dual template synthesis of meso-/microporous zeolites have been investigated by using the large cetyltrimethyl ammonium bromide (CTAB) surfactant template (which is usually employed to synthesize ordered mesoporous silicas) and small zeolite molecular templates.^{44, 56} At the end, only intimate mixtures of small zeolite crystals and amorphous mesoporous silica were prepared. It has been shown

that the two templates functioning in a sequential way directed the formation of mesoporous silica phase by CTAB followed by formation of zeolite phase assisted by molecular zeolite template.^{49, 57} A recent report by Hensen et al. showed that the synthesis of crystalline mesoporous SSZ-13 zeolite by combining N,N,N-trimethyl-1-adamantanammonium hydroxide and $C_{22}H_{45}-N^+(CH_3)_2-(CH_2)_4-N^+(CH_3)_2-C_4H_9Br_2$, however, was successful, presenting the potential of meso-/microporous zeolites synthesis using partial replacement of the molecular zeolite template (microporogen) by a surfactant molecule (mesoporogen).⁵⁸ Therefore, it seems that the design of new simple dual template synthesis strategies with the ability to overcome the incompatibility between the two templates and the potential to be applicable to a wide range of meso-/microporous zeolites with various structures is demanding.

1.5.1. Dual template synthesis of meso-/microporous lamellar zeolites

Even though various combinations of dual templates, including molecular zeolite templates and large organic surfactants have been used to produce hierarchical meso-/microporous zeolite structures by different researchers^{56, 58-60}, but producing an ordered mesoporous zeolite structure is still a big challenge. A breakthrough in the synthesis of hierarchical zeolites was the application of one template with dual-scale functionality (meso-/microporogen) introduced by Ryoo et al.^{43, 61} They synthesized a polydiquatery ammonium surfactant template ($[C_{22}H_{45}-N^+(CH_3)_2-C_6H_{12}-N^+(CH_3)_2-C_6H_{13}]Br_2$, C₂₂₋₆₋₆) and used it in the zeolization process, which led to the coherent assembly of the zeolite layer and the surfactant molecules to produce two-dimensional (2D) lamellar MFI zeolite nanosheet structures. The resulted lamellar

zeolite structures showed high catalytic performances compared to their solely microporous zeolite counterparts in different reactions involving bulky molecules such as methanol-to-hydrocarbon conversion.^{61, 62} The poly-quaternary ammonium portion of the surfactant templates the microporous MFI layer pore structure, while the long alkyl tail (-C₂₂H₄₅) serves as a space-filler between the MFI layers to form the lamellar mesostructure. The detailed structural effects of the surfactant molecule such as number of ammonium groups, length of the surfactant tail, type of alkyl moieties in the terminal ammonium, and etc. on formation of layered MFI zeolite structures have also been investigated by Ryoo et al.⁶³

The near single unit-cell thickness (2-3 nm) of the MFI nanosheets produced using this new template synthesis route introduced by Ryoo et al. could open new opportunities to tune their structure and control the molecular transport with nanometer (nm)-accuracy during the reactions involving bulky molecules, but the layered zeolite structure collapsed after removing the template by calcination^{18, 61, 64} and the mesoporosity of the synthesized sample decreased to high extent. Therefore, the pillaring process using inorganic tetraethyl orthosilicate (TEOS) was carried out as the second step of the zeolite synthesis by Ryoo and co-workers to produce pillars between the zeolite layers and preserve the zeolite ordered layered structure upon calcination.⁴³ Using a combination of the small organic molecular zeolite template and the large organic surfactant as dual templates might be a proper strategy to generate the zeolite nanosheet assemblies with preserved mesoporosity after calcination without any need to run the pillaring process for this purpose. The surfactant template and molecular template hypothetically can direct the formation of

zeolite lamellae of the meso-/microporous zeolite structures and the microporous pillars between the zeolite layers, respectively.

Other morphological lamellar zeolite structures using C_{22-6-6} as the template have also been synthesized by other researchers for different applications. For example, Nair et al.⁶⁵ used two-step synthesis approach to produce hybrid of lamellar-bulk MFI zeolite structures which involved the pre-synthesis of the bulk MFI zeolite core by tetrapropylammonium hydroxide (TPAOH) as the molecular template, followed by the epitaxial growth of the 2D MFI zeolite lamellae on it using C_{22-6-6} as the template. The control over the sizes of the microporous and mesoporous domains was achieved by employing MFI bulk zeolite with different particle sizes and changing the synthesis conditions for the lamellar shell. These synthesized MFI structures were used to fabricate a composite zeolite/polymer membrane. The resulted membrane showed high separation efficiency for mixture of carbon dioxide (CO_2) and methane (CH_4) which was explained by the high degree of zeolite-polymer adhesion during the formation of these composite membranes due to the roughened yet highly porous surface morphology of the hybrid lamellar-bulk MFI zeolite particles.⁶⁵

Again, it seems that a new simple one-step synthesis method combining the zeolite molecular template and the surfactant molecule together as dual templates while adjusting the relative concentration of them in the synthesis recipe is a good strategy to produce different morphological zeolite structures with new textural properties between those related to bulk microporous zeolite or highly mesoporous multi-lamellar 2D zeolite nanosheet assemblies. Thus, the potential application of

these new synthesized meso-/microporous lamellar zeolite structures with various morphologies is kept as broad as possible.

1.5.2. Tuning the catalytic performance of meso-/microporous lamellar zeolites

Catalysis is one of the most important applications of zeolites. The acidity of the zeolites originates from replacement of tetrahedral Si atoms in their structures by Al atoms. Trivalent Al atoms (Al^{+3}) are tetrahedrally coordinated by oxygen in the crystalline zeolite framework. This causes a charge mismatch, which is compensated by the extra-framework cations such as sodium ions (Na^+). The Na^+ ions can be exchanged with other cations like K^+ or H^+ . The H^+ -ionic form of the zeolites after ion-exchange process can exhibit Lewis acidity and also Brønsted acidity properties. The Brønsted acid sites are attributed to bridging OH groups between Al and Si tetrahedra, while the Lewis acid sites have been associated to the presence of extra-framework aluminum (Al_{EF}) species mainly showing octahedral structures.²² Therefore, adding the Al to the synthesis recipe of zeolites in order to produce acid sites in zeolite structures is a key factor that needs to be investigated for their catalytic applications.

It is well known that Si/Al ratio affects the morphology, acidity, hydrophobicity/hydrophilicity, textural characteristics, and catalytic performance of the zeolites.^{43, 66-68} As mentioned earlier, meso-/microporous zeolites have higher reaction rates and/or different selectivity and stability compared to their solely microporous zeolite analogues. The better catalytic performance observed for meso-/microporous zeolites is usually attributed to the enhanced accessibility provided to the active sites of these structures for reactants and facilitated mass transport

properties originating from the unique morphology of these materials.⁶⁹⁻⁷² A few researchers such as Ryoo et al.⁷³ have reported the presence of acid sites with different strength on the external surface of the meso-/microporous lamellar MFI structures compared to those inside the micropores, however, the role of external acidity (active sites on external surface and in pore mouth region) on the catalytic performance of the meso-/microporous zeolite materials has not been yet studied/understood comprehensively. Therefore, it is necessary to study the spatial distribution of different types of acid sites and their influences on the catalytic performance of the template synthesized meso-/microporous lamellar zeolites carefully to evaluate the potential of tuning the acidity of these zeolite catalysts beside their textural properties for industrially important catalytic reactions involving bulky molecules such as Friedel-Crafts alkylation/acylation and also etherification/esterification reactions.

1.6. Dual template synthesis of meso-/microporous composite zeolites

Composites of two or more different types of zeolites have attracted continuous attention during the past decade. The reason is that most of the newly developed catalytic processes are so complex that single component catalysts cannot easily provide the high performance requirements related to these processes and composite catalysts which combine the two or more different components as catalysts, are much more efficient for this purpose.⁷⁴⁻⁷⁷ For example, in order to achieve high separation power, zeolites must have pore diameters close to the species that are to be separated. However, such zeolites have been reported to often have low

adsorption capacity.^{74, 78, 79} Similarly, zeolites with high separation power usually show low catalytic activity due to intracrystalline diffusion constraints.^{74, 76, 80} Therefore, zeolites with multiple level porosities are desired to achieve concurrently effective adsorption, separation, and catalysis. Thus, production of such composite catalysts has great importance and has been studied extensively by many researchers.⁸¹ These composite catalysts usually show high activity, remarkable selectivity, and good resistance to deactivation in comparison to single component catalysts or their physical mixtures.

The composite zeolite system has added advantages of large interfacial area of the catalyst components, special nano-confinement, multifunctionality, and spatially separating functions of each zeolite component according to its unique structure. Thus, synergistic effects of different components of the zeolite composite on catalytic performance of the composite as a single unit, increase the composite catalyst efficiency for complicated and multi-step reactions needing multi operation units and multi-step isolation of reaction intermediates.⁸¹⁻⁸³ However, despite the above mentioned advantages of composite zeolites over single component zeolite catalysts, the available methods for their synthesis are usually multi-step and tedious to carry out. The reason is the difference of lattice parameters and hydrothermal synthesis conditions (such as time and temperature) for the formation of different types of zeolite framework which makes the synthesis of these composites a difficult task, so it is necessary to develop a one-step synthesis route for facile production of these composite zeolites.^{75, 84-86}

Using a simple one-step dual template synthesis method by selecting the proper templates necessary for production of each zeolite framework component of the zeolite composite and optimizing the synthetic recipe and conditions might be a good strategy to produce meso-/microporous zeolite composites with wider range of applications compared to single type zeolite catalysts. For example a combination of C₂₂₋₆₋₆ as the template for lamellar MFI formation and a molecular zeolite template for other types of zeolites such as BEA, MOR, and LTA can be used as dual templates to produce different meso-/microporous lamellar zeolite composites such as BEA/MFI, MOR/MFI, and LTA/MFI, respectively.

1.7. Research objectives

The main objective of this research work is to create a simple and tunable dual template synthesis strategy to precisely engineer the hierarchical meso-/microporous lamellar zeolites at the micro- and mesoporosity levels in one-step by using molecular ammonium cation (microporogen) and polyquaternary ammonium surfactant (mesoporogen) as dual templates in order to maximize their transport and catalytic properties. The central thesis of this research is that it is possible to systematically control the composition of the dual templates and therefore, the templating consequences on the porosity and acidity of the synthesized zeolite structures.

1.8. Thesis outline

This dissertation which focuses on fabrication of meso-/microporous zeolite structures using template synthesis method for tuning their structural properties and

catalytic performances is divided into 6 chapters. Chapter 2 describes a simple dual template synthesis strategy developed to achieve one-step design of meso/microporous MFI nanosheet assemblies. Molecular template TPAOH and diquatery ammonium surfactant molecule C_{22-6-6} were used as the dual templates. The results indicate that the morphology and mesoporosity and as a result catalytic activity of the synthesized nanosheets assemblies can be simply tailored by adjusting the molar ratio of the templates in the zeolite synthesis recipe and the proposed dual template synthesis method has the potential to be extended to other types of zeolites by choosing proper templates.

Chapter 3 focuses on using the introduced one-step dual template synthesis method in chapter 2 for facile fabrication of hybrid lamellar-bulk MFI (HLBM) zeolite structures consisting of a lamellar MFI zeolite structure on the surface of the bulk MFI zeolite core. The influences of several parameters including the concentration of the templates, hydrothermal synthesis time, and ageing temperature and time on the HLBM formation were investigated. The sizes of lamellar and bulk domains in these zeolite structures and as a result their meso- and micro-porosity can be modulated by simply tuning these parameters. A possible growth scheme for the formation of these HLBM structures is discussed. The ability to form hybrid zeolite particles with tunable meso-/microporosity is important to keep their potential application as broad as possible. The dual template synthesis approach presented in chapter 3 is potentially applicable to form other types of hybrid lamellar-bulk zeolite materials.

Chapter 4 describes the application of the synthesized HLBM zeolites in chapter 3 for acid-catalyzed reactions of benzyl alcohol in mesitylene after adding the aluminum to the zeolite synthesis recipe. The results reveal that parallel alkylation and etherification reactions are tailored by the tunable external surface area and external acidity of the HLBM zeolites and highlight the role of external acidity of meso-/microporous zeolites with variable strength in determining the selectivity of acid-catalyzed reactions. These results extend the scope of observed catalytic behavior of meso-/microporous materials beyond those reflecting only the facilitated mass transport and accessibility to the internal acid sites.

Chapter 5 reports the successful attempt for extending the synthesis procedure developed in Chapter 2 for synthesis of hybrid core-shell structures of MFI to other types of zeolite composites containing two different types of zeolite structures by choosing proper templates that resulted in production of core-shell bulk BEA-lamellar MFI (BBLM) composite zeolites in one-step. The catalysis tests showed that BBLM zeolites had significant higher activity and durability than single zeolites or their physical mixture. The one-step dual template synthesis method described herein is versatile and facile, which may prove to be a general platform for core-shell hierarchical zeolite design in the unit-cell scales of zeolites and with potentially broader applicability to other porous materials.

Chapter 6 summarizes the progress in synthesizing different meso-/microporous lamellar zeolite structures with tunable structural and catalytic performance using the developed one-step dual template synthesis method. Possible

future research opportunities for production of meso-/microporous zeolites using the proposed dual templating synthesis method are also outlined in chapter 6.

Chapter 2: Dual template synthesis of meso-/microporous MFI zeolite nanosheet assemblies with tailored activity in catalytic reactions

2.1. Introduction

As discussed in section 1.3 of chapter 1, traditional microporous zeolite structures are widely used in catalysis, adsorption, ion-exchange, and separation processes in chemical and petrochemical industries mainly because of their well-defined structure and shape selectivity of their angstrom-size micropores,^{1, 14, 20, 44, 63, 87-91} but they have limited accessibility for relatively large reactant molecules due to the restricted access and slow transport to or from the active sites in the relatively small micropores.^{30, 32, 92} Hierarchical zeolites contain both micro- and mesopores, which allow for facile pore access and fast transport of bulky molecules and thereby enable beneficial effects on the activity, selectivity, and/or stability in a wide range of catalyzed reactions. Aromatization⁹³, isomerization^{93, 94}, alkylation^{38, 69, 95}, cracking^{39, 94}, pyrolysis^{36, 96}, hydrodesulfurization⁷¹, and the synthesis of relatively bulky molecules for the pharmaceutical, fragrance, and agrochemical industries³⁷ are some examples of these catalytic reactions.

The methods for synthesis of hierarchical zeolites have been extensively studied, including exfoliation or pillaring of layered zeolites⁹⁷⁻⁹⁹, growth of zeolites in templates^{37, 100, 101}, desilication or dealumination of microporous zeolites^{102, 103}, and synthesis of very thin zeolite nanosheets⁶¹. Zeolite templates, either small molecular

zeolite templates or large organic assemblies, are commonly added to aid the growth of hierarchical zeolite structures in many of these synthesis processes.^{51, 54, 57, 58, 104}

Traditionally, the small molecular zeolite templates are alkali metal ions or organic amine/ammonium cations whose sizes are similar to or smaller than the zeolite micropore dimensions to assist micropore formation. For example, tetrapropylammonium hydroxide (TPAOH) is usually used as a molecular template to produce microporous MFI zeolites.¹⁰⁵⁻¹⁰⁹ On the other hand, large organic assemblies such as surfactant micelles, polymers, and carbon beads are usually used to create mesopores. A breakthrough in the synthesis of hierarchical zeolites was the application of gemini-type, diquatery ammonium surfactants in the zeolization process as single templates (mesoporegens), which led to the coherent assembly of the zeolite layer and the surfactants to produce two dimensional (2D) lamellar MFI zeolite nanosheet structures.⁶¹ The layered structure of these MFI zeolites is collapsed after template removal by calcination (see Figure 2.1).^{18, 54, 61} Accordingly, a pillaring treatment of the zeolite lamellae is required in order to preserve the ordered mesoporous structure of the zeolite catalyst.⁴³ Thus, a one-step synthesis of the meso-

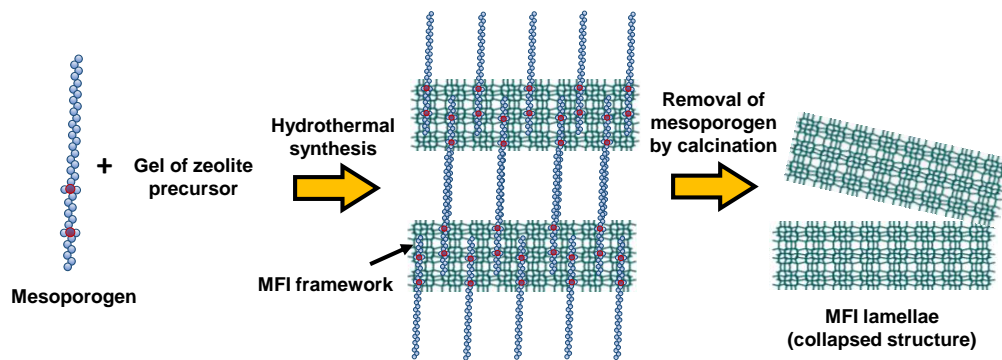


Figure 2.1. Production of MFI zeolite lamellae using diquatery ammonium surfactant as mesoporegen by single template method.

/microporous MFI zeolite nanosheet assemblies with preserved mesoporosity is desired.

Usually the methods used for meso-/microporous zeolites synthesis such as demetallation and templating methods are multi-step processes. Moreover, the mesoporous and microporous domains in these materials generally have limited tunability. The use of mixed template systems (dual templates) such as a small organic molecular zeolite template to assist micropore formation (microporogen) and a large organic surfactant to create mesopores (mesoporogen) might be an appropriate strategy to generate the MFI nanosheet assemblies with preserved mesoporosity. The surfactant template and molecular template hypothetically direct the formation of zeolite lamellae of the hierarchical materials and the microporous zeolite pillar between zeolitic lamellae, respectively (see Figure 2.2).

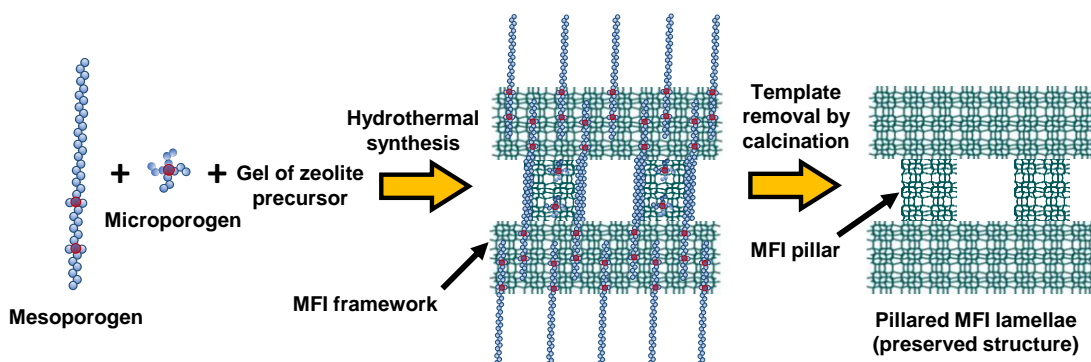


Figure 2.2. Production of supported zeolite lamellae by dual template method (hypothesized scheme).

As discussed before in section 1.5 of chapter 1, dual template synthesis method using small molecular zeolite templates have been successfully employed for production of microporous zeolites and adjusting their peoperties such as acid site

location,^{51, 54, 57, 58, 104} but attempts to synthesize crystalline hierarchical meso-/microporous zeolites by mixing the large organic surfactant molecules and small zeolite molecular templates have been reported to be unsuccessful because of the incompatibility of the two templates.^{56, 59, 60} Thus, it is necessary to develop a proper dual template synthesis method with the capability to overcome this issue in designing meso-/microporous zeolite structures for different applications.

Here, we have employed a simple and easy to run dual template synthesis strategy to achieve one-step design of meso-/microporous MFI nanosheet assemblies with tailored morphology, mesoporosity, and catalyst activity. A combination of the emerging diquatery ammonium surfactant template ($[\text{C}_{22}\text{H}_{45}\text{-N}^+(\text{CH}_3)_2\text{-C}_6\text{H}_{12}\text{-N}^+(\text{CH}_3)_2\text{-C}_6\text{H}_{13}]\text{Br}_2$, C₂₂₋₆₋₆) and the MFI zeolite molecular template (TPAOH) were used as dual templates to assist the formation of mesopores and micropores, respectively, respectively. The composition of the dual templates in the synthesis was systematically modulated and their templating consequences on the zeolite morphology, porosity, and catalytic performance were investigated. The number of Brønsted acid sites contained within each catalyst was assessed in chemical titration studies using dimethyl ether (DME) as a probe molecule. The reactivity of Brønsted acid sites in MFI nanosheet assemblies was evaluated by ethanol dehydration reactions under strict kinetic control conditions. The catalytic performance of Brønsted acid sites in these zeolites under diffusion constrained conditions was examined by the liquid phase catalytic conversion of benzyl alcohol in mesitylene. Our previous study showed that the parallel reactions, alkylation of mesitylene with benzyl alcohol and self-etherification of benzyl alcohol in catalytic conversion of

benzyl alcohol in mesitylene, could be controlled to occur over either external or internal Brønsted acid sites of the catalysts.¹⁶ The alkylation reactions occurred exclusively on external surface of the catalysts due to the exclusion of bulky mesitylene molecules from micropores of MFI show meso-/microporous zeolites enable efficient surface catalysis. The self-etherification reactions occurred exclusively in internal surface of the catalysts by selective deactivation of external acid sites using 2,6-di-tert-butylpyridine (DTBP) titrants show that the meso-/microporous zeolite can mitigate the diffusion constraints due to the reduced diffusion length. In the present study, we used these reactions to evaluate the catalytic performances of the as-obtained MFI zeolite nanosheet assemblies. For comparison to zeolites consisting exclusively of microporous features, the rate and selectivity of Brønsted acid sites for ethanol and liquid phase benzyl alcohol reactions were investigated for ZSM-5 (commercial MFI) under the same experimental conditions.

2.2. Experimental section

2.2.1. Materials for catalyst synthesis and reactions

TPAOH (40wt%), tetrapropylammonium bromide (TPABr, 98%), and benzyl alcohol (99+%) were supplied by Alfa Aesar. Aluminum sulfate hydrate ($\text{Al}_2(\text{SO}_4)_3 \cdot 16\text{H}_2\text{O}$, 98.0-102.0%) was purchased from Mallinckrodt Chemicals. Tetraethyl orthosilicate (TEOS, 98%), sodium hydroxide (NaOH, $\geq 97.0\%$), ammonium hydroxide solution (NH_4OH , 28.0-30.0%), *N,N,N',N'*-tetramethyl-1,6-diaminohexane ($> 99\%$), diethyl ether (DEE), absolute ethanol (200 proof), 1-

bromohexane (98%), ammonium nitrate (NH_4NO_3 , $\geq 99.0\%$), sulfuric acid (H_2SO_4 , 95.0-98.0%), and 2,6-di-tert-butylpyridine (DTBP, $\geq 97\%$) were supplied by Sigma-Aldrich. 1-bromodocosane ($> 98.0\%$) was purchased from TCI, Tokyo Kasei. Acetonitrile (HPLC grade, $< 0.010\%$ H_2O), toluene, and mesitylene (99%, extra pure) were supplied by Fisher Chemicals, VWR International, and Acros Organics, respectively. Deionized (DI) water was used through the experiment. Commercial MFI (CBV 8014) with Si/Al molar ratio of ~ 40 was purchased from Zeolyst International.

The polyquaternary ammonium surfactant was synthesized following a reported procedure⁶¹ as follows: 18.5 g of 1-bromodocosane and 86 g of *N,N,N',N'*-tetramethyl-1,6-diaminohexane were dissolved in 500 mL of acetonitrile/toluene mixture (1:1, v/v) in the glove box. The mixture was then transferred out of the glove box and reacted at 343 K under magnetic stirring (500 rpm) for 10 h. After cooling to ambient temperature, the precipitated product was filtered, washed with DEE, and dried in a vacuum oven at 343 K overnight. A 28 g sample of the resultant product and 12.5 g of 1-bromohexane were dissolved in 150 mL of acetonitrile in the glove box, and then refluxed at 358 K under magnetic stirring (500 rpm) for 10 h in a fume hood. After cooling to ambient temperature, the product was filtered, washed with DEE, and dried in a vacuum oven at 343 K overnight. The as-obtained product was the surfactant $[\text{C}_{22}\text{H}_{45}\text{-N}^+(\text{CH}_3)_2\text{-C}_6\text{H}_{12}\text{-N}^+(\text{CH}_3)_2\text{-C}_6\text{H}_{13}]\text{Br}_2$, designated as C_{22-6-6} .

2.2.2. Dual template synthesis of MFI zeolites

The molar composition of the recipe used for dual template synthesis of MFI zeolites was as follows: $30\text{Na}_2\text{O}/1\text{Al}_2\text{O}_3/100\text{SiO}_2/10\text{C}_{22-6-6}/x\text{TPAOH}/4000\text{H}_2\text{O}/18\text{H}_2\text{SO}_4$, where x equals to 1, 2, 3, 5, 8, 12, and 20, respectively, as listed in Table 2.1. Typically, the hydrothermal synthesis was performed by dissolving 0.7 g NaOH in 3.0682 g DI water, dissolving 0.4 g H_2SO_4 in 4.2 g DI water, and subsequently adding the basic solution dropwise to the acidic solution under vigorous stirring. After cooling the mixture to ambient temperature, $\text{Al}_2(\text{SO}_4)_3 \cdot 16\text{H}_2\text{O}$ was dissolved in it. TPAOH and TEOS were then added sequentially to the mixture and the mixture was stirred vigorously at room temperature for 20 h using a magnetic stirrer. Finally, the mixture was mixed with a C_{22-6-6} solution that was prepared by dissolving 2.1876 g C_{22-6-6} in 15 g DI water at 333 K. After continuously mixing for 2 h at room temperature, the resultant zeolite synthesis gel was transferred into a Teflon-lined stainless-steel autoclave, followed by crystallization for 5 days in rotating Teflon-lined stainless-steel autoclave at 423 K. After crystallization, the zeolite product was filtered, washed with DI water, and dried at 343 K overnight. The as-obtained samples were named MFI-10/1, MFI-10/2, MFI-10/3, MFI-10/5, MFI-10/8, MFI-10/12, and MFI-10/20, respectively after the usage of C_{22-6-6} and TPAOH during synthesis. For comparison, a multi-lamellar MFI was synthesized using the method reported by Ryoo's group⁶¹, which was same as the dual template synthesis of MFI zeolites except that there was no addition of TPAOH. The as-synthesized multi-lamellar sample was designated as MFI-10/0. All zeolite samples were calcined in dry air (1.67 mL s^{-1} , ultrapure, Airgas) by increasing the

temperature from ambient temperature to 873 K at 0.0242 K s⁻¹ and holding the sample at 873 K for 6 h. The Si/Al ratio of each zeolite sample was tentatively controlled to be same by modulating the amount of Si and Al precursors during the zeolite synthesis. MFI-10/2, MFI-10/5, MFI-10/12 and MFI-10/20 were resynthesized by replacing the TPAOH with TPABr in the synthesis recipe as control experiments in order to study the effect of pH changes due to the presence of TPAOH on the morphology of the MFI samples.

Table 2.1. Compositions for crystallization of zeolite nanosheet assemblies by dual template synthesis method.

Catalyst	Composition in molar ratios						
	C ₂₂₋₆₋₆	TPAOH	SiO ₂	Na ₂ O	Al ₂ O ₃	H ₂ O	H ₂ SO ₄
MFI-10/0	10	0	100	30	1	4000	18
MFI-10/1	10	1	100	30	1	4000	18
MFI-10/2	10	2	100	30	1	4000	18
MFI-10/3	10	3	100	30	1	4000	18
MFI-10/5	10	5	100	30	1	4000	18
MFI-10/8	10	8	100	30	1	4000	18
MFI-10/12	10	12	100	30	1	4000	18
MFI-10/20	10	20	100	30	1	4000	18

2.2.3. Ion-exchange of zeolite catalysts

The as-calcined multi-lamellar MFI and dual template synthesized zeolite samples were ion-exchanged three times using 1 M aqueous NH₄NO₃ (weight ratio of zeolite to NH₄NO₃ solution = 1:10) at 353 K for 12 h, and subsequently, collected by centrifugation, washed with deionized water four times, and dried at 343 K overnight.

No ion-exchange process was applied to the commercial MFI since it was purchased in the NH_4^+ -form. All zeolite samples in their NH_4^+ -form were treated in dry air (1.67 mL s^{-1} , ultrapure, Airgas) by increasing the temperature from ambient temperature to 823 K at 0.0242 K s^{-1} and holding the sample at 823 K for 4 h in order to thermally decompose NH_4^+ to NH_3 and H^+ and make the MFI zeolite samples ready for catalytic reactions.

2.2.4. Catalyst characterization

The morphologies and crystal sizes of the synthesized samples were examined by scanning electron microscopy (SEM, Hitachi SU-70) and transmission electron microscopy (TEM, JEM 2100 LaB6). The powder X-Ray diffraction (XRD) data were collected to determine the crystalline phase and ordering structure of the synthesized zeolite nanosheet assemblies. The low and wide angle XRD data were obtained using Bruker D8 Advance Lynx Powder Diffractometer (LynxEye PSD detector, sealed tube, $\text{Cu } K_\alpha$ radiation with $\text{Ni } \beta$ -filter). Nitrogen (N_2) and argon (Ar) adsorption-desorption measurements were carried out at 77 K and 87 K on an Autosorb-iQ analyzer (Quantachrome Instruments), respectively. Prior to the adsorption-desorption analysis, calcined zeolite samples were evacuated overnight at 623 K and 1 mm Hg. Si and Al contents were determined by inductively coupled plasma optical emission spectroscopy (ICP-OES, Department of Earth Sciences, University of Minnesota). All magic angle spinning nuclear magnetic resonance (MAS NMR) spectra were recorded at a field of 11.7 T (Bruker Avance 500). ^{29}Si MAS NMR spectra were recorded at 99.37 MHz using 4 mm rotors at a spinning

speed of 8 kHz, a dwell time of 16.65 μ s, a $\pi/2$ pulse of 4.0 μ s, and a recycle delay of 60 s. All spectra were referenced with respect to tetramethylsilane (0 ppm). ^{27}Al MAS NMR spectra were recorded at 130.34 MHz using 4 mm rotors at 14 kHz spinning speed, a dwell time of 0.5 μ s, a selective $\pi/18$ pulse of 0.3 μ s, and a recycle delay of 0.1 s. An aqueous solution of aluminum sulfate (0.1 M) was used as the external reference (0 ppm).

2.2.5. Determination of acid sites

The number of Brønsted acid sites in each zeolite sample was determined via dimethyl ether (DME) titration experiments given that the active Brønsted acid sites participate in reactions of DME with H^+ to form surface methyl groups, $\text{CH}_3\text{OCH}_3 + 2[\text{SiO}(\text{H})\text{Al}] = 2[\text{SiO}(\text{CH}_3)\text{Al}] + \text{H}_2\text{O}$.^{110, 111} The experimental setup and reaction conditions for chemical titration of acid sites were same as those described by Liu et al.¹¹² Typically, the DME titration experiment was carried out in a tubular packed-bed quartz reactor (10 mm inner diameter) under atmospheric pressure. The catalyst samples (~ 0.05 g) were supported on a coarse quartz disk inside the reactor and were treated in He (50 mL min^{-1} , ultrapure, Airgas) at 773K (1 K min^{-1}) for 3 h prior to cooling in He flow to the reaction temperature of 423K. A mixture of DME/Ar/He (50 mL min^{-1} ; 24.8% DME, 25.2% Ar, and 50% He; Airgas) was introduced by He during each pulse with 120 s intervals. The effluent, physisorbed DME, and water formed upon dehydration reactions were subsequently removed by He (50 mL min^{-1}) for 2.5–3.5 h. A gas chromatograph (Agilent 7890A GC) equipped with a methyl-siloxane capillary column (HP-1, $50.0 \text{ m} \times 320 \mu\text{m} \times 0.52 \mu\text{m}$) connected to

a flame ionization detector (FID) and a packed column (SUPELCO HAYESEP R 80/100 mesh packed column, 12ft) connected to a thermal conductivity detector (TCD) was used to record the titration curves of DME, and the number of Brønsted acid sites was calculated on the basis of these curves using a DME/H⁺ ratio of 0.5. The fourier transform infrared (FTIR) spectra of adsorbed pyridine were used to determine the type and concentration of Brønsted and Lewis acid sites in the catalyst. The spectra were recorded at 393 K under a He atmosphere using a spectrophotometer (Equinox 55, Bruker) equipped with a SpectraTech Collector II diffuse reflectance accessory and the Praying MantisTM High Temperature Reaction Chamber (Harrick). Prior to the measurement, the zeolite sample was dried at 823 K under a He flow for 1 h. After cooling the sample to 393 K, adsorption of pyridine was performed by flowing a mixed pyridine and He gas stream through the catalyst. Following adsorption, the sample was heated to 523 K under a flowing He to desorb the physisorbed pyridine, was cooled to room temperature, and then FTIR spectra were recorded in the range of 4000-400 cm⁻¹ with 128 scans at an effective resolution of 2 cm⁻¹.

2.2.6. Ethanol dehydration reactions

The same experimental setup described for DME chemical titration studies was used for studying ethanol (C₂H₅OH) dehydration reactions on zeolite samples. Catalyst samples (0.015 g - 0.100 g) were treated in He (0.0083 mL s⁻¹, ultrapure, Airgas) at 773 K (0.0167 K s⁻¹) for 3 h prior to cooling in He flow to the reaction temperature. Steady-state ethanol dehydration reactions were carried out under

atmospheric pressure, in the temperature range of 384-425 K, and under conditions of differential conversion ($< 2.0\%$). C_2H_5OH reactant was introduced into flowing gas streams as a liquid using a syringe pump (New Era Pump Systems, Inc.). Liquid ethanol ($2.85 \times 10^{-7} - 2.4 \times 10^{-6} \text{ mol s}^{-1}$) was vaporized at 383 K into a gas flow which contained He ($0.55\text{-}9.4 \text{ mL s}^{-1}$ at normal temperature and pressure, NTP condition) and Ar ($0.0137\text{-}0.0297 \text{ mL s}^{-1}$ at NTP condition, Airgas) as internal standard. The same gas chromatograph (Agilent 7890A GC) described in section 2.2.5 was used to calibrate and separate the reactants and products.

2.2.7. Catalytic conversion of benzyl alcohol in mesitylene

The catalytic performance of acid site in the synthesized zeolite samples under diffusion constrained conditions was investigated by the liquid phase catalytic conversion of benzyl alcohol in mesitylene. This liquid phase reaction was carried out in a three-necked round bottom flask (100 mL) equipped with a reflux condenser and heated in a temperature controlled oil bath under atmospheric pressure and magnetic stirring (1" stirring bar and 500 rpm stirring speed) conditions. The experimental setup for this catalytic reaction has been shown in Figure 2.3. In a typical experiment, 15 mL of mesitylene was added to the desired amount of zeolite catalyst, which had been activated at 823 K in flowing air (1.67 mL s^{-1}) for 4 h. The reaction mixture was maintained for 0.5 h at the required reaction temperature and stirring conditions and then 0.25 mL of benzyl alcohol was added. This moment of addition of benzyl alcohol to the reaction mixture was taken as the initial reaction time. Liquid samples

were withdrawn at regular time intervals and analyzed by the same gas chromatograph described in section 2.2.5.

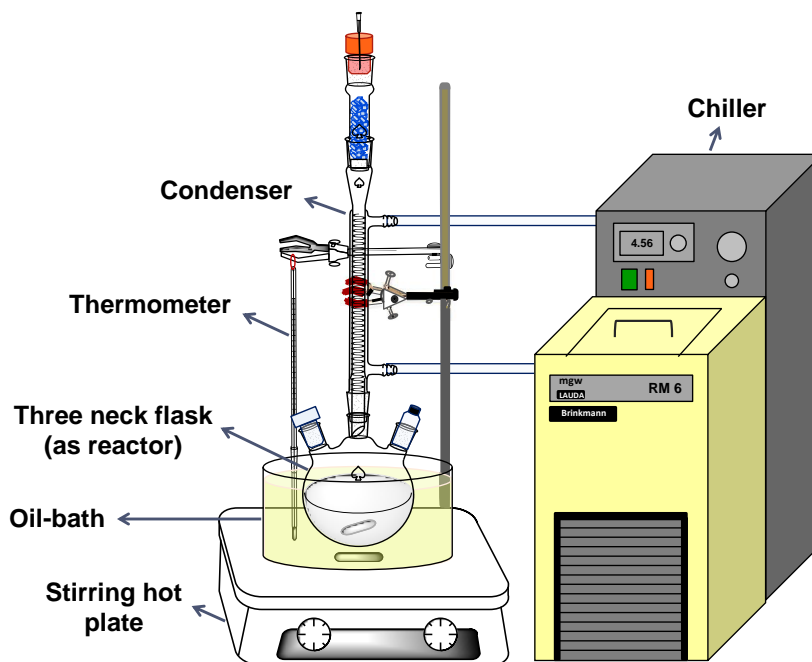


Figure 2.3. Experimental setup for catalytic conversion of benzyl alcohol in mesitylene.

The DTBP poisoning experiment was carried out under the same reaction conditions described above except adding DTBP into the reactant suspension. Typically, zeolite catalyst, DTBP, and mesitylene were added to the reactor in sequence, and then the reactant mixture was held at the reaction conditions for 2.5 h before adding the benzyl alcohol. Excess amount of DTBP (moles of DTBP were 5 times higher than that of active sites in zeolite catalyst) and longer mixing time prior to the benzyl alcohol addition ensured base molecules (DTBP) completely poisoned active sites on the geometric and mesoporous surfaces (external surfaces) of zeolite catalysts. The influence of external mass transfer limitations on the reaction rates was

ruled out by running the reactions at a high enough stirring speed (500 rpm), showing a further increase in the stirring speed did not enhance the reaction rate. The reactant mixture without addition of zeolite catalysts showed no conversion of benzyl alcohol under the investigated reaction conditions.

2.3. Results and discussion

2.3.1. Textural properties of zeolite catalysts

SEM was employed for direct visualization of different crystal morphologies of meso-/microporous MFI zeolite nanosheet assemblies. Figure 2.4 shows the representative SEM images for MFI zeolites synthesized by using different molar ratios of C_{22-6-6} /TPAOH (refer to Table 1). The MFI-10/0 sample, shown in Figure 2.4(A), is comprised of intertwined nanosheet-like particles with randomly organized structure, similar to multilamellar MFI reported by Na et al.^{61, 113} With addition of small quantity of TPAOH to the synthesis recipe, as shown by MFI-10/1 and MFI-10/2 in Figure 2.4(B)-(C), the crystal morphology similar to that of MFI-10/0 is observed, but the MFI nanosheets become thicker. A continual increase of TPAOH in the synthesis recipe increases the thickness of the MFI nanosheets and changes the nanosheet arrangement to a house-of-cards like morphology, as shown in Figure 2.4(D)-(F). Finally, the further increase of TPAOH concentration in the synthesis recipe (MFI-10/12 and MFI-10/20) resulted in dense plate-like particles, as illustrated in Figure 2.4(G)-(H). SEM only shows the surface morphology of the zeolite

samples. A close examination on each sample was conducted by TEM observation (results shown in Figure 2.5). Figure 2.5(A)-(C) shows that MFI-10/0, MFI-10/1, and

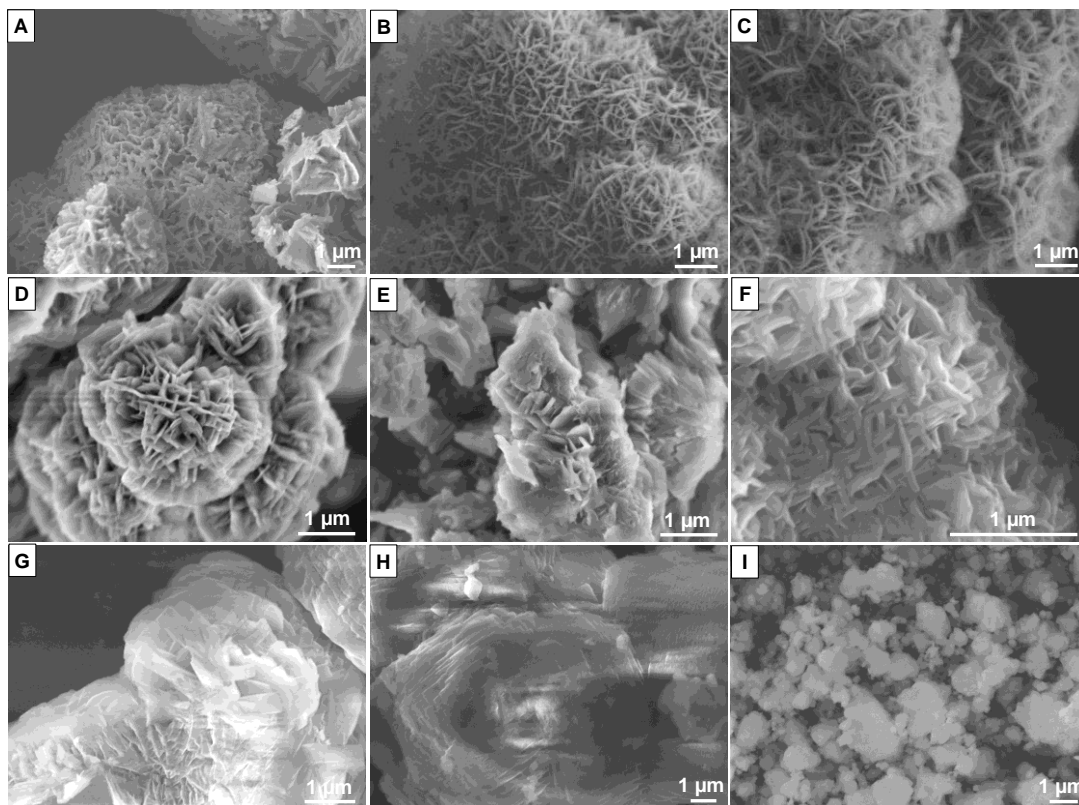


Figure 2.4. SEM images of MFI zeolites obtained with C_{22-6-6} /TPAOH molar ratio of (A) 10/0, (B) 10/1, (C) 10/2, (D) 10/3, (E) 10/5, (F) 10/8, (G) 10/12, and (H) 10/20, respectively, in the dual template synthesis. (I) Commercial MFI with Si/Al ratio of ~ 40 was used for comparison.

MFI-10/2 have uniform plate-like morphologies ranging from the center to the surface of the zeolite nanosheet assemblies. MFI-10/3, MFI-10/5, and MFI-10/8 samples shown in Figure 2.5(D)-(F), however, contain a fraction of ordered needle-like zeolite nanocrystals attached to the plate-like nanosheet structures. With a further increase in TPAOH content in the synthesis recipe, the MFI nanosheets grew into

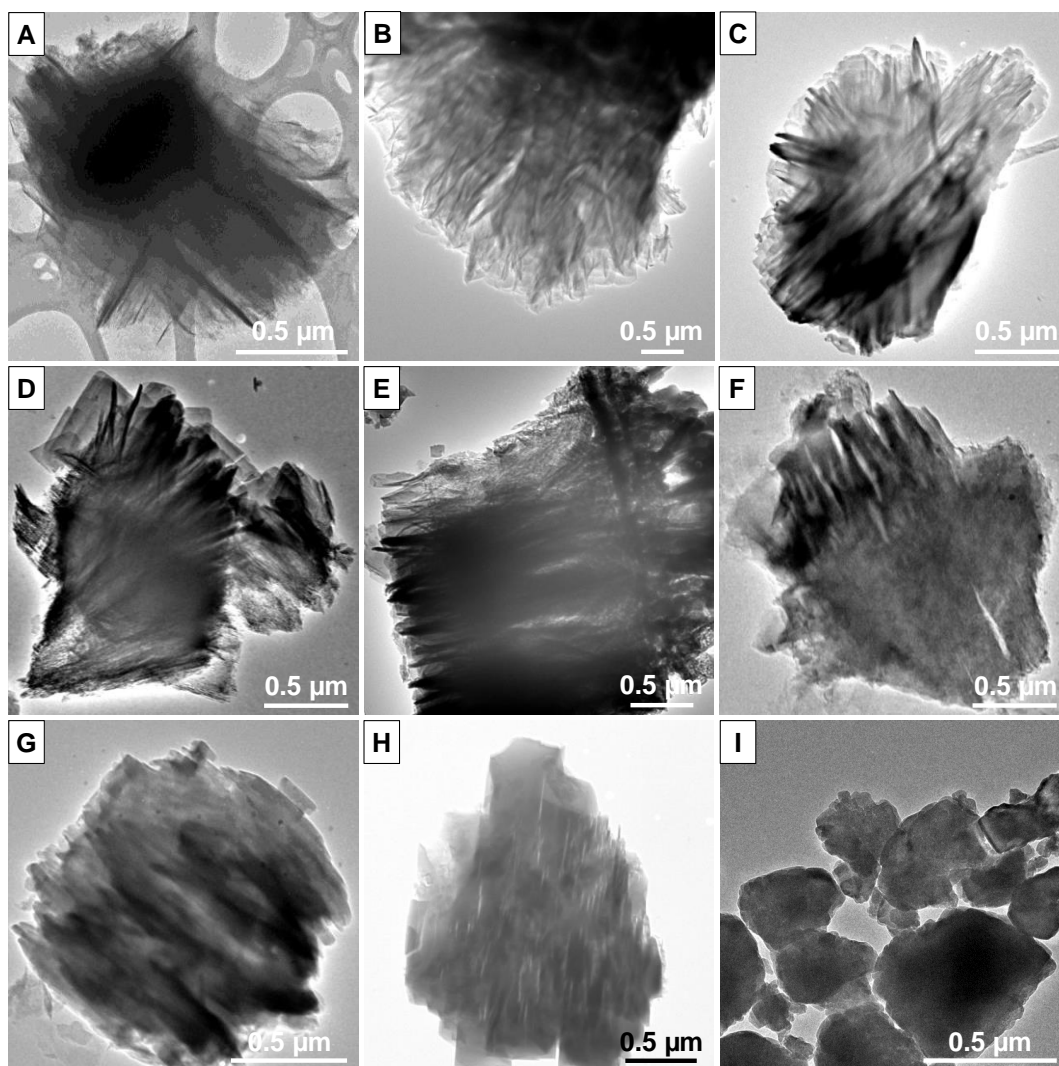


Figure 2.5. TEM images of MFI zeolites obtained with C_{22-6-6} /TPAOH molar ratio of (A) 10/0, (B) 10/1, (C) 10/2, (D) 10/3, (E) 10/5, (F) 10/8, (G) 10/12, and (H) 10/20, respectively, in the dual template synthesis. (I) Commercial MFI with Si/Al ratio of ~ 40 was used for comparison.

uniform thick plates assembled into bulk particles, as shown in Figure 2.5(G)-(H).

It has been reported that C_{22-6-6} surfactant comprises of a hydrophilic organic amine group where the zeolite is formed and a hydrophobic alkyl group self-assembled into a specific lamellar micellar structure which limits the subsequent growth of the zeolite. The combination of these two groups is responsible for the

formation of stable 2D MFI nanosheets.^{61, 63, 114} The reduction of hydrophobic alkyl length in the polyquaternary ammonium surfactants results in thick zeolite nanosheets formation in the synthesis.^{14, 63, 114} The shorter alkyl group does not have sufficient hydrophobic interaction with the alkyl groups in neighboring molecules to form a specific micellar structure, which causes 3-dimensional (3D) growth of the zeolite crystals. The growth of thick zeolite nanosheets with increasing TPAOH content in the present study indicates that the TPAOH might act as a co-template which stays close to C₂₂₋₆₋₆ alkyl groups inducing 3D growth of the crystals. However, when the content of TPAOH in the synthesis is appropriate such as C₂₂₋₆₋₆/TPAOH ratios of 10/3-10/8, TPAOH might result in sparse growth of MFI nanocrystals in MFI nanosheet assemblies, which can hypothetically act as ‘pillar’ to preserve multilamellar MFI mesoporosity upon collapses of zeolite nanosheets by calcination. Figure 2.4(I) and Figure 2.5(I) show commercial MFI is comprised of irregular shaped particles with sizes ranging from 50 nm to 3000 nm.

Figure 2.6 shows the XRD patterns of the synthesized zeolite samples before template removal by calcination. The wide angle XRD patterns (Figure 2.6(A)) confirm that all samples are highly crystallized MFI, resembling the characteristic of a crystalline MFI reported by Ryoo et al.⁶¹ The low-angle XRD patterns in Figure 2.6(B) indicate that all the zeolite nanosheet assemblies have the multilamellar features. The presence of first ($2\theta \sim 1.5^\circ$) and second ($2\theta \sim 4.6^\circ$) reflections (refer to Figure 2.6(A)-(B)) in samples MFI-10/0, MFI-10/1, and MFI-10/2 are well resolved, demonstrating that the long-range structural order in these materials is excellent.

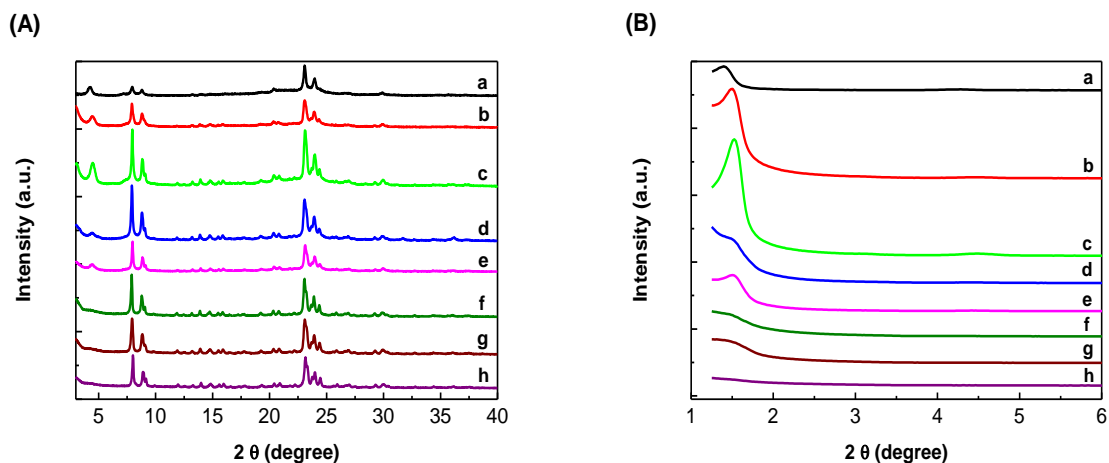


Figure 2.6. Wide angle (A) and low angle (B) XRD patterns of MFI zeolites synthesized with C₂₂₋₆₋₆/TPAOH molar ratio of (a) 10/0, (b) 10/1, (c) 10/2, (d) 10/3, (e) 10/5, (f) 10/8, (g) 10/12, and (h) 10/20, respectively.

In samples MFI-10/3 - MFI-10/20, the reflections of the low angle XRD are gradually less resolved with increasing TPAOH content in the synthesis recipe, showing the long-range structural order decreases which might be caused by the growth of MFI nanoparticles attached to the zeolite nanosheets. The XRD patterns of the zeolite nanosheet assemblies were re-measured after removal of the organic templates by calcination (data not shown). All the samples had the characteristic signature reflections of crystalline MFI diffraction patterns, while the low angle reflection peaks disappeared for all the investigated samples, indicating that the long-range order of the lamellar structures was destroyed by collapses of zeolite lamellar structures during the calcination.

N₂ adsorption-desorption isotherms were used to reveal the porosity features of MFI zeolites synthesized by the dual template method. Figure 2.7(A) shows the synthesized samples exhibit type-IV N₂ isotherms with a hysteresis loop corresponding to capillary condensation in mesopores.^{115, 116} At the relatively low

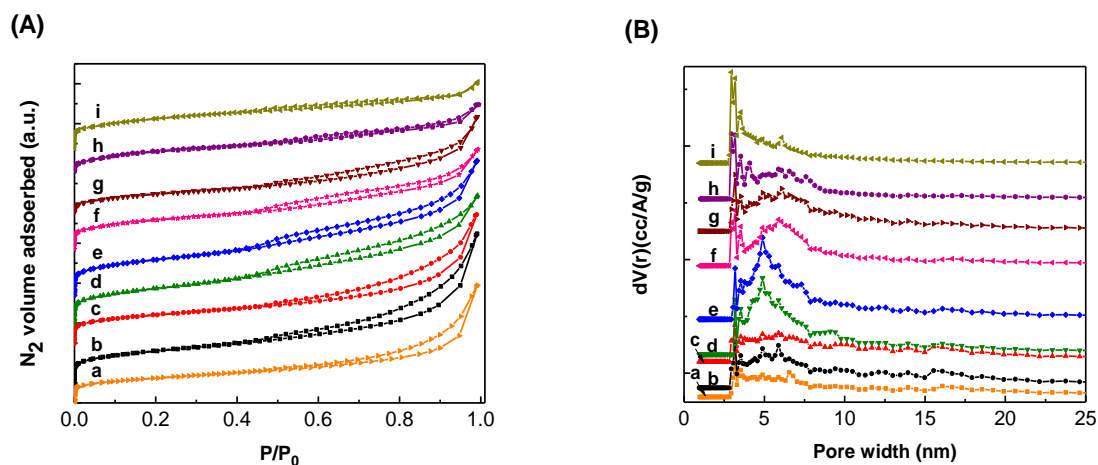


Figure 2.7. N₂ adsorption-desorption isotherms (A) and the corresponding pore size distributions (B) as derived from N₂ sorption (NLDFT on the adsorption branch) of MFI zeolite obtained with C₂₂₋₆₋₆/TPAOH molar ratio of (a) 10/0, (b) 10/1, (c) 10/2, (d) 10/3, (e) 10/5, (f) 10/8, (g) 10/12, and (h) 10/20, respectively. (i) Commercial MFI with Si/Al ratio of ~ 40 was used for comparison.

pressures ($p/p_0 < 0.45$), all the MFI samples have similar isotherms, which indicate that they have similar microporous structures. An increase in the adsorption volume in this pressure region implies the presence of mesopores created by dual templating of the samples in the synthesis. In the higher relative pressure region ($p/p_0 = 0.45-1.0$), the samples show different hysteresis loops, indicating they have different mesoporous and/or macroporous structures. For MFI-10/0, MFI-10/1, and MFI-10/2, the hysteresis loops have the general type B form, which indicates these materials have disordered pores and the distribution of pore size and/or shape is not well defined.^{115, 116} MFI-10/3, MFI-10/5, and MFI-10/8, however, show the hysteresis loops with the general form of type A, which means that these materials consist of well-defined cylindrical-like pore channels.^{115, 116} The shift of the hysteresis to the lower relative pressures from MFI-10/0 to MFI-10/8 in Figure 2.7(A) indicates that the mesopore size decreases. A further increase of TPAOH quantity in the dual

template synthesis shows the decrease in mesoporosity, as indicated by the diminishing hysteresis loops in N₂ isotherms of MFI-10/12 and MFI-10/20. Commercial MFI does not show obvious hysteresis loop which is consistent with the absence of mesopores in this material. The N₂ isotherm data clearly show that the pore sizes and shapes of zeolite nanosheet assemblies are systematically modulated by tuning the ratios of the dual templates (TPAOH and C₂₂₋₆₋₆) in the synthesis recipe.

The pore size distributions of all MFI samples, synthesized with different molar ratios of the C₂₂₋₆₋₆/TPAOH, were derived from N₂ sorption (nonlocal density functional theory (NLDFT) on the adsorption branch of isotherms), shown in Figure 2.7(B). MFI-10/0, MFI-10/1, and MFI-10/2 have broad distribution of mesopore diameters, which is consistent with the random aggregation of MFI nanosheets. MFI-10/3, MFI-10/5, and MFI-10/8 show broad pore distributions in this region but the peaks are narrower with maximum mesopore sizes of ~ 4.9, 4.9, and 5.9 nm, respectively. For MFI-10/12 and MFI-10/20 samples, the porosity is reduced in comparison with the samples synthesized with less amount of TPAOH due to the 3D growth of the samples into bulk crystals. The trend of mesopore distribution across the synthesized MFI samples is consistent with the morphology analysis of the samples by SEM and TEM observations. Table 2.2 summarizes the textural properties of the catalysts, micropore volume (V_{micro}), total pore volume (V_{total}), mesopore volume (V_{meso}), external surface area (S_{ext}), micropore surface area (S_{micro}), and BET surface area (S_{BET}), that were determined from the N₂ adsorption-desorption data. The fractions of mesopore volume and external surface area were calculated by $V_{\text{meso}}/V_{\text{total}}$ and $S_{\text{ext}}/S_{\text{BET}}$, respectively. An initial increase and then a decrease in the values of

$V_{\text{meso}}/V_{\text{total}}$ and $S_{\text{ext}}/S_{\text{BET}}$ with decreasing C_{22-6-6}/TPAOH ratios in the dual template synthesis of these catalysts quantitatively reveals the trend of mesopore surface area and volume with the tailored dual template ratios.

Table 2.2. Textural properties of zeolite catalysts determined from N_2 adsorption-desorption data.

Catalyst	V_{micro}^a [$\text{cm}^3 \text{g}^{-1}$]	V_{total}^b [$\text{cm}^3 \text{g}^{-1}$]	V_{meso}^c [$\text{cm}^3 \text{g}^{-1}$]	S_{micro}^a [$\text{m}^2 \text{g}^{-1}$]	S_{BET}^d [$\text{m}^2 \text{g}^{-1}$]	S_{ext}^a [$\text{m}^2 \text{g}^{-1}$]	$V_{\text{meso}}/V_{\text{total}}^e$	$S_{\text{ext}}/S_{\text{BET}}^f$
MFI-10/0	0.087	0.371	0.284	196	448	253	0.766	0.564
MFI-10/1	0.087	0.406	0.319	200	462	262	0.785	0.567
MFI-10/2	0.088	0.410	0.322	201	427	227	0.785	0.531
MFI-10/3	0.074	0.502	0.429	141	517	376	0.853	0.727
MFI-10/5	0.087	0.464	0.377	160	494	334	0.812	0.676
MFI-10/8	0.080	0.461	0.381	174	468	294	0.826	0.628
MFI-10/12	0.094	0.445	0.351	206	495	289	0.789	0.585
MFI-10/20	0.110	0.333	0.223	263	492	229	0.670	0.466
Commercial MFI	0.104	0.297	0.193	249	466	217	0.650	0.466

^a Determined from t-method; ^b Determined from adsorbed volume at $p/p_0 = 0.95$; ^c $V_{\text{meso}} = V_{\text{total}} - V_{\text{micro}}$; ^d Determined from multi-point BET method; ^e Fraction of mesopore volume; ^f Fraction of external surface area.

A further characterization on porosity of the catalysts was performed with Ar isotherm followed by pore size distribution analysis by NLDFT method. The results have been shown in Figure 2.8. The shape of isotherms measured by Ar (Figure 2.8(A)) is similar to that observed in Figure 2.7(A) using N_2 sorption analysis confirming that the synthesized MFI zeolite catalyst samples using different molar ratios of the C_{22-6-6}/TPAOH have similar microporous and different mesoporous and/or macroporous structures. Figure 2.8(B) shows the pore size distribution of the

synthesized zeolite catalysts and commercial MFI extracted from the Ar sorption data using NLDFT method. The peak centered at ~ 0.55 nm is assigned to the micropore of MFI zeolites. The small peak below 2 nm might be due to a phase transition in the Ar as adsorbate, which has been previously reported for certain MFI zeolite structures.^{117, 118} The third peak ranging from 4-6 nm is assigned to the mesopores present in the catalysts. MFI-10/0, MFI-10/1, and MFI-10/2 have less mesopores, which is consistent with the random aggregation of MFI nanosheets to form large macropores. MFI-10/3, MFI-10/5, and MFI-10/8 show clear mesopores in this region. For MFI-10/12 and MFI-10/20 samples, the porosity is reduced in comparison to those samples synthesized using less amount of TPAOH due to the 3D growth of the samples into bulk crystals. The commercial MFI has less mesoporosity compared to the zeolite samples synthesized by the dual template approach. These results are in good agreement with those observed in Figure 2.7(B) using N₂ sorption analysis.

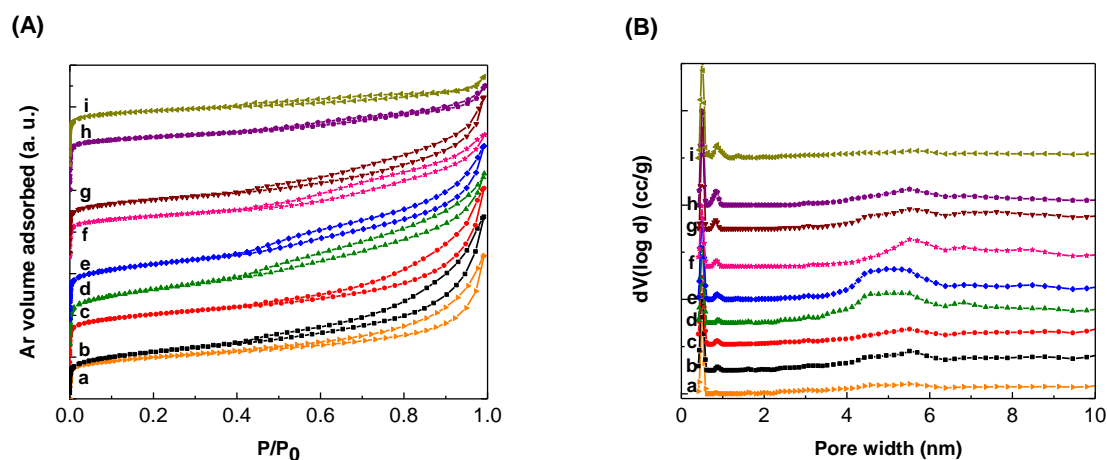


Figure 2.8. Ar adsorption-desorption isotherms (A) and the corresponding pore size distributions (B) as derived from Ar sorption (NLDFT on the adsorption branch) of MFI zeolite obtained with C₂₂₋₆₋₆/TPAOH molar ratio of (a) 10/0, (b) 10/1, (c) 10/2, (d) 10/3, (e) 10/5, (f) 10/8, (g) 10/12, and (h) 10/20, respectively. (i) Commercial MFI with Si/Al ratio of ~ 40 was used for comparison.

Table 2.3 shows the textural parameters of the synthesized zeolite catalysts analyzed from adsorption branch of Ar isotherms. The BET surface area (S_{BET}), external surface area (S_{ext}), and total pore volume (V_t) of the MFI-10/3, MFI-10/5, and MFI-10/8 are higher than the other MFI samples synthesized using different molar ratios of $C_{22-6-6}/TPAOH$, which is consistent with the textural parameters extracted from N_2 isotherms and presented in Table 2.2. The smaller micropore volumes of these three catalysts in comparison to the other synthesized catalysts are due to the increased mesopores in these zeolites. It has been reported that the meso-structuring of zeolite samples generally sacrifices their microporosity to some extent.¹¹⁹ The fractions of mesopore surface area (S_{ext}/S_{BET}) and mesopore volume

Table 2.3. Textural property of zeolite catalyst measured by Ar adsorption-desorption isotherm.

Catalyst	V_{micro}^a [cm ³ g ⁻¹]	V_{total}^b [cm ³ g ⁻¹]	V_{meso}^c [cm ³ g ⁻¹]	S_{micro}^a [m ² g ⁻¹]	S_{BET}^d [m ² g ⁻¹]	S_{ext}^a [m ² g ⁻¹]	V_{meso}/V_{total}^e	S_{ext}/S_{BET}^f
MFI-10/0	0.063	0.277	0.214	141	310	169	0.773	0.544
MFI-10/1	0.058	0.314	0.256	143	364	221	0.815	0.608
MFI-10/2	0.059	0.365	0.306	160	369	209	0.838	0.567
MFI-10/3	0.041	0.413	0.372	124	414	290	0.901	0.701
MFI-10/5	0.052	0.402	0.350	150	421	272	0.871	0.645
MFI-10/8	0.050	0.379	0.329	142	422	280	0.867	0.664
MFI-10/12	0.083	0.356	0.273	194	373	179	0.767	0.480
MFI-10/20	0.106	0.265	0.159	262	392	130	0.600	0.331
Commercial MFI	0.114	0.217	0.103	282	393	111	0.474	0.282

^a Determined from t-method; ^b Determined from adsorbed volume at $p/p_0 = 0.95$; ^c $V_{meso} = V_{total} - V_{micro}$; ^d Determined from multi-point BET method; ^e Fraction of mesopore volume; ^f Fraction of external surface area.

($V_{\text{meso}}/V_{\text{total}}$) versus the dual template ratios extracted from Ar sorption data show a volcano-like trend, consistent with the trend observed for $S_{\text{ext}}/S_{\text{BET}}$ and $V_{\text{meso}}/V_{\text{total}}$ versus the C_{22-6-6}/TPAOH ratios, respectively for the zeolite catalysts using N_2 sorption analysis (see Table 2.2).

2.3.2. Acidity of zeolite catalysts

The aluminum content of the zeolites synthesized by the dual template method was determined by elemental analysis (ICP-OES). Table 2.4 shows that the Si/Al ratios of all the samples are around 45, slightly lower than the Si/Al ratios determined from Si and Al precursors used in the synthesis recipe which is 50. The number of active Brønsted acid sites in each zeolite catalyst was determined via DME titration experiments assuming that the active Brønsted acid sites participate in reactions of DME with H^+ to form surface methyl groups.^{111, 112} The total number of active Brønsted acid sites in each MFI zeolite catalyst (represented by Si/Al ratio) determined via DME titration experiments is similar to that of ICP-OES elemental analysis, implying that Brønsted acid sites are the dominant acid species in the studied zeolite samples.

The type and concentration of acid sites were further evaluated by FTIR spectra of the adsorbed pyridine on the selected MFI-10/0, MFI-10/2, MFI-10/5, MFI-10/12, and commercial MFI catalysts, and the result is shown in Figure 2.9. The absorption band at 1545 cm^{-1} is typical of pyridine interacting with Brønsted acid sites, while the absorption band around 1455 cm^{-1} is assigned to the interaction of pyridine with Lewis acid sites in the zeolite catalysts.^{120, 121} Figure 2.9 shows that

1545 cm^{-1} and 1455 cm^{-1} bands exist in the spectra of all the measured zeolite samples, indicating the co-existence of Brønsted and Lewis acid sites in these catalysts. The molar ratios of Brønsted to Lewis acid sites in each of the selected synthesized MFI zeolite catalysts were calculated from the areas of absorption peaks

Table 2.4. Acidity of the zeolite catalyst measured by elemental analysis and chemical titrations; Rate constants (k_{meas}) of DEE production at 383 K, measured activation energies of DEE synthesis (ΔE_{meas}) and entropies of MFI zeolite catalysts (ΔS_{meas}).

Catalyst	Si/Al ^a	Si/Al ^b	k_{meas} ($\times 10^4 \text{ mol (mol H}^+)^{-1} \text{ s}^{-1}$)	ΔE_{meas}^c (kJ mol^{-1})	ΔS_{meas}^d ($\text{J mol}^{-1} \text{ K}^{-1}$)
MFI-10/0	49	50	2.4	100	-66
MFI-10/1	46	51	2.4	96	-77
MFI-10/2	45	48	2.5	99	-70
MFI-10/3	44	47	2.8	98	-70
MFI-10/5	44	49	3.2	100	-65
MFI-10/8	48	51	2.4	101	-64
MFI-10/12	50	54	2.5	99	-69
MFI-10/20	47	50	3.2	104	-54
Commercial MFI	43	41	2.4	101	-64

^a Determined from elemental analysis (ICP-OES). ^b Determined by dimethyl ether (DME) titration and errors are ± 5 . ^c Errors are $\pm 3 \text{ kJ mol}^{-1}$. ^d Errors are $\pm 4 \text{ J mol}^{-1} \text{ K}^{-1}$.

at 1545 cm^{-1} and 1455 cm^{-1} , respectively. The Beer's law, $A = \epsilon c D$, is employed in the calculation of molar ratios from absorption peak areas, where A is the absorbance (integrated absorption peak area), ϵ is the molar extinction coefficient ($\text{cm } \mu\text{mol}^{-1}$), c is the concentration of the acid sites ($\mu\text{mol dm}^{-3}$), and D is the thickness of the zeolite

pellet (cm). The molar ratio of Brønsted to Lewis acid sites in each catalyst can be evaluated from $c_{\text{Brønsted}}/c_{\text{Lewis}} = (A_{1545\text{cm}^{-1}}/A_{1455\text{cm}^{-1}}) \times (D_{1455\text{cm}^{-1}}/D_{1545\text{cm}^{-1}}) \times (\epsilon_{1455\text{cm}^{-1}}/\epsilon_{1545\text{cm}^{-1}})$. Under the assumptions that D is the same for absorption peaks centered at 1545 cm^{-1} and 1455 cm^{-1} , and the values of ϵ are $1.67\text{ cm } \mu\text{mol}^{-1}$ for the 1545 cm^{-1} band characteristic of pyridine on a Brønsted acid site and $2.22\text{ cm } \mu\text{mol}^{-2}$ for the 1455 cm^{-1} band of pyridine on a Lewis acid site,¹²⁰ the equation for calculation of

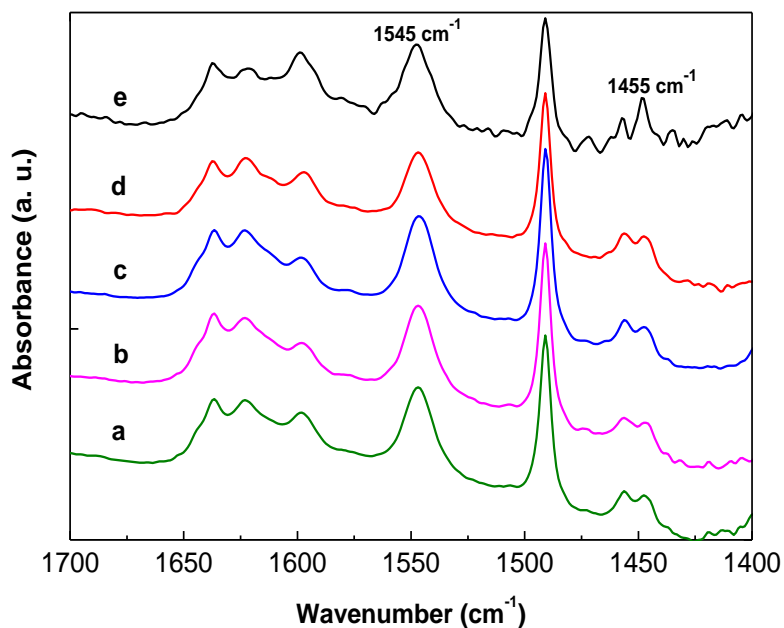


Figure 2.9. FTIR spectra of adsorbed pyridine on selected MFI zeolites obtained with $\text{C}_{22-6-6}/\text{TPAOH}$ molar ratio of (a) 10/12, (b) 10/5, (c) 10/2, and (d) 10/0, respectively. (e) Commercial MFI with Si/Al ratio of ~ 40 was used for comparison.

molar ratio of Brønsted to Lewis acid sites in the catalyst is simplified as, $c_{\text{Brønsted}}/c_{\text{Lewis}} = (A_{1545\text{cm}^{-1}}/A_{1455\text{cm}^{-1}}) \times (2.22 / 1.67) = 1.33 \times (A_{1545\text{cm}^{-1}}/A_{1455\text{cm}^{-1}})$. The integrated areas of absorption peaks centered at 1545 cm^{-1} and 1455 cm^{-1} and the molar ratios of Brønsted to Lewis acid sites calculated in each catalyst are

summarized in Table 2.5. The molar ratios of Brønsted-to-Lewis acid site are 7.06, 7.97, 7.93, 8.21, and 9.75, for the MFI-10/0, MFI-10/2, MFI-10/5, MFI-10/12, and commercial MFI catalysts, respectively. The similar Brønsted-to-Lewis acid site ratios reveal that the modulation in textural and morphological properties of the catalysts does not influence their acidic properties intensely.

Table 2.5. Concentration of Brønsted and Lewis acid sites of selected zeolite catalysts measured by FTIR spectra of adsorbed pyridine at 393 K.

Catalyst	Integrated peak area		Molar ratio of Brønsted to Lewis acid sites
	Brønsted acid	Lewis acid	
MFI-10/0	2.04	0.38	7.06
MFI-10/2	2.65	0.44	7.97
MFI-10/5	2.40	0.40	7.93
MFI-10/12	2.45	0.40	8.21
Commercial MFI	1.80	0.25	9.75

Solid state NMR was employed to investigate the local bonding environment in the synthesized MFI zeolite catalysts. Figure 2.10(A) shows the ^{29}Si single pulse (SP) NMR spectra of the selected MFI-10/2, MFI-10/5, and MFI-10/12 zeolite samples. Two well resolved peaks (at -113 and -103 ppm) can be observed in the ^{29}Si SP NMR spectrum of these MFI zeolites, which correspond to crystallographically nonequivalent Q^4 tetrahedral sites (Q^n stands for $\text{X}_{4-n}\text{Si}[\text{OSi}]_n$)^{41, 122-124} and Q^3 sites arising from the silanol groups on the zeolite surface¹²⁵. The similar Q^4 and Q^3 peaks in these catalysts suggest that there is a similar local bonding environment in these meso-/microporous MFI zeolites.

^{29}Si CP MAS NMR spectra of the selected three MFI zeolites are shown in Figure 2.10(B). These materials show similar spectra with three peaks around -92, -103, and -113 ppm, corresponding to the Q^2 , Q^3 , and Q^4 silanol species, as labeled in the spectra. Figure 2.10(C) shows the ^{27}Al MAS NMR spectra of these MFI zeolite samples. The peak at 55 ppm is due to the tetrahedrally coordinated framework aluminum (Al_F)⁶¹, while the peak around 0 ppm is due to an octahedral coordination typical of extra-framework Al (Al_EF). The fractions of the Al_EF in MFI-10/2, MFI-10/5, and MFI-10/12 catalysts were calculated from the intensities of the peaks around 0 ppm and 55 ppm in the spectra, which are ~ 9%, 7%, and 3%, respectively.

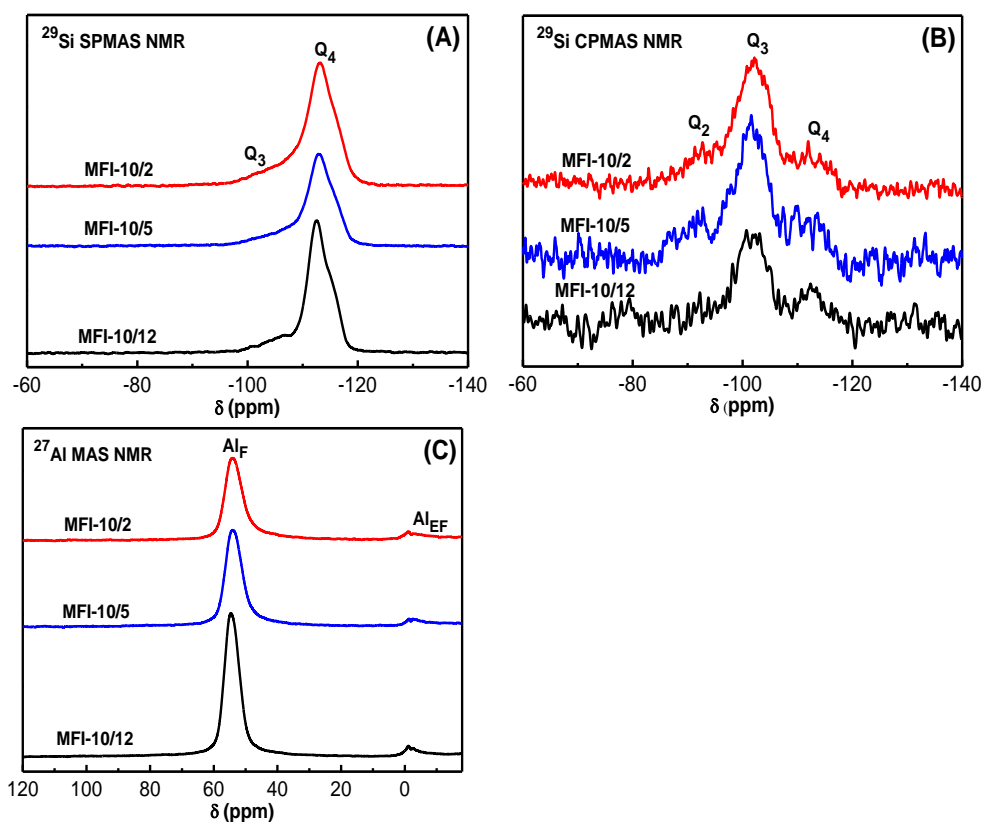


Figure 2.10. Multinuclear solid state NMR spectra of MFI zeolites obtained with C₂₂₋₆₋₆/TPAOH molar ratio of 10/2, 10/5, and 10/12: (A) ^{29}Si MAS NMR, (B) ^{29}Si CP MAS NMR, and (C) ^{27}Al MAS NMR.

2.3.3. Ethanol dehydration reactions

Ethanol dehydration has been proposed as a model catalytic reaction to assess the dimensions of the microporous environment of the acidic hydroxyl group.¹²⁶⁻¹²⁹ The reaction was carried out under strictly kinetic controlled conditions. Under these reaction conditions, rigorous elimination of transport artifacts allows investigating the intrinsic activity of acid sites in the MFI assemblies synthesized by the dual template approach. The ethanol dehydration reaction over MFI catalyst involves the adsorption of ethanol on the Brønsted acid site of the zeolite and the consequent transformation of ethanol into ethylene via a unimolecular reaction or to DEE via a bimolecular reaction.¹³⁰ Ethanol dehydration is predominantly a bimolecular reaction at low temperature, whereas the unimolecular reaction path prevails at high temperature because the formation of ethanol dimeric species is energetically more favorable than the formation of ethanol monomers.¹²⁶ In the present study, no ethylene was observed in the effluent stream over all MFI zeolites, indicating that the ethanol dehydration reaction over all these catalysts occurred through a bimolecular pathway consistent with reports in the literature.^{126, 129}

The Arrhenius plots (the natural logarithm of regressed rate constants versus the inverse temperature) of the ethanol dehydration over the MFI zeolites catalysts are shown in Figure 2.11. The plots are parallel to each other which indicate similar activation energies for ethanol dehydration. Table 2.4 lists the measured activation energy (ΔE_{meas}), entropies (ΔS_{meas}), and rate constants at 383 K (k_{meas}) for DEE formation over MFI zeolites. The site time yield of DEE differs among the zeolites by up to a factor of 1.3. Activation energies (96-104 kJ mol⁻¹) and entropies (within a

range of -77 to $-54 \text{ J mol}^{-1} \text{ K}^{-1}$) are comparable. These results imply that Brønsted acid sites in MFI materials synthesized by the dual template method have similar catalytic activities which are comparable to commercial MFI zeolite possessing only micropores when measured under strict kinetic control.

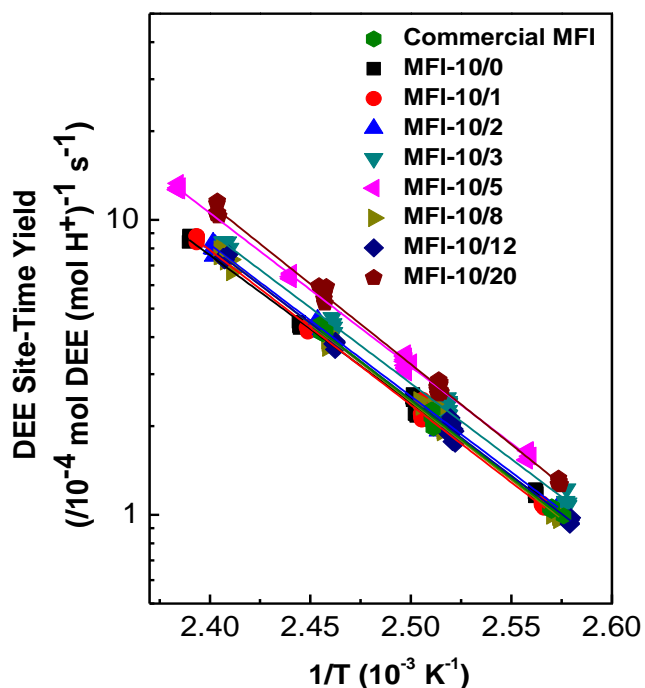


Figure 2.11. Measured rate constants of DEE production over MFI zeolite catalysts synthesized by the dual template method.

2.3.4. Benzyl alcohol reactions over zeolite catalysts

The liquid phase catalytic conversion of benzyl alcohol in mesitylene was employed to examine the catalytic performances of the synthesized MFI nanosheet assemblies in diffusion-constrained reactions. The reaction scheme shown in Figure 2.12 indicates that benzyl alcohol (A) is consumed simultaneously via mesitylene (B)

alkylation ($A+B \rightarrow H_2O + C$, 1,3,5-trimethyl-2-benzylbenzene) and self-etherification ($A+A \rightarrow H_2O + E$, dibenzyl ether) reactions.

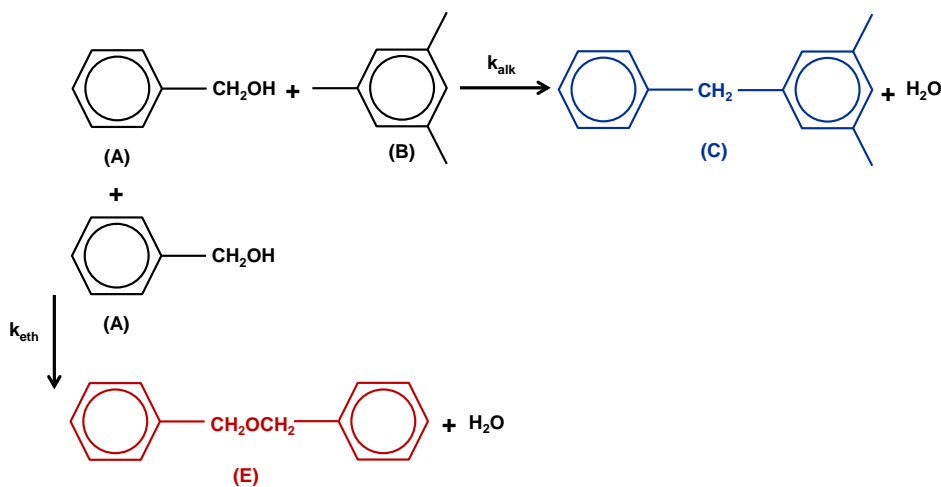


Figure 2.12. Scheme for mesitylene alkylation (k_{alk}) and benzyl alcohol self-etherification (k_{eth}) reactions over MFI zeolite catalysts.

Previous studies¹⁶ have indicated that the bulky mesitylene cannot enter the micropores of MFI zeolite so that the alkylation occurs exclusively on the external surface active acid sites of the catalyst. The self-etherification of benzyl alcohol occurs on both external and internal surface acid sites. It has been reported that the steric resistance hinders the access of bulky DTBP molecules to acid sites located in micropores of MFI-type zeolites.^{112, 131-133} The selective poisoning of the external acid sites using the DTBP titrant allows the self-etherification reaction to occur exclusively on the internal surface active sites of the zeolite catalysts. The apparent rate constants of the reactions were evaluated to examine the catalytic performance of Brønsted acid sites on the external surface and in zeolite micropores of the MFI nanosheet assemblies synthesized by the dual template method. The following

paragraphs illustrate the assumptions and calculation details of this rate constants evaluation.

An excess amount of mesitylene was used in catalytic reaction of benzyl alcohol with mesitylene (molar ratio of mesitylene to benzyl alcohol = 45:1), so the alkylation reaction can be approximated as pseudo-first order in the limiting reactant A, benzyl alcohol. The rate equation is:

$$\frac{dC_C}{dt} = k_{\text{alk}} M_B C_A \quad (2-1)$$

where C_C is 1,3,5-trimethyl-2-benzylbenzene concentration in solution (mol L^{-1}), t is the reaction time (s), k_{alk} is the specific rate constant (per Brønsted acid site, $[\text{mol H}^+]^{-1} \text{s}^{-1}$), M_B (mol H^+) is the total number of Brønsted acid sites present in the batch reactor calculated from the Si/Al ratios determined from DME titration (Table 2.4), and C_A is benzyl alcohol concentration in solution (mol L^{-1}). Self-etherification reaction can also be approximated as the first order with respect to the reactant A. The

selectivity of both reactions, $\alpha = \frac{2C_E}{C_C}$, is nearly constant for each catalyst in the

reaction, where C_E is dibenzyl ether concentration in solution (mol L^{-1}). Then, the concentration of 1,3,5-trimethyl-2-benzylbenzene, C_C , can be described as a function of benzyl alcohol concentration and selectivity:

$$C_C = \frac{C_A^0 - C_A}{1 + \alpha} \quad (2-2)$$

where C_A^0 is the initial benzyl alcohol concentration in solution (mol L^{-1}). By substitution of C_C into equation (2-1), the rate equation becomes:

$$\frac{dC_A}{dt} = -k_{\text{alk}} M_B (1 + \alpha) C_A \quad (2-3)$$

Integration of equation (2-3) gives the rate integral form of the rate equation (2-4):

$$\ln \frac{C_A^0}{C_A} = k_{\text{alk}} M_B (1 + \alpha) t = k_{\text{alk,app}} t \quad (2-4)$$

The apparent rate constant $k_{\text{alk,app}} = k_{\text{alk}} M_B (1 + \alpha)$, in s^{-1} , is determined from the benzyl alcohol concentration versus time (t , s^{-1}) measurements. The rate equation for etherification reaction can be derived similarly and the equation is:

$$\ln \frac{C_A^0}{C_A} = k_{\text{eth}} M_B \left(\frac{\alpha}{1 + \alpha} \right) t = k_{\text{eth,app}} t \quad (2-5)$$

where k_{eth} is the specific rate constant (per Brønsted acid site, $[\text{mol H}^+]^{-1} \text{s}^{-1}$) and

$k_{\text{eth,app}} = k_{\text{eth}} M_B \left(\frac{\alpha}{1 + \alpha} \right)$, in s^{-1} , is determined from the benzyl alcohol concentration

versus time (t , s^{-1}) measurements. In the presence of DTBP, the rate constant for the self-etherification reaction occurring on the internal acid sites is $k_{\text{eth,app}} = k_{\text{eth}} M_B$.

Table 2.6 shows the rate constants of mesitylene alkylation and benzyl alcohol self-etherification reactions in the absence and presence of DTBP and also the selectivity for these reactions over the synthesized MFI zeolite catalysts. Benzyl alcohol reaction with mesitylene was used as a model of Friedel-Crafts alkylation reactions in our studies in order to understand the catalytic properties of the synthesized catalysts. The higher selectivity to alkylation reactions of the synthesized catalysts indicates that they can improve the selectivity to desired alkylated products compared to that of commercial MFI catalysts (see Table 2.6).

Table 2.6. Rate constants of mesitylene alkylation, benzyl alcohol self-etherification and selectivity for alkylation and self-etherification reactions.

Catalyst	Reaction rate constant ($10^3 \text{ s}^{-1} [\text{mol H}^+]^{-1}$) ^a				Selectivity (α)
	In absence of DTBP		In presence of DTBP		In absence of DTBP
	k_{alk}	k_{eth}	k_{alk}	$k_{\text{eth,int}}$	$2C_E/C_C$
MFI-10/0	35.2	314	0	98	9.5
MFI-10/1	68.9	687	0	253	9.6
MFI-10/2	80.6	659	0	291	8.3
MFI-10/3	140.8	1409	0	627	8.8
MFI-10/5	111.2	1254	0	496	10.6
MFI-10/8	95.2	1505	0	453	11.6
MFI-10/12	76.3	865	0	352	10.8
MFI-10/20	68.0	649	0	209	6.8
Commercial MFI	26.3	642	0	126	15.4

^a Rate parameters determined by least-squares regression; Uncertainties in regressed rate parameters are within $\pm 4\%$ of the reaction rate constant, twice the standard error. Normalized to total number of Brønsted acid sites determined by DME titration.

Figure 2.13 shows the plots for determination of rate constants and rate constants of the parallel reactions of benzyl alcohol with mesitylene over the synthesized MFI nanosheet assemblies under the conditions where all active sites of the zeolite catalysts were unperturbed in the reaction (Figure 2.13(A)) and under the conditions where DTBP had been added to the reaction mixture to selectively titrate acid sites located on the external surface and mesopores (Figure 2.13(B)). The conversion data were fitted well to a pseudo-first order rate law expressed in equations (2-4) and (2-5), respectively. In the absence of the DTBP titrant (Figure

2.13(C)-(D) and Table 2.6), the rate constants for conversion of benzyl alcohol into dibenzyl ether and 1,3,5-trimethyl-2-benzylbenzene increased with initial increase of TPAOH content in the synthesis recipe and reached a maximum when C_{22-6-6}/TPAOH molar ratios were 10/3, 10/5, and 10/8. Afterward, the rate constants decreased with further increase in TPAOH contents as shown for samples MFI-10/12 and MFI-10/20. The catalytic activity is consistent with the textural properties of the synthesized catalysts investigated by SEM, TEM, and N_2/Ar isotherm analysis. Pérez-Ramirez et al.⁹⁶ defined hierarchy factor (product of $(V_{\text{micro}}/V_{\text{total}}) \times (S_{\text{meso}}/S_{\text{BET}})$) to describe the interplay between the catalytic function located in the micropores and the accessibility function provided by the mesopores of the hierarchical zeolites in benzene alkylation reactions. A similar analysis on mesitylene alkylation reaction rate versus hierarchy factor of the synthesized catalysts using different molar ratios of C_{22-6-6}/TPAOH , however, did not show a linear relationship with each other. A plausible explanation is that mesitylene alkylation only occurred on the external surface and mesopore of the catalysts;¹⁶ thus, only the external surface area ($S_{\text{meso}}/S_{\text{BET}}$) in the hierarchy factor is responsible for the catalytic reaction. The rate constants of mesitylene alkylation reaction were further rationalized as a function of fractions of mesopore surface area of the catalysts ($S_{\text{ext}}/S_{\text{BET}}$). As shown in Figure 2.13(F), the linear plot of k_{alk} versus $S_{\text{ext}}/S_{\text{BET}}$ indicates that the alkylation reaction rate is proportional to the external surface area of the catalysts. The rate constants of self-etherification reaction are attributed to the active sites located on external surface and in micropores of the catalysts. Therefore, the correlation of k_{eth} versus $S_{\text{ext}}/S_{\text{BET}}$ cannot be simply used to interpret the catalytic data collected in the self-etherification

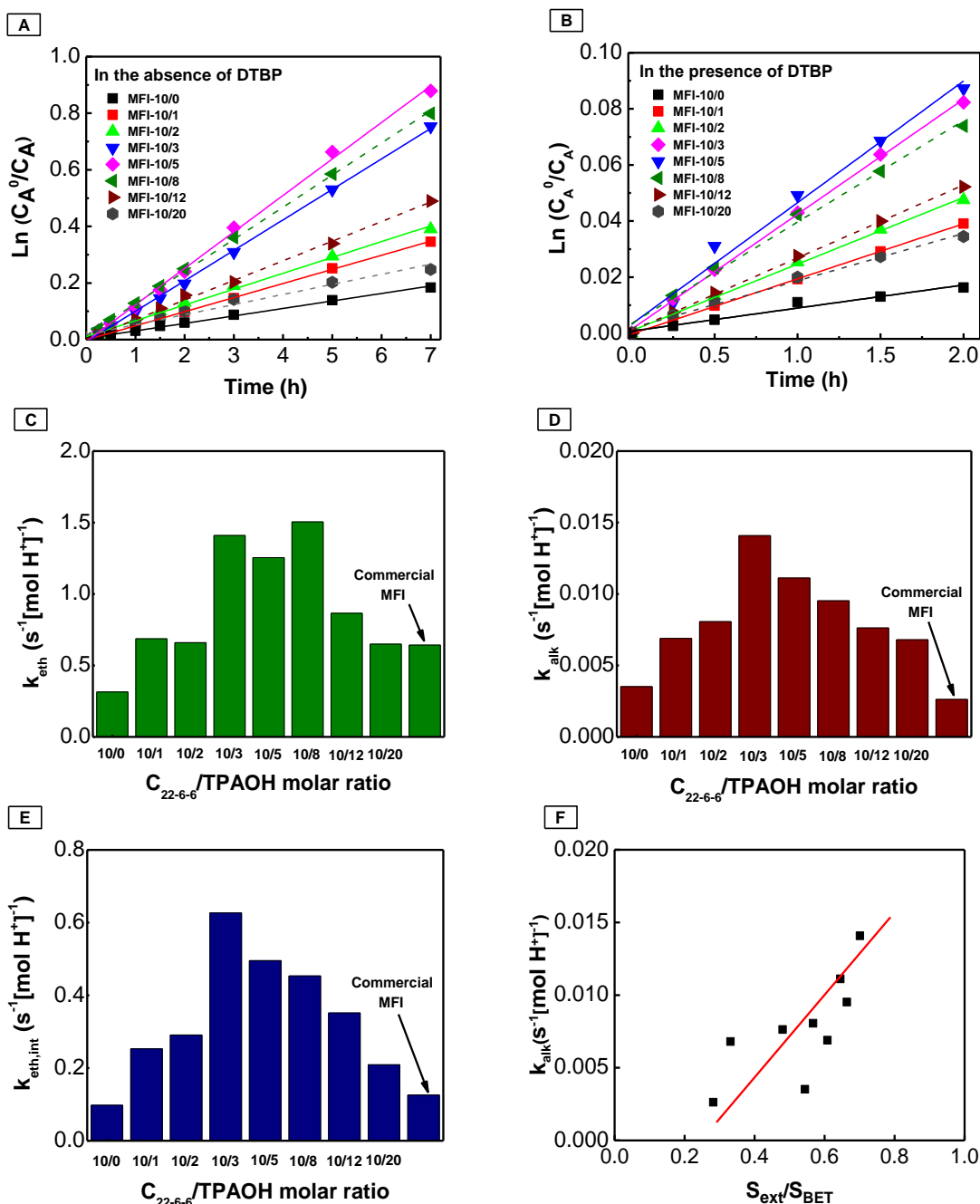


Figure 2.13. Plots for determination of rate constants of benzyl alcohol conversion in the absence of DTBP (A) and in the presence of DTBP (B), respectively. (C)-(D) are rate constants of dibenzyl ether and 1,3,5-trimethyl-2-benzylbenzene formation, respectively, in the absence of DTBP. (E) is the rate constant of dibenzyl ether formation in the presence of DTBP. (F) is the rate constant of 1,3,5-trimethyl-2-benzylbenzene formation in the absence of DTBP versus fraction of external surface area.

reaction. However, the same volcano-shaped plots of k_{eth} versus catalysts in Figure 2.13(C) and S_{ext}/S_{BET} versus catalysts shown in Figure 2.14 suggest that the external and mesopore surface area of the catalysts intensively contribute to the observed catalytic behavior. In addition, the values of k_{eth} were reduced by a factor ~ 3 when the external acid sites were deactivated by DTBP present in the reaction (Figure 2.13(C) and 2.13(E) and Table 2.6). These results indicate that the MFI-10/3, MFI-10/5, and MFI-10/8 samples have higher mesopore surface area and volume so that they allow more efficient surface catalysis compared to MFI nanosheet assemblies synthesized with low or high TPAOH concentration in the recipe. It should be mentioned that the analysis on the reaction rate constants presented here is based on the assumption that the distribution of Brønsted acid sites in the synthesized zeolite structures is uniform.

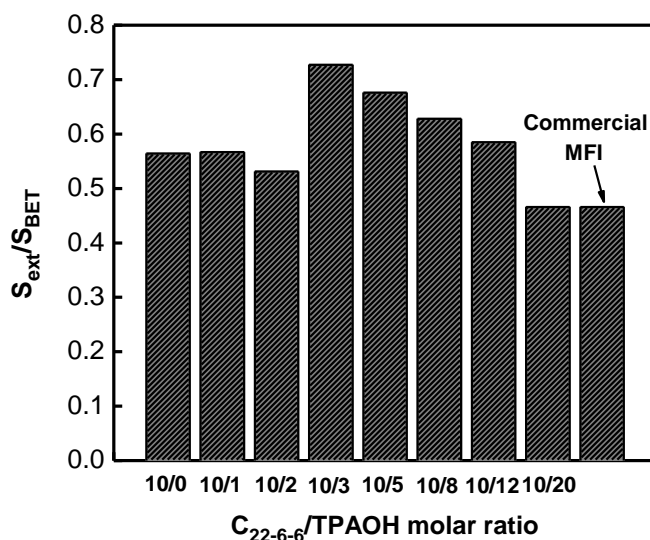


Figure 2.14. S_{ext}/S_{BET} (extracted from N_2 isotherms) versus MFI catalysts synthesized with $C_{22-6-6}/TPAOH$ molar ratio of 10/0, 10/1, 10/2, 10/3, 10/5, 10/8, 10/12, and 10/20, respectively. Commercial MFI was used for comparison.

In the presence of DTBP titrant, MFI zeolites maintained the residual activity that only catalyzed self-etherification reaction in the micropores of the catalysts as shown in Figure 2.13(E). The previous study on self-etherification reaction in the micropores of pillared MFI and self-pillared MFI together with several conventional zeolites with different crystallite sizes showed that the observed differences in apparent reaction rates of these catalysts can be fully accounted for by diffusion limitations, a plot of effectiveness factor versus the Thiele modulus.¹⁶ The higher reaction rates in MFI-10/3, MFI-10/5, and MFI-10/8 catalysts indicate that they may mitigate the diffusion constraints more efficiently compared to the other synthesized MFI nanosheet catalysts. It should be noted that the Thiele modulus of the synthesized MFI catalysts by dual template approach cannot be determined based on the particle size and shape because it consists of a mixture of aggregates. The activity of the meso-/microporous MFI nanosheet structures is higher than that of commercial MFI catalyst. The catalytic performance of these MFI nanosheet assemblies is consistent with their textural properties discussed in section 2.3.1, which indicates that the MFI nanosheet assemblies have similar intrinsic catalytic activity but different porosity and pore size distributions that result in different performances in diffusion constrained reactions.

The one-step dual template synthesis of hierarchical zeolites with tunable textural and catalytic properties by simply varying the ratio of templates in the synthetic recipe represents a low-cost approach toward hierarchical materials production for broad potential industrial applications. Although C₂₂₋₆₋₆ surfactant is relatively expensive, the synthetic protocol developed here only involves one reaction

and processing step. The wide range of template ratios allows a facile adjustment of pore size, pore volume, and mesopore surface area of the hierarchical zeolite structures.

2.3.5. Effect of pH changes due to the presence of TPAOH in the synthesis recipe on catalyst morphology

Different control experiments were carried out by replacing the TPAOH with TPABr as molecular template in the synthesis recipe of MFI catalysts in order to check the effect of pH changes due to the presence of TPAOH on the morphology of the MFI samples produced. Figure 2.15(A)-(D) show the SEM images of the MFI structures produced by C_{22-6-6} /TPABr molar ratio of 10/2, 10/5, 10/12, and 10/20, respectively.

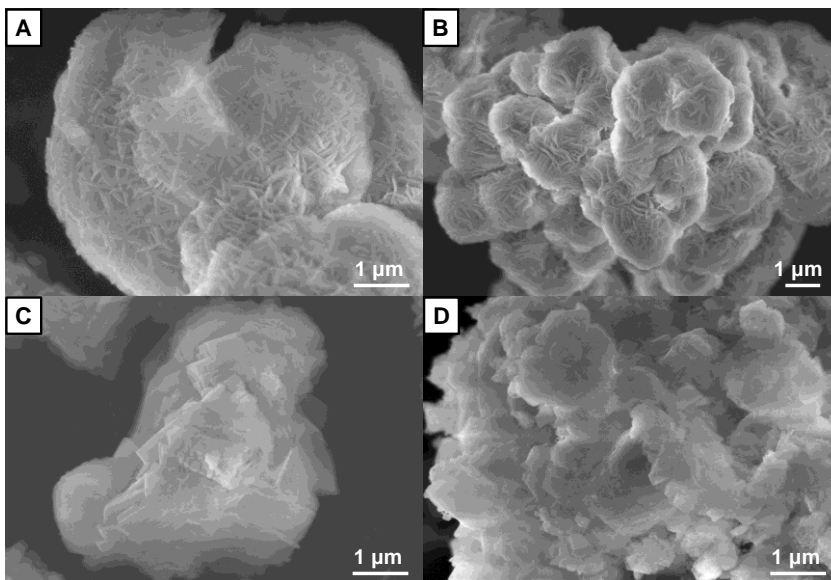


Figure 2.15. SEM images of MFI zeolites obtained with C_{22-6-6} /TPABr molar ratio of (A) 10/2, (B) 10/5, (C) 10/12, and (D) 10/20, respectively, in the dual template synthesis.

In comparison to the SEM images of MFI samples produced by the same molar ratio of C₂₂₋₆₋₆/TPAOH in Figure 2.4, these samples show similar morphology, indicating that the pH changes due to the presence of TPAOH in the zeolite synthesis recipe, cannot be considered as an important factor for tailoring the zeolite structural properties. Instead, the dual templates and the ratios of the dual templates in the synthesis are responsible for the formation of the meso-/microporous MFI zeolite assemblies with modulated structural and textural properties.

2.4. Concluding remarks

The dual template synthesis approach has been investigated to find the conditions that result in one-step preparation of hierarchical MFI nanosheet assemblies with tunable porosity and catalytic performances. Molecular zeolite template TPAOH and bulky multi-quaternary ammonium surfactant (C₂₂₋₆₋₆) were employed as templates in this study. By tuning the molar ratios of the dual templates (C₂₂₋₆₋₆/TPAOH of 10/0 to 10/20), the morphology and porosity of the resultant zeolite nanosheet assemblies were systematically modulated. The presence of TPAOH induced the growth of the zeolite lamellae into 3D directions, even though when an appropriate concentration of TPAOH was used, the resultant catalyst had a narrower pore size distribution, in which the zeolite nanocrystals might act as ‘pillar’ to preserve the mesoporosity upon collapse of lamellar structures during calcination. The intrinsic activity of the catalysts evaluated by ethanol activation reactions under strict kinetically controlled conditions showed that all the synthesized catalysts had comparable dehydration rates to commercial MFI zeolite. In the diffusion constrained

reactions that was exemplified by the liquid phase catalytic conversion of benzyl alcohol in mesitylene, the MFI catalysts synthesized by the dual templates with molar ratios of $C_{22-6-6}/TPAOH = 10/3-10/8$ showed the highest surface catalytic activities, indicating that these materials contained larger fraction of external surface acid sites in consistent with textural property analysis results. The catalytic performance over acid sites in zeolite micropores showed that MFI-10/3–MFI-10/8 could mitigate the diffusion constraints more effectively compared to MFI-10/0–MFI-10/2 and MFI-10/12–MFI-10/20 samples. The present study demonstrates that the molecular template TPAOH can be used as a secondary template to tailor the textural and catalytic properties of MFI nanosheet assemblies primarily guided by C_{22-6-6} templates. Detailed investigation on the effects of dual templates in the meso-/microporous zeolite synthesis indicates a general approach towards designed synthesis of hierarchical catalysts for targeted catalytic reactions.

Chapter 3: One-step dual template synthesis of hybrid lamellar-bulk MFI zeolite

3.1. Introduction

The meso-/microporous zeolites, coupling the structural feature of microporosity and the fast mass transport consequence of mesoporosity in a single material^{8, 33-35, 92}, are being studied intensively for many applications such as catalysts possessing the capacity of overcoming the mass-transfer constraints^{80, 101, 114, 134, 135} and the building blocks of thin zeolite membranes for gas separations^{99, 136}. Methods for the synthesis of meso-/microporous zeolites have been extensively studied, including templated synthesis using multifunctional structure-directing agents (SDAs)^{61, 63}, post-synthesis processing such as exfoliation/pillaring of layered zeolites^{97, 112, 113, 137, 138} and desilication/dealumination of microporous zeolites^{45, 59, 119, 139, 140}, and epitaxial and rotational overgrowth of microporous zeolites^{16, 65, 141-143}. The as-obtained hierarchical meso-/microporous zeolites generally consist of three dimensional (3D) zeolite crystals with mesopores between or inside the microporous zeolitic domains or two dimensional (2D) exfoliated zeolite nanosheets. Moreover, the mesoporous and microporous domains in these zeolite materials generally have limited tunability. Facile methods for the synthesis of meso-/microporous zeolites with tunable porosities and two dimensional-three dimensional (2D-3D) hybrid domain structures in a single material are highly desired in order to keep the potential applications for these zeolite structures as broad as possible.

Recently, the desilication method has been advanced to tune the meso-/microporosity in the meso-/microporous zeolite materials.^{17, 20} A hierarchy factor, a product of the relative micropore volume and relative mesopore surface area, has been defined to describe the tunability of the meso-/microporosity in the desilicated zeolites.¹⁷ Furthermore, an epitaxial growth of mesoporous lamellar MFI on the bulk MFI to synthesize the 2D-3D hybrid MFI zeolite has also been reported.¹⁴ The control over the sizes of the microporous and mesoporous domains in the 2D-3D hybrid MFI zeolite was achieved by employing the bulk zeolite with different particle sizes and changing the synthesis conditions for the lamellar shell. It should be noted that the 2D-3D hybrid MFI structures were prepared by a two-step synthesis approach, which involved the pre-synthesis of the bulk zeolite core followed by the epitaxial growth of the 2D zeolite lamellae on it. Therefore, it is desirable to develop a simple approach for synthesis of hierarchical hybrid zeolite materials with tunable microporous and mesoporous domains.

Here in this study, a simple one-step dual template strategy has been introduced to achieve facile synthesis of hybrid lamellar-bulk MFI (HLBM) zeolite with tunable meso-/microporosity, consisting of a lamellar zeolite structure on the surface of the bulk zeolite core. Tetrapropylammonium hydroxide (TPAOH) and $[\text{C}_{22}\text{H}_{45}\text{-N}^+(\text{CH}_3)_2\text{-C}_6\text{H}_{12}\text{-N}^+(\text{CH}_3)_2\text{-C}_6\text{H}_{13}]\text{Br}_2$ (C_{22-6-6}) were used as the templates in HLBM zeolite synthesis to assist the formation of the bulk core and lamellar shell of the HLBM structures, respectively.

In the dual template synthesis approach explained in chapter 2, the concentration of C_{22-6-6} was kept constant in the synthesis recipe and the

concentration of TPAOH was changed. The results showed that the morphology, textural properties, and catalytic performance of the synthesized multi-lamellar MFI zeolites can be tailored simply by tuning the concentration of these dual templates in the synthetic recipe. In this case, an opposite approach was chosen by tuning the C_{22-6-6} concentration while keeping the TPAOH concentration constant in the synthesis recipe. TPAOH is the traditional molecular zeolite template to assist micropore formation in bulk MFI zeolite¹⁴⁴, while C_{22-6-6} is an emerging surfactant that leads to the coherent assembly of the zeolite layer and the surfactant to produce two dimensional lamellar MFI zeolite nanosheet structures⁶¹. By using TPAOH and C_{22-6-6} as dual templates in the zeolite synthesis recipe, with higher concentration ratios of TPAOH compared to C_{22-6-6} , hypothetically, it is expected that the two templates function sequentially and cooperatively in directing the bulk core and lamellar shell formation simultaneously in this hybrid zeolite structure (see Figure 3-1).

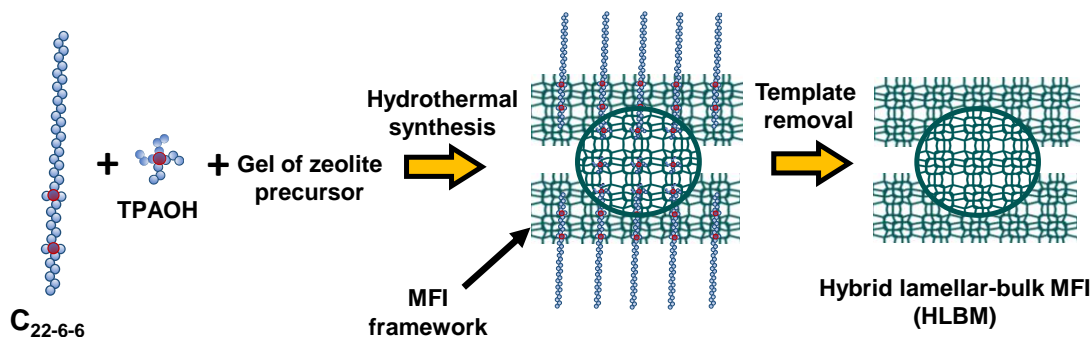


Figure 3.1. Schematic illustration of HLBM zeolite synthesis.

In order to tune the size of the core and shell in these HLBM zeolite structures and as thus their textural properties, the influences of several parameters on the

HLBM zeolite formation were investigated, including concentration of C₂₂₋₆₋₆, hydrothermal synthesis time, and ageing temperature and time prior to hydrothermal crystallization.

3.2. Experimental section

3.2.1. Materials for zeolite synthesis

Tetrapropylammonium hydroxide (TPAOH, 40 wt%) aqueous solution was supplied by Alfa Aesar. Tetraethyl orthosilicate (TEOS, 98% purity) was purchased from Sigma-Aldrich. Deionized (DI) water was used throughout the experiment. C₂₂₋₆₋₆ was synthesized using the same method introduced in section 2.2.1 of chapter 2.

3.2.2. Dual template synthesis of HLBM zeolite

The recipe used for dual template synthesis of the HLBM zeolite was as follows: 100SiO₂/*x*C₂₂₋₆₋₆/36TPAOH/4000H₂O, where *x* equals to 1, 3, 5, and 7, respectively. Typically, the synthesis was performed by mixing 5.075 g TPAOH with 11.5 g DI water. Then, 5.78 g TEOS was added to the mixture and the mixture was stirred vigorously at room temperature for 8 h. Finally, this solution was mixed with a C₂₂₋₆₋₆ solution that was prepared by dissolving desired amount of C₂₂₋₆₋₆ in 8.5 g DI water at 333 K. After continuous mixing for 2 h at room temperature, the resultant gel was transferred into a Teflon-lined stainless-steel autoclave, followed by hydrothermal synthesis for 120 h by tumbling the autoclave vertically at 30 rpm in an oven heated at 423 K. The as-obtained samples were named based on the molar ratio

of C₂₂₋₆₋₆ and TPAOH templates used in the synthesis recipe, as listed in Table 3.1. After synthesis, the zeolite product was filtered, washed with DI water, dried, and calcined using the same procedure mentioned before in section 2.2.2 of chapter 2. In order to examine the effects of dual templates on the hybrid zeolite structure formation, control experiments were carried out using the same recipe described above, but with either single TPAOH or single C₂₂₋₆₋₆ template. The as-obtained products were designated as MFI-0/36 and MFI-3/0, respectively.

Table 3.1. Compositions for synthesis of HLBM zeolites by dual template method.

Zeolite	Composition in molar ratios			
	C ₂₂₋₆₋₆	TPAOH	SiO ₂	H ₂ O
MFI-0/36	0	36	100	4000
MFI-1/36	1	36	100	4000
MFI-3/36	3	36	100	4000
MFI-5/36	5	36	100	4000
MFI-7/36	7	36	100	4000
MFI-3/0	3	0	100	4000

3.2.3. Materials characterization

Scanning electron microscope (SEM) images of the samples were collected on a Hitachi SU-70 electron microscope. Transmission electron microscope (TEM) images were obtained on a JEM 2100 LaB6 electron microscope. Powder X-Ray diffraction (XRD) patterns were recorded using a Bruker D8 Advance Lynx Powder Diffractometer (LynxEye PSD detector, sealed tube, *Cu K_α* radiation with *Ni β*-filter). The nitrogen (N₂) and argon (Ar) adsorption-desorption measurements were carried

out using an Autosorb-iQ analyzer (Quantachrome Instruments) at 77 K and 87 K, respectively. Prior to the measurement, samples were evacuated overnight at 623 K and 1 mm Hg. The thermogravimetric analysis (TGA) was conducted in a TGA instrument (2950, TA Instruments, Inc.) under a mixed air and N₂ flow of 100 mL min⁻¹ (40% air, 60% N₂) with a heating rate of 10 K min⁻¹ from 303 K to 873 K.

3.3. Results and discussion

3.3.1. HLBM structure formation assisted by dual templates

To examine the effect of dual templates on the formation of HLBM zeolite, the synthesis was comparatively carried out using the synthesis recipes comprised of single TPAOH template, single C₂₂₋₆₋₆ template, and dual C₂₂₋₆₋₆ and TPAOH templates, respectively. Figure 3.2 shows the XRD patterns of as-obtained products before calcination. The reflections in the wide-angle XRD patterns ($2\theta \sim 7-40^\circ$) of MFI-0/36 and MFI-3/36 in Figure 3.2(B) resemble the characteristic of crystalline MFI, which confirms that zeolite structure can be formed under the investigated synthesis conditions. The absence of reflection peaks in the wide-angle XRD patterns of MFI-3/0 sample indicates that the as-obtained material is amorphous. The low-angle XRD patterns ($2\theta \sim 1.2-7^\circ$) of these three samples are remarkably different. Four reflection peaks ($2\theta \sim 1.5^\circ, 3.0^\circ, 4.0^\circ, \text{ and } 6.0^\circ$) are shown for the MFI-3/36 sample in Figure 3.2(A), which is similar to the pillared MFI zeolite reported by Ryoo and co-workers,¹¹³ demonstrating that this material has a good long-range lamellar

structural order. MFI-0/36 and MFI-3/0 do not show any diffraction peaks in the low-angle XRD pattern, indicating the non-existence of lamellar structure in both samples.

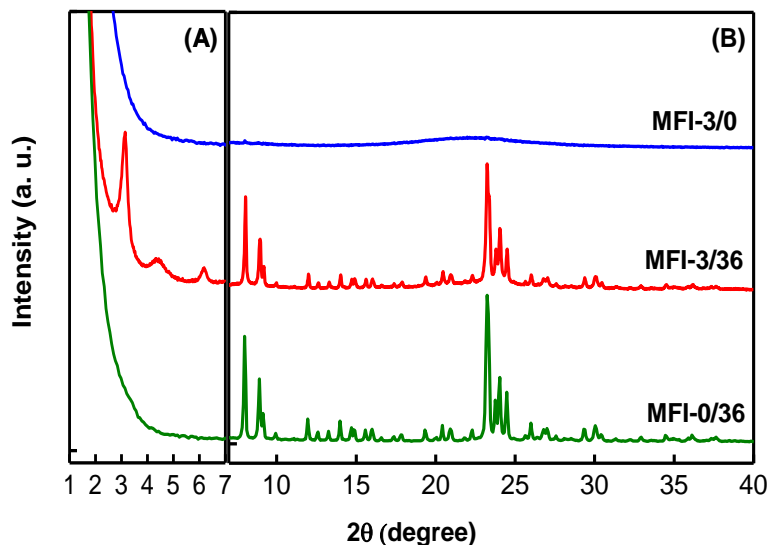


Figure 3.2. Low-angle (A) and wide-angle (B) XRD patterns of MFI-0/36, MFI-3/36, and MFI-3/0 after 120 h of hydrothermal synthesis.

Figure 3.3 shows the morphologies of MFI-0/36, MFI-3/36, and MFI-3/0 samples visualized by SEM and TEM observations. The representative SEM images in Figure 3.3(A), (C), and (E) indicate that these three samples have distinct morphologies. MFI-0/36 sample (Figure 3.3(A)) consists of short cylinder-like bulk MFI particles with an average width of ~ 300 nm and thickness of ~ 200 nm and well crystallized smooth surfaces. MFI-3/36 (Figure 3.3(C)) contains faba bean-like particles with an average width of ~ 500 nm and thickness of ~ 250 nm, respectively and rough surfaces. A side-view of the zeolite particle (circled in Figure 3.3(C)) shows that it has a lamellar structure on the surface. MFI-3/0 sample (Figure 3.3(E)) is composed of aggregated spherical particles with sizes of ~ 25 nm. TEM images of

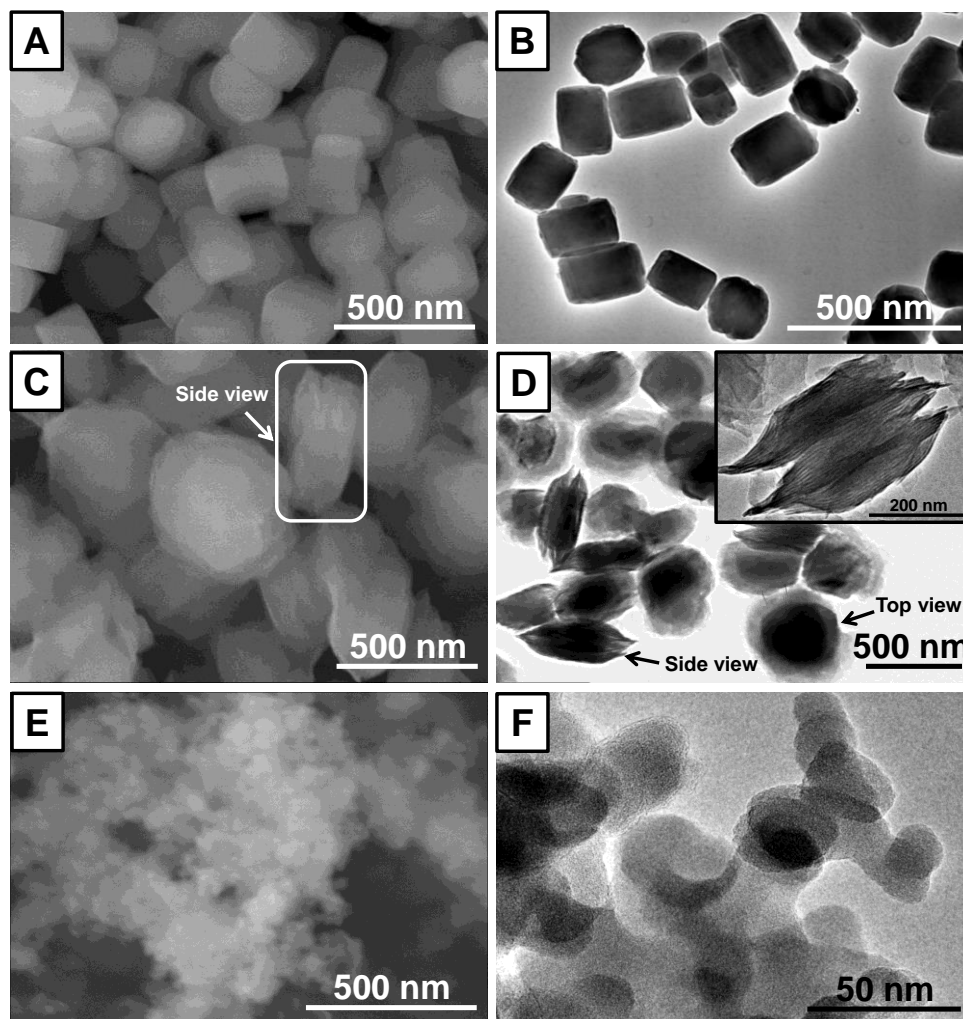


Figure 3.3. SEM and TEM images of HLB zeolites after 120 h of hydrothermal synthesis. (SEM: (A) MFI-0/36, (C) MFI-3/36, and (E) MFI-3/0. TEM: (B) MFI-0/36, (D) MFI-3/36, and (F) MFI-3/0. Inset picture in (C) shows the side view of the MFI-3/36 particles and inset picture in (D) shows the HRTEM image for MFI-3/36.)

the MFI-0/36, MFI-3/36, and MFI-3/0 samples in Figure 3.3(B), (D), and (F), respectively, confirm the morphologies of these samples observed under SEM. The top-view of the particles in Figure 3.3(D) demonstrates that MFI-3/36 contains a bulk core and lamellar shell structure, as visualized by the dark region in the center and the grey area at the edge of the particle, respectively. The bulk core size of MFI- 3/36 is ~ 300 nm, similar to the sizes of bulk MFI-0/36 in Figure 3.3(A) and (B). The high

resolution TEM (HRTEM) image of MFI-3/36 (inset image in Figure 3.3(D)) confirms the crystalline structure of the lamellar shell.

Argon (Ar) adsorption-desorption isotherms (Figure 3.4) were used to reveal the textural properties of the MFI-0/36 and MFI-3/36 zeolite samples. MFI-0/36 shows the typical isotherm for bulk MFI zeolite, while MFI-3/36 exhibits type-IV isotherm, in which a hysteresis loop is clearly seen, corresponding to the capillary condensation of Ar in the mesoporous structures. Non-local density functional theory (NLDFT) pore size analysis based on the adsorption branches of the isotherms further indicates the presence of mesopores (~5 nm) in the MFI-3/36 zeolite (inset image in Figure 3.4). The Ar isotherms and pore size distribution data for these samples are in good agreement with their structural features characterized by XRD, SEM, and TEM observations, further confirming the formation of HLBM zeolite structures by the

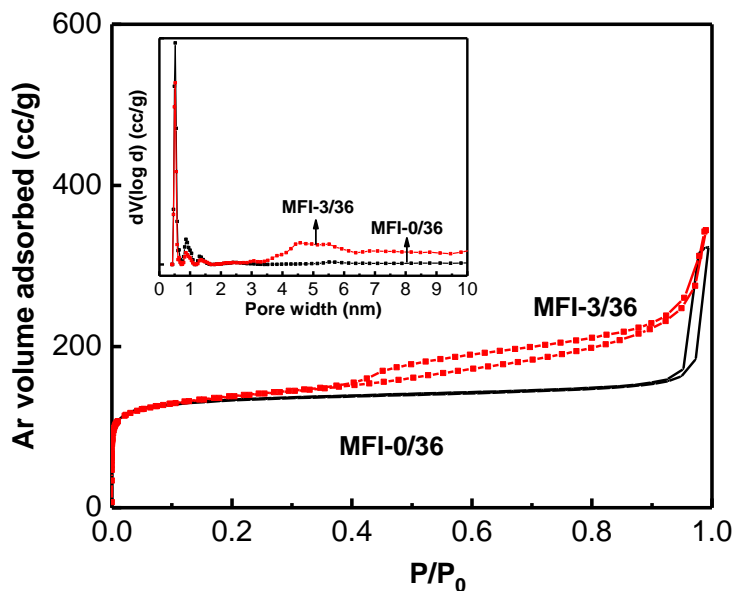


Figure 3.4. Ar adsorption-desorption isotherm and the corresponding NLDFT pore size distribution (inset image) of MFI-0/36 and MFI-3/36 zeolite samples.

dual template synthesis method. The sole presence of C₂₂₋₆₋₆ in the studied synthesis conditions, however, only generated amorphous product. This result suggests that a cooperative interaction between C₂₂₋₆₋₆ and TPAOH templates might exist to direct the formation of the HLBM structure in a single zeolite particle.

3.3.2. Scheme for the formation of the HLBM structure

To further our understanding of the HLBM zeolite formation and the functions of C₂₂₋₆₋₆ and TPAOH templates in the synthesis, we examined the evolution of the MFI-3/36 zeolite structure as a function of the hydrothermal synthesis time. The experimental conditions used in this study were the same as those used in the synthesis of MFI-3/36 in Figure 3.3(C) and (D), except that the hydrothermal synthesis time was reduced to 0 h (i.e., right after ageing for 8 h at room temperature), 3 h, 6 h, 12 h, 24 h, and 72 h, respectively. The wide-angle XRD patterns in Figure 3.5 confirm the non-existence of crystalline material in the synthetic gel before the start of hydrothermal synthesis and the presence of crystalline MFI structures after 3 h, 6 h, 12 h, 24 h, and 72 h of hydrothermal synthesis (see Figure 3.5(B)). The reflections at $2\theta \sim 2^\circ$ and 4° in the low-angle XRD patterns of MFI-3/36 (see Figure 3.5(A)) after 0 h, 3 h, 6 h, and 12 h of hydrothermal synthesis are indexed as hexagonal structure of MCM-41⁵⁷, which indicate the presence of amorphous silica with an ordered structure. After 24 h and 72 h of hydrothermal synthesis, reflections at $2\theta \sim 1.5^\circ$ and 3° were observed, which are indexed as the multi-lamellar MFI structure.^{42, 43} The decreases in peak intensity of reflections at 2θ

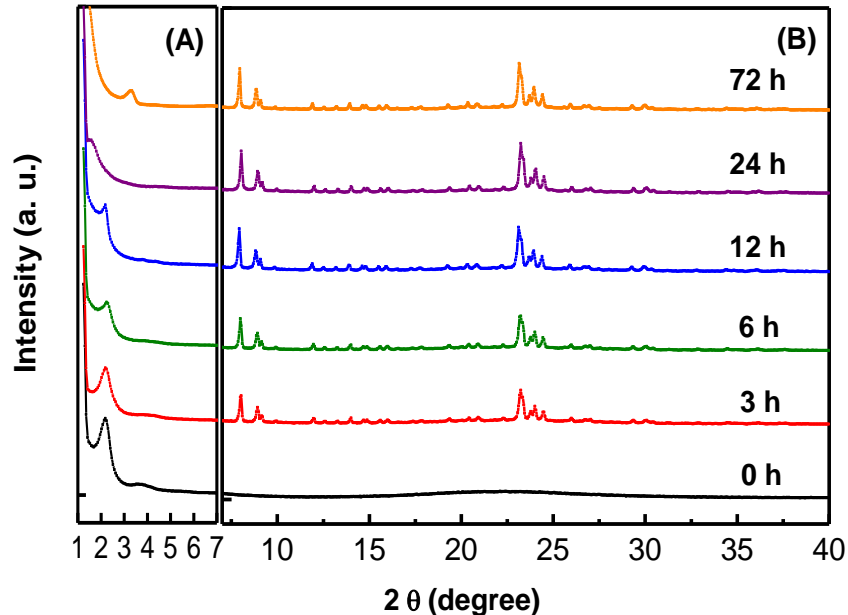


Figure 3.5. Low-angle (A) and wide-angle (B) XRD patterns of MFI-3/36 after 0 h, 3 h, 6 h, 12 h, 24 h, and 72 h hydrothermal synthesis, respectively.

$\sim 2^\circ$ and 4° and increases in peak intensity of the reflections at $2\theta \sim 1.5^\circ$ and 3° with the hydrothermal synthesis time suggest a phase transformation from the amorphous silica phase to crystalline zeolite materials in the formation of the hybrid lamellar-bulk MFI-3/36 zeolite.

Figure 3.6 shows the SEM images of MFI-3/36 at different hydrothermal synthesis times. After ageing the zeolite synthetic gel at room temperature for 8 h, the sample mainly consists of spherical hollow particles with a range of sizes (Figure 3.6(A)). After 3 h of hydrothermal synthesis (Figure 3.6(B)), the sample contains a mixture of irregular hollow particles and small short cylinder-like bulk MFI particles. With a further increase in the synthesis time to 6 h and 12 h (Figure 3.6(C) and 3.6(D), respectively), the bulk MFI particles grow bigger accompanied by the

disappearance of the hollow spherical particles. After 24 h of synthesis, the lamellar zeolite structure around the bulk zeolite core emerges (Figure 3.6(E)). By increasing the synthesis time to 72 h (Figure 3.6(F)) and 120 h (Figure 3.3(C)), the lamellar shell on the surface of bulk zeolite core becomes more observable. The evolution of the HLBM zeolite particles from morphology observations is consistent with the XRD data discussed before (Figure 3.5).

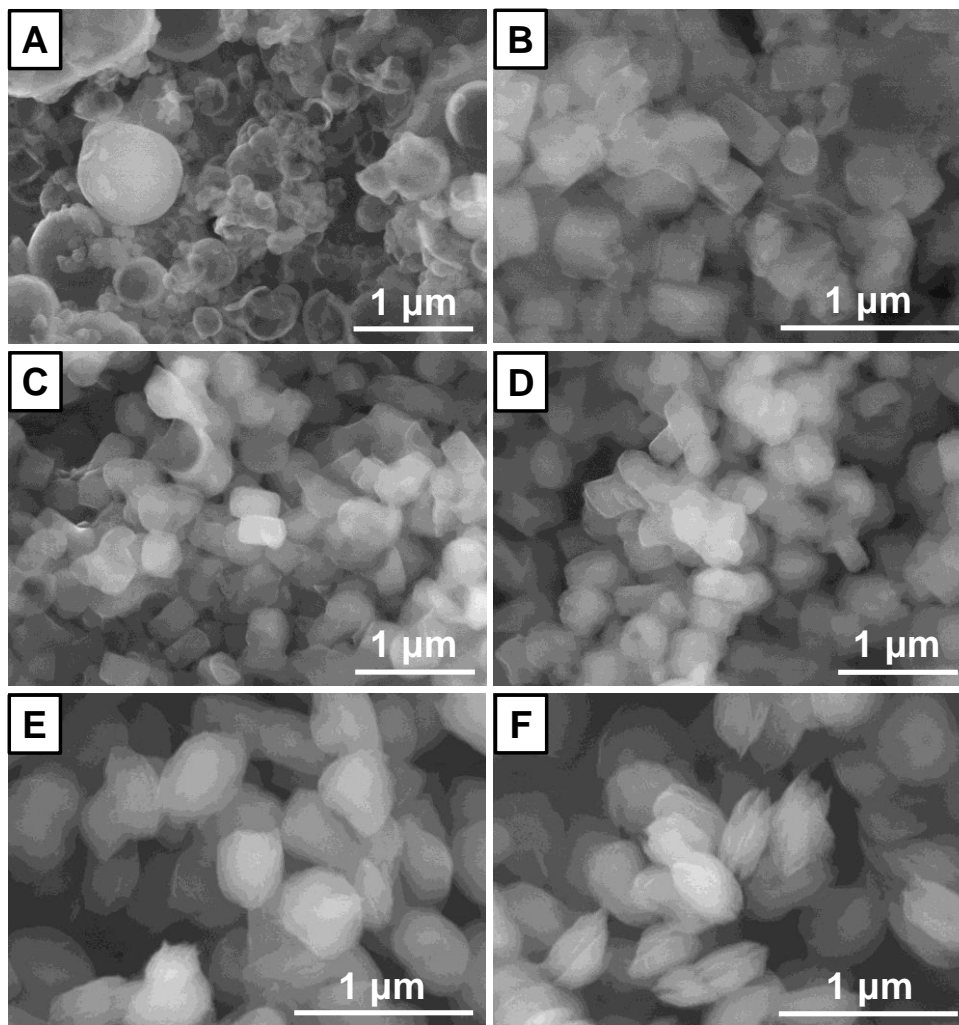


Figure 3.6. SEM images of MFI-3/36 after (A) 0 h, (B) 3 h, (C) 6 h, (D) 12 h, (E) 24 h, and (F) 72 h of hydrothermal synthesis, respectively.

A nitrogen (N₂) adsorption-desorption measurement was further conducted to study the textural property changes of MFI-3/36 samples with hydrothermal synthesis time. The isotherms shown in Figure 3.7(A) illustrate that the MFI-3/36 materials synthesized at 423 K for 0 h, 3 h, 6 h, and 12 h have type-IV N₂ isotherms of MCM-41 structure.⁵⁷ After 24 h, 72 h, and 120 h synthesis, isotherms have micro- and mesoporous zeolite features.^{43, 61} The NLDFT pore size distributions of these samples (Figure 3.7(B)) determined from the adsorption branch of the isotherms demonstrate that all these samples have similar narrow pore size distributions with average sizes of ~3.5 nm and ~4.7 nm before and after 12 h of hydrothermal synthesis, respectively. The isotherm data are in good agreement with the XRD and SEM observations on the growth of MFI-3/36 over the synthesis time.

The evolution of the MFI-3/36 structure with hydrothermal synthesis time suggests a possible growth scheme for the hybrid lamellar-bulk 2D-3D zeolite with the assistance of the C₂₂₋₆₋₆ and TPAOH templates. After ageing at room temperature for 8 h, the zeolite synthetic gel formed amorphous silica materials with ordered porosity with the assistance of C₂₂₋₆₋₆ template. When the synthetic gel was held under the hydrothermal crystallization condition, the bulk zeolite particles formed with the assistance of TPAOH template. The growth of bulk zeolite was accompanied by the consumption of the amorphous silica material. As a result, the sample was comprised of amorphous MCM-41 and crystalline MFI phases at the earlier stage of the hydrothermal synthesis (for example, before 12 h). An epitaxial growth of the lamellar structure that was directed by C₂₂₋₆₋₆ template occurred on the surface of the bulk MFI particles by extending the synthesis time beyond 24 h. After 72 h of

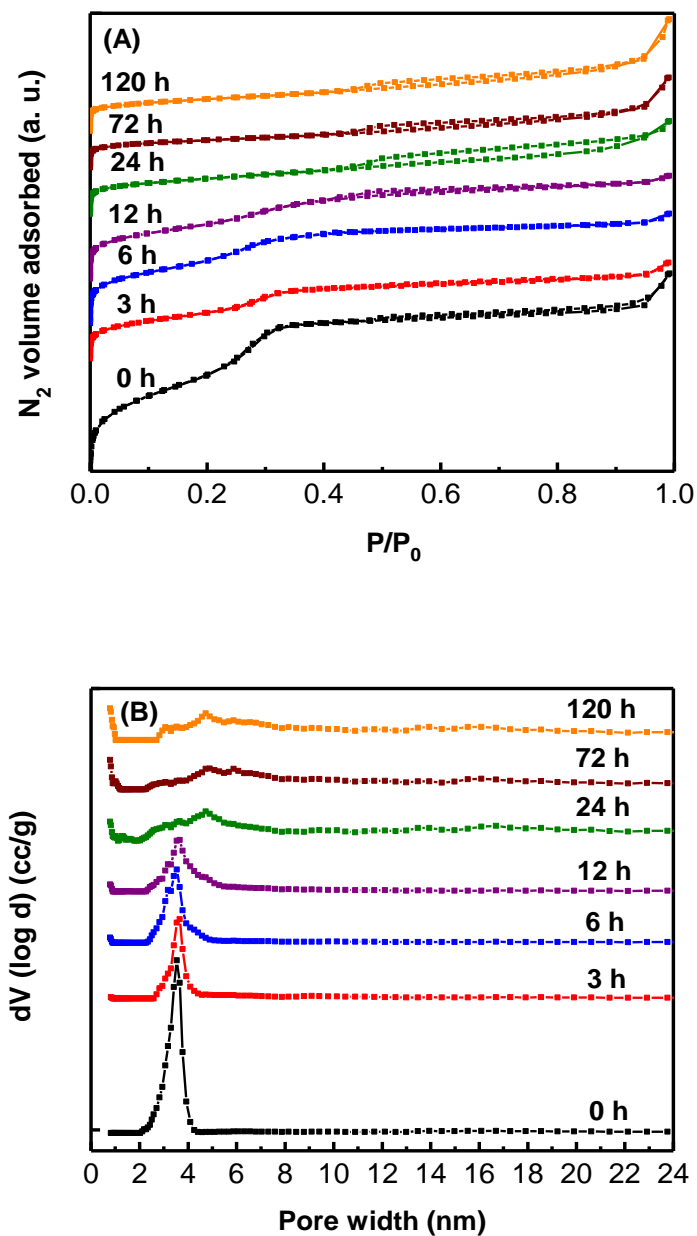


Figure 3.7. N_2 adsorption-desorption isotherms (A) and the corresponding NLDFT pore size distributions (B) of MFI-3/36 after 0 h, 3 h, 6 h, 12 h, 24 h, 72 h, and 120 h hydrothermal synthesis, respectively.

hydrothermal synthesis, the crystallization of lamellar shell structure was completed, as indicated by the disappearance of amorphous silica material in the MFI-3/36

sample. The formation of the amorphous MCM-41 phase, followed by bulk MFI zeolite in the initial stage of the synthesis, indicates the sequential functions of C₂₂₋₆₋₆ and TPAOH, which was consistent with dual template synthesis using cetyltrimethyl ammonium bromide (CTAB) and TPAOH templates.^{56, 57, 60} However, in the later stage of the synthesis, an epitaxial growth of zeolite lamellae directed by C₂₂₋₆₋₆ transformed the amorphous silica material to crystalline zeolite, and thus resulted in the formation of hybrid lamellar shell-bulk core crystalline zeolite, which is in contrast to the intimate mixture of amorphous silica and crystalline zeolite produced from the CTAB and TPAOH templates.⁵⁷ A cooperative function between C₂₂₋₆₋₆ and TPAOH is expected to exist, because single C₂₂₋₆₋₆ or TPAOH can only produce amorphous silica or bulk zeolite particles, respectively, under the investigated synthesis conditions.

3.3.3. Domain sizes of the lamellar shell tuned by C₂₂₋₆₋₆ concentration

To explore the capability of tuning the lamellar and/or bulk domain sizes, and thus the meso-/micro-porosity of the HLBM zeolites, we investigated the effect of C₂₂₋₆₋₆ concentration on the HLBM zeolite structures. Figure 3.8 shows the morphologies of MFI-1/36, MFI-5/36, and MFI-7/36, respectively. The MFI-1/36 particles in Figure 3.8(A) and (B) have similar morphologies and sizes to those of MFI-0/36 (Figure 3.3(A) and (B)), but they have relatively rougher crystal surfaces. A close examination of the particles in Figure 3.8(B), as shown by the inset image, indicates that the rough surface is composed of a lamellar structure. The SEM image in Figure 3.8(C) and TEM images in Figure 3.8(D) and (F), respectively,

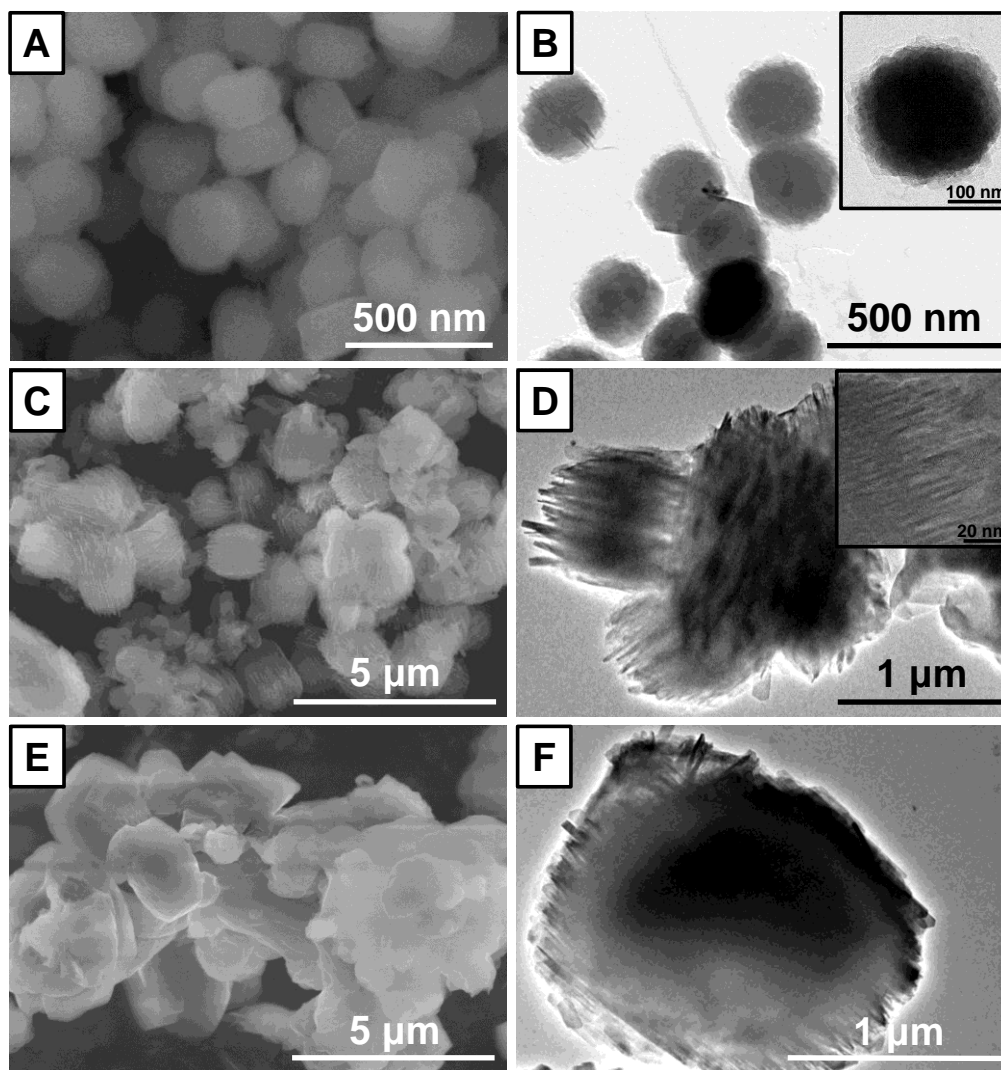


Figure 3.8. SEM and TEM images of HLBM zeolite after 120 h of hydrothermal synthesis. (SEM: (A) MFI-1/36, (C) MFI-5/36, and (E) MFI-7/36. TEM: (B) MFI-1/36, and (D), (F) MFI-5/36. Inset picture in (B) show the TEM of MFI-1/36 at high magnification and inset picture in (D) shows HRTEM image for MFI-5/36.)

which correspond to MFI-5/36 sample, show clearly visible lamellar shell structure. The HRTEM image (inset in Figure 3.8(D)) confirms the crystalline structure of the lamellar shell in MFI-5/36 sample. A statistical analysis on the HLBM particle sizes and bulk zeolite core sizes indicates that MFI-0/36, MFI-1/36, and MFI-3/36 have similar bulk core sizes, while the layered shell thickness increases with increasing the

C_{22-6-6} concentration in the dual template synthesis. Moreover, the growth of the lamellar shell on the HLBM particles was preferential along the width directions (*i.e.*, a-c direction of the MFI zeolite). The epitaxial growth of the lamellar shell in the dual template synthesis is consistent with the epitaxial growth of zeolite lamellae on bulk zeolite with different particle sizes reported by Nair and co-workers.⁶⁵ A further increase in the concentration of C_{22-6-6} in the synthesis gel led to a continuous growth of the zeolite along the width direction, and thus resulted in the formation of large HLBM zeolite particles (MFI-5/36) and interconnection among the HLBM zeolite particles (MFI-7/36). Figure 3.8(E) shows that MFI-7/36 consists of irregular plate-like zeolite aggregates with width in the range of several micrometers. Some bulk MFI particles are also visible in MFI-7/36, indicating the non-uniformity of the product that might be due to the competition of the dual templates in executing their functions in the synthesis. The changes in shell thickness of the HLBM zeolite particles with the C_{22-6-6} concentration confirm the capability of tuning the domain sizes of the lamellar shell by simply varying the concentration of C_{22-6-6} in the synthesis. The involvement of C_{22-6-6} in the dual template synthesis was further confirmed by conducting the thermogravimetric analysis of the as-obtained HLBM samples. As shown in Figure 3.9, the weight loss of HLBM particles increases with increasing the C_{22-6-6} concentration in the dual template synthesis.

The XRD patterns of MFI-1/36, MFI-5/36, and MFI-7/36 zeolites are shown in Figure 3.10. The reflections in the wide-angle and low-angle XRD patterns confirm the formation of crystalline lamellar-bulk zeolite structures under the investigated synthesis conditions. The reflections at $2\theta \sim 1.5^\circ, 3.0^\circ, 4.0^\circ,$ and 6.0° exist in the

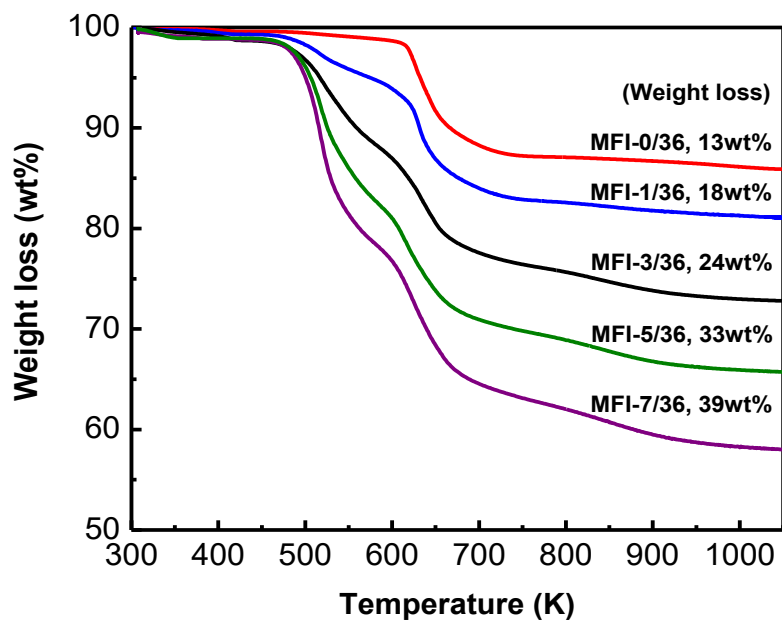


Figure 3.9. TGA curves of HLBM zeolite synthesized using different C_{22-6-6} concentration in the recipe.

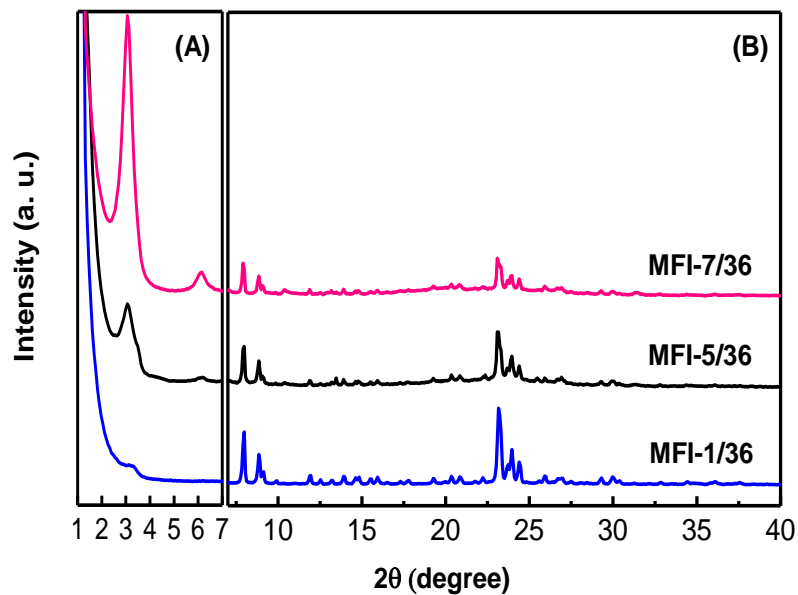


Figure 3.10. Low-angle (A) and wide-angle (B) XRD patterns of MFI-1/36, MFI-5/36, and MFI-7/36 after 120 h of hydrothermal synthesis.

XRD patterns of these three samples and their intensities increase gradually with increasing the C_{22-6-6} concentrations, which demonstrates that the long-range structural order in these materials increases with increasing the C_{22-6-6} concentration.

The textural properties of MFI-1/36, MFI-5/36, and MFI-7/36, together with MFI-0/36 and MFI-3/36 discussed before were analyzed from N_2 adsorption-desorption isotherms. Table 3.2 shows the Brunauer-Emmett-Teller (BET) surface area (S_{BET}), external surface area (S_{ext}), total pore volume (V_t), micropore volume (V_{micro}) and mesopore volume (V_{meso}) of each sample analyzed from the corresponding N_2 isotherm. The increase in BET surface area, external surface area, total pore volume, and mesopore volume from MFI-0/36, MFI-1/36, MFI-3/36, to MFI-5/36 samples is consistent with an increase of the C_{22-6-6} concentration in the dual template synthesis of these samples. The further increase of the C_{22-6-6} concentration in the synthesis (for example, MFI-7/36) led to a decrease in these textural properties. The variation of the textural properties of the HLBM zeolites by

Table 3.2. Textural properties of HLBM zeolites synthesized using different C_{22-6-6} content in the recipe measured by N_2 adsorption-desorption method.

Zeolite	S_{BET}^a ($m^2 g^{-1}$)	S_{ext}^b ($m^2 g^{-1}$)	V_t^c ($cm^3 g^{-1}$)	V_{micro}^b ($cm^3 g^{-1}$)	V_{meso}^d ($cm^3 g^{-1}$)
MFI-0/36	474	162	0.33	0.13	0.20
MFI-1/36	478	187	0.35	0.12	0.23
MFI-3/36	537	259	0.44	0.12	0.33
MFI-5/36	467	279	0.49	0.08	0.41
MFI-7/36	343	242	0.31	0.05	0.26

^a Determined from multi-point BET method. ^b Determined from t -plot method. ^c total pore volume determined from NLDFT method. ^d Calculated from $V_{meso} = V_t - V_{micro}$.

changing the C₂₂₋₆₋₆ concentration in the synthesis recipe indicates the feasibility of systematic tuning of the textural properties of HLBM zeolites by simply tuning the C₂₂₋₆₋₆ template content in the dual template synthesis.

3.3.4. Domain sizes of the bulk core tuned by ageing temperature or time

In order to maximize the capability of tuning the structural and textural properties of the HLBM zeolite particles, the domain size of the bulk zeolite core is expected to be simply varied. It is reported that the ageing temperature and/or time prior to the hydrothermal crystallization affect the sizes of the bulk zeolite crystals because the number of nuclei is influenced by these ageing conditions.^{7, 145} Therefore, we tried to study the tuning of the bulk zeolite core sizes by ageing the zeolite synthetic gel at different temperatures or times.

The experimental conditions used for the synthesis of MFI-5/36 and MFI-3/36 were used as the base cases for the studies on the effects of ageing temperature and ageing time, respectively. In addition to ageing the synthetic gel for MFI-5/36 at room temperature (298 K) described before, the synthetic gel was aged at 323 K, 353 K, and 373 K, respectively. The SEM images and inset plots in Figure 3.11(A)-(D) show that by increasing the ageing temperature from 298 K to 373 K, the average particle size of MFI-5/36 samples decreases from ~1300 nm to ~300 nm. The textural property analysis based on N₂ isotherms on these samples in Table 3.3 shows that the BET surface area, external syrface area, total pore volume, and mesopore volume of the zeolite samples increase with increase in the ageing temperature. Similarly, an increase in the ageing time (from 2 h to 16 h) leads to the decrease in particle sizes in the synthesis of hybrid lamellar-bulk MFI-3/36, as shown by the SEM images in

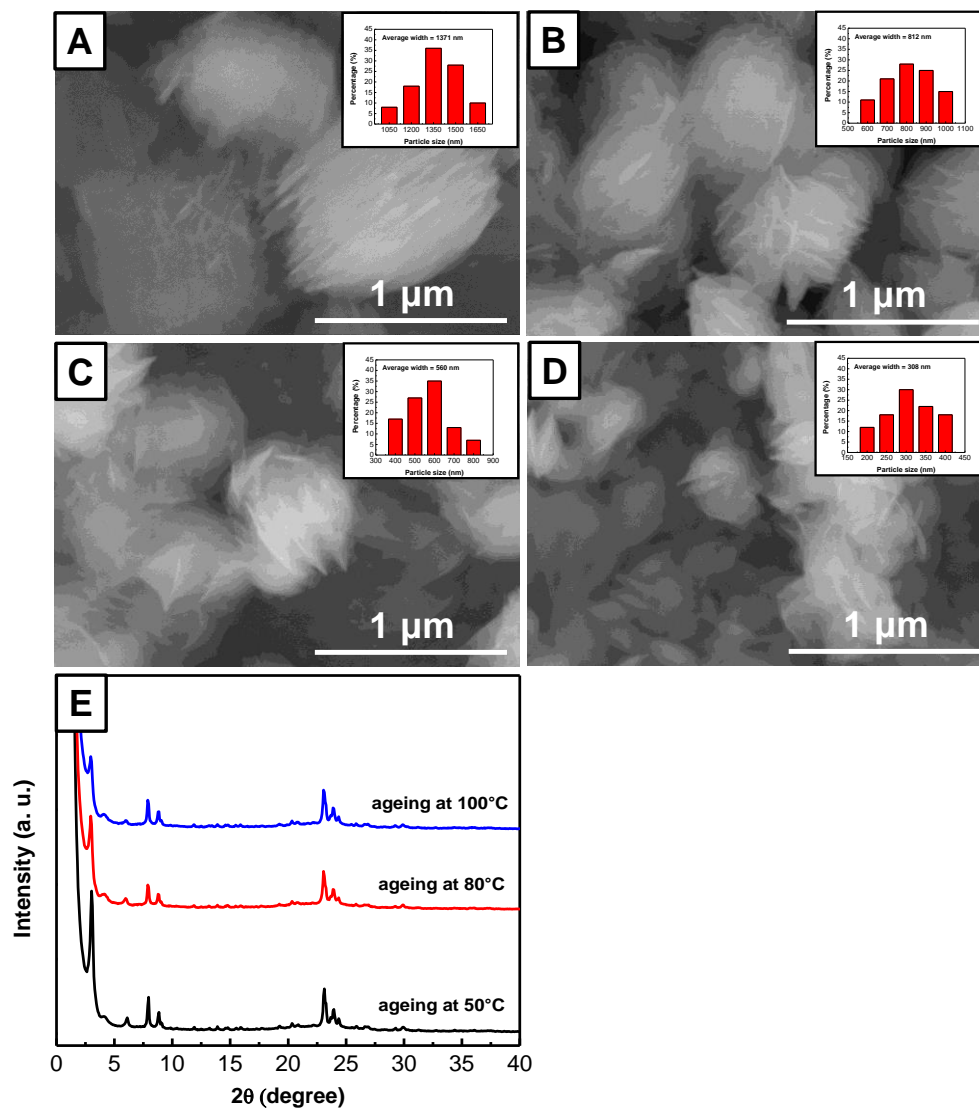


Figure 3.11. SEM images and particle size distributions (inset) of MFI-5/36 sample synthesized at ageing temperature of (A) 298 K, (B) 323 K, (C) 353 K, and (D) 373 K, respectively. The SEM image of MFI-5/36 at 298 K is represented here for comparison purpose. (E) shows XRD patterns of these samples.

Figure 3.12. The inset plots in Figure 3.12 indicate that the average width of the HLBM particles decreases from ~611 nm to ~433 nm when the ageing time increases from 2 h to 16 h. The textural property analysis based on N₂ isotherms on these samples in Table 3.4 demonstrates an increase in the BET surface area and external

Table 3.3. Textural properties of MFI-5/36 zeolite synthesized at different ageing temperatures measured by N₂ adsorption-desorption method.

Ageing temperature (K)	S_{BET}^a (m ² g ⁻¹)	S_{ext}^b (m ² g ⁻¹)	V_t^c (cm ³ g ⁻¹)	V_{micro}^b (cm ³ g ⁻¹)	V_{meso}^d (cm ³ g ⁻¹)
298	467	279	0.49	0.08	0.41
323	500	281	0.61	0.10	0.51
353	528	334	0.69	0.08	0.61
373	539	315	0.72	0.09	0.62

^a Determined from multi-point BET method. ^b Determined from t-plot method. ^c Total pore volume determined from NLDFT method. ^d Calculated from $V_{\text{meso}} = V_T - V_{\text{micro}}$

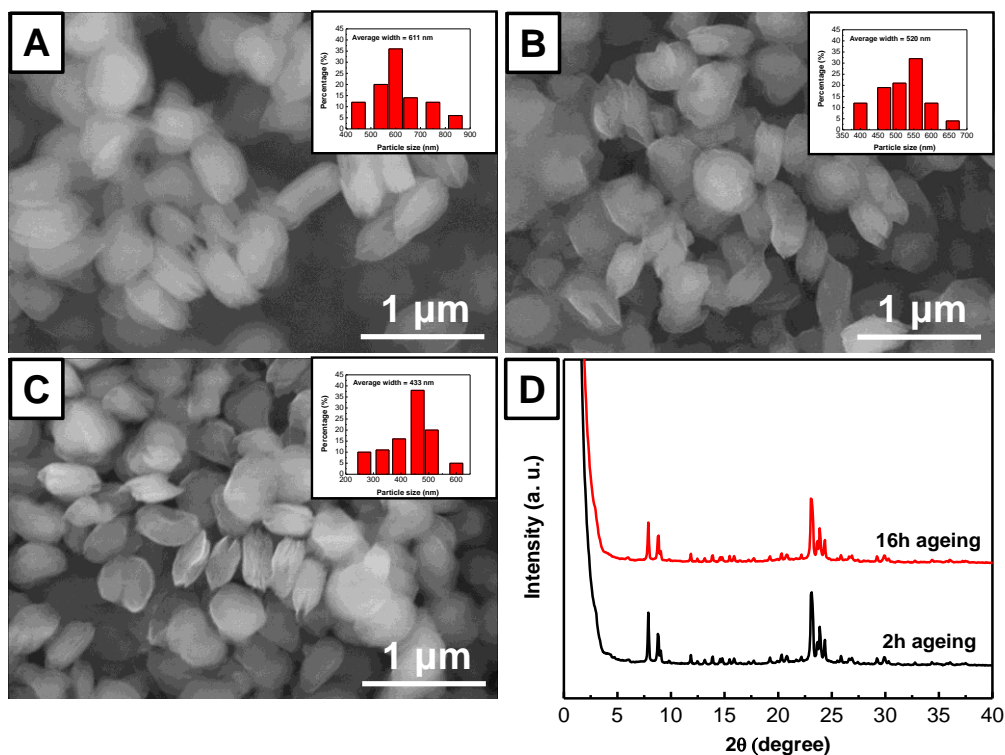


Figure 3.12. SEM images and particle size distributions (inset) of MFI-3/36 synthesized at ageing time of (A) 2 h, (B) 8 h, and (C) 16 h, respectively. The SEM image of MFI-3/36 at 8 h is represented here for comparison purpose. (D) shows XRD patterns of these samples.

surface area of the zeolite samples with increasing the ageing time. The decrease in HLBM particle sizes with increase in the ageing temperature or time of the zeolite synthetic gel might be caused by the increased number of nuclei under these conditions. Moreover, the XRD patterns of these samples have shown in Figure 3.11(E) and 3.12(D) confirm that all of them are crystalline MFI. These results indicate that by simply selecting the ageing temperature or time, the textural properties of the HLBM particles can be modulated. The facile synthesis of meso-/microporous zeolites with tunable domain sizes and textural properties in a single material is important to keep their potential applications as broad as possible.^{8, 118}

Table 3.4. Textural properties of MFI-3/36 zeolite synthesized using different ageing times measured by N₂ adsorption-desorption method.

Ageing time (h)	S _{BET} ^a (m ² g ⁻¹)	S _{ext} ^b (m ² g ⁻¹)	V _t ^c (cm ³ g ⁻¹)	V _{micro} ^b (cm ³ g ⁻¹)	V _{meso} ^d (cm ³ g ⁻¹)
2	287	163	0.50	0.09	0.41
8	537	259	0.44	0.11	0.33
16	581	332	0.58	0.11	0.47

^a Determined from multi-point BET method. ^b Determined from *t*-plot method. ^c Total pore volume determined from NLDFT method. ^d Calculated from $V_{meso} = V_t - V_{micro}$.

3.4. Concluding remarks

Hybrid lamellar-bulk MFI (HLBM) zeolites were successfully synthesized by a facile one-step dual template synthesis method. The TPAOH and C₂₂₋₆₋₆ templates were employed in the synthesis, which function sequentially and cooperatively in

directing the bulk core and lamellar shell formation in the hybrid zeolite structure. The growth of HLBM zeolite structure as a function of synthesis time indicates that the bulk core formed in the early stage of the zeolite crystallization, followed by the lamellar shell growth on the bulk core. The influence of the C₂₂₋₆₋₆ concentration on the HLBM zeolite structure was investigated, showing that the thickness of the mesoporous lamellar shell increases with increasing the C₂₂₋₆₋₆ content in the synthesis recipe. The study on the effect of ageing temperature and time prior to the hydrothermal crystallization shows that HLBM particle sizes decrease with increasing ageing temperature or time, which might be caused by the increased number of nuclei formed under these conditions. The variation on the domain sizes of the lamellar shell and bulk core, and thus the textural properties of the HLBM zeolite samples by simply modulating the content of the C₂₂₋₆₋₆ template and/or ageing conditions indicates that the dual template synthesis method is a simple approach to achieve desirable zeolite properties. The ability to tune systematically the textural properties of the HLBM zeolites is important for applications of a specific zeolite structure in composite membrane fabrication for separation applications or hierarchical micro-/mesoporous zeolite catalysts for catalytic reactions. The dual template synthesis approach may be applicable to other hybrid zeolite materials when proper templates are selected.

Chapter 4: The role of external acidity of meso-/microporous zeolites in determining selectivity for acid-catalyzed reactions of benzyl alcohol

4.1. Introduction

The meso-/microporous zeolites couple the catalytic features of microporosity and the improved mass transport consequence of mesoporosity in a single material, possessing the capacity of overcoming the mass-transfer constraints and the resultant low catalyst utilization, a major drawback in most reactions catalyzed by the conventional microporous zeolites.^{31, 75, 80, 108, 146, 147} A variety of zeolites containing structured porosity on micro- and mesopore levels have been created in the past decade^{1, 33, 92, 148} and the catalytic tests showed that the meso-/microporous zeolites have higher reaction rates and/or different selectivity in comparison with their microporous zeolite analogues which consist exclusively of the microporosity. The enhanced catalytic reaction rate and/or altered selectivity on meso-/microporous zeolites has been attributed to the enhanced accessibility to active sites and transport characteristics of these materials^{17, 70, 72, 149}, while the role of external acidity (active sites on external surface and in pore mouth region) and systematically tailoring selectivity of external acid sites in the meso-/microporous zeolite materials have remained rarely accessible.

In chapter 3, a simple one-step synthesis route for the production of the hybrid lamellar-bulk MFI (HLBM) zeolite with tunable meso-/microporous domains by a

mixed template system (dual templates) was developed. The crystalline bulk zeolite core and lamellar zeolite shell were formed simultaneously in the hydrothermal crystallization step with the assistance of dual templates, tetrapropyl ammonium hydroxide (TPAOH) and diquatery ammonium surfactant ($[\text{C}_{22}\text{H}_{45}\text{-N}^+(\text{CH}_3)_2\text{-C}_6\text{H}_{12}\text{-N}^+(\text{CH}_3)_2\text{-C}_6\text{H}_{13}]\text{Br}_2$, (C_{22-6-6})), respectively. By tuning the concentration of C_{22-6-6} and the synthesis conditions such as ageing temperature and time of the zeolite synthetic gel in the syntheses, the domain sizes of the lamellar shell and bulk core and thus the meso- and microporosity of the HLBM zeolite particles are simply modulated. The capability of tuning the lamellar and bulk domain sizes of the HLBM zeolite creates the opportunity of designing materials with spatially controlled morphology that have potential advantages for various applications. For example, the similar type of hybrid zeolitic structure, prepared by epitaxial growth of a layered MFI zeolite on the surface of a pre-synthesized bulk MFI, showed enhanced permeability for CO_2 and good CO_2/CH_4 selectivity for gas separations than bare bulk MFI zeolite when they were processed into HLBM zeolite/polyimide and bulk MFI zeolite/polyimide composite membranes.¹⁴ This performance enhancement is due to the highly roughened surface morphology of HLBM zeolite that results in excellent adhesion to a dense glassy polymer. The chemical compositions, particularly acid sites associated with framework Al, could also be spatially modulated. The spatially modulated acid sites would influence the performance of zeolite materials, notably in the area of catalysis.

In this work, the aim is to study the physicochemical properties and catalytic behaviors of HLBM zeolites prepared by one-step dual template assisted synthesis

method. X-ray diffraction (XRD), scanning electron microscopy (SEM), transmission electron microscopy (TEM), nuclear magnetic resonance (NMR), argon (Ar) adsorption and Fourier transformation infrared (FTIR) spectroscopy of adsorbed pyridine were used to characterize the structural and acidity properties of HLBM zeolite materials. The spatial distribution of acid sites, either on external surface/pore mouth region or in micropores of HLBM zeolite, was identified by organic base titration method. The catalytic behavior of external acid sites in HLBM zeolite catalysts was tested using a parallel reaction, alkylation of mesitylene by benzyl alcohol to 1,3,5-trimethyl-2-benzylbenzene and self-etherification of benzyl alcohol to dibenzyl ether, respectively (scheme shown in Figure 2.12, chapter 2).

4.2. Experimental section

4.2.1. Synthesis of HLBM zeolite catalysts

The composition of $100\text{SiO}_2/x\text{C}_{22-6-6}/36\text{TPAOH}/0.5\text{Na}_2\text{O}/y\text{Al}_2\text{O}_3/4000\text{H}_2\text{O}$, where the template molar ratios ($\text{C}_{22-6-6}/\text{TPAOH}$, $x/36$) were 0/36, 1/36, 3/36, and 5/36, respectively, and y varied from 0.1 to 0.7 for HLBM-3/36 zeolite sample, was used for HLBM zeolite synthesis. The as-obtained zeolite samples were named after the $\text{C}_{22-6-6}/\text{TPAOH}$ ratio, which are HLBM-0/36, HLBM-1/36, HLBM-3/36, and HLBM-5/36, respectively. HLBM-0/36 is simply a conventional microporous MFI zeolite. For consistency in nomenclature, HLBM-0/36 is designated for conventional MFI zeolite in this paper.

The method for synthesis of HLBM zeolite catalysts was similar to the one reported in chapter 3 (section 3.2.2). The HLBM zeolite was prepared by dissolving

0.0111 g sodium hydroxide (NaOH, $\geq 97\%$ purity) in 11.5 g deionized water (DI) followed by addition of 5.075 g tetrapropylammonium hydroxide (TPAOH, 40% (w/w)) to the solution. Then, 0.0567 g of aluminum isopropoxide was dissolved in the solution using sonication at room temperature for 0.5 h. Afterward, 5.78 g tetraethyl orthosilicate (TEOS, 98% purity) was added, and the resultant mixture was stirred vigorously at room temperature for 8 h. The C₂₂₋₆₋₆ solution that was prepared by dissolving the desired amount in 8.5 g of DI water at 333 K was added to above mixture. The resultant zeolite synthesis gel was continuously stirred at room temperature for 2 h before transferring it into a Teflon-lined stainless-steel autoclave. Finally, crystallization of zeolite was conducted for 5 days in the autoclaves tumbling vertically in an oven heated at 423 K. After crystallization, the zeolite sample was filtered, washed with DI water, and dried at 343 K overnight.

The as-synthesized HLBM zeolite was then calcined at 873 K for 6 h in flowing air (1.67 mL s⁻¹, ultrapure air, Airgas), ion-exchanged three times using 1 M aqueous ammonium nitrate (NH₄NO₃) (weight ratio of zeolite to NH₄NO₃ solution = 1:10) at 353 K for 2 h, and subsequently, collected by centrifugation, washed with DI water three times, and dried at 343 K overnight. All zeolite samples in their NH₄⁺ form were treated in air (1.67 mL s⁻¹, ultrapure air, Airgas) by increasing the temperature from ambient to 823 K at 0.167 K s⁻¹ rate and holding them at this temperature for 4 h. All catalytic reactions were carried out after converting the zeolites into their proton-forms.

4.2.2. Characterization of HLBM zeolite catalysts

SEM images of the HLBM samples were recorded on a Hitachi SU-70 electron microscope. TEM images were collected by a JEM 2100 LaB6 electron microscope. Powder XRD patterns were recorded using a Bruker D8 Advance Lynx Powder Diffractometer (LynxEye PSD detector, sealed tube, $Cu K_{\alpha}$ radiation with $Ni \beta$ -filter) in the 2θ range from 1.25 to 40 degree. The Nitrogen (N_2) and argon (Ar) sorption isotherms were measured using an Autosorb-iQ analyzer (Quantachrome Instruments) at 77 and 87 K, respectively. Si and Al contents of each sample were determined by inductively coupled plasma optical emission spectroscopy (ICP-OES, Optima 4300 DV instruments, Perkin-Elmer). The magic angle spinning NMR (MAS NMR) spectra were recorded at a field of 9.4 T (Bruker DSX 300) and 11.7 T (Bruker Avance 500) for ^{29}Si and ^{27}Al , respectively. ^{29}Si MAS NMR spectra were recorded at 59.63 MHz using 4 mm rotors at a spinning speed of 10 kHz, a dwell time of 19.95 μs , a $\pi/2$ pulse of 5.0 μs and a recycle delay of 60 s. The spectra were referenced with respect to 3-(trimethylsilyl)-1-propanesulfonic acid salt (0 ppm). ^{27}Al MAS NMR spectra were recorded at 130.34 MHz using 4 mm rotors at 14 kHz spinning speed, a dwell time of 0.5 μs , a selective $\pi/18$ pulse of 0.3 μs and a recycle delay of 0.1 s. An aqueous solution of aluminum sulfate (0.1 M) was used as the reference (0 ppm). The type and concentration of acid sites in the HLBM catalysts were determined by FTIR spectra of adsorbed pyridine using Nicolet 6700 spectrophotometer (Thermo-Scientific) equipped with high temperature reaction chamber in conjunction with Praying MantisTM diffuse reflection accessory (Harrick). Prior to the measurement, the zeolite sample was pretreated at 823 K (rate of 4.55 K s⁻¹) under Ar flow of 0.83

mL s⁻¹ for 1 h. The catalyst sample was then cooled down to 393 K and exposed to pyridine by flowing Ar through pyridine saturator for 0.25 h. After adsorption of pyridine, the sample was heated to 523 K (rate of 4.55 K s⁻¹) under Ar flow for 1 h in order to desorb the physisorbed pyridine, cooled to the temperature of 393 K, and then FTIR spectra were collected with 32 scans and at an effective resolution of 2 cm⁻¹.

4.2.3. Determination of external surface, pore mouth, and internal Brønsted acid sites

The Si/Al ratio in each HLBM zeolite sample was analyzed by elemental analysis (inductively coupled plasma optical emission spectroscopy, ICP-OES). The total number of Brønsted acid sites, defined as total acid sites, was determined via dimethyl ether (DME) titration experiment given that the Brønsted acid sites participate in reactions of DME with H⁺ to form surface methyl groups, $\text{CH}_3\text{OCH}_3 + 2[\text{SiO}(\text{H})\text{Al}] = 2[\text{SiO}(\text{CH}_3)\text{Al}] + \text{H}_2\text{O}$. The number of active Brønsted acid sites on the external surface and in micropore mouth of zeolites, defined as external acid sites, was measured by 2,6-di-tert-butylpyridine (DTBP) titration during methanol dehydration reactions since the bulky DTBP molecule has limited accessibility to acid sites located in micropores of the medium-pore zeolites. The number of external surface acid sites was quantified by triphenyl phosphine (TPP) titration during methanol reaction. The sterically bulky molecular structure and moderate base strength of TPP suggest that it preferentially accesses to acid sites on the external surface of the HLBM zeolite catalysts^{15, 150, 151}. The experimental setup

and reaction conditions for chemical titration of acid sites were same as those described in chapter 2 (section 2.2.5 and 2.2.6). The Brønsted acid sites only accessible to DME titrant were defined as the internal acid sites. The fraction of external Brønsted acid sites was calculated by the ratio of the number of Brønsted acid sites accessible to DTBP titrant to the number of Brønsted acid sites accessible to DME titrant. Similarly, the fraction of external surface acid sites was calculated by the ratio of the number of Brønsted acid sites accessible to TPP to the number of Brønsted acid sites accessible to DME titrant. The fraction of pore mouth acid sites was calculated by the deduction of fraction of external surface acid sites from that of the external acid sites of HLBM zeolite samples.

4.2.4. Catalytic conversion of benzyl alcohol in mesitylene

The liquid phase catalytic conversion of benzyl alcohol (Sigma-Aldrich, 99.95% purity) in mesitylene (Sigma-Aldrich, 99% purity) was carried out in a three-necked round bottom flask (100 mL) equipped with a reflux condenser and heated in a temperature controlled oil bath under atmospheric pressure and magnetic stirring (1" stirring bar, 500 rpm stirring speed) conditions, similar to what reported in section 2.2.7 of chapter 2. In a typical experiment, 15 ml of mesitylene was added to the desired amount of zeolite catalyst, which had been activated at 823 K in flowing air (1.67 mL s^{-1}) for 4 h. The reaction mixture was maintained for 0.5 h at the required reaction temperature and stirring conditions and then 0.25 ml of benzyl alcohol was added. This moment of benzyl alcohol addition was taken as the initial reaction time. Liquid samples were withdrawn at regular time intervals and analyzed by a gas

chromatograph (Agilent 7890A) equipped with a methylsiloxane capillary column (HP-1, 50.0 m x 320 μm x 0.52 μm) connected to a flame ionization detector (FID) to calibrate and separate the reactants and products.

The DTBP poisoning experiment was operated under the same reaction conditions mentioned above except adding DTBP into the reactant suspension. Typically, zeolite catalyst, DTBP, and mesitylene were added to the reactor in sequence, and then the reactant mixture was held at the reaction conditions for 2.5 h before benzyl alcohol was added. Excess mixing time prior to benzyl alcohol addition ensured base molecules completely poisoned active sites on the geometric and mesoporous surfaces (external surfaces) of zeolite catalysts. The influence of external mass transfer limitations on the reaction rates was ruled out by running the reactions at a high enough stirring speed (500 rpm), showing a further increase in the stirring speed did not enhance the reaction rate anymore. The reactant mixture without addition of zeolite catalysts showed no conversion of benzyl alcohol at the investigated reaction conditions.

4.3. Results and discussion

4.3.1. Structural properties of HLBM zeolite catalysts

The scheme for formation of HLBM silicalite zeolite has been studied in chapter 3. It is shown that a cooperative function between TPAOH and C₂₂₋₆₋₆ templates leads to formation of microporous core and lamellar shell materials, respectively, in the HLBM zeolite. The modulation of dual template ratios in the synthesis tailors the relative quantity of microporous MFI core and lamellar MFI

shell, respectively, and thus the structure and textural properties of HLBM zeolites. The synthesis of HLBM zeolite catalysts studied here is expected to follow the same scheme since the synthesis recipe is same as that of HLBM silicalite except the addition of aluminum source. Figure 4.1 shows XRD patterns of the synthesized HLBM zeolite catalysts. The diffraction peaks in each sample resembles the characteristic of a crystalline MFI^{14, 61}, confirming the successful crystallization of HLBM zeolite. The diffraction peaks in the low-angle range ($2\theta < 7^\circ$) of the XRD patterns indicate the evolution of the multi-lamellar feature of the HLBM zeolite with increasing C₂₂₋₆₋₆ content in the dual template assisted zeolite synthesis.

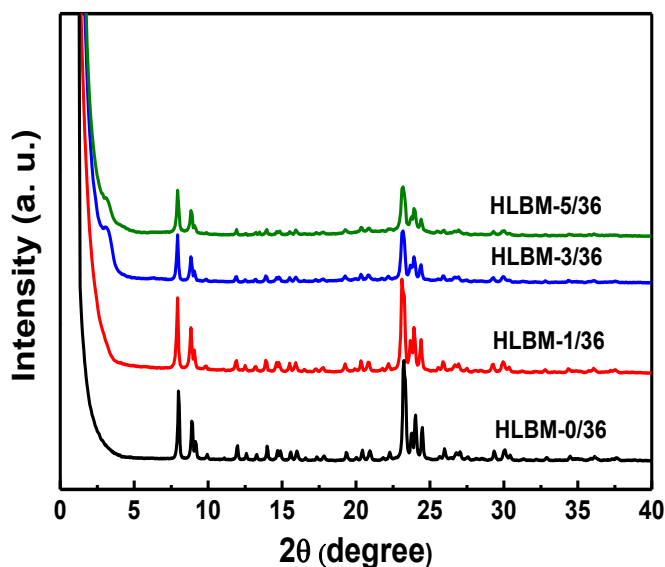


Figure 4.1. XRD patterns of synthesized HLBM-0/36, HLBM-1/36, HLBM-3/36, and HLBM-5/36 zeolite catalysts.

The morphologies of HLBM zeolite catalysts are shown by the SEM and TEM images in Figure 4.2. The HLBM-0/36 zeolite (Figure 4.2(A)-(B)) consists of

short cylindrical particles with an average width of ~ 200 nm and thickness of ~ 150 nm and well crystallized smooth surfaces. The HLBM-1/36 particles in Figure 4.2(C) have similar morphologies to those of HLBM-0/36, but they have relatively rougher crystal surfaces and larger particle sizes. A close examination of the HLBM-1/36 particles in Figure 4.2(D) indicates that the rough surface is composed of a lamellar structure. The SEM images in Figure 4.2(E) and 4.2(G) and TEM images in Figure 4.2(F) and 4.2(H), respectively, which correspond to HLBM-3/36 and HLBM-5/36 samples, show clearly visible lamellar shell structures. The thickness of lamellar shell in HLBM-3/36 increased compared to HLBM-1/36, and these lamellae in the shell are parallel to each other. In HLBM-5/36, however, the lamellae in the shell are incorporated into a network covered on the surface of the core zeolite. In some cases, the core seems to be dissolved, and the lamellar zeolite forms a hollow shell. The morphology transformation with increasing C_{22-6-6} used in the dual template synthesis suggests that relative quantity of the meso- and microporous domains can be manipulated in the HLBM zeolite samples.

Based upon the respective dimensions of lamellar and bulk MFI structures in the TEM images, the mass fractions of lamellar shell in HLBM zeolite particles can be estimated if the densities of both structures are known. The density of as-made lamellar MFI is 1.54 g mL^{-1} , while the density of calcined layered MFI is not known. From the densities of the bulk calcined MFI and as-made bulk MFI, which are 1.73 g mL^{-1} and 2.05 g mL^{-1} ,^{114, 152}, respectively, the density of calcined lamellar MFI is estimated to be $1.54 \times (1.73/2.05) = 1.30 \text{ g mL}^{-1}$. The mass fractions of lamellar shell in HLBM-1/36, HLBM-3/36 and HLBM-5/36 zeolite samples are then calculated to

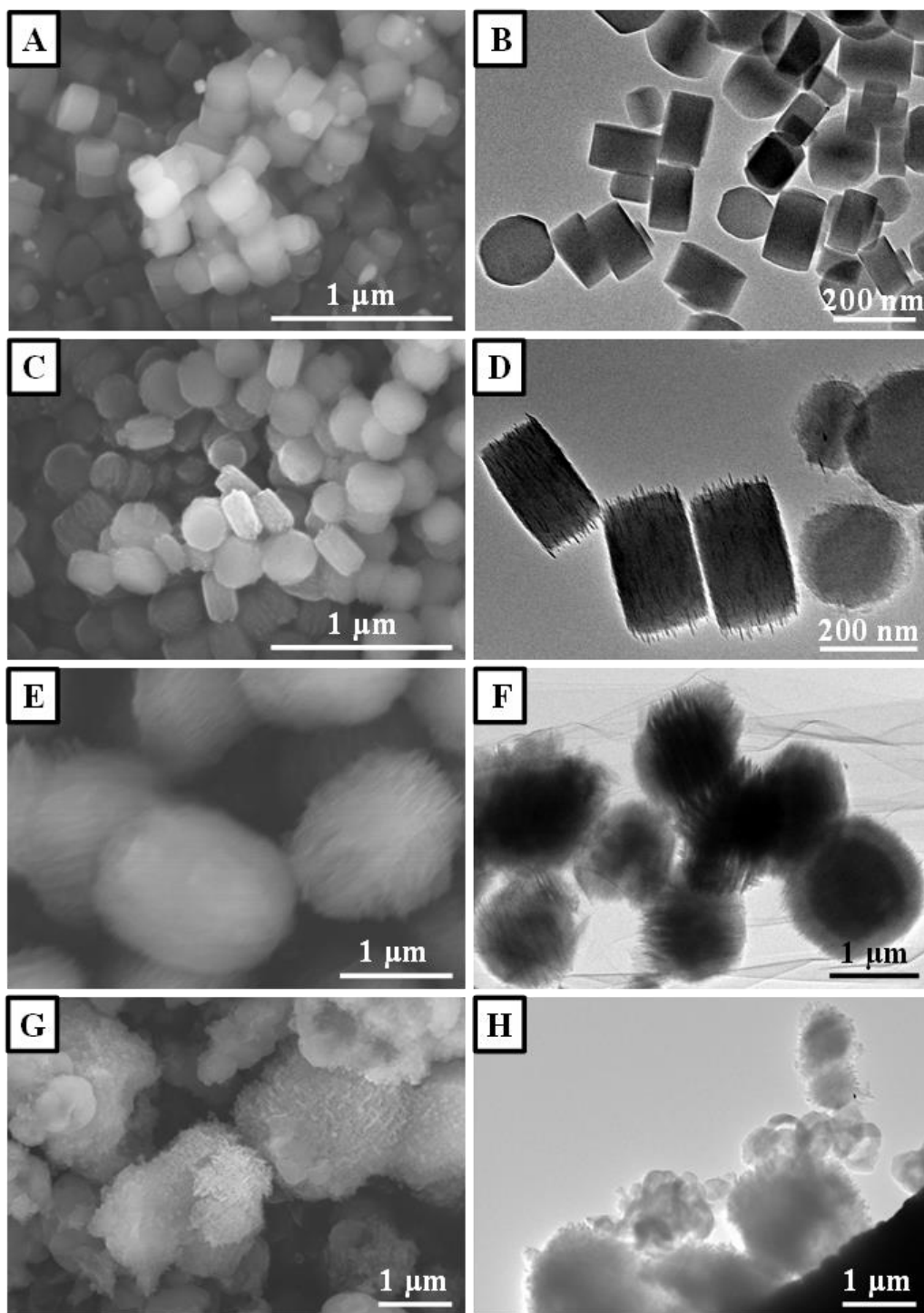


Figure 4.2. SEM and TEM images of HLBM zeolite with Si/Al=300 after 5 days of hydrothermal synthesis. (SEM: (A) HLBM-0/36, (C) HLBM-1/36, (E) HLBM-3/36, and (G) HLBM-5/36. TEM: (B) HLBM-0/36, (D) HLBM-1/36, (F) HLBM-3/36, and (H) HLBM-5/36.)

be 25%, 50% and 65%, respectively. It should be noted that this is quite rough estimation since arcuate density and packing structure of lamellar shell in each HLBM zeolite is not known.

Figure 4.3 shows the high resolution TEM images of HLBM-1/36, HLBM-3/36, and HLBM-5/36 zeolite samples. The morphology of HLBM-1/36 (Figure 4.3(A)-(C)), HLBM-3/36 (Figure 4.3(D)-(F)) and HLBM-5/36 (Figure 4.3(G) and (H)) is similar to porcupine sensory message ball with length of little nerve-stimulating bumps increased from HLBM-1/36 to HLBM-5/36. The lattice fringes of

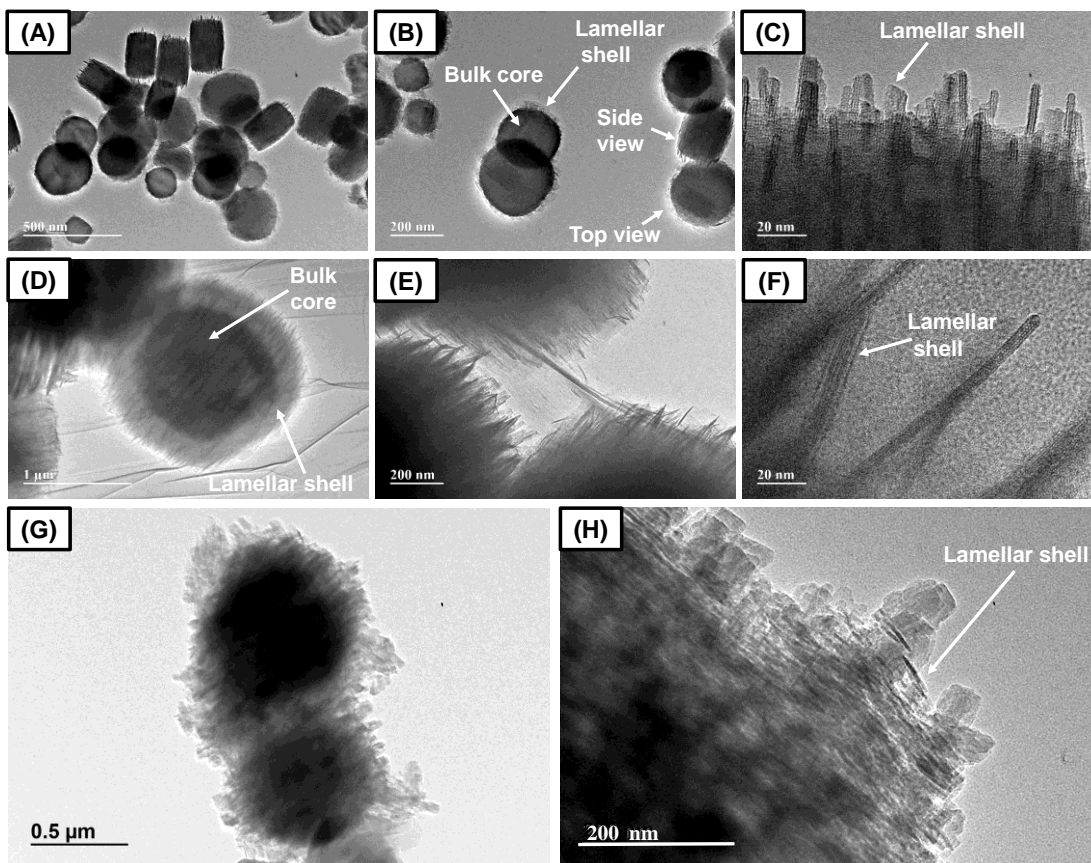


Figure 4.3. High resolution TEM images of HLBM zeolite with Si/Al=300 after 5 days of hydrothermal synthesis. ((A)-(C): HLBM-1/36; (D)-(F): HLBM-3/36, and (G)-(H): HLBM-5/36, respectively.)

the mesoporous lamellar shell are clearly visible in these TEM images which indicate the mesoporous shell of the HLBM zeolite is crystallized. Figure 4.3 also suggests that microporous and mesoporous structures in HLBM zeolite are organized and interconnected. This unique morphology offers a pathway for tailoring the physicochemical properties of hierarchical meso-/microporous zeolite materials in the area of catalysis.

In order to study the effect of Si/Al ratio on morphology and textural properties of the HLBM zeolite catalysts, HLBM-3/36 samples with Si/Al ratios of 500, 300 (presented in Figure 4.2), 150, 100, and 75, respectively, were synthesized. Figure 4.4 shows the SEM images of these HLBM zeolite samples. The morphology of these samples is influenced by the Si/Al ratios in the synthesis. Typically, the long-range ordering of the lamellar shell in HLBM-3/36 structures decreased when the Si/Al ratio was lowered in the synthesis recipe.

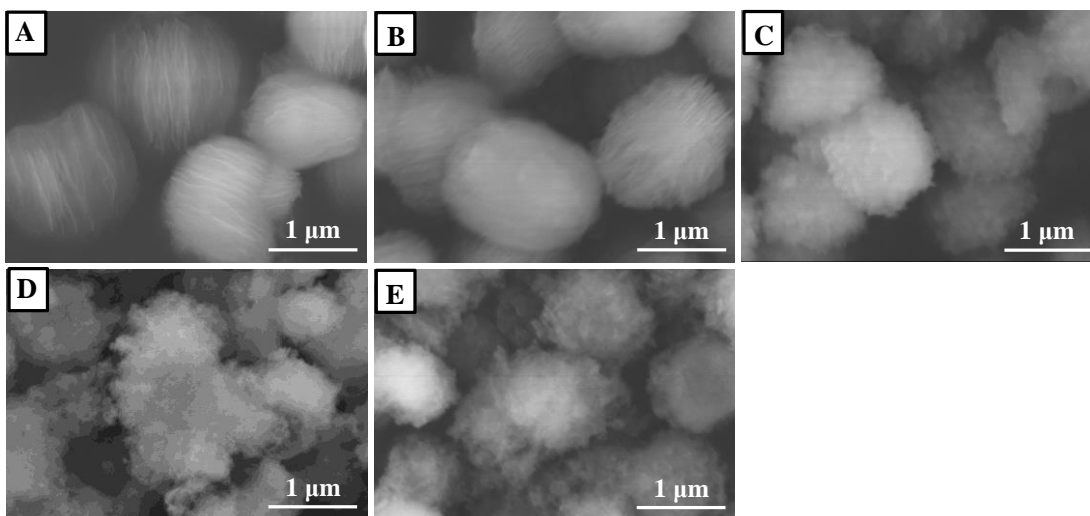


Figure 4.4. SEM images of synthesized HLBM-3/36 zeolite samples, which were obtained using Si/Al molar ratio of (A) 500, (B) 300, (C) 150, (D) 100, and (E) 75, respectively. (HLBM-3/36 with Si/Al ratio=300 has been represented here for comparison purpose.)

4.3.2. Textural properties of HLBM zeolite catalysts

The textural properties of HLBM zeolites were analysed by the Ar adsorption-desorption isotherms, as shown in Figure 4.5 and Table 4.1. As expected, the mesoporosity and external surface area of the HLBM zeolites increase with increasing C_{22-6-6} content in the zeolite synthesis recipe (Figure 4.5(A) and Table 4.1). Non-local density functional theory (NLDFT) pore size analysis was derived from the adsorption branch of Ar isotherms on the basis of spherical/cylindrical pore model. Figure 4.5(B) illustrates the presence of dual micropore and mesopore systems in HLBM zeolites and the mesopore peak intensity increase from HLBM-0/36 to HLBM-5/36 samples showing the formation of more uniform mesopores in size by increasing the C_{22-6-6} content in the synthesis recipe.

Table 4.1 summarizes the textural properties of the synthesized HLBM zeolites with different molar ratios of the dual templates. The external surface area, mesopore volume, and total pore volume increase by increasing the C_{22-6-6} content in the zeolite synthesis recipe. This is caused by the production and growth of the mesoporous lamellar shell in HLBM zeolite structures. The micropore volume and micropore surface area, however, show opposite trend with C_{22-6-6} content in the synthesis recipe. The decrease in micropore volume and micropore surface area upon mesostructuring a zeolite material in the present study is consistent with those reported for mesoporous zeolite prepared by demetalization^{45, 153} or pillaring of layered zeolite nanosheets¹⁵⁴. The generation of mesoporosity in the zeolite samples seems to sacrifice slightly the microporosity of zeolite materials.

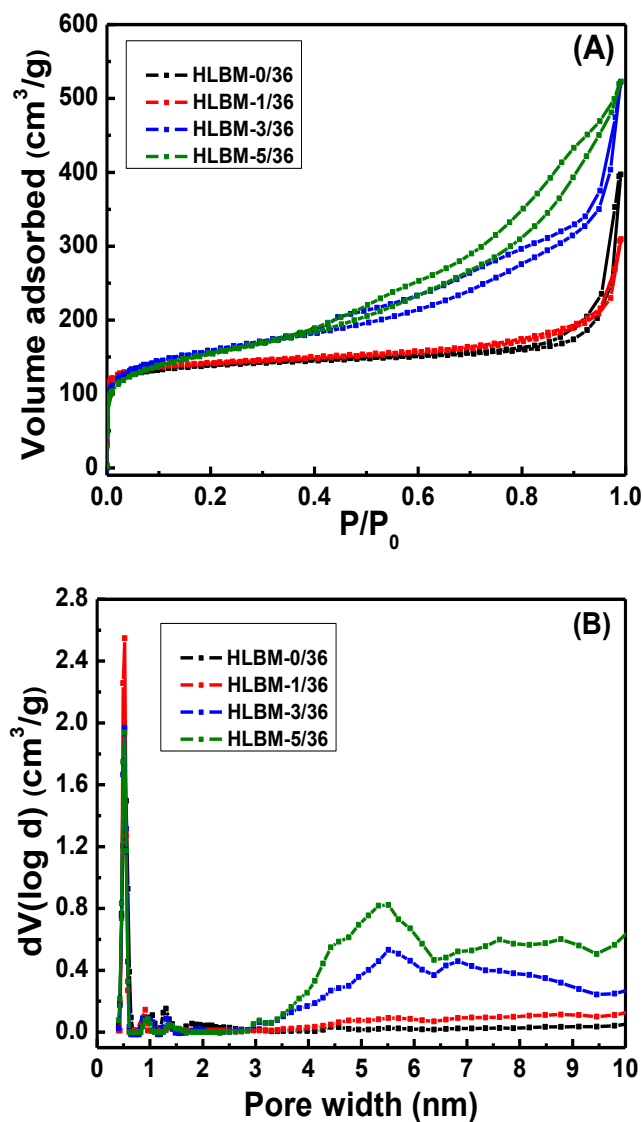


Figure 4.5. Ar adsorption-desorption isotherms (A) and the corresponding NLDFT pore size distributions (B) derived from Ar adsorption branch of the HLBM zeolite catalysts.

It should be noted that the Si/Al ratios in the dual template assisted synthesis influenced the morphology of the resultant HLBM zeolite. By lowering the Si/Al ratio, the long-range ordering of the lamellae shell in HLBM zeolite is slowly diminished, as shown by the SEM images in Figure 4.4. The textural properties of HLBM zeolite samples, however, are not influenced obviously by changing Si/Al

ratios in the synthesis, as indicated by similar surface areas and pore volumes of the HLBM-3/36 samples with different Si/Al ratios in Table 4.2.

Table 4.1. Textural properties of the HLBM zeolite catalysts determined from Ar isotherms.

Catalyst	V_{micro}^a [cm ³ g ⁻¹]	S_{micro}^a [m ² g ⁻¹]	S_{ext}^a [m ² g ⁻¹]	V_t^b [cm ³ g ⁻¹]	$V_{\text{meso}} = V_t - V_{\text{micro}}$ [cm ³ g ⁻¹]	S_{BET}^c [m ² g ⁻¹]
HLBM-0/36	0.127	310	130	0.540	0.413	441
HLBM-1/36	0.094	258	187	0.571	0.477	445
HLBM-3/36	0.088	224	258	0.690	0.602	481
HLBM-5/36	0.069	187	334	0.763	0.694	521

^a Determined from t-plot method; ^b Determined by NLDFT method; ^c Determined from Brunauer, Emmett, and Teller (BET) method.

Table 4.2. Textural properties of HLBM-3/36 zeolite catalysts with different Si/Al molar ratios.

Si/Al molar ratio	V_{micro}^a [cm ³ g ⁻¹]	S_{micro}^a [m ² g ⁻¹]	S_{external}^a [m ² g ⁻¹]	V_t^b [cm ³ g ⁻¹]	$V_{\text{meso}} = V_t - V_{\text{micro}}$ [cm ³ g ⁻¹]	S_{BET}^c [m ² g ⁻¹]
500	0.091	216	289	0.627	0.536	505
300	0.097	229	336	0.654	0.557	565
150	0.094	226	318	0.617	0.523	544
100	0.090	210	325	0.642	0.552	534
75	0.094	217	288	0.615	0.521	504

^a Determined by t-plot method from N₂ isotherms. ^b Determined by NLDFT method from N₂ isotherms. ^c Determined from Brunauer, Emmett, and Teller (BET) method.

4.3.3. Acidity properties of HLBM zeolite catalysts

Table 4.3 lists the Si/Al ratios and the number of Brønsted acid sites of HLBM zeolite samples determined by ICP-OES measurement and DME titration, respectively. The number of external active sites of each catalyst was determined from DTBP titrations, and is also shown in Table 4.3. The fractions of external acid sites ($f_{B,ext}$) were calculated by the ratio of the number of Brønsted acid sites determined from DTBP titration to the number of Brønsted acid sites determined from DME titration. It is known that the bulky DTBP molecules have limited accessibility to Brønsted acid sites located in micropores in MFI-type zeolites^{132, 133}. The increase in fractions of external acid sites from HLBM-0/36 to HLBM-5/36 reflects that the acid sites associated with framework Al is spatially modulated between the mesoporous lamellar shell and microporous bulk core domains in HLBM zeolites.

Table 4.3. Si/Al ratio and acidity of HLBM zeolite catalysts.

Catalyst	Si/Al ratio ^a	Total Al sites ^a ($\times 10^5$, mol H ⁺ g ⁻¹)	Total Brønsted acid sites ^b ($\times 10^5$, mol H ⁺ g ⁻¹)	External Brønsted acid sites ^c ($\times 10^5$, mol H ⁺ g ⁻¹)	$f_{B,ext}$ ^d (%)	B/L acid site ratio ^e
HLBM-0/36	50	2.22	2.14	0.09	4	5.64
HLBM-1/36	55	2.01	2.30	0.18	8	5.22
HLBM-3/36	52	2.13	2.09	0.25	12	4.88
HLBM-5/36	64	1.74	1.74	0.28	16	3.58

^a Determined from elemental analysis (ICP-OES); ^b Determined by DME titration; ^c Determined by DTBP titration; ^d The fraction of external Brønsted acid sites calculated by (number of Brønsted acid sites by DTBP titration / number of Brønsted acid sites by DME titration); ^e Calculated from FTIR spectra of adsorbed pyridine.

The external acidity commonly results from acid sites located on the external surface and at the pore mouth region of the hierarchical zeolite catalysts¹⁵⁵⁻¹⁵⁷. The creation of mesoporosity or delamination in HLBM zeolites increases the number of acid sites both in the pore mouth region and on the external surface compared to the microporous MFI zeolite. To identify the locations (on the external surface or in the pore mouth region) of external acid sites in HLBM zeolites, the organic base titration with TPP molecule was conducted. TPP titrant has moderate base strength and bulky molecular structure, and thus it is expected to anchor on the external surface acid sites^{15, 150, 151}. The difference between the number of acid sites determined by DTBP and TPP titrations indicates the number of acid sites located in the pore mouth region of the catalysts. Additionally, silylation of external acid sites of HLBM zeolites by atomic layer deposition (ALD) of tris(dimethylamino)silane (TDMAS) precursor followed by DTBP titration was also conducted to analyze the external surface and pore mouth acid sites in HLBM zeolites. The bulky TDMAS cannot enter the micropores of MFI zeolite, but preferentially stays at the pore mouth region, similar to that of silylation of zeolite with tetraethyl orthosilicate precursor^{122, 158, 159}. The DTBP titration of HLBM zeolites after ALD-SiO₂ modifications determines the number of external surface acid sites, while the difference from that determined from DTBP titration in the absence of ALD-SiO₂ modification suggests the number of pore mouth acid sites. Table 4.4 shows the fractions of external surface and pore mouth acid sites determined by both methods. Clearly, the number of acid sites in the pore mouth region is lower than that on the external surface of HLBM zeolites. The fractions of both types of external acid sites increase with varying the MFI zeolite

structure from HLBM-0/36 to HLBM-5/36, similar to those obtained from DTBP titration of HLBM zeolites discussed before.

Table 4.4. External acidity (external surface and in the pore mouth region) of HLBM zeolite catalysts.

Catalyst	External acidity determined by TPP titration ^a		External acidity determined by ALD-SiO ₂ deposition ^c		Average value of external acidity	
	$f_{B, \text{ ext surf}}^a$ (%)	$f_{B, \text{ pore mouth}}^b$ (%)	$f_{B, \text{ ext surf}}^c$ (%)	$f_{B, \text{ pore mouth}}^d$ (%)	$f_{B, \text{ ext surf}}^e$ (%)	$f_{B, \text{ pore mouth}}^f$ (%)
HLBM-0/36	2.8	1.2	2.1	1.9	2.5	1.5
HLBM-1/36	5.2	2.8	4.8	3.2	5.0	3.0
HLBM-3/36	8.7	3.3	8.5	3.5	8.6	3.4
HLBM-5/36	11.8	4.2	10.7	5.3	11.3	4.8

^a Determined from TPP titration experiment; ^b Calculated by $f_{B, \text{ pore mouth}}^b = f_{B, \text{ ext}} - f_{B, \text{ ext surf}}^a$, where $f_{B, \text{ ext}}$ was determined by DTBP titration; ^c Determined by DTBP titration of HLBM zeolites after ALD-SiO₂ modification; ^d Calculated by $f_{B, \text{ pore mouth}}^d = f_{B, \text{ ext}} - f_{B, \text{ ext surf}}^c$; ^e Calculated by $f_{B, \text{ ext surf}}^e = (f_{B, \text{ ext surf}}^a + f_{B, \text{ ext surf}}^c)/2$; ^f Calculated by $f_{B, \text{ pore mouth}}^f = (f_{B, \text{ pore mouth}}^b + f_{B, \text{ pore mouth}}^d)/2$.

Solid state NMR was employed to investigate the local bonding environment in the synthesized HLBM zeolite catalysts. Figure 4.6(A) shows the ²⁹Si single pulse (SP) NMR spectra of HLBM-1/36, HLBM-3/36, and HLBM-5/36 zeolite samples. Two resolved peaks (at -113 and -103 ppm) can be observed in the ²⁹Si SP NMR spectrum of these MFI zeolites, which correspond to crystallographically nonequivalent Q⁴ tetrahedral sites (Qⁿ stands for X_{4-n}Si[OSi]_n)^{41, 122-124} and Q³ sites arising from the silanol groups on the zeolite surface.¹²⁵ The similar Q⁴ and Q³ peaks in these catalysts to those reported for pillared MFI zeolite⁴² suggest that there is a similar local bonding environment in these meso-/microporous HLBM and pillared MFI zeolites. Figure 4.6(B) shows the ²⁷Al MAS NMR spectra of the HLBM zeolite

samples. The peak at 55 ppm is due to the tetrahedrally coordinated framework aluminum (Al_F)^{42, 124}, while the peak around 0 ppm is due to an octahedral coordination typical of extra-framework Al (Al_{EF}). The fractions of the extra-framework Al in these HLBM zeolite samples should be insignificant quantity since the peak around 0 ppm is very small compared to that around 55 ppm in the spectra.

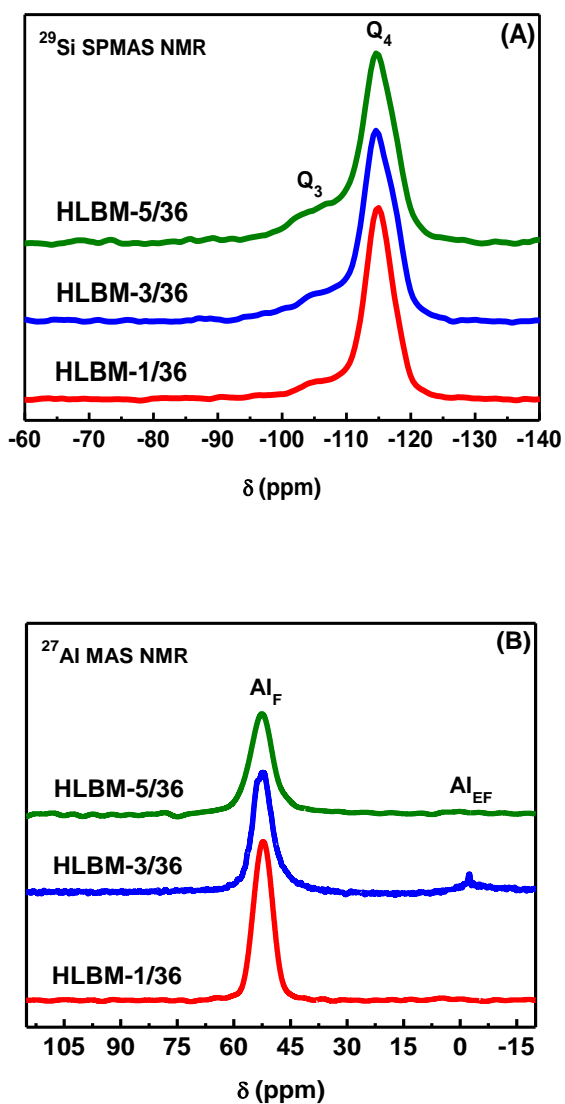


Figure 4.6. Solid state ^{29}Si SP MAS NMR (A) and ^{27}Al MAS NMR (B) spectra of HLBM zeolite catalysts.

The type and concentration of acid sites were evaluated by FTIR spectra of the adsorbed pyridine on the HLBM zeolite catalysts, and the results are shown in Figure 4.7. The absorption band at 1545 cm^{-1} is typical of pyridine interacting with Brønsted acid sites, while the absorption band around 1455 cm^{-1} is assigned to the interaction of pyridine with Lewis acid sites in the zeolite catalysts.^{120, 121} Figure 4.7(A) shows that 1545 cm^{-1} and 1455 cm^{-1} bands exist in the spectra of all the HLBM zeolite samples, indicating the co-existence of Brønsted and Lewis acid sites in these catalysts. The concentrations of the individual Brønsted and Lewis acid sites were calculated from the integrated intensities of the 1545 cm^{-1} ($1.67\text{ cm}^2\text{ }\mu\text{mol}^{-1}$ as a molar extinction coefficient) and 1455 cm^{-1} ($2.22\text{ cm}^2\text{ }\mu\text{mol}^{-1}$ as a molar extinction coefficient) bands, respectively using the same method explained in section 2.3.2 of chapter 2. Table 4.3 shows the molar ratios of Brønsted-to Lewis (B/L) acid site for these four HLBM zeolite catalysts. The B/L acid site ratio decreases from HLBM-0/36 to HLBM-5/36, which reveals that modulation in morphological and textural properties of the HLBM catalysts intensely influence their acidity properties. A correlation between the B/L acid site ratio and the relative external surface area ($S_{\text{ext}}/S_{\text{BET}}$) of HLBM zeolite samples is shown in Figure 4.7(B). The B/L acid site ratio increases with decreasing the relative external surface area of the HLBM catalysts, clearly illustrating the influence of spatially controlled morphology on the acidity of HLBM zeolite. The increase in Lewis acidity from HLBM-0/36 to HLBM-5/36 is resulted from the increasing quantity of lamellar shell structures. It has been reported that the two-dimensional zeolite structures possess increased number of

Lewis acid sites due to the missing connectivities in the third dimension of the zeolite structure.^{45, 123, 160}

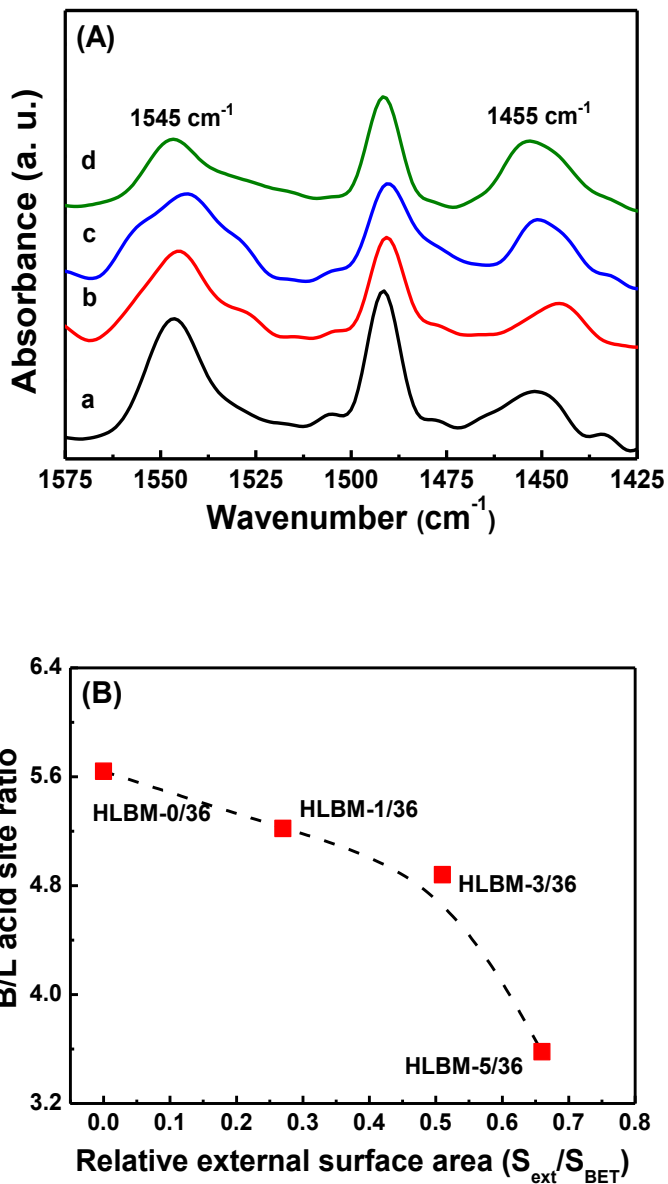


Figure 4.7. (A) FTIR spectra of adsorbed pyridine ((a) HLBM-0/36, (b) HLBM-1/36, (c) HLBM-3/36, and (d) HLBM-5/36, respectively) on HLBM zeolite catalysts and (B) B/L acid site ratio versus relative external surface area of HLBM zeolite catalysts.

4.3.4. Catalytic performance of HLBM zeolite catalysts

The liquid phase catalytic conversion of benzyl alcohol in mesitylene, reaction scheme shown in section 2.3.4 of chapter 2 (Figure 2.12), was employed to examine the catalytic consequences for the selectivity of external acidity in meso-/microporous HLBM zeolites. The parallel reactions, alkylation and etherification, of benzyl alcohol produce 1,3,5-trimethyl-2-benzylbenzene and dibenzyl ether products, respectively. The series reactions convert the reaction intermediate, dibenzyl ether, to the alkylation product, 1,3,5-trimethyl-2-benzylbenzene.⁷⁰ The kinetic diameter of mesitylene (0.87 nm) is apparently larger than micropore sizes of MFI zeolites¹⁶¹. It is expected that the alkylation reaction exclusively occurs on the external acid sites of the HLBM zeolites, while etherification of benzyl alcohol can take place over the internal and external acid sites or only over the internal acid sites of the HLBM zeolites depends on absence or presence of DTBP molecules to poison the external acid sites, respectively.

The apparent rate constants of the parallel reactions over the meso-/microporous HLBM catalysts were evaluated at 348 K, excess amount of mesitylene (molar ratio of mesitylene to benzyl alcohol = 45:1), rigorous agitation, and less than 10% conversion of benzyl alcohol to eliminate the influences of catalyst deactivation, external mass transfer limitation, or deficiency of dibenzyl ether product due to series reactions. The detailed mathematical analysis of catalytic reactions of benzyl alcohol in mesitylene over internal and external acid sites of the HLBM zeolites that accounts the activity of the external and internal active sites and the internal diffusion has been explained in the following sections.

4.3.4.1. Mesitylene alkylation over external acid sites of HLBM zeolites

Because an excess amount of mesitylene was used, the alkylation reaction can be approximated as pseudo-first order in the limiting reactant A, benzyl alcohol. The rate equation is,

$$\frac{dC_C}{dt} = k_{alk,extsurf} M_B f_{B,extsurf} C_A \quad (4-1)$$

where C_C is 1,3,5-trimethyl-2-benzylbenzene concentration in solution (mol L^{-1}), t is the reaction time (s), $k_{alk,extsurf}$ is the specific rate constant (per external surface Brønsted acid site, $[\text{mol H}^+]^{-1} \text{ s}^{-1}$), M_B (mol H^+) is the total moles of Brønsted acid sites present in the batch reactor, and $f_{B,extsurf}$ is the external surface Brønsted acid site fraction (Table 4.4), and C_A is benzyl alcohol concentration in solution (mol L^{-1}). As shown later in this section, self-etherification reaction can also be approximated as the first order in the reactant A. The selectivity for these reactions, $\alpha = \frac{2C_E}{C_C}$, is nearly constant for each catalyst (Table 4.5, Figure 4.8), where C_E is dibenzyl ether concentration in solution (mol L^{-1}). The concentration of 1,3,5-trimethyl-2-benzylbenzene, C_C , can then be described as a function of benzyl alcohol concentration and selectivity,

$$C_C = \frac{C_A^0 - C_A}{1 + \alpha} \quad (4-2)$$

where C_A^0 is the initial benzyl alcohol concentration in solution (mol L^{-1}).

Substituting C_C into equation (4-1), the rate equation becomes:

$$\frac{dC_A}{dt} = -k_{alk,extsurf} M_B f_{B,extsurf} (1 + \alpha) C_A \quad (4-3)$$

Integration of equation (4-3) gives the benzyl alcohol concentration in solution as a function of time (t):

$$\ln \frac{C_A^0}{C_A} = k_{alk,extsurf} M_B f_{B,extsurf} (1 + \alpha) t = k_{alk,app} t \quad (4-4)$$

The apparent rate constant, $k_{alk,app} = k_{alk,extsurf} M_B f_{B,extsurf} (1 + \alpha)$, in s^{-1} , is determined from the benzyl alcohol concentration versus time measurements in reactions over HLBM-type zeolites (plots in Figure 4.8).

Table 4.5. Rate constants of mesitylene alkylation and benzyl alcohol etherification and selectivity for alkylation and etherification reactions.

Catalyst	Reaction rate constant ^a				Selectivity (α)
	In absence of DTBP		In presence of DTBP		In absence of DTBP
	$k_{alk,extsurf} f_{B,extsurf}^b$ ($10^{-3} s^{-1}$ [total mol H ⁺] ⁻¹)	$k_{alk,extsurf}^c$ ($10^{-3} s^{-1}$ [external surf mol H ⁺] ⁻¹)	$k_{alk,int}^d$ ($10^{-6} L s^{-1}$ [mol H ⁺] ⁻¹)	$k_{eth,app,int}^d$ ($10^{-6} L s^{-1}$ [mol H ⁺] ⁻¹)	$2C_E/C_C$
HLBM-0/36	2.2	79	0	272	556
HLBM-1/36	5.9	113	0	364	149
HLBM-3/36	77.6	892	0	885	10.4
HLBM-5/36	178.8	1515	0	922	3.7

^aRate parameters determined by least-squares regression; Uncertainties in regressed rate parameters are within $\pm 4\%$ of the reaction rate constant, twice the standard error. ^bNormalized to total number of Brønsted acid sites determined by DME titration. ^cNormalized to number of external Brønsted acid sites determined by DTBP uptake measurement. ^dNormalized to concentration of internal Brønsted acid sites (internal acid sites = acid sites determined by DME).

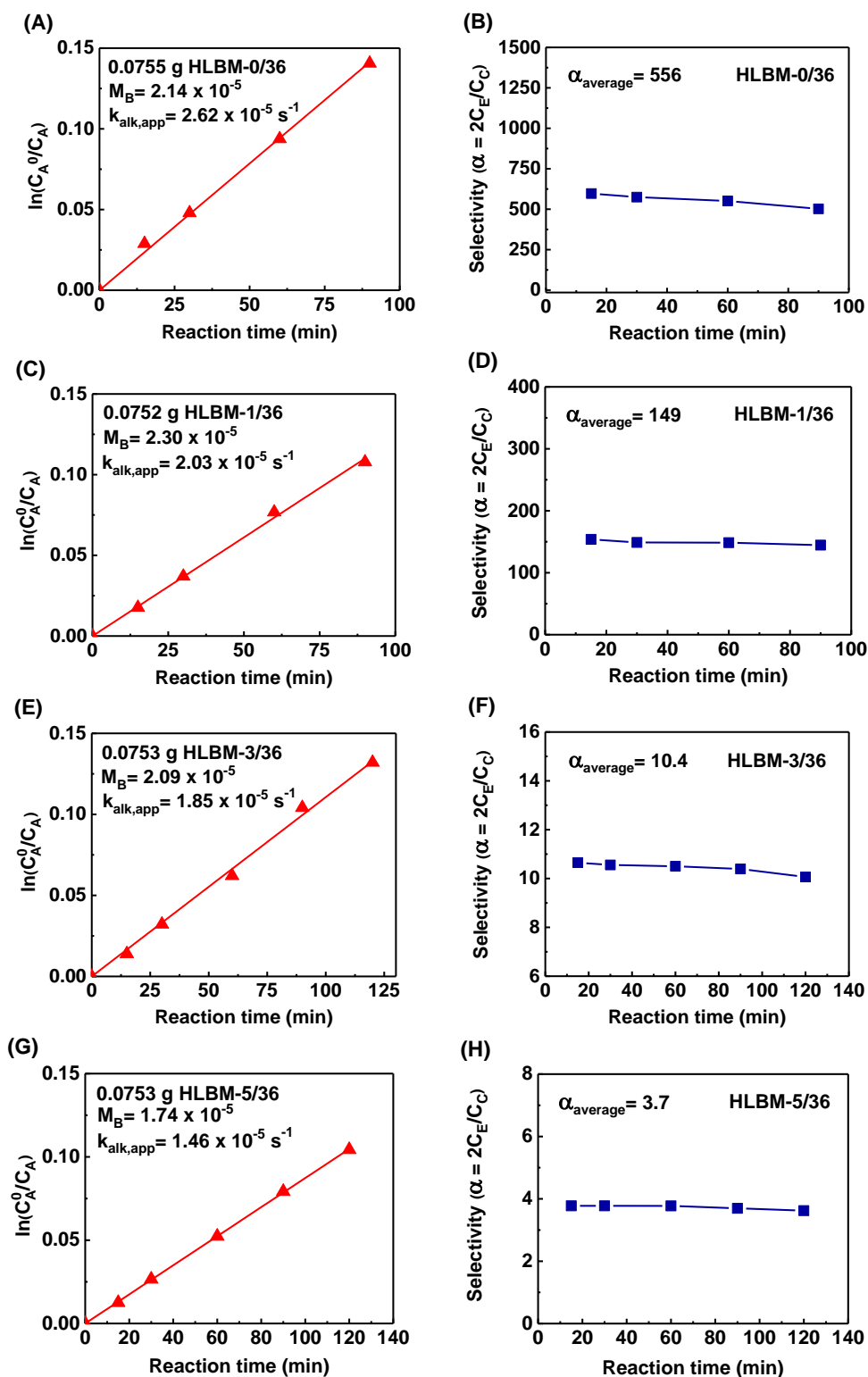
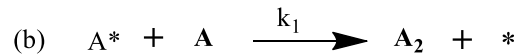


Figure 4.8. Plots for rate constant and selectivity determination for mesitylene alkylation reactions over HLBM zeolite catalysts. The slope of each plot is the apparent rate constant, $k_{alk,app}$.

4.3.4.2. Self-etherification of benzyl alcohol over internal acid sites in HLBM zeolites

Self-etherification of benzyl alcohol in mesitylene can be described by a two-step reaction involving adsorbed benzyl alcohol (A) in the zeolite pores. Benzyl alcohol (A) adsorbs on the Brønsted acid site (*) to give species A*, which then reacts with another benzyl alcohol molecule to give the dibenzyl ether (A₂) and a free acid site (*).



The rate equation is,

$$-\frac{1}{2} \frac{dC_A}{dt} = \frac{k_1 K_1 C_{H^+} \bar{C}_A^2}{1 + K_1 \bar{C}_A} \quad (4-5)$$

where \bar{C}_A (mol L⁻¹) is the adsorbed benzyl alcohol concentration on the catalyst, t is the reaction time (s), K_1 is adsorption equilibrium constant for benzyl alcohol in the catalyst, k_1 is self-etherification rate constant (L [mol H⁺]⁻¹ s⁻¹), and C_{H^+} ([mol H⁺] L⁻¹) is the Brønsted acid site concentration inside the catalyst. The catalytic self-etherification reaction can be approximated as first order with respect to adsorbed benzyl alcohol concentration (\bar{C}_A) and first order with respect to Brønsted acid site concentration (C_{H^+}) inside the catalyst under the assumption that the Brønsted acid sites are predominately covered by reactant A to satisfy $1 \ll K_1 \bar{C}_A$. Then, the rate equation is,

$$-\frac{d\bar{C}_A}{dt} = k_{\text{eth,int}} C_{\text{H}^+} \bar{C}_A \quad (4-6)$$

where the specific self-etherification rate constant per internal surface Brønsted acid site, $k_{\text{eth,int}} = 2k_1$ is a second order rate constant ($\text{L} [\text{mol H}^+]^{-1} \text{s}^{-1}$) and $k_{\text{eth,int}} C_{\text{H}^+}$ unit is s^{-1} . The differential equation that describes steady state diffusion and reaction of benzyl alcohol is,

$$D_A \frac{d^2 \bar{C}_A}{dx^2} - k_{\text{eth,int}} C_{\text{H}^+} \bar{C}_A = 0 \quad (4-7)$$

where D_A is the diffusion coefficient of benzyl alcohol in the catalyst ($\text{m}^2 \text{s}^{-1}$) and x is the length variable of the catalyst particle. The catalyst is assumed to be slab-like particle.

Using the following boundary conditions,

$$(a) \ x = x_p, \bar{C}_A = \bar{C}_{\text{AS}} \quad (\text{on the external surface of the catalyst particle})$$

$$(b) \ x = 0, \frac{d\bar{C}_A}{dx} = 0 \quad (\text{at the center of the catalyst particle})$$

the concentration profile of benzyl alcohol obtained from equation (4-7) is,

$$\bar{C}_A = \frac{\bar{C}_{\text{AS}}}{\cosh f} \cosh \left(f \frac{x}{x_p} \right) \quad (4-8)$$

in which $\phi = x_p \sqrt{\frac{k_{\text{eth,int}} C_{\text{H}^+}}{D_A}}$ is the Thiele modulus and \bar{C}_{AS} is the concentration of A at the pore entrance of the catalyst (mol L^{-1}). The characteristic length, x_p (m), is defined as half the thickness of the zeolite crystal along the b -axis.

Assuming quasi-steady state reaction-diffusion and reaction taking place only inside the pores, a mass balance in the batch reactor gives,

$$\frac{S_{\text{cat}}}{V_{\text{sol}}} D_A \frac{d\bar{C}_A}{dx} \Big|_{x=x_p} = - \frac{dC_A}{dt} \quad (4-9)$$

where S_{cat} (m^2) and V_{sol} (L) are the total external surface area of the catalyst and the total volume of solution present in the batch reactor, respectively. By substituting

$$\bar{C}_{\text{AS}} = \frac{KC_A}{1 + KC_A} \bar{C}_A^{\text{max}} \quad (\text{in which the adsorption equilibrium constant } (K = 62 \text{ L mol}^{-1})$$

and the maximum adsorbed concentration of benzyl alcohol in the catalyst ($\bar{C}_A^{\text{max}} = 1.35 \text{ mol L}^{-1}$) were determined from isotherms of $17 \mu\text{m}$ and $1.4 \mu\text{m}$ silicalite samples⁴ and on the basis of zeolite density of $1,800 \text{ kg m}^{-3}$) into equation (4-9) and integrating, we obtain,

$$\frac{V_{\text{sol}}}{C_{\text{H}^+} V_{\text{cat}}} \left[\ln \frac{C_A^0}{C_A} + K(C_A^0 - C_A) \right] = k_{\text{eth,int}} K \bar{C}_A^{\text{max}} \frac{\tanh \phi}{\phi} t \quad (4-10)$$

where V_{cat} (L) gives the volume of catalyst used in a certain C_A vs. t run and where C_A^0 is the initial benzyl alcohol concentration in solution (mol L^{-1}). All parameters in equation (4-10) are known except $k_{\text{eth,int}}$ and D_A ; these parameters do not depend on the particle size of the zeolite and can be determined as follows. In the absence of diffusion limitation, since $\frac{\tanh(\phi)}{\phi} \approx 1$, equation (4-10) becomes:

$$\frac{V_{\text{sol}}}{C_{\text{H}^+} V_{\text{cat}}} \left[\ln \frac{C_A^0}{C_A} + K(C_A^0 - C_A) \right] = k_{\text{eth,int}} K \bar{C}_A^{\text{max}} t \quad (4-11)$$

From the C_A vs. t data of pillared MFI and self-pillared MFI (SPP)⁴, we can

determine $k_{\text{eth,int}} = \frac{(k_{\text{eth,int}})_{\text{pillaredMFI}} + (k_{\text{eth,int}})_{\text{self-pillaredMFI}}}{2} = 0.00111 \frac{\text{L}}{[\text{mol H}^+] \text{s}}$. In the

presence of severe diffusion limitations, $\frac{\tanh(\phi)}{\phi} \approx \frac{1}{\phi}$. Therefore, with $k_{\text{eth,int}}$ known,

we can find $D_A = 6.12 \times 10^{-20} \frac{\text{m}^2}{\text{s}}$ from the C_A vs. t data of the 17 μm ($x_p = 8.5 \mu\text{m}$)

MFI catalyst⁴. With $k_{\text{eth,int}}$ and D_A determined, we can now attempt to describe the entire set of data from all HLBM catalysts. The customary way of doing this is using an effectiveness factor versus Thiele modulus, η vs. ϕ , diagram. We rewrite equation (4-10) as follows,

$$\frac{V_{\text{sol}}}{C_{\text{H}^+} V_{\text{cat}} K \bar{C}_A^{\text{max}}} \left[\ln \frac{C_A^0}{C_A} + K(C_A^0 - C_A) \right] = k_{\text{eth,app,int}} t \quad (4-12)$$

where $k_{\text{eth,app,int}} = k_{\text{eth,int}} \frac{\tanh(\phi)}{\phi} = 0.00111 \frac{\text{L}}{[\text{mol H}^+] \text{s}} \times \frac{\tanh(\phi)}{\phi}$ is determined from the

experimental data C_A vs. t for each catalyst (Table 4.5). We define an effectiveness

factor $\eta = \frac{k_{\text{eth,app,int}}}{k_{\text{eth,int}}}$ as the ratio of the apparent rate constant ($k_{\text{eth,app,int}}$) over the

intrinsic rate constant ($k_{\text{eth,int}}$). The effectiveness factor for each HLBM zeolite

catalyst determined this way is given in Table 4.6. $k_{\text{eth,app,int}}$ for HLBM zeolite

catalysts can be evaluated using the experimental data by plotting the

$\ln\left(\frac{C_A^0}{C_A}\right) + K(C_A^0 - C_A)$ data versus reaction time t for each catalyst and finding the

slope of the resulted linear plot (Figure 4.9).

Table 4.6. Effectiveness factor analysis of internal etherification reaction in HLBM zeolite catalysts.

Catalyst	Effectiveness factor (η)	$C_{H^+}^a$ ([mol H ⁺] L ⁻¹)
HLBM-0/36	0.25	0.489
HLBM-1/36	0.33	0.507
HLBM-3/36	0.80	0.440
HLBM-5/36	0.83	0.349

^aDetermined by moles of internal Brønsted acid sites over volume of catalyst.

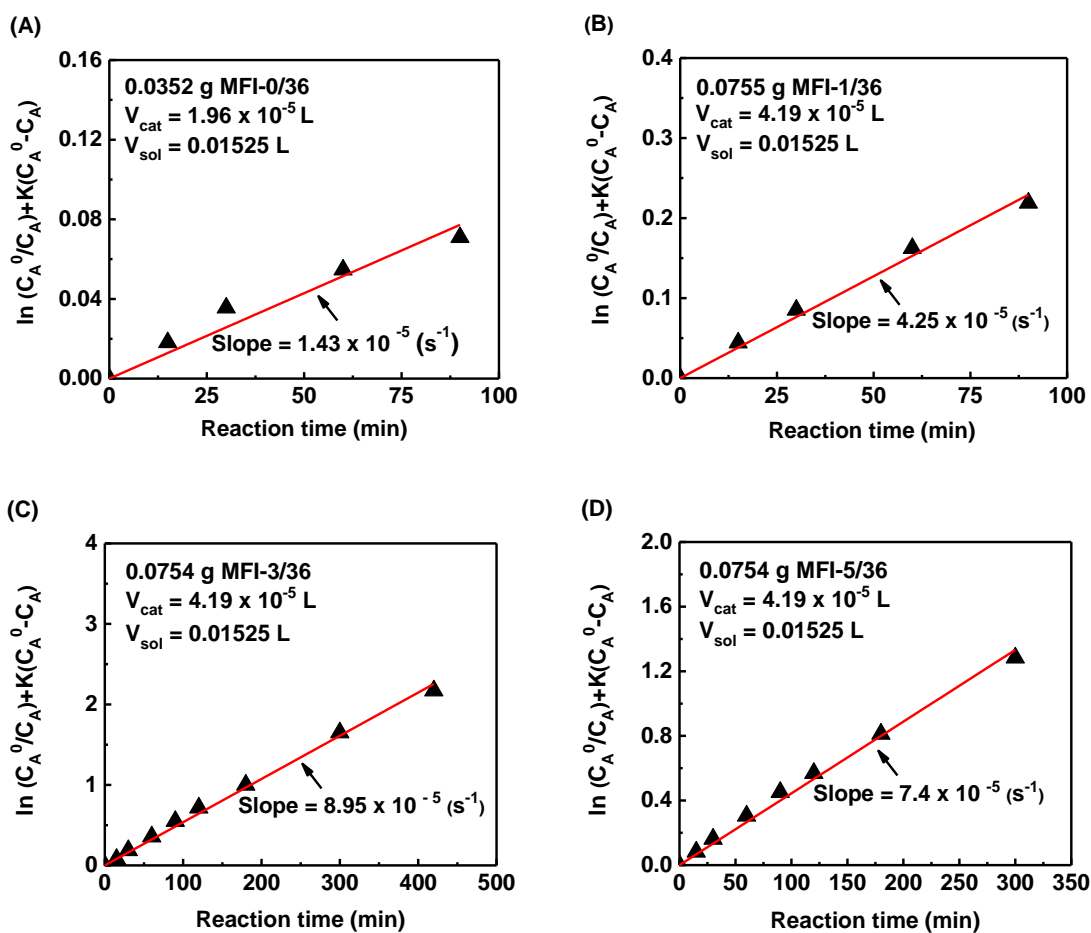


Figure 4.9. Plots for rate constant determination for benzyl alcohol etherification over HLBM zeolite catalysts. (A) HLBM-0/36, (B) HLBM-1/36, (C) HLBM-3/36, and (D) HLBM-5/36. (Slope of the linear plot is $k_{eth,app,int} C_{H^+} V_{cat} \overline{K} C_A^{\max} / V_{sol}$, from which $k_{eth,app,int}$ can be evaluated given that other parameters have been determined as shown in Table 4.6, section 4.3.4.3, and inset information in each plot.)

4.3.4.3. Benzyl alcohol self-etherification on external acid sites of HLBM zeolites

Following the same approach as in section 4.3.4.2, self-etherification over HLBM zeolites in the absence of DTBP titrant molecules can also be described by a two-step reaction involving adsorbed benzyl alcohol (A) on the zeolite external surface and in the zeolite micropores. A material balance in the reactor now gives instead of equation (4-9) the following equation:

$$-\frac{dC_A}{dt} = \frac{S_{cat}}{V_{sol}} D_A \frac{d\bar{C}_A}{dx} \Big|_{x=x_p} + (k_{alk,extsurf} + k_{eth,ext}) M_B f_{B,ext} C_A \quad (4-13)$$

where $k_{eth,ext}$ is the specific rate constant (per external surface Brønsted acid site, [mol H^+] $^{-1}$ s $^{-1}$) of self-etherification reaction on the catalyst external surface. Assuming that there is no mass transfer resistance (often referred to as pore mouth resistance) from external surface to the micropore entrance, in the presence of external alkylation and external self-etherification reactions on the HLBM catalyst surface, the concentration profile of benzyl alcohol in the HLBM micropores is same as that described in equation (4-8). From the concentration profile of benzyl alcohol in micropores in equation (4-8), the first term on the right-hand side of equation (4-13) can be written as:

$$\frac{S_{cat}}{V_{sol}} D_A \frac{d\bar{C}_A}{dx} \Big|_{x=x_p} = \frac{V_{cat}}{V_{sol}} k_{eth,int} C_{H^+} \bar{C}_A^{\max} \frac{\tanh \phi}{\phi} \frac{KC_A}{1 + KC_A} \quad (4-14)$$

By substituting equation (4-14) into equation (4-13), the material balance in the reactor can be expressed as follows:

$$-\frac{dC_A}{dt} = \frac{V_{cat}}{V_{sol}} k_{eth,int} C_{H^+} \bar{C}_A^{\max} \frac{\tanh \phi}{\phi} \frac{KC_A}{1 + KC_A} + (k_{alk,extsurf} + k_{eth,ext}) M_B f_{B,ext} C_A \quad (4-15)$$

In the general case of external and internal reactions in the absence of external liquid phase diffusion and mesopore mass transfer limitations, we have $2C_E + C_C + C_A = C_A^0$. The concentration of dibenzyl ether in solution (C_E) can then be described as a function of benzyl alcohol concentration and selectivity for both alkylation and etherification reactions (α):

$$C_E = \frac{C_A^0 - C_A}{1 + \alpha} \frac{\alpha}{2} \quad (4-16)$$

The material balance on the self-etherification reaction over external and internal active sites of HLBM zeolites can be described by equation (4-17):

$$\frac{d2C_E}{dt} = -\frac{dC_A}{dt} \frac{\alpha}{1 + \alpha} = \frac{\alpha}{1 + \alpha} \left[\frac{V_{cat}}{V_{sol}} k_{eth,int} C_{H^+} \bar{C}_A^{\max} \frac{\tanh \phi}{\phi} \frac{KC_A}{1 + KC_A} + (k_{eth,ext}) M_B f_{B,ext} C_A \right] \quad (4-17)$$

Similarly, the material balance on alkylation reactions on the external surface of catalysts can be expressed by equation (4-18), which is same as equation (4-1):

$$\frac{dC_C}{dt} = k_{alk,extsurf} M_B f_{B,extsurf} C_A \quad (4-18)$$

The selectivity for these reactions can then be expressed by combining equations (4-15) and (4-16) as follows considering that it is time invariant:

$$\alpha = \frac{d2C_E}{dC_C} = \frac{\frac{V_{cat}}{V_{sol}} k_{eth,int} C_{H^+} \bar{C}_A^{\max} \frac{\tanh \phi}{\phi} \frac{KC_A}{1 + KC_A} + (k_{eth,ext}) M_B f_{B,ext} C_A}{k_{alk,extsurf} M_B f_{B,ext} C_A} \frac{\alpha}{1 + \alpha} \quad (4-19)$$

In the studied reaction conditions conversion is lower than 10%. Assuming that there is no concentration drop for benzyl alcohol from the zeolite particle surface to the bulk of the solution and there is no effect of mesopore mass transfer in HLBM

zeolites, then $KC_A \approx KC_A^0$, where C_A^0 is the initial bulk concentration of benzyl alcohol. Then, equation (4-19) can be simplified as:

$$\alpha = \frac{\frac{V_{\text{cat}}}{V_{\text{sol}}} k_{\text{eth,int}} C_{\text{H}^+} \frac{\tanh \phi}{\phi} K \bar{C}_A^{\text{max}}}{\left(1 + KC_A^0\right) k_{\text{alk,extsurf}} M_B f_{\text{B,ext}}} + \frac{k_{\text{eth,ext}}}{k_{\text{alk,extsurf}}} - 1 \quad (4-20)$$

From the definitions of V_{cat} , C_{H^+} , M_B , and $f_{\text{B,ext}}$ (see sections 4.3.4.1 and 4.3.4.2) $V_{\text{cat}} C_{\text{H}^+} = M_B(1 - f_{\text{B,ext}})$ is the total moles of internal Brønsted acid sites in the reactor. By substituting \bar{C}_A^{max} and $V_{\text{cat}} C_{\text{H}^+} = M_B(1 - f_{\text{B,ext}})$ into equation (4-20), the selectivity for both reactions is re-written as:

$$\alpha = \frac{(1 - f_{\text{B,ext}}) \eta k_{\text{eth,int}} K \bar{C}_A^{\text{max}}}{f_{\text{B,ext}} V_{\text{sol}} k_{\text{alk,extsurf}} (1 + KC_A^0)} + \frac{k_{\text{eth,ext}}}{k_{\text{alk,extsurf}}} - 1 \quad (4-21)$$

The external etherification rate constant ($k_{\text{eth,ext}}$) can be calculated by rearranging equation (4-21),

$$k_{\text{eth,ext}} = \left[1 + \alpha - \frac{(1 - f_{\text{B,ext}}) \eta k_{\text{eth,int}} K \bar{C}_A^{\text{max}}}{f_{\text{B,ext}} V_{\text{sol}} k_{\text{alk,extsurf}} (1 + KC_A^0)} \right] k_{\text{alk,extsurf}} \quad (4-22)$$

Table 4.7 shows the external self-etherification rate constant across the HLBM catalysts with different crystallite sizes, indicating that the external self-etherification activity is different (by a factor of ~10) across the HLBM zeolites with different domain sizes. The selectivity for alkylation and etherification reactions of external acid sites, defined as $\alpha' = \frac{k_{\text{eth,ext}}}{k_{\text{alk,extsurf}}}$, is shown in Table 4.7.

In comparison with the selectivity for both reactions of the total active sites (α), the external acid sites show the similar selectivity for each reaction, which

indicates that the reaction selectivity is dominated by the activity of external acid sites of the HLBM catalysts.

Table 4.7. Rate constants of etherification and alkylation on external acid sites and selectivity of external acid sites in HLBM zeolite catalysts.

Catalyst	Reaction rate constant ^a		Selectivity (α)
	$k_{\text{eth, ext}}^b$ ($10^{-3} \text{ s}^{-1} [\text{external mol H}^+]^{-1}$)	$k_{\text{alk, extsurf}}^b$ ($10^{-3} \text{ s}^{-1} [\text{external surf mol H}^+]^{-1}$)	$k_{\text{eth, ext}}/k_{\text{alk, extsurf}}$
HLBM-0/36	27318	79	515
HLBM-1/36	8886	113	131
HLBM-3/36	4060	892	7.7
HLBM-5/36	2780	1515	3.1

^aRate parameters determined by least-squares regression; Uncertainties in regressed rate parameters are within $\pm 4\%$ of the reaction rate constant, twice the standard error. ^bNormalized to number of external Brønsted acid sites determined by DTBP uptake measurement.

Considering the detailed mathematical analysis presented for determination of parallel etherification and alkylation reaction rate constants of benzyl alcohol in mesitylene over internal and external acid sites of the HLBM zeolite catalysts, now we can analyze the catalytic performance of these catalysts for these two parallel reactions. Figure 4.10(A) and (B) show the measured rate constants for conversion of benzyl alcohol in the parallel alkylation and etherification reactions over meso-/microporous HLBM zeolite catalysts under conditions where all active sites of the zeolite catalysts were unperturbed (Figure 4.10(A)) and perturbed (Figure 4.10(B), by DTBP titrant), respectively.

The measured rate constants were obtained by simply fitting the data using a pseudo-first order rate law. In the absence of the DTBP titrant, the HLBM zeolites

had an increasing alkylation rate while decreasing etherification rate with increasing C_{22-6-6}/TPAOH ratios employed in the catalyst synthesis. The selectivity ($\alpha = 2C_E/C_C$, C_E and C_C are the concentrations of dibenzyl ether and 1,3,5-trimethyl-2-benzylbenzene in solution (mol L^{-1}), respectively) of the parallel reactions is listed in Table 4.5, indicating alkylation reaction was favored with increasing mesoporous domain in the HLBM zeolites. In addition, the selectivity differs by ~ 2 orders of magnitude across these four HLBM zeolite catalysts.

The consequences for the remarkable difference in selectivity of the parallel reactions were explored using DTBP titration to selectively poison the acid sites on the external environment (external surface acid sites and acid sites in pore mouth region) of catalysts since the steric resistance hinders the access of bulky DTBP molecules to acid sites located in micropores of HLBM zeolites. In the presence of DTBP titrant, HLBM zeolite samples maintained the residual activity for etherification reaction as shown in Figure 4.10(B), suggesting that the etherification reaction occurs on both internal and external environments of HLBM catalysts although the alkylation reaction exclusively happens on the external surface environment of HLBM catalysts.

The parallel reactions were also carried out over HLBM zeolites after ALD- SiO_2 modifications. Similar alkylation rate and slightly lower etherification reaction rate were observed compared to results present in Figure 4.10(A), suggesting that acid sites in pore mouth region were active for etherification reaction but not involved in alkylation reaction. The selective poisoning of external surface acid sites of HLBM zeolites was conducted by addition of TPP in the parallel reactions. The alkylation

reaction disappeared and similar etherification rates to those in Figure 4.10(B) were observed from this test. These results also indicate that alkylation takes place on the external surface acid sites and etherification reaction occurs over external surface acid sites, acid sites in pore mouth, and acid sites in micropore of HLBM zeolites. The explicit elucidation of catalytic performance of these three types of acid sites in etherification reaction requires further analysis of effects of internal diffusion in the HLBM zeolites, in which complexity of the reaction-diffusion data analysis is beyond the scope of the present study. Therefore, we simply limit our analysis to external surface acid sites in alkylation reaction, external acid sites (on external surface and in pore mouth region) in etherification reaction, and internal acid sites in etherification reaction, respectively, as discussed below.

The involvement of acid sites on external and internal environments of HLBM zeolites in catalyzing parallel alkylation and etherification reactions of benzyl alcohol in mesitylene is therefore systematically evaluated by correlating the reactions occurring at each location to their corresponding rate constants evaluated from catalytic results in the absence and presence of DTBP titrant, respectively. The rate constants can be separated into $k_{\text{alk,ext surf}}$ (per external surface Brønsted acid site, $[\text{mol H}^+]^{-1}\text{s}^{-1}$), $k_{\text{eth,ext}}$ (per external Brønsted acid site, $[\text{mol H}^+]^{-1}\text{s}^{-1}$), and $k_{\text{eth,int}}$ (per internal Brønsted acid site, $[\text{mol H}^+]^{-1}\text{s}^{-1}$), corresponding to the alkylation reaction on the external surface environment, etherification on the external environment (external surface acid site and acid site in pore mouth region), and etherification in the internal microporous environment, respectively as discussed before. The alkylation reaction data were fitted well to a pseudo-first order rate law:

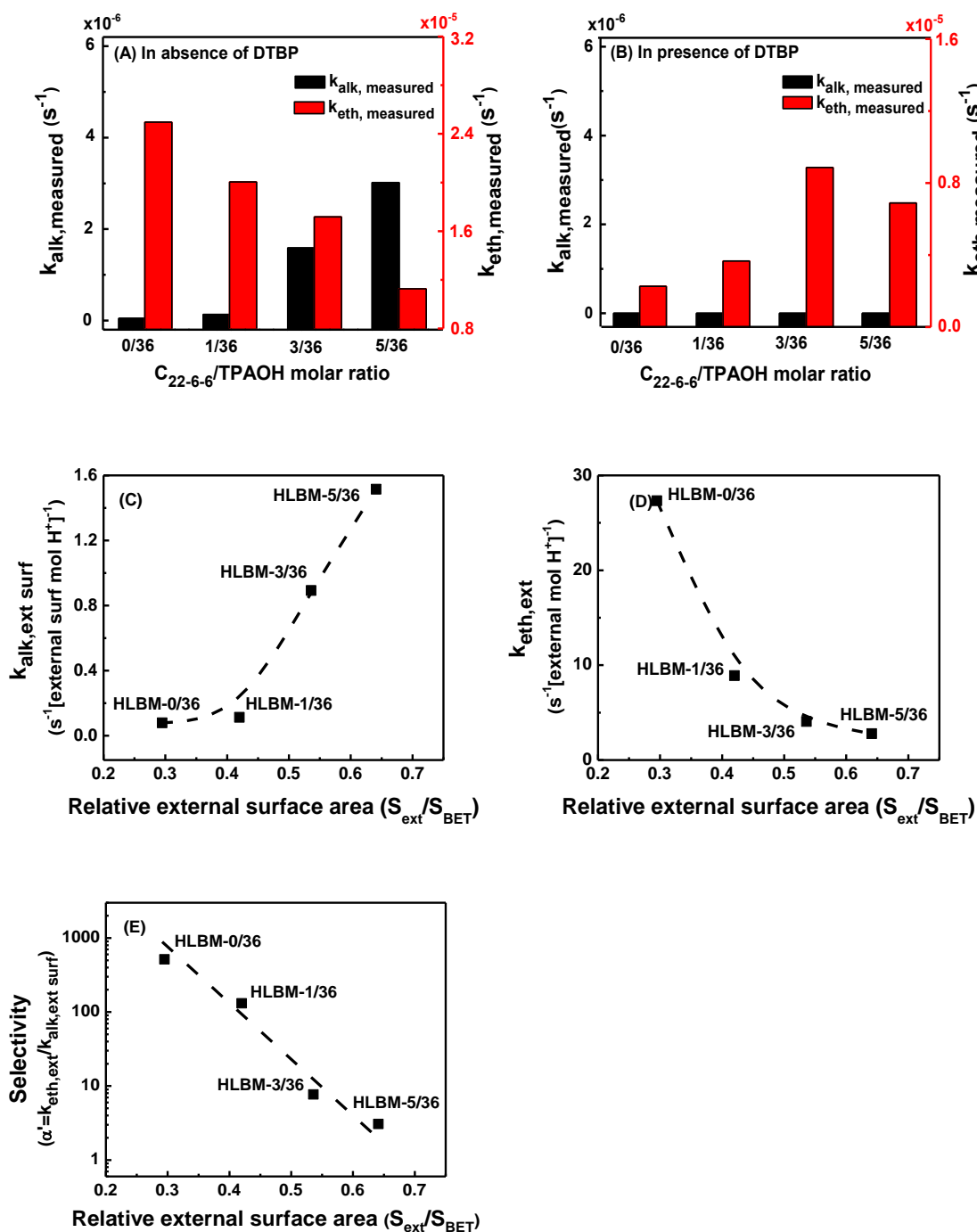


Figure 4.10. Measured alkylation and etherification rate constants of benzyl alcohol with mesitylene reaction in absence of DTBP (A) and in presence of DTBP (B), rate constants of alkylation on external surface acid sites (C) and etherification on external acid sites (D), and selectivity (E) versus relative external surface area of HLBM zeolite catalysts.

$\ln \frac{C_A^0}{C_A} = k_{\text{alk,ext surf}} M_B f_{\text{B,ext surf}} (1 + \alpha)t = k_{\text{alk,app}} t$, where C_A^0 is the initial benzyl alcohol concentration in solution (mol L⁻¹), C_A is benzyl alcohol concentration in solution (mol L⁻¹), M_B (mol H⁺) is the total moles of Brønsted acid sites present in the batch reactor, $f_{\text{B,ext surf}}$ is the external surface Brønsted acid site fraction (Table 4.4), and t is the reaction time (s), respectively, to solve the apparent rate constants.

Figure 4.10(C) shows that $k_{\text{alk,ext surf}}$ increases by increasing the relative external surface area of the HLBM zeolite catalysts. The internal reaction rate ($k_{\text{eth,int}}$) coupled with internal mass transport limitations on HLBM zeolites can be rigorously described by a Thiele Modulus treatment, as the previous work^{4, 162} on treatment of zeolites with different crystallite sizes. The catalytic activity of unit-cell thick pillared MFI and self-pillared MFI (SPP) is presumed as the intrinsic kinetic behavior. By employing D_A (diffusion coefficient of benzyl alcohol in the catalysts (m²s⁻¹), evaluated from 17 μm MFI in the previous work⁴) and the intrinsic catalytic rate behavior, the effectiveness factor (η) of each HLBM catalysts can be evaluated. The difference in effectiveness factor (Table 4.6) across the HLBM zeolite catalysts indicates that they have different internal etherification catalytic behaviors.

We aimed to compare the etherification and alkylation rate constants on the external environment of HLBM zeolite catalysts. Although alkylation rates correspond to external surface acid sites, etherification rates contain two contributions, one from external sites (external surface and pore mouth) and one from reaction inside the micropores (internal) as discussed before. In order to obtain external etherification rates for HLBM catalysts, the contribution of internal

etherification rates should be subtracted. The later can be measured independently by deactivating the external active sites with DTBP titration and therefore, deconvolution of the two contributions to the overall rate can be accomplished. The analysis presented in detail in this section before, provides the $k_{eth,ext}$ for each HLBM zeolite catalyst (Table 4.7).

Figure 4.10(D) shows the rate constants of external etherification reaction decreases with S_{ext}/S_{BET} of the HLBM zeolite catalysts, which is opposite to the trend of $k_{alk,ext\ surf}$ versus S_{ext}/S_{BET} . The selectivity to etherification versus alkylation on external acid sites, defined as $\alpha' = \frac{k_{eth,ext}}{k_{alk,ext\ surf}}$ (Figure 4.10(E) and Table 4.7), consistently decreases with increasing relative external surface area of the HLBM catalysts. The results and analysis presented here demonstrate substantial differences of external surface catalytic behavior of the HLBM zeolite catalysts.

In order to further understand the catalytic behavior of the external acid sites in HLBM zeolites, we conducted the experiments to accumulatively poison the external acid sites of HLBM-3/36 and HLBM-5/36 samples in the benzyl alcohol reactions by controlled addition of DTBP during the reaction. The detailed calculations have been provided in the following section.

4.3.4.4. Partial poisoning experiments

The external etherification rate constant in the presence of DTBP to partially poison the external acid sites was calculated by using equation (4-23):

$$k_{\text{eth,ext}} = \left[1 + \alpha - \frac{(1 - f_{\text{B,ext}}) \eta k_{\text{eth,int}} K \bar{C}_A^{\text{max}}}{(1 - x) f_{\text{B,ext}} V_{\text{sol}} k_{\text{alk,ext,surf}} (1 + K C_A^0)} \right] k_{\text{alk,ext,surf}} \quad (4-23)$$

where x is the fraction of external acid sites that was poisoned by the DTBP organic base molecules. Similarly, the external alkylation rate constant in the partial poisoning experiments was assessed from equation (4-24):

$$\frac{dC_c}{dt} = k_{\text{alk,ext,surf}} M_B f_{\text{B,ext,surf}} (1 - x) C_A \quad (4-24)$$

where x is the fraction of external surface acid sites that was poisoned by DTBP organic base molecules. Table 4.8 and Figure 4.11 show the $k_{\text{alk,ext}}$ and $k_{\text{eth,ext}}$ across the HLBM-3/36 and HLBM-5/36 with different fractions of active external acid sites poisoned. The results suggest that $k_{\text{alk,ext}}$ decreases when the number of external acid sites poisoned with DTBP molecules increases, but $k_{\text{eth,ext}}$ is relatively constant and does not change significantly when the number of external acid sites poisoned with DTBP increased.

Figure 4.11(A) shows that $k_{\text{eth,ext}}$ (per remaining active external acid sites) is close to a constant with the increasing number of external active sites poisoned in both HLBM-3/36 and HLBM-5/36 catalysts, suggesting that etherification exclusively occurred on external environment of catalysts is not influenced significantly by the type or strength of the external active sites. Figure 4.11(B) demonstrates that $k_{\text{alk,ext,surf}}$ (per remaining active external surface acid sites) decreases with continuous addition of DTBP to poison the external surface acid sites, indicating that external surface acid sites responded differently for the external surface alkylation reaction from external etherification reaction. The prompt drop in alkylation activity (> 50%) with a small fraction of external surface acid site (~ 10%)

Table 4.8. Rate constants of etherification and alkylation reactions on remaining active external acid sites in HLBM zeolite catalysts when the external acid sites were cumulatively poisoned by DTBP.

Catalyst	x (%) ^a	x (%) ^b	Reaction rate constant ^c	
			$k_{\text{eth, ext}}^d$ ($10^{-3} \text{ s}^{-1} [\text{external mol H}^+]^{-1}$)	$k_{\text{alk, extsurf}}^d$ ($10^{-3} \text{ s}^{-1} [\text{external surf mol H}^+]^{-1}$)
HLBM-3/36	0	0	4060	892
	13	18	5000	423
	17	23	5895	344
	26	36	3962	127
HLBM-5/36	0	0	2780	1515
	10	13	2945	535
	13	17	1577	307
	20	26	1726	150
	39	53	2785	45

^a x is percentage of external acid sites poisoned by DTBP. ^b x is percentage of external surface acid sites poisoned by DTBP. ^cRate parameters determined by least-squares regression; Uncertainties in regressed rate parameters are within $\pm 4\%$ of the reaction rate constant, twice the standard error. ^dNormalized to number of external Brønsted acid sites determined by DTBP uptake measurement.

poisoned and the slow drop in activity with a large fraction of external surface poisoned acid sites imply that some of the individual external surface acid sites are very active while others are insignificant in enabling the alkylation reaction, which might result from the different acid strengths of the external surface acid sites. Additionally, the steric resistance from adsorbed DTBP on external surface acid sites might contribute to the non-linear activity loss behavior observed in Figure 4.11(B). The cumulative poisoning experiment suggests that individual external surface acid sites in HLBM zeolites contribute differently to external surface alkylation reaction.

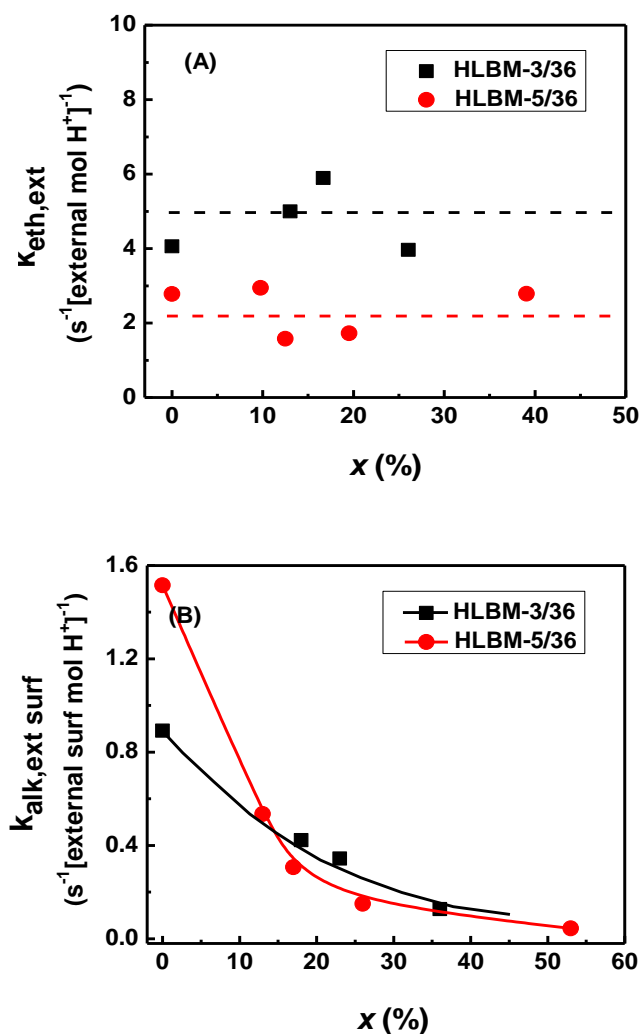


Figure 4.11. Rate constants of etherification on external acid sites (A) and alkylation on external surface acid sites (B) of HLBM-3/36 and HLBM-5/36, respectively, with accumulative addition of DTBP to poison the external acid sites. (x (%) is the percentage of active external acid sites (A) and the percentage of active external surface acid sites (B) that were poisoned by DTBP.)

4.4. Concluding remarks

A scenario of catalytic reactions of benzyl alcohol in mesitylene over the meso-/microporous HLBM zeolite catalysts has been elucidated based on the catalytic

results in the absence and presence of DTBP titrant together with the tunable dual meso-/microporosity of the zeolites. The distinct selectivity differences in parallel etherification and alkylation of benzyl alcohol in mesitylene across the HLBM zeolites are attributed to the different external acid site environments that catalyzed reactions with variant rates in HLBM zeolites. The measured rate behavior of etherification and alkylation reactions on external environment of HLBM zeolites scales with the relative external surface area and B/L acidity of the catalysts. A systematic study of HLBM zeolites with cumulative poisoning of their external acid sites revealed that alkylation reaction rate (per remaining active external surface acid site) on external environment monotonically decreased with increasing number of acid sites poisoned on the external surface areas of HLBM zeolites. The external etherification reaction rate (per remaining active external acid site) was not influenced significantly by the cumulative poisoning of the catalysts. The present study exemplified for the first time that the external acidity in meso-/microporous HLBM zeolites is vital in impacting the selectivity of the parallel catalytic reactions.

Chapter 5: BEA nanosponge@ultra-thin lamellar MFI prepared in one-step: Integration of 3D and 2D zeolites into core-shell composite for efficient alkylation reactions

5.1. Introduction

Zeolites are a class of crystalline aluminosilicates with uniform and ordered networks of micropores that provide size/shape selective molecular discrimination for adsorption, separation, and catalysis applications.¹⁶³⁻¹⁶⁵ The single type of framework in conventional zeolite, however, hinders the practical application of zeolite in achieving simultaneous separation-adsorption or separation-catalysis for some industrial processes.^{74-77, 166} To achieve high separation power, zeolites must have pore diameters close to those of species to be separated, but such zeolites often have low adsorption capacity.^{74, 78, 79} Similarly, zeolites with high separation power usually show low catalytic activity due to intracrystalline diffusion constraints.^{74, 80, 166} Therefore, zeolites with multiple level porosities are desired to achieve concurrently effective adsorption, separation, and catalysis.

Intensive research has been conducted to create hierarchical zeolites with multi-level porosity¹⁶⁷⁻¹⁶⁹ or zeolite composites with multiple framework structures^{76, 148, 170, 171} for above mentioned applications. The hierarchical meso-/microporous zeolites, coupling the structural feature of microporosity and the fast mass transport consequence of mesoporosity in a single material, are promising materials to overcome mass-transfer constraints in catalysis. Zeolite composites, combining different types of pore topologies, crystalline characteristics, and acid properties into

single particles, result in multiple levels of microporosity and compensated acidity to enable excellent catalytic performances.^{75, 93, 170} The integration of hierarchical meso-/microporosity into zeolite composites is expected to further advance their performance in combined adsorption, separation, and catalysis applications. For example, Valtchev et al.⁷⁵ reported the zeolite BEA-core@silicalite-1-shell composite beads in which BEA core (up to 500 μm in diameter) was comprised of a hierarchical meso- and macroporous structure to enable fast transport to the micropores. The silicalite-1 shell (~ 1 μm thick) functioned as a separating component in the hierarchical BEA-core@silicalite-1-shell composite.

The synthesis of zeolite composites has been reported via epitaxial^{14, 88, 170, 172, 173} or overgrown^{74, 76, 84, 155, 174, 175} methods. In epitaxial growth, the pre-synthesized zeolite particles are added into the precursor yielding another type of zeolite crystals. This synthesis method has been used for formation of core-shell^{14, 170} or bi-phase^{81, 176, 177} structured zeolite composites that have similar framework structures. The overgrown method is generally used to create core-shell zeolite composites that have different framework structures. In overgrown synthesis method, the incompatibility between chemical compositions and crystallization conditions of the core and shell zeolite crystals is circumvented by the preliminary seeding of core crystals with shell nanoparticles to induce the growth of the shell. Combinations of dissimilar zeolites such as core-shell BEA@MFI,^{74, 79} MOR@MFI,⁷⁶ BEA@LTA⁷⁶ and FAU@BEA⁸⁴ composites have been successfully synthesized by this method. It should be noted that both epitaxial and overgrown methods require multiple synthesis steps and have limited capability of creating the multi-level porosities in the zeolite composites. The

synthesis of hierarchical zeolite composite with dissimilar framework types in one-step, however, has not been previously reported in literature.

Here, we use the facile one-step dual template synthesis strategy developed and discussed in previous chapters of this dissertation to construct hierarchical zeolite composites containing dissimilar framework structures and dual meso-/microporosity via synergistic integration of two-dimensional (2D) layered MFI and three-dimensional (3D) bulk BEA zeolites as depicted in Figure 5.1. In contrast to previous

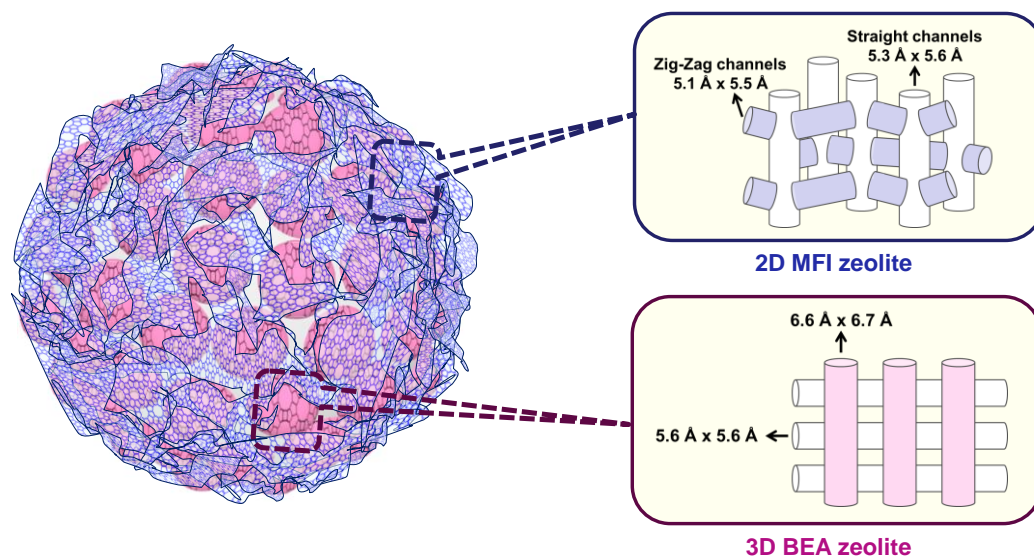


Figure 5.1. Schematic representation of 3D bulk BEA- 2D lamellar MFI composite.

epitaxial growth or overgrown methods, both BEA and MFI zeolite phases in the bulk BEA-lamellar MFI (BBLM) composites are supposed to form sequentially in one-step under the assistance of tetraethyl ammonium hydroxide (TEAOH) and diquatery ammonium surfactant ($[\text{C}_{22}\text{H}_{45}\text{-N}^+(\text{CH}_3)_2\text{-C}_6\text{H}_{12}\text{-N}^+(\text{CH}_3)_2\text{-C}_6\text{H}_{13}]\text{Br}_2$, (C_{22-6-6})) templates, respectively. TEAOH is the traditional molecular template to

assist BEA zeolite synthesis¹⁴⁴; while C₂₂₋₆₋₆ leads to the coherent assembly of the zeolite layer and the surfactant to produce 2D lamellar MFI zeolite nanosheet structures⁶¹. Therefore, combination of these two templates in the synthesis recipe theoretically should lead to the production of BBLM zeolite composites.

5.2. Experimental section

5.2.1. Materials for catalyst synthesis and reactions

Tetraethylammonium hydroxide (TEAOH, 35 wt%) aqueous solution, aluminum isopropoxide (metal basis) (Al[OCH(CH₃)₂]₃, 99.99+% purity), and 2,6-di-tertbutyl-pyridine (DTBP, 97+% purity) were purchased from Alfa Aesar. Ludox colloidal silica (30 wt%), sodium hydroxide (NaOH, ≥97.0% purity), and ammonium nitrate (NH₄NO₃, ≥ 99.0%) were bought from Sigma-Aldrich. Deionized (DI) water was used throughout the experiment. Diquaternary ammonium surfactant ([C₂₂H₄₅-N⁺(CH₃)₂-C₆H₁₂-N⁺(CH₃)₂-C₆H₁₃]Br₂, (C₂₂₋₆₋₆)) was synthesized based on the method reported by Ryoo et al.⁶¹ and the C₂₂₋₆₋₆ synthesis method has also been described in chapter 2 of this dissertation.

5.2.2. Zeolite composite synthesis

The recipe used for dual template synthesis of the BEA@MFI zeolite composite was as follows: 100SiO₂/1.4Na₂O/1Al₂O₃/x C₂₂₋₆₋₆/36TEAOH/1692H₂O, where *x* equals to 0, 1, 3, and 9, respectively. Typically, the synthesis was performed by dissolving 0.0667 g NaOH into 8.7353 g TEAOH (35 wt %). Then, 11.5487 g

Ludox silica (30 wt %) and 0.236 g $\text{Al}[\text{OCH}(\text{CH}_3)_2]_3$ were added to the mixture and the mixture was sonicated at room temperature for 0.5 h until complete dissolution of $\text{Al}[\text{OCH}(\text{CH}_3)_2]_3$. Finally, this solution was mixed with a C_{22-6-6} solution that was prepared by dissolving the desired amount of C_{22-6-6} in 3.8462 g DI water at 333 K. After continuous mixing for 2 h at room temperature, the resultant gel was transferred into a Teflon-lined stainless-steel autoclave, followed by hydrothermal synthesis for 14 days by tumbling the autoclave vertically at 30 rpm in an oven heated at 423 K.

After synthesis, the zeolite product was filtered, washed with DI water, and dried at 343 K overnight. The as-obtained sample was named BBLM- x /36 based on the molar ratio of C_{22-6-6} and TEAOH templates used in the synthesis recipe. Conventional microporous BEA zeolite was synthesized using the same recipe mentioned above without adding any C_{22-6-6} ($x=0$) as the template for comparison, and it was designated as BEA.

All the as-synthesized zeolite samples were calcined in flowing air (100 mL min^{-1} , ultrapure, Airgas) by increasing the temperature from ambient temperature to 873 K at 1.45 K min^{-1} and holding the sample at 873 K for 6 h. The calcined samples were then ion-exchanged three times using 1 M aqueous NH_4NO_3 (weight ratio of zeolite to NH_4NO_3 solution = 1:10) at 353 K for 12 h, and subsequently, collected by centrifugation, washed with DI water three times, and dried at 343 K overnight. The second calcination in dry air (100 mL min^{-1} , ultrapure, Airgas) was conducted by increasing the temperature from ambient temperature to 823 K at 1.45 K min^{-1} and holding the sample at this condition for 4 h to thermally decompose NH_4^+ to NH_3 and

H⁺. Eventually, the zeolite samples in the H⁺-form were used for acidity characterization and catalytic reaction tests discussed later.

5.2.3. Materials characterization

Powder X-Ray diffraction (XRD) patterns were collected by a Bruker D8 Advance Lynx Powder Diffractometer (LynxEye PSD detector, sealed tube, *Cu K α* radiation with *Ni β* -filter). Scanning electron microscopy (SEM) and transmission electron microscopy (TEM) observations of the samples were performed using a Hitachi SU-70 and a JEM 2100 LaB6 electron microscope, respectively. The argon (Ar) adsorption-desorption isotherms were measured using an Autosorb-iQ analyzer (Quantachrome Instruments) at 87 K. Prior to the measurement, samples were evacuated overnight at 623 K and 1 mm Hg. Si and Al contents of zeolite samples were determined by inductively coupled plasma optical emission spectroscopy (ICP-OES, iCAP 6500 dual view).

The magic angle spinning NMR (MAS NMR) spectra were recorded at a field of 7 T (Bruker DSX 300) and 9.4 T (Bruker Avance III 400) for ²⁹Si and ²⁷Al, respectively. ²⁹Si MAS NMR spectra were recorded at 59.63 MHz using 4 mm rotors at a spinning speed of 10 kHz, a dwell time of 19.95 μ s, a $\pi/2$ pulse of 5.0 μ s, and a recycle delay of 60 s. The spectra were referenced with respect to 3-(trimethylsilyl)-1-propanesulfonic acid salt. ²⁷Al MAS NMR spectra were recorded at 104.21 MHz using 4 mm rotors at 10 kHz spinning speed, a dwell time of 1.006 μ s, a selective $\pi/10$ pulse of 3 μ s, and a recycle delay of 2 s. An aqueous solution of aluminum nitrate (0.1 M) was used as the reference.

The acidity of the zeolite was evaluated by ammonia temperature programmed desorption (NH₃-TPD) method using an Autosorb-iQ instrument (Quantachrome, ASIQM0000-4) equipped with a thermal conductivity detector (TCD). In the measurement, 0.1 g catalyst sample was loaded into a quartz reactor and heated at a rate of 10 K min⁻¹ to 873 K under He (40 mL min⁻¹) and maintained at this temperature for 2 h. After being cooled to 373 K under He stream, the catalyst sample was exposed to NH₃ (30 mL min⁻¹, ultrapure, Airgas) stream for 0.5 h. Physisorbed NH₃ was then removed by flowing He gas (40 mL min⁻¹) for 2 h. Afterwards, the catalyst sample was ramped to 1023 K at a ramp rate of 10 K min⁻¹, and the NH₃-TPD profile was recorded during this step.

5.2.4. Determination of external and internal Brønsted acid sites

The total number of Brønsted acid sites, defined as total acid sites, was determined via dimethyl ether (DME) titration experiment given that the Brønsted acid sites participate in reactions of DME with H⁺ to form surface methyl groups, $\text{CH}_3\text{OCH}_3 + 2[\text{SiO}(\text{H})\text{Al}] = 2[\text{SiO}(\text{CH}_3)\text{Al}] + \text{H}_2\text{O}$.^{42, 110}

The number of active Brønsted acid sites on the external surface of zeolites, defined as external acid sites that comprise of acid sites on the geometrical external surface and in pore-mouth region of the catalysts, was measured by 2,6-di-tertbutylpyridine (DTBP) titration during methanol dehydration reactions since the bulky DTBP molecule has limited accessibility to acid sites located in micropores of the medium-pore zeolites^{132, 133}.

The experimental setup and reaction conditions for chemical titration of acid sites were same as those described in chapter 2 of this dissertation. The Brønsted acid sites only accessible to DME titrant were defined as the internal acid sites. The fraction of external Brønsted acid sites was calculated by the ratio of the number of Brønsted acid sites accessible to DTBP titrant to the number of Brønsted acid sites accessible to DME titrant.

5.2.5. Catalytic conversion of benzyl alcohol in mesitylene

The liquid phase catalytic conversion of benzyl alcohol in mesitylene was conducted to examine the catalytic performance of the BBLM zeolite composites. The reaction setup consisted of a three-necked round bottom flask (100 mL) equipped with a reflux condenser and heated in a temperature controlled oil bath under atmospheric pressure and magnetic stirring (1" stirring bar, 500 rpm stirring speed) conditions same as that explained before in chapters 2 and 4 of this dissertation.

In a typical experiment, 15 mL of mesitylene was added to the desired amount of zeolite catalyst. The reaction mixture was maintained for 0.5 h at the required reaction temperature and stirring conditions and then 0.25 mL of benzyl alcohol was added. This moment of adding benzyl alcohol to the reaction mixture was taken as the initial reaction time. Liquid samples were withdrawn at regular time intervals and analyzed by a gas chromatograph (Agilent 7890A) equipped with a methylsiloxane capillary column (HP-1, 50.0 m x 320 μm x 0.52 μm) connected to a flame ionization detector (FID) to calibrate and separate the reactants and products.

5.3. Results and discussion

5.3.1. BBLM structure formation assisted by dual templates

To examine the effect of dual templates on the formation of BBLM zeolite composites, the synthesis was comparatively carried out using the recipe comprised of TEAOH, C₂₂₋₆₋₆, as well as dual TEAOH and C₂₂₋₆₋₆ templates (molar ratio of C₂₂₋₆₋₆/TEAOH: 1/36, 3/36, and 9/36), respectively. The usage of bare C₂₂₋₆₋₆ template in the synthesis led to amorphous product (data is not shown here), while bare TEAOH or the combinational usage of TEAOH and C₂₂₋₆₋₆ templates resulted in crystalline zeolite products. Figure 5.2 shows the XRD patterns of the as-synthesized BEA and BBLM zeolite composites. The co-existence of TEAOH and C₂₂₋₆₋₆ templates in the synthesis led to the crystallization of both BEA and MFI zeolites. An increase in concentration of C₂₂₋₆₋₆ in the recipe resulted in an increase in MFI zeolite quantity, as indicated by the increase in peak intensity of the MFI diffraction peaks in Figure 5.2. The emergence of the diffraction peak around $2\theta \sim 4^\circ$ in BBLM-9/36 suggests that a multi-lamellar MFI structure^{18, 43} started to form in this synthesis recipe, while only disordered or one and half unit-cell thick MFI nanosheets formed in BBLM-1/36 and BBLM-3/36 zeolite composite samples.

The SEM and TEM observations were conducted to understand the morphological characteristics of the BBLM zeolite composites. Figure 5.3(A) shows that the BEA zeolite contains spherical particles with an average size of ~250 nm. When a small amount of C₂₂₋₆₋₆ (C₂₂₋₆₋₆/TEAOH = 1/36, i.e., BBLM-1/36) was added into the BEA synthesis gel, the size of BEA particles was increased ~2 times and the very near surface seems to be covered by a silk-like material (Figure 5.3(B)). BBLM-

3/36 in Figure 5.3(C) shows that the particles have similar sizes to BEA particles, but a very rough surface comprised of interdigitated nanosheets was observed. A further increase in C_{22-6-6} content in the synthesis, as shown by BBLM-9/36 (Figure 5.3(D)), led to aggregation of BEA particles which are covered by a MFI “skin” layer. The SEM images demonstrate that the BEA and MFI zeolites in the BBLM-type zeolite composite are integrated into single particles, not a random physical mixture of both types of zeolite phases.

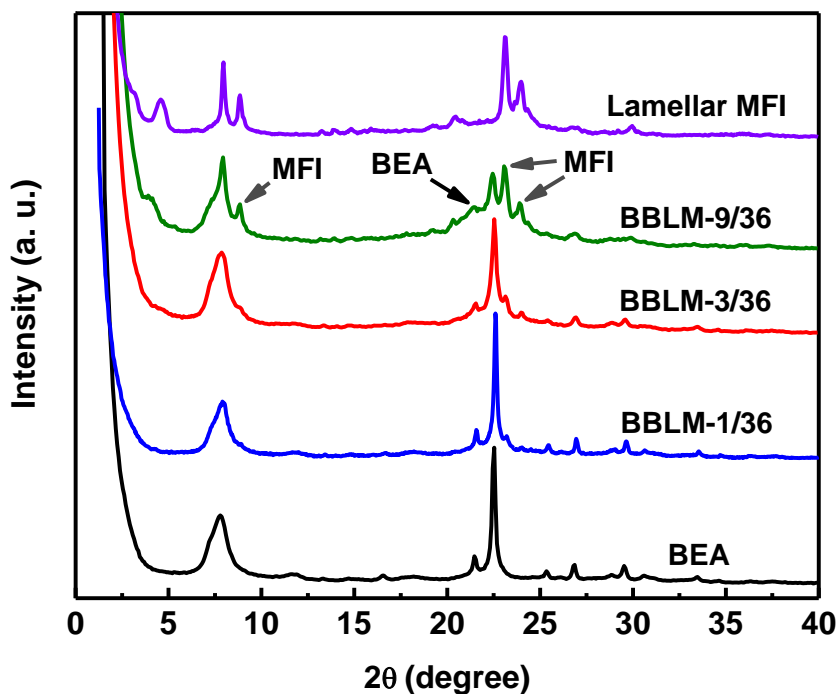


Figure 5.2. XRD patterns of BEA and BBLM zeolite composites after 14 days of hydrothermal synthesis. XRD pattern of lamellar MFI catalyst has been presented for comparison purpose.

The integrity of the MFI and BEA zeolites in the BBLM zeolite composites was further examined by the TEM observation. Figure 5.4(A)-(C) confirm the

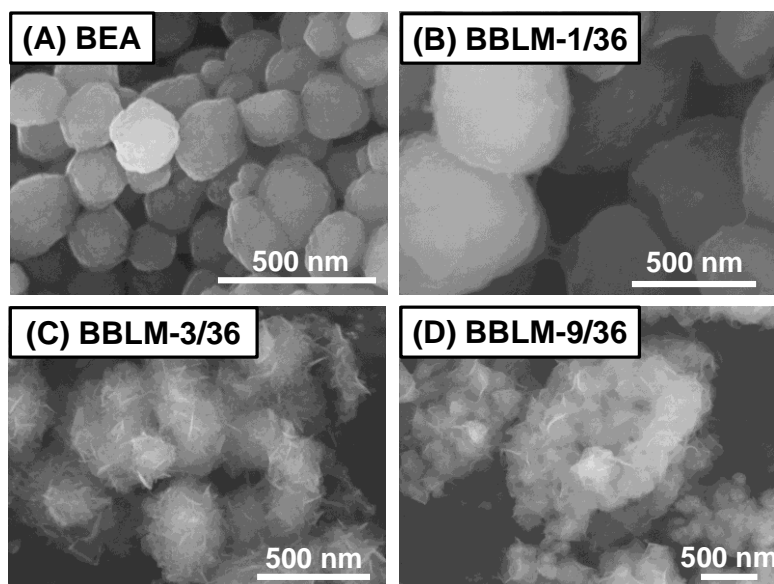


Figure 5.3. SEM images of BEA (A), BBLM-1/36 (B), BBLM-3/36 (C), and BBLM-9/36 (D), respectively, after 14 days of hydrothermal synthesis.

presence of single BEA zeolite particles with relatively smooth surfaces. Figure 5.4(D)-(F) show that BBLM-1/36 contains fractioned BEA particles with intraparticle voids (Figure 5.4(D)) and channeled surface (Figure 5.4(F)). The 2D MFI nanosheets are observed in Figure 5.4(E), which lie in parallel with the BEA surface, contrast to the vertical epitaxial growth of 2D MFI nanosheets from MFI zeolite surface in case of HLBM zeolites discussed in chapter 3 and 4 of this dissertation. It should be mentioned that the number of 2D MFI nanosheets is not enough to fully cover the bulk BEA particle in BBLM-1/36 sample. BBLM-3/36 has a BEA-core/lamellar MFI-shell composite structure (Figure 5.4(G)), in which a number of 2D MFI nanosheets aggregate and/or wrinkle together to form a ‘skin’ layer for bulk BEA zeolite particle. The bulk BEA was further fractioned into a nanosponge-like structure, which was verified by visualization of the core component in BBLM-3/36 (Figure 5.4(H)) after partially peeling off the ‘skin’-like MFI nanosheet shell by

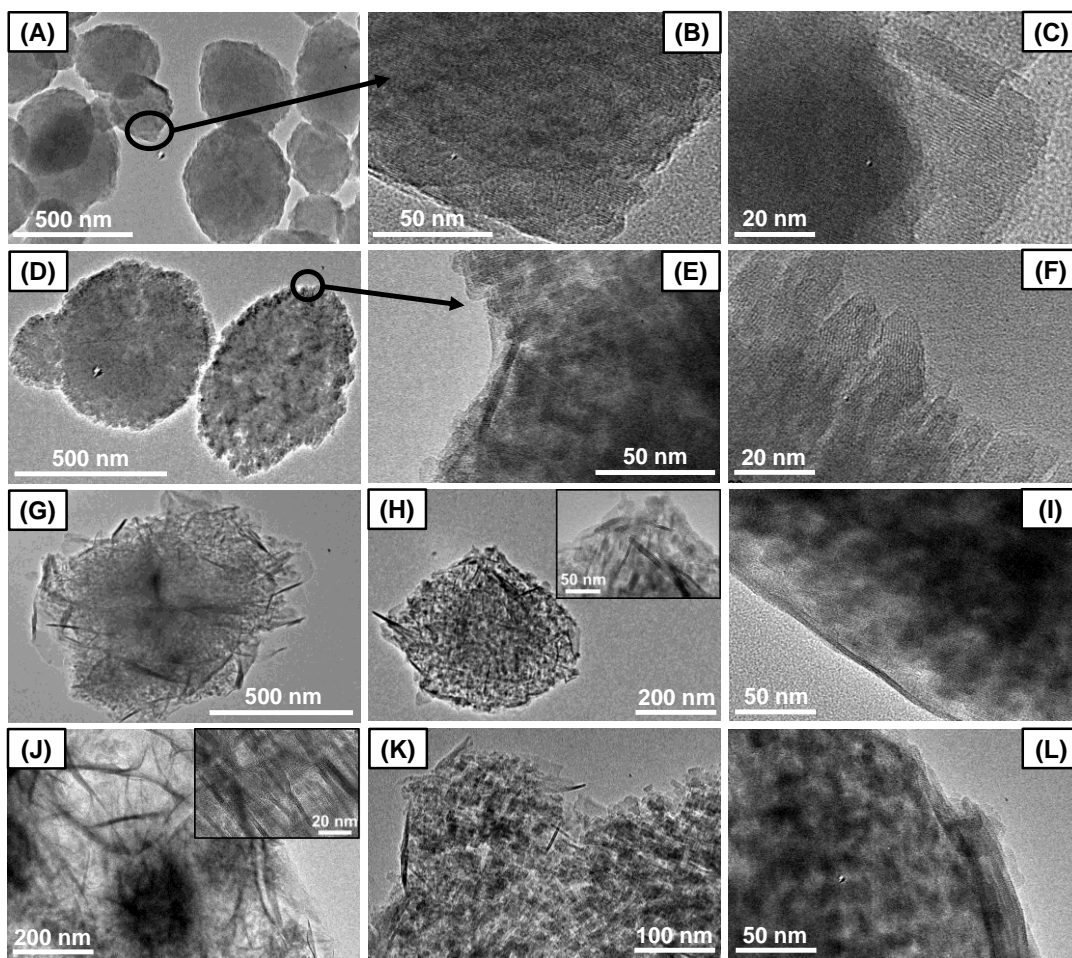


Figure 5.4. TEM images of BEA (A), (B), and (C), BBLM-1/36 (D), (E), and (F), BBLM-3/36 (G), (H), and (I), and BBLM-9/36 (J), (K), and (L) zeolite composite catalysts with Si/Al=50 after 14 days of hydrothermal synthesis.

sonication. A closer look of the nanosponge-like core (inset in Figure 5.4(H)) illustrates that BEA particles with sizes of ~10-20 nm and internal voids with equivalent sizes co-exist uniformly through the core component. Some MFI nanosheets seem to penetrate into the nanosponge-like BEA core, as shown in Figure 5.4(H). The core-shell interface in the BBLM-3/36 sample was also carefully examined, showing MFI nanosheet stays closely on the surface of the BEA core (Figure 5.4(I)). The intimate growth of some 2D lamellar MFI zeolite in the BEA

core body and more importantly the close contact between ultra-thin 2D MFI shell and BEA core surface guarantee the communication between MFI shell and BEA core in the BBLM zeolite composites. Figure 5.4(J)-(L) demonstrate the structural features of the BBLM-9/36 sample, which contains nanosponge-like BEA core (Figure 5.4(K)) and 2D lamellar MFI shell, similar to BBLM-3/36. The thickness of the shell, i.e., the number of 2D MFI nanosheets, covered on the core surface, is increased (Figure 5.4(J and L)). The increase of C_{22-6-6} content in the synthesis recipe led to more growth of lamellar MFI in the zeolite composite. The SEM and TEM images show that the BBLM zeolite composites contain not only a simple core-shell structure, but also an interdigitated structure extended to the bulk BEA core. Additionally, both thin lamellar MFI shell and bulk BEA core are comprised of hierarchical meso-/microporosity. Therefore, such unique structures lead to intimate communication between micropores of two different types of zeolites, which was further studied by the catalytic reactions to be discussed later in this chapter.

5.3.2. Scheme for formation of BBLM zeolite composite

To understand the formation scheme of BBLM zeolite composite and the functionality of C_{22-6-6} and TEAOH templates in the synthesis, the growth of the BBLM-3/36 as a function of the hydrothermal synthesis time (1, 3, 7, and 14 days, respectively) was examined. After 1 day of hydrothermal synthesis, the resultant sample mainly consisted of amorphous material, indicated by the featureless XRD pattern in Figure 5.5 and irregular particle shapes in Figure 5.6(A). When the hydrothermal synthesis continued for 3 days, the BEA zeolite was formed, as indexed

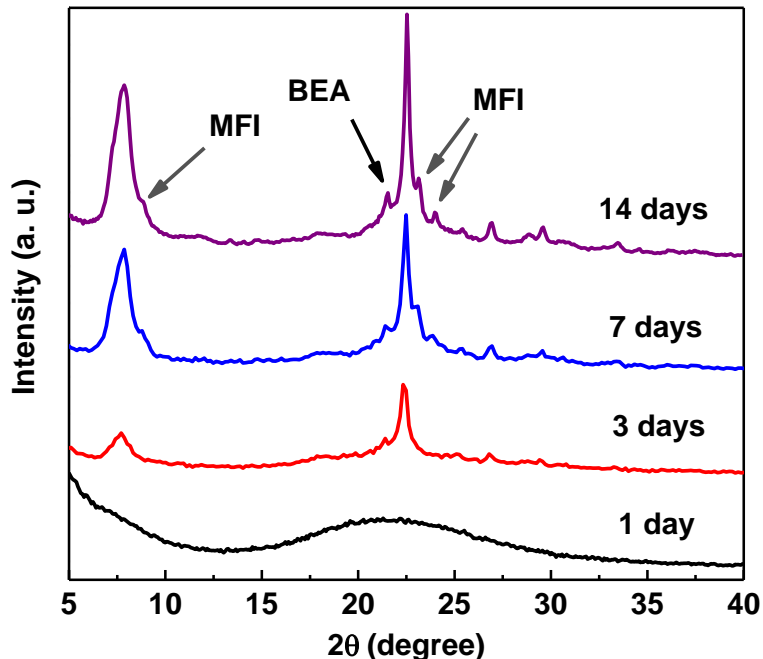


Figure 5.5. XRD patterns of BBLM-3/36 zeolite composite after 1 day, 3 days, 7 days, and 14 days hydrothermal synthesis, respectively.

by the XRD diffraction peaks and the nearly spherical particles in Figure 5.6(B). The co-existence of ‘skin’-like material that stayed around the BEA particles was also observed in this sample. When the synthesis time was extended to 7 days, the XRD pattern in Figure 5.5 shows the appearance of MFI zeolite in the sample, and the as-obtained sample contains irregular small debris-like particles covered on the BEA core (Figure 5.6(C)). The synthesis time of 14 days led to transformation of irregular small particles into lamellar nanosheet particles (Figure 5.6(D)) and the XRD diffraction pattern indicates that the as-crystallized material is MFI, besides the BEA core that has formed since 3 days of hydrothermal synthesis.

The Ar isotherms and non-local density functional theory (NLDFT) pore size distributions were further used to track the transformation of the materials in the

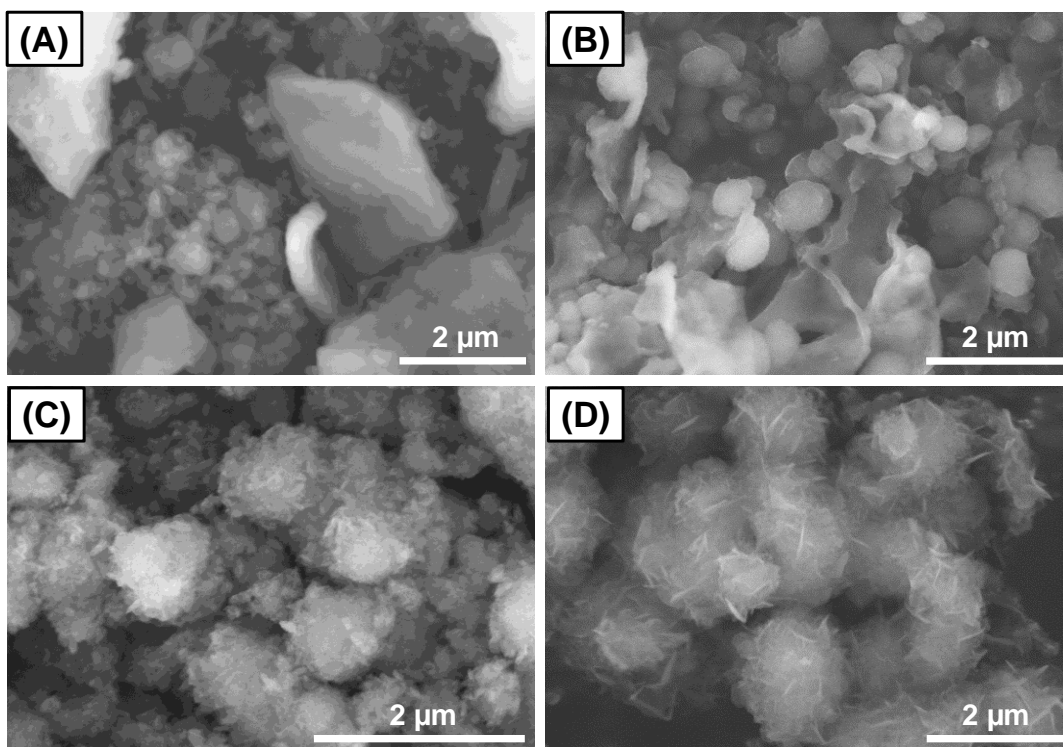


Figure 5.6. SEM images of BBLM-3/36 zeolite composite after (A) 1 day, (B) 3 days, (C) 7 days, and (D) 14 days hydrothermal synthesis, respectively.

BBLM-3/36 growth. Figure 5.7 illustrates that the BBLM-3/36 material has the type-IV isotherm with ~ 5 nm mesopore after 1 day of hydrothermal synthesis, similar to aluminosilicate MCM-41¹⁷⁸ material. After 3 days of synthesis, the isotherm of BBLM-3/36 exhibits both micro- and mesoporous features, with micropore size of ~ 0.61 nm and mesoporosity reduced compared to 1 day of synthesis. The appearance of the micropore size of ~ 0.61 nm confirms the crystallization of BEA zeolite in the synthesis. The decrease in mesoporosity and increase in microporosity (Table 5.1) as well as a left-shifting of micropore size (~ 0.58 nm, inset in Figure 5.7(B)) are observed after the synthesis time was extended to 7 and 14 days, respectively. The results suggest the growth of lamellar MFI on the BEA zeolite core by consuming the

amorphous materials existed in the sample. It should be noted that the textural properties of BBLM-3/36 after 7 days of synthesis remained similarly to that after 14 days, although the morphology was progressed into layered nanosheet structures.

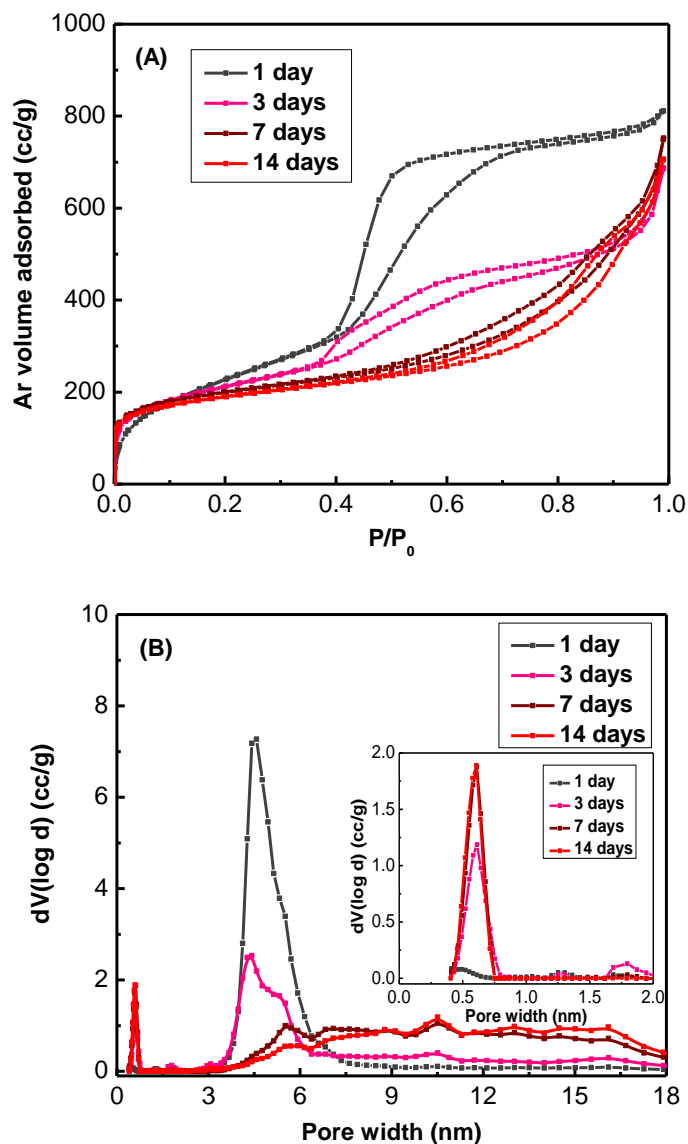


Figure 5.7. Ar adsorption-desorption isotherms (A) and the corresponding NLDFT pore size distributions (B) derived from Ar adsorption branch of isotherms for the BBLM-3/36 zeolite composite after 1 day, 3 days, 7 days, and 14 days hydrothermal synthesis, respectively. The inset image in Figure 6(B) shows the NLDFT micro pore size distribution of BBLM-3/36 zeolite composite.

Table 5.1. Textural properties of the BBLM-3/36 zeolite composite at different synthesis times determined from Ar isotherms.

Synthesis time	V_{micro}^a [cm ³ g ⁻¹]	S_{micro}^a [m ² g ⁻¹]	S_{ext}^a [m ² g ⁻¹]	V_t^b [cm ³ g ⁻¹]	$V_{\text{meso}} = V_t - V_{\text{micro}}$ [cm ³ g ⁻¹]	S_{BET}^c [m ² g ⁻¹]
1 day	0	0	781	1.005	1.005	781
3 days	0.033	119	538	0.875	0.842	658
7 days	0.110	224	328	0.976	0.866	552
14 days	0.118	239	331	1.012	0.894	570

^a Determined from t-plot method; ^b Determined by NLDFT method; ^c Determined from Brunauer, Emmett, and Teller (BET) method.

The evolution of BBLM-3/36 structure with hydrothermal synthesis time suggests a possible growth scheme for the BBLM 2D-3D zeolite composite with the assistance of C₂₂₋₆₋₆ and TEAOH templates. In the initial stage of the synthesis, the zeolite synthetic gel formed amorphous materials with ordered mesoporosity under the assistance of C₂₂₋₆₋₆ template. With the progression of the synthesis, the bulk BEA zeolite particles started to form with the assistance of TEAOH template. The growth of bulk BEA zeolite was accompanied by the consumption of the amorphous ordered material. Upon extension of the synthesis time beyond 7 days, the crystallization of MFI zeolite directed by C₂₂₋₆₋₆ template occurred, and then the lamellar MFI-shell structure evolved at the last stage of the synthesis (up to 14 days). The formation of the amorphous ordered phase followed by formation of the bulk BEA zeolite in the initial stage of the synthesis indicates the sequential functions of C₂₂₋₆₋₆ and TEAOH, which was consistent with dual template synthesis using cetyltrimethylammonium bromide (CTAB) and TEAOH templates⁵⁶. In the later stage of the synthesis, a transformation of the amorphous material to crystalline lamellar MFI zeolite was

realized under direction of C_{22-6-6} , and thus resulted in the formation of BBLM zeolite composite. A cooperative and sequential functioning between C_{22-6-6} and TEAOH is expected in the synthesis process of BBLM zeolite composites because single C_{22-6-6} or TEAOH can only produce amorphous or bulk BEA particles, respectively, under the same synthesis conditions.

5.3.3. Textural properties of BBLM zeolite composites

Figure 5.8 shows the textural properties of the synthesized BBLM zeolite composites. For comparison purpose, lamellar MFI synthesized following the recipe reported by Ryoo et al.⁶¹ was included in the analyses. Generally, BEA or BBLM composite samples have higher Ar uptake than the lamellar MFI (Figure 5.8(A)) because BEA has relatively large micropore sizes^{179, 180}. At the relative pressure of $P/P_0 > 0.5$, the BBLM zeolite composites have higher Ar uptake than bare BEA zeolite due to the mesoporosity in the BEA core and lamellar MFI shell in the zeolite composite. The NLDFT pore size distribution data in Figure 5.8(B) reveals that the mesoporosity increases from BBLM-1/36 to BBLM-3/36 and then to BBLM-9/36 sample. All of these composite samples have higher mesoporosity than lamellar MFI zeolite, which is consistent with the morphologies determined from SEM and TEM observations before.

A closer look on the micropore size distribution in the BBLM, BEA and lamellar MFI zeolite samples is shown in Figure 5.8(C). The bare BEA and lamellar MFI zeolites have the characteristic micropore sizes of 0.64 nm and 0.50 nm, respectively. The transition of the micropore pore sizes from BEA to MFI was

achieved in the BBLM-1/36, BBLM-3/36, and BBLM-9/36, showing the micropore sizes center at 0.63 nm, 0.60 nm, and 0.55 nm, respectively. The cumulative pore volume versus the pore width of these samples (Figure 5.8(D)) further confirms the existence of both MFI and BEA zeolite frameworks in the BBLM zeolite composites.

The textural properties of the BBLM zeolite composites were also summarized in Table 5.2. The total pore volume (V_t), mesopore volume (V_{meso}), external surface area (S_{ext}), and Brunauer-Emmett-Teller (BET) surface area (S_{BET}) of BBLM zeolite composite increase with increasing C_{22-6-6} concentration in the

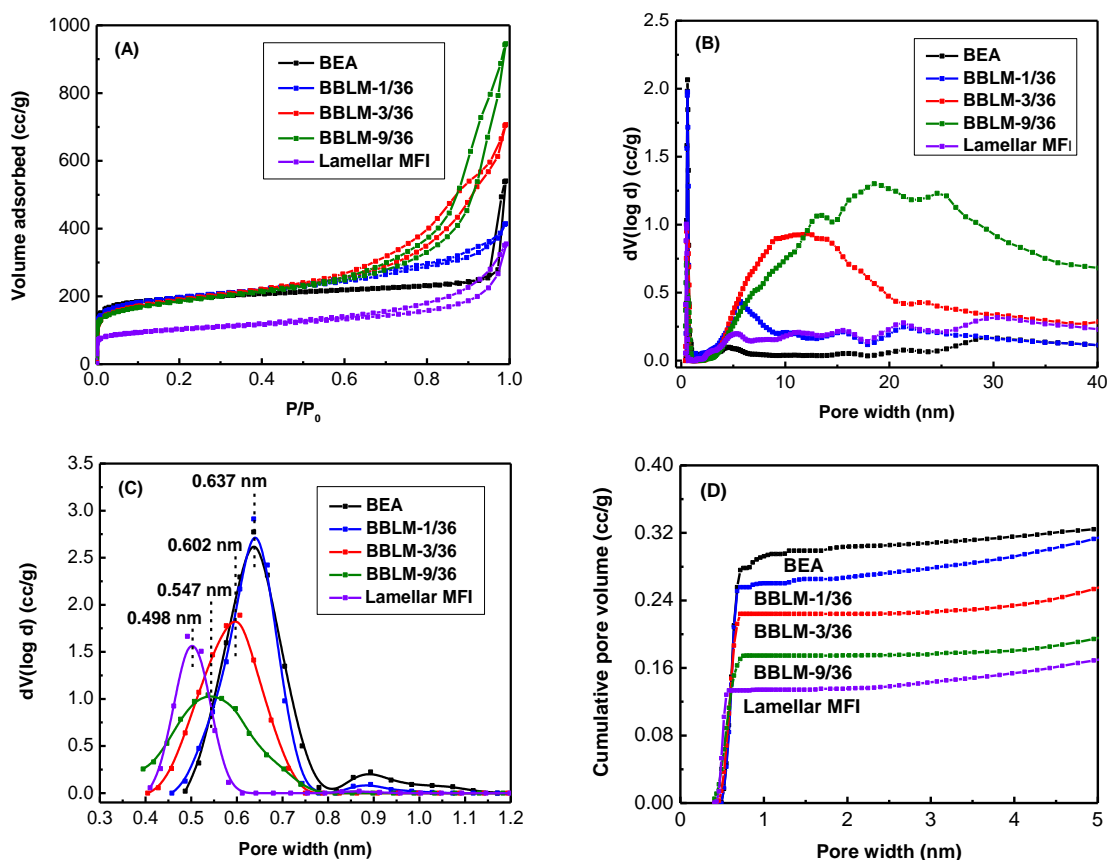


Figure 5.8. Ar adsorption-desorption isotherms (A), the corresponding NLDFT pore size distributions (B)-(C) derived from Ar adsorption branch of isotherms, and cumulative pore volume versus pore size (D) of the BEA, lamellar MFI, and BBLM zeolite composites.

Table 5.2. Textural properties of the BEA and BBLM zeolite composites determined from Ar isotherms.

Catalyst	V_{micro}^a [cm ³ g ⁻¹]	S_{micro}^a [m ² g ⁻¹]	S_{ext}^a [m ² g ⁻¹]	V_t^b [cm ³ g ⁻¹]	$V_{\text{meso}} = V_t - V_{\text{micro}}$ [cm ³ g ⁻¹]	S_{BET}^c [m ² g ⁻¹]
BEA	0.184	349	145	0.506	0.559	493
BBLM-1/36	0.171	290	234	0.630	0.468	525
BBLM-3/36	0.118	239	331	1.012	0.894	570
BBLM-9/36	0.072	199	389	1.357	1.285	587
Lamellar MFI	0.063	141	169	0.462	0.399	310

^a Determined from t-plot method; ^b Determined by NLDFT method; ^c Determined from Brunauer, Emmett, and Teller (BET) method.

one-step dual template synthesis recipe. This is due to the facts of fractioning of bulk BEA core into nanosponge-like structure and formation of mesoporous 2D lamellar MFI nanosheets directed by C₂₂₋₆₋₆ template. The micropore volume (V_{micro}) and micropore surface area (S_{micro}) of these zeolite composites, however, decrease with an increase in C₂₂₋₆₋₆ content due to the formation of more MFI zeolite that has smaller pore sizes.

It should be noted that the measured micropore volumes of BBLM zeolite composites lie between the respective micropore volumes of the bare BEA (0.184 cm³ g⁻¹) and lamellar MFI (0.063 cm³ g⁻¹). Based on the micropore volumes in Table 5.2, the mass fraction of BEA in the BBLM composite particles can be calculated, showing that the mass fractions of BEA in BBLM-1/36, BBLM-3/36 and BBLM-9/36 are 89%, 45%, and 7%, respectively.

5.3.4. Acidity of BBLM zeolite composites

In order to understand acidity and acid site distribution in the BBLM zeolite composites, a combination of ICP-OES, DME and DTBP titrations, solid state NMR, and NH₃-TPD analyses were conducted. Table 5.3 shows the Si/Al ratio is slightly increased from bare BEA to the BBLM-9/36 sample. The decrease in Al content with an increase in the lamellar MFI structure in the BBLM zeolite composites suggests that the acid site distribution may not be uniform in the BBLM zeolites. The location of the acid sites was further explored by the DME and DTBP titrations, indicated by the fraction of external acid sites ($f_{B,ext}$) of each zeolite composite which represents the percentage of active sites that can be accessible by DTBP molecule.

Table 5.3 shows that $f_{B,ext}$ decreases from 86% to 79% and then to 64% in the BBLM-1/36, BBLM-3/36, and BBLM-9/36 samples, respectively. The measured $f_{B,ext}$ in bare BEA and lamellar MFI are 85% and 27%, respectively. On the basis of DTBP molecule accessibility to active sites in bare BEA and lamellar MFI samples, the mass fractions of BEA in each BBLM zeolite composite can be calculated to be 100%,

Table 5.3. Acidity, acid site distribution and fraction of BEA content in the BBLM zeolite composites.

Catalyst	Si/Al ^a	Fraction of external acid sites $f_{B,ext}$ ^b (%)	Mass fraction of BEA ^c (%)	Mass fraction of BEA ^d (%)
BEA	22	85	100	100
BBLM-1/36	24	86	89	100
BBLM-3/36	27	79	45	88
BBLM-9/36	30	64	7	62

^a Determined by ICP-OES analysis; ^b Determined by DTBP titration; ^c Determined based on the micropore volume extracted from Ar adsorption-desorption measurements. ^d Determined based on the DTBP titration measurements.

88%, and 62% for BBLM-1/36, BBLM-3/36, and BBLM-9/36, respectively. The higher mass fractions of BEA in BBLM composites estimated by this method compared to those calculated from micropore volumes of these zeolites suggests that the number of acid sites in the lamellar MFI is less than that in the BEA core in the BBLM zeolite composites.

Solid state NMR was employed to investigate the local bonding environment in the BBLM zeolite composites. Figure 5.9(A) shows the ^{29}Si single pulse (SP) NMR spectra of BEA and BBLM zeolites. Two resolved peaks (at -113 and -103 ppm) can be observed in the spectra, which correspond to crystallographically nonequivalent Q^4 tetrahedral sites (Q^n stands for $\text{X}_{4-n}\text{Si}[\text{OSi}]_n$)^{41, 122-124} and Q^3 sites arising from the silanol groups on the zeolite surface¹²⁵. The slight increase in the Q^3 peak intensity from bare BEA to BBLM-9/36 suggests that more defects in the local bonding environment are formed which is caused by the formation of more 2D lamellar MFI in these BBLM zeolite composites.

Figure 5.9(B) shows the ^{27}Al MAS NMR spectra of these zeolite samples. The peak at 55 ppm is assigned to the tetrahedrally coordinated framework aluminum (Al_F)^{42, 124}, while the peak around 0 ppm is designated to an octahedral coordination of extra-framework Al (Al_EF). The fractions of the extra-framework Al in BBLM-1/36, BBLM-3/36 and BBLM-9/36 samples are calculated from the intensities of the peak at around 0 ppm over the peak around 55 ppm in the ^{27}Al NMR spectra to be < 9%, suggesting that quite similar Al bonding environments exist in all the BBLM zeolite composite samples.

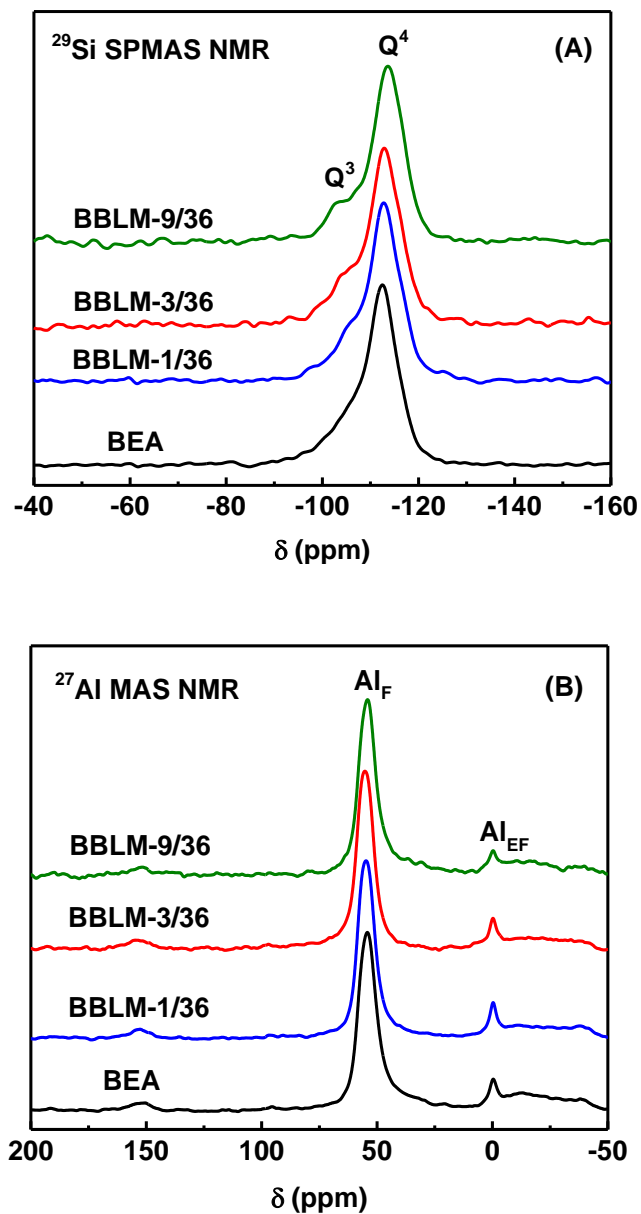


Figure 5.9. Solid-state ^{29}Si SP MAS NMR (A) and ^{27}Al MAS NMR (B) spectra of the BEA and BBLM zeolite composites.

NH_3 -TPD profiles were measured to evaluate the strength of acid sites in the BBLM zeolite composites. Figure 5.10 shows two desorption peaks in the high temperature range of 450–700 K and low temperature range of 350–450 K, respectively, in each BBLM composite, bare BEA and lamellar MFI samples. The

high temperature desorption peak has been assigned to the adsorption of NH_3 by acid sites, while the low temperature desorption peak is ascribed to the physisorbed NH_3 in the catalysts.^{122, 171, 181, 182} When the sample is transitioned from BEA to BBLM and then to lamellar MFI zeolites in Figure 5.10, the high temperature and low temperature desorption peaks in the NH_3 -TPD profiles shift towards higher and lower temperatures, respectively. Concurrently, the peak intensities at both temperature ranges decrease. The broadening in peak width and decrease in peak height in Figure 5.10 indicate that the types and strengths of acid sites in BBLM zeolites are diversified, lying between bare BEA and lamellar MFI zeolites. Multiple types of acid sites with variant strengths have been identified to exist in lamellar MFI zeolites.^{123, 183-185} The integration of 2D lamellar MFI in the BBLM zeolite composites, spontaneously, leads to the diversification of the acidity in the resultant samples.

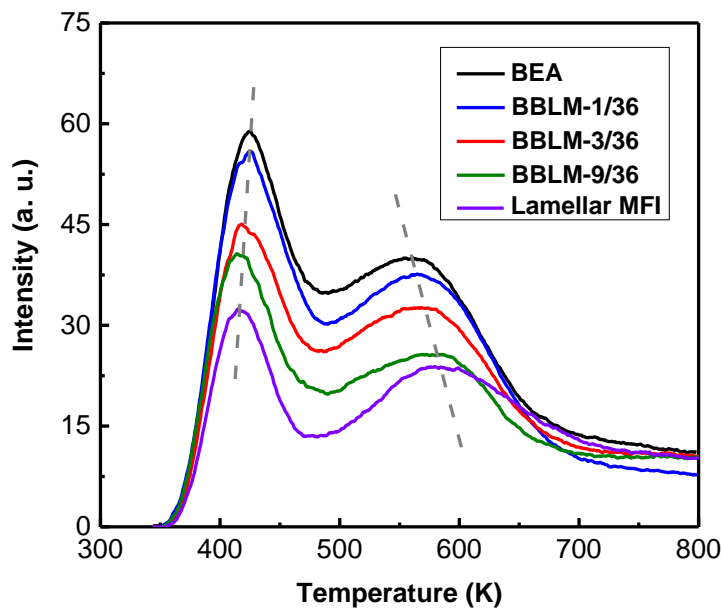


Figure 5.10. NH_3 -TPD profiles of the BEA, lamellar MFI and BBLM zeolite composites.

5.3.5. Catalytic performance of BBLM zeolite composites

The catalytic performance of the BBLM zeolite composites were tested in catalytic conversion of benzyl alcohol in mesitylene. Our previous studies^{162, 167} discussed in chapter 2 and 4 of this dissertation show that benzyl alcohol is simultaneously converted to 1,3,5-trimethyl-2-benzylbenzene and dibenzyl ether by mesitylene alkylation and benzyl alcohol self-etherification reactions, respectively over MFI zeolite catalysts. For comparison purpose, the same reaction was carried out over bare BEA and physical mixture of the BEA and lamellar MFI zeolites, respectively. The mass fraction of BEA in the physical mixture of BEA and lamellar MFI zeolites was controlled to be the same as that in BBLM-3/36 zeolite composite.

Figure 5.11(A) shows that the conversion of benzyl alcohol at the reaction time of 7 h over the zeolite catalysts follows the order of bare BEA < mixture of BEA and lamellar MFI < BBLM-1/36 < BBLM-9/36 < BBLM-3/36. A close look at the benzyl alcohol conversion in the initial stage of reaction (< 0.5 h, Figure 5.11(B)) indicates, however, the conversion of benzyl alcohol is in the order of bare BEA > BBLM-3/36 > BBLM-9/36 > mixture of BEA and lamellar MFI > BBLM-1/36.

The discrepancy between the benzyl alcohol conversions over the catalysts at the initial and long-term reaction stages indicates the change in activity and stability of the catalysts through the course of the catalytic reactions. The highest benzyl alcohol conversion at reaction time less than 0.5 h and lowest conversion at reaction time of 7 h over bare BEA zeolite suggests that BEA has the highest activity and fast deactivation rate among all the tested catalysts. On the other hand, the BBLM zeolite composites have the relatively lower initial rates but much enhanced stability

compared to bare BEA. Particularly, BBLM-3/36 has the comparable initial activity to bare BEA but with the highest stability in the tested zeolite samples. The physical mixture of BEA and lamellar MFI zeolite has only slightly better stability than BEA, although it has equivalent composition to BBLM-3/36 zeolite composite. The increase in 2D lamellar MFI content in the BBLM zeolite composites (from BEA to BBLM-1/36 and then to BBLM-3/36) led to an increase in both catalytic activity and stability in the catalytic benzyl alcohol reaction. A further increase (i.e., from BBLM-3/36 to BBLM-9/36), however, resulted in a reduction in the catalytic performances in this reaction.

The performance of BBLM zeolite composites in catalytic reactions depends on the acidity, pore structure, and crystallite size of both BEA and MFI zeolites.^{186, 187} MFI zeolite consists of two interconnected 10-membered ring (10-MR) channel systems: one is straight running along the *b*-axis direction (0.53 x 0.56 nm) and the other is zigzag running parallel to the *a*-axis direction (0.51 x 0.55 nm). BEA zeolite structure consists of 12-MR straight channels of a free aperture of 0.66 x 0.67 nm viewed along *a*-axis and 12-MR zigzag channels of 0.56 x 0.56 nm viewed along *c*-axis. The 3D pore systems and pores running along the *a*- and *b*-axes, respectively, in both BEA and MFI zeolites guarantee the ease of pore communication in the BBLM composites for any molecules smaller than micropore sizes of MFI. The ultra-thin lamellar MFI with straight channel normal to the BEA surface (visualized from TEM images in Figure 5.4) even intensifies the communication between two zeolite structures.

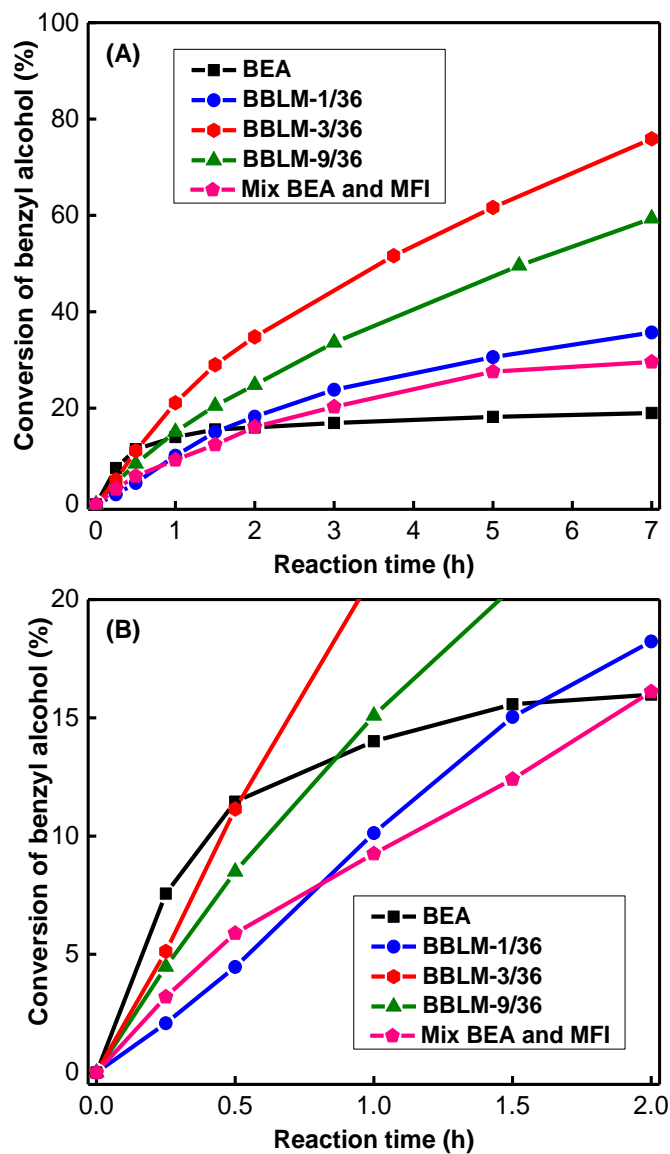


Figure 5.11. Conversion of benzyl alcohol in mesitylene versus reaction time of 7 h (A) and 2 h (B) over BBLM zeolite composite catalysts. BEA and physical mixture of BEA/lamellar MFI zeolites were included for comparison.

The high initial reaction rates observed in Figure 5.11(A) across all the tested zeolite samples indicate that stronger acidity and larger micropore of BEA than 2D lamellar MFI are responsible for higher activity. This high activity also led to fast growth of alkylated aromatics, polyalkylaromatics, and even polycondensated

carbonaceous products to deactivate the catalysts. Studies on Friedel-Crafts alkylation reactions over acidic zeolite catalysts have suggested that the high acidity, large zeolite micropore size, and larger zeolite crystallite sizes exacerbate the deactivation rates of the catalysts, which is due to the pore-mouth blockage or local poisoning of active sites by irreversible adsorption of carbonaceous residues.¹⁸⁸⁻¹⁹⁰ Therefore, bare BEA zeolite in the present study had the fastest deactivation behavior. The BBLM zeolite composites contain 2D lamellar MFI zeolite nanosheet that has smaller micropore size than BEA, low acidity due to diversification of acid sites, together with small BEA crystallite sizes and mesoporosity due to fractioning of bulk BEA. All these characteristics contribute to the highly enhanced catalyst stability of BBLM zeolites.

The decrease in the catalytic performance of BBLM-9/36 compared to BBLM-3/36 might be due to the thick coverage of the BEA zeolite surfaces by lamellar MFI (as shown by the TEM image in Figure 5.4 (J)-(L)), which prevents the facile mass transport. The ultra-thin (~3-10nm) 2D MFI nanosheets functions as soft patches that conforms to the BEA nanosponge and lead to facile transport of reactant or products formed in the core compartments in the BBLM-3/36 composite. The incomplete coverage of BEA in the BBLM-1/36 sample caused a slight increase in catalytic performance, but much lower than BBLM-3/36. Therefore, the unique structural scenario of BBLM-3/36 zeolite composite together with modulated acidity enabled the observed performances in the catalytic reactions of benzyl alcohol in mesitylene for BBLM zeolite composites.

5.4. Concluding remarks

The core-shell bulk BEA-lamellar MFI (BBLM) zeolite composites were innovatively synthesized by a facile one-step dual template method. The TEAOH and C₂₂₋₆₋₆ were employed as templates, which function sequentially and cooperatively in directing the bulk BEA core and lamellar MFI shell formation and fractioning of BEA into nanosponge-like structure in the zeolite composites. The variation on the acidity, domain sizes of the 2D lamellar MFI shell and bulk BEA core, and thus the textural properties of the BBLM zeolite samples were realized by simply modulating the content of the C₂₂₋₆₋₆ template in the synthesis. The concurrent occurrence of low acidity, small BEA crystallite sizes and mesoporosity in the BBLM zeolite composites enabled high catalytic activity and stability of BBLM zeolites in the reactions of benzyl alcohol with mesitylene. The conformation of ultra-thin 2D MFI nanosheets on BEA-core, in which straight micropore channels of MFI is normal to the BEA, allows a positive transmission way of reactant from the smaller micropore channel of MFI zeolite to the relatively larger one of BEA zeolite. The synthesis of BBLM core-shell bi-phase zeolite composites in single particles offers a pathway for tuning the physicochemical properties of zeolite materials, particularly beneficial for heterogeneous catalysis. The simple one-step dual template synthesis approach may prove to be a general platform for hierarchical zeolite composite design that could potentially be applicable to the other nanoporous materials when proper templates are selected.

Chapter 6: Conclusions and future work

6.1. Conclusions

Meso-/microporous zeolites combining the structural features of microporous zeolites with fast mass transport properties of mesoporous zeolites in a single material overcome the limitations of traditional microporous zeolites and enhance the catalyst utilization for reactions involving bulky molecules in important industrial emerging applications such as refinery of heavy petroleum residues^{191, 192} and processing of heavy bio-feedstocks^{193, 194}. Even though, significant progress has been made in synthesis of meso-/microporous zeolites during last decades¹¹⁴, but these individual methods have their own limitations in achieving the synthetic protocols involving few processing steps and designing the meso-/microporous zeolites with tunable textural and catalytic properties.

The most important strategy explored to design meso-/microporous zeolites with uniform pore size/shapes at nanometer scale is templating synthesis of lamellar meso-/microporous zeolite structures using a di-quaternary ammonium surfactant molecule.⁶¹ These ultrathin two dimensional (2D) zeolites having a large number of accessible catalytic sites on the external surface of the zeolitic nanosheets and low diffusion limitations due to the presence of mesopores can increase the activity, selectivity, and stability (catalyst lifetime) for reactions of bulky molecules such as methanol to gasoline conversion reactions.¹⁹⁵ The issue arises from the layered zeolite structure which collapses after calcination and template removal, therefore making the pillaring step necessary to keep the mesoporosity of the synthesized 2D lamellar

zeolite structure and its functionality in the above mentioned reactions.¹¹³ Thus, the suggested synthesis method is a multi-step and tedious process to carry out. In this dissertation we have tried to address these issues and suggest a new templating synthesis method to easily design meso-/microporous lamellar zeolite structures with various morphologies and tunable textural and catalytic properties in one-step.

First we developed a simple one-step dual template synthesis route for production of 2D lamellar MFI zeolite nanosheet assemblies. A small molecular template (tetrapropyl ammonium hydroxide, TPAOH) and a polyquaternary ammonium surfactant molecule ($[\text{C}_{22}\text{H}_{45}\text{-N}^+(\text{CH}_3)_2\text{-C}_6\text{H}_{12}\text{-N}^+(\text{CH}_3)_2\text{-C}_6\text{H}_{13}]\text{Br}_2$, C_{22-6-6}) were used as dual templates (chapter 2). The results showed that by simply tuning the molar ratio of these two templates ($\text{C}_{22-6-6}/\text{TPAOH}=10/0-10/20$) in the zeolite synthesis recipe, the morphology and porosity of these zeolite structures can be modulated. The molecular template TPAOH can be used as a secondary template to produce zeolite pillars between the MFI zeolite nanosheet assemblies primary guided by C_{22-6-6} template. The catalytic reaction of benzyl alcohol with mesitylene over the synthesized zeolite catalysts revealed the direct correlation between the zeolite textural properties adjusted by the molar ratio of the dual templates in the synthesis recipe and activity of the synthesized catalysts. The proposed one-step dual template synthesis method for production of meso-/microporous MFI zeolites can be followed as a general simple one-step approach for rational design of hierarchical catalysts for specific catalytic reactions involving bulky molecules.

After successful synthesis of 2D lamellar zeolite nanosheet assemblies using the proposed simple one-step dual template synthesis method by tuning the

concentration of the TPAOH in the synthesis recipe, we chose an opposite approach by changing the concentration of the C₂₂₋₆₋₆ while keeping the TPAOH concentration constant in the zeolite synthesis recipe (chapter 3). The results demonstrated that hybrid lamellar-bulk MFI (HLBM) zeolite structures are formed through the sequential and cooperative function of the two templates. The effect of several parameters such as concentration of C₂₂₋₆₋₆, hydrothermal synthesis time, and ageing temperature and time prior to the hydrothermal crystallization on HLBM formation was studied. The growth of HLBM zeolites as a function of the hydrothermal synthesis time showed that an amorphous zeolite phase is formed first using C₂₂₋₆₋₆ as the template which is converted to the crystalline bulk zeolite core at early stages of the crystallization under the assistance of TPAOH and finally the lamellar zeolite shell grows on the surface of the zeolite core by the help of C₂₂₋₆₋₆ as the template. The size of the lamellar shell and bulk core increase by increasing the C₂₂₋₆₋₆ concentration in the recipe and decreasing the time or temperature of ageing, respectively. The cooperative functionality of the dual templates in this proposed approach is very important since most of the previous attempts to produce meso-/microporous zeolites by mixture of molecular template and surfactant molecules has not been successful and resulted in production of crystalline microporous zeolite and amorphous mesoporous structures as two separate phases.^{56, 59, 60} Moreover, the synthesis of hybrid core-shell zeolite structures in one-step is a challenging task, so the zeolite core is usually produced first and then the zeolite shell is grown on it using different methods such as epitaxial growth.^{65, 74-76, 170} Furthermore, adjusting the zeolite core needs the synthesis of new zeolite particles with a different particle size.⁶⁵

Therefore, the proposed one-step dual template synthesis method used in this work can overcome the disadvantages of the available methods and be used to design hybrid core-shell zeolite composites and systematically tune their textural properties by adjusting the molar ratio of the dual templates and synthesis conditions in order to keep the potential application of the resulted meso-/microporous zeolite structures for different applications such as separation and catalysis as broad as possible.

Since catalysis is one of the most important applications of the meso-microporous zeolites especially when bulky molecules are involved and HLBM zeolite structures can be considered as transitional zeolite structures between 3D traditional microporous zeolites and completely 2D lamellar zeolite structures, so systematic study on variations in porosity, acidity, and consequent catalytic properties of these HLBM zeolites is necessary. Therefore, catalytic performance of the synthesized HLBM zeolite structures in acid-catalyzed reactions has been studied in chapter 3 by adding the aluminum to their synthesis recipe.

The higher catalytic efficiency of the meso-/microporous zeolites including lamellar zeolites is usually attributed to the facilitated mass transport and access to the active sites provided by their structural properties such as high mesoporosity compared to their microporous 3D zeolite counterparts.⁶⁹⁻⁷² However, the role of the external acid sites with variable strength formed during the zeolite formation on catalytic performance of the meso-/microporous zeolites has not been studied well. In chapter 4, a systematic study of the HLBM zeolites with tunable meso-/microporosity domain sizes achieved by a dual template assisted synthesis revealed that the catalytic selectivity of the zeolites for parallel etherification and alkylation reactions of benzyl

alcohol in mesitylene is tuned by the external surface area and external acidity of these catalysts. It has been shown that the fractions of external Brønsted acid sites are modulated when the domain sizes of the lamellar shell and bulk core are varied in HLBM zeolite structures. The cumulative poisoning of the external acid sites of the HLBM catalysts with base molecules of different sizes showed the presence of acid sites with different strength on the external environment of the HLBM zeolites which influenced the external etherification reaction, but not as significantly as the alkylation reaction. The evidence shown in this work for the role of external acid sites with variable strength on the selectivity of the meso-/microporous HLBM zeolites extends the scope of the observed catalytic behavior of meso-/microporous materials beyond those only reflecting transport effects and accessibility of active sites.

After production of different morphological structures of MFI zeolite (lamellar 2D nanosheets and HLBM structures) using the proposed one-step dual template synthesis in this work, we tried to investigate the possibility of extending this synthesis route for production of other zeolite composites containing two different types of zeolite frameworks in one-step by choosing proper templates. The core-shell bulk BEA nanosponge-lamellar MFI (BBLM) zeolite composites were innovatively synthesized (chapter 5) using the tetraethylammonium hydroxide (TEAOH) and C₂₂₋₆₋₆ as templates. TEOH and C₂₂₋₆₋₆ functioned sequentially and cooperatively in directing the bulk BEA core and lamellar MFI shell formation and fractioning of BEA into nanosponge-like structure in the BBLM zeolite composites. The variation on the acidity, domain sizes of the 2D lamellar MFI shell and bulk BEA core, and thus the textural properties of the BBLM zeolite samples were obtained by

simply adjusting the concentration of the C₂₂₋₆₋₆ template in the recipe. The occurrence of low acidity, small BEA crystallite sizes and mesoporosity in the BBLM zeolite composites enabled high catalytic activity and stability of BBLM zeolites in the reactions of benzyl alcohol with mesitylene compared to BEA or MFI as single catalysts or their physical mixture. It should be noted that, synthesis of zeolite composites of two or more different types of zeolites is not an easy task because of the difference in crystal lattice parameters and synthesis conditions (such as temperature and time) necessary for production of each type of zeolite framework. Therefore, the synthesis of composite zeolites of different types is usually carried out in multiple-steps.^{74, 76} Thus, the proposed simple one-step dual template synthesis approach can be used instead for production of meso-/microporous heterogeneous catalysts when a combination of structural and catalytic characteristics of single component catalysts and their synergistic effects are needed for high catalytic efficiency in the targeted reactions of bulky molecules.

6.2. Future work

Following the investigation results of dual template synthesis of meso-/microporous lamellar zeolites with different morphologies and tunable textural and catalytic properties reported in this dissertation, a number of new projects can be pursued, such as:

- 1) Further investigation on the effect of template structure on type and morphology of the synthesized zeolites and their catalytic performance. C₂₂₋₆₋₆ and TPAOH has been used as the dual templates for production of lamellar MFI nanosheet zeolite

assemblies in this work. C₂₂₋₆₋₆ and TPAOH were used as mesoporogen and microporogen, respectively and the effect of their molar ratio in the synthesis recipe on zeolite structural properties and catalytic performance was studied. Ryoo and coworkers have reported that the structure of the multi-ammonium surfactants such as N-N spacer length, number of ammonium groups, and hydrophobic tail length affect the lamellar MFI zeolite nanosheet formation.⁶³ For example, the thickness of the nanosheets can be increased by increasing the number of ammonium groups in the structure of the surfactant molecule. Moreover, TPAOH is only one of the common molecular templates for production of conventional microporous zeolites which is usually used to produce MFI zeolite and there are other templates such as TEOH, TMAOH, and TBAOH that can be used as the molecular template for the dual template synthesis method we have developed in this work to see if it is possible to control the type and morphology of the produced zeolite structure and as a result its meso-/microporosity and catalytic properties or not. TMAOH, TEOH, and TBAOH are usually used to produce microporous MOR, BEA, and FAU zeolites, respectively. Table 6.1 lists some of the possible combination of the dual templates that can be employed for this purpose.

Table 6.1. Examples of the different proposed dual template structures can be used for synthesis of lamellar zeolite nanosheet assemblies. The general synthesis recipe is $30\text{Na}_2\text{O}/1\text{Al}_2\text{O}_3/100\text{SiO}_2/10\text{mesoporogen}/x\text{microporogen}/4000\text{H}_2\text{O}/18\text{H}_2\text{SO}_4$, where x equals to 1, 2, 3, 5, 8, 12, and 20, respectively.

Studied effect	Microporogen	Mesoporogen
Microporogen type	$\begin{array}{c} \text{Me} \\ \\ \text{Me}-\text{N}^+-\text{OH}^- \\ \\ \text{Me} \end{array}$	$\begin{array}{c} \text{Me} \\ \\ \text{C}_{22}\text{H}_{45}-\text{N}^+ \left[\begin{array}{c} \text{Me} \\ \\ \text{C}_6\text{H}_{12}-\text{N}^+ \\ \\ \text{Me} \end{array} \right] \text{C}_6\text{H}_{13} \\ \\ \text{Me} \end{array} \quad n=1$
	$\begin{array}{c} \text{Et} \\ \\ \text{Et}-\text{N}^+-\text{OH}^- \\ \\ \text{Et} \end{array}$	$\begin{array}{c} \text{Me} \\ \\ \text{C}_{22}\text{H}_{45}-\text{N}^+ \left[\begin{array}{c} \text{Me} \\ \\ \text{C}_6\text{H}_{12}-\text{N}^+ \\ \\ \text{Me} \end{array} \right] \text{C}_6\text{H}_{13} \\ \\ \text{Me} \end{array} \quad n=1$
	$\begin{array}{c} \text{Bu} \\ \\ \text{Bu}-\text{N}^+-\text{OH}^- \\ \\ \text{Bu} \end{array}$	$\begin{array}{c} \text{Me} \\ \\ \text{C}_{22}\text{H}_{45}-\text{N}^+ \left[\begin{array}{c} \text{Me} \\ \\ \text{C}_6\text{H}_{12}-\text{N}^+ \\ \\ \text{Me} \end{array} \right] \text{C}_6\text{H}_{13} \\ \\ \text{Me} \end{array} \quad n=1$
Number of ammonium groups in mesoporogen	$\begin{array}{c} \text{Pr} \\ \\ \text{Pr}-\text{N}^+-\text{OH}^- \\ \\ \text{Pr} \end{array}$	$\begin{array}{c} \text{Me} \\ \\ \text{C}_{22}\text{H}_{45}-\text{N}^+ \left[\begin{array}{c} \text{Me} \\ \\ \text{C}_6\text{H}_{12}-\text{N}^+ \\ \\ \text{Me} \end{array} \right] \text{C}_6\text{H}_{13} \\ \\ \text{Me} \end{array} \quad n=0$
	$\begin{array}{c} \text{Pr} \\ \\ \text{Pr}-\text{N}^+-\text{OH}^- \\ \\ \text{Pr} \end{array}$	$\begin{array}{c} \text{Me} \\ \\ \text{C}_{22}\text{H}_{45}-\text{N}^+ \left[\begin{array}{c} \text{Me} \\ \\ \text{C}_6\text{H}_{12}-\text{N}^+ \\ \\ \text{Me} \end{array} \right] \text{C}_6\text{H}_{13} \\ \\ \text{Me} \end{array} \quad n=2$
	$\begin{array}{c} \text{Pr} \\ \\ \text{Pr}-\text{N}^+-\text{OH}^- \\ \\ \text{Pr} \end{array}$	$\begin{array}{c} \text{Me} \\ \\ \text{C}_{22}\text{H}_{45}-\text{N}^+ \left[\begin{array}{c} \text{Me} \\ \\ \text{C}_6\text{H}_{12}-\text{N}^+ \\ \\ \text{Me} \end{array} \right] \text{C}_6\text{H}_{13} \\ \\ \text{Me} \end{array} \quad n=3$

Me, Et, Pr, and Bu stand for methyl, ethyl, propyl, and butyl, respectively.

- 2) Fabrication of bulk core-lamellar shell composites of two different zeolites in one-step in order to combine the unique properties of each of them in a single material with adjustable and multi-functional properties. Here in this work the

developed one-step dual template synthesis method has been used for production of MFI/MFI and BEA/MFI zeolite composites only. According to the Structural Commission of the IZA report^{196, 197}, there are 213 different zeolite framework structures, thus there is a wide range of options to choose for synthesis of various hybrid zeolite materials containing two different types of zeolites. For example, beside MFI and BEA, MOR and FAU are also among the most important industrial catalysts¹⁹⁸, so simple one-step synthesis of MOR/MFI and FAU/MFI composites can be investigated by choosing proper molecular zeolite templates in combination with C₂₂₋₆₋₆ surfactant as dual templates. For example TMAOH and TBAOH can be examined as molecular templates for production of MOR and FAU, respectively. The application of these new synthesized composites can be assessed for separation processes (such as membrane synthesis) and catalysis (by choosing proper probing reactions).

- 3) Extending the applications of the synthesized BEA/MFI composites using dual template synthesis method developed in this work. The benzyl alcohol conversion in mesitylene was studied as an example of alkylation reactions over the synthesized BEA/MFI catalysts throughout this research work. It is necessary to find more applications for these synthesized catalysts to confirm the significance of the proposed one-step dual template synthesis used for their fabrication. For example, conversion of abundant and cheap bio-feedstocks such as glucose to more useful bio-chemicals such as 5-(ethoxymethyl)furfural (EMF) over these BEA/MFI composites can be studied. One of the most important applications of EMF is using it as a biofuel alternative for gasoline and diesel for transportation purposes.^{199, 200} EMF is usually produced from fructose or

glucose in multi-step processes using different types of catalysts.²⁰¹ For instance, tin-containing BEA zeolite (Sn-BEA) can be used as a catalyst for isomerization of glucose to fructose and Amberlyst 131 catalyst to convert fructose to EMF in ethanol, respectively.¹⁹⁹ The simple one-step dual template synthesis recipe for BEA/MFI composite suggested in this work can be modified to include Sn as precursor and as a result Sn-BEA/MFI composites can be synthesized. Then, the resulting composite can be used for one-pot conversion of glucose to EMF in ethanol as depicted in Figure 6.1. Theoretically it should be possible to convert the glucose to fructose over Sn-BEA core of the composite zeolite and then convert the fructose to EMF over acid sites of the lamellar MFI shell in the synthesized composite, but experimental results need to be obtained to confirm this possibility.

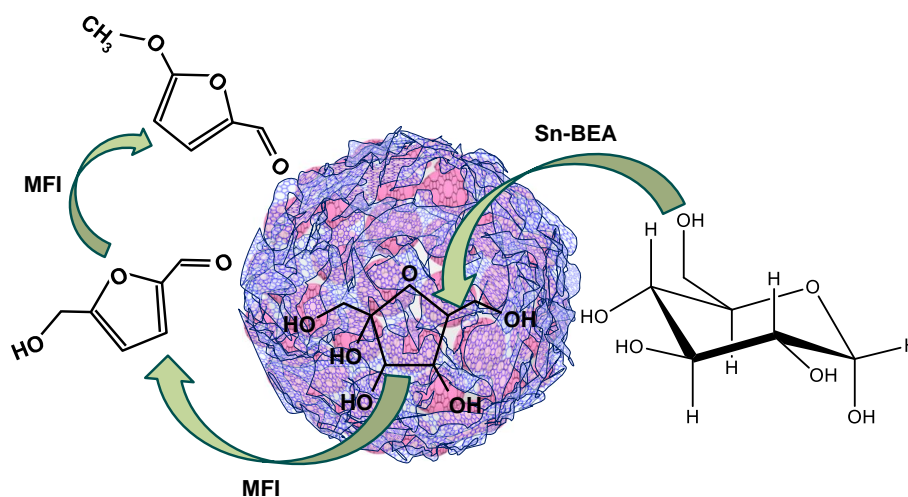


Figure 6.1. Schematic representation of one-pot synthesis of EMF from glucose over Sn-BEA/MFI zeolite composite fabricated by one-step dual template synthesis method. Red circles and blue sheets depict the Sn-BEA zeolite and lamellar MFI zeolite structures, respectively.

References

1. Cundy, C. S.; Cox, P. A., The Hydrothermal Synthesis of Zeolites: History and Development from the Earliest Days to the Present Time. *Chem. Rev.* **2003**, 103, (3), 663-702.
2. Davis, M. E., Ordered porous materials for emerging applications. *Nature* **2002**, 417, (6891), 813-821.
3. Zaarour, M.; Dong, B.; Naydenova, I.; Retoux, R.; Mintova, S., Progress in zeolite synthesis promotes advanced applications. *Micropor. Mesopor. Mat.* **2014**, 189, 11-21.
4. Chen, L.-H.; Li, X.-Y.; Rooke, J. C.; Zhang, Y.-H.; Yang, X.-Y.; Tang, Y.; Xiao, F.-S.; Su, B.-L., Hierarchically structured zeolites: synthesis, mass transport properties and applications. *J. Mater. Chem.* **2012**, 22, (34), 17381-17403.
5. Holm, M. S.; Taarning, E.; Egeblad, K.; Christensen, C. H., Catalysis with hierarchical zeolites. *Catal. Today* **2011**, 168, (1), 3-16.
6. Szostak, R., *Molecular Sieves: Principles of Synthesis and Identification*. 2nd edition, Blackie Academic and Professional, London 1998.
7. Byrappa, K.; Yoshimura, M., *Handbook of hydrothermal technology*. 2nd edition, William Andrew: 2012.
8. Möller, K.; Bein, T., Mesoporosity - a new dimension for zeolites. *Chem. Soc. Rev.* **2013**, 42, (9), 3689-3707.
9. Roth, W. J.; Nachtigall, P.; Morris, R. E.; Čejka, J., Two-Dimensional Zeolites: Current Status and Perspectives. *Chem. Rev.* **2014**, 114, (9), 4807-4837.

10. Qinhu, X.; Aizhen, Y., Hydrothermal synthesis and crystallization of zeolites. *Prog. Cryst. Growth Ch.* **1991**, 21, (1), 29-70.
11. Moliner, M.; Rey, F.; Corma, A., Towards the Rational Design of Efficient Organic Structure-Directing Agents for Zeolite Synthesis. *Angew. Chem. Int. Ed.* **2013**, 52, (52), 13880-13889.
12. Davis, M. E.; Lobo, R. F., Zeolite and molecular sieve synthesis. *Chem. Mater.* **1992**, 4, (4), 756-768.
13. Feijen, E. J. P.; Martens, J. A.; Jacobs, P. A., Zeolites and their Mechanism of Synthesis. In *Studies in Surface Science and Catalysis*, J. Weitkamp, H. G. K. H. P.; Hölderich, W., Eds. Elsevier: 1994; Vol. 84, pp 3-21.
14. Kim, K.; Ryoo, R.; Jang, H. D.; Choi, M., Spatial distribution, strength, and dealumination behavior of acid sites in nanocrystalline MFI zeolites and their catalytic consequences. *J. Catal.* **2012**, 288, 115-123.
15. Castaño, P.; Elordi, G.; Olazar, M.; Aguayo, A. T.; Pawelec, B.; Bilbao, J., Insights into the coke deposited on HZSM-5, H β and HY zeolites during the cracking of polyethylene. *Appl. Catal. B: Environmental* **2011**, 104, (1-2), 91-100.
16. Zhang, X. Y.; Liu, D. X.; Xu, D. D.; Asahina, S.; Cychoz, K. A.; Agrawal, K. V.; Al Wahedi, Y.; Bhan, A.; Al Hashimi, S.; Terasaki, O.; Thommes, M.; Tsapatsis, M., Synthesis of Self-Pillared Zeolite Nanosheets by Repetitive Branching. *Science* **2012**, 336, (6089), 1684-1687.
17. Abelló, S.; Bonilla, A.; Pérez-Ramírez, J., Mesoporous ZSM-5 zeolite catalysts prepared by desilication with organic hydroxides and comparison with NaOH leaching. *Appl. Catal. A: General* **2009**, 364, (1-2), 191-198.

18. Kim, J.; Park, W.; Ryoo, R., Surfactant-Directed Zeolite Nanosheets: A High-Performance Catalyst for Gas-Phase Beckmann Rearrangement. *ACS Catal.* **2011**, 1, (4), 337-341.
19. Yilmaz, B.; Muller, U., Catalytic Applications of Zeolites in Chemical Industry. *Top. Catal.* **2009**, 52, (6-7), 888-895.
20. Cejka, J.; Centi, G.; Perez-Pariente, J.; Roth, W. J., Zeolite-based materials for novel catalytic applications: Opportunities, perspectives and open problems. *Catal. Today* **2012**, 179, (1), 2-15.
21. Eilertsen, E. A.; Ogino, I.; Hwang, S. J.; Rea, T.; Yeh, S.; Zones, S. I.; Katz, A., Nonaqueous Fluoride/Chloride Anion-Promoted Delamination of Layered Zeolite Precursors: Synthesis and Characterization of UCB-2. *Chem. Mater.* **2011**, 23, 5404-5408.
22. Primo, A.; Garcia, H., Zeolites as catalysts in oil refining. *Chem. Soc. Rev.* **2014**, 43, (22), 7548-7561.
23. Agrawal, K. V. Dispersible Exfoliated Zeolite Nanosheets and Their Application in High Performance Zeolite Membrane. University of Minnesota, 2013.
24. Choi, J.; Lai, Z.; Ghosh, S.; Beving, D. E.; Yan, Y.; Tsapatsis, M., Layer-by-Layer Deposition of Barrier and Permselective c-Oriented-MCM-22/Silica Composite Films. *Ind. Eng. Chem. Res.* **2007**, 46, (22), 7096-7106.
25. Lai, Z.; Bonilla, G.; Diaz, I.; Nery, J. G.; Sujaoti, K.; Amat, M. A.; Kokkoli, E.; Terasaki, O.; Thompson, R. W.; Tsapatsis, M.; Vlachos, D. G., Microstructural Optimization of a Zeolite Membrane for Organic Vapor Separation. *Science* **2003**, 300, (5618), 456-460.

26. Kondo, M.; Komori, M.; Kita, H.; Okamoto, K.-i., Tubular-type pervaporation module with zeolite NaA membrane. *J. Membr. Sci.* **1997**, 133, (1), 133-141.
27. Tsapatsis, M., Molecular sieves in the nanotechnology era. *AIChE J.* **2002**, 48, (4), 654-660.
28. Lin, C. C. H.; Dambrowitz, K. A.; Kuznicki, S. M., Evolving applications of zeolite molecular sieves. *Can. J. Chem. Eng.* **2012**, 90, (2), 207-216.
29. Mintova, S.; Jaber, M.; Valtchev, V., Nanosized microporous crystals: emerging applications. *Chem. Soc. Rev.* **2015**, 44, (20), 7207-7233.
30. Corma, A., From microporous to mesoporous molecular sieve materials and their use in catalysis. *Chem. Rev.* **1997**, 97, (6), 2373-2419.
31. Groen, J. C.; Abelló, S.; Villaescusa, L. A.; Pérez-Ramírez, J., Mesoporous beta zeolite obtained by desilication. *Micropor. Mesopor. Mat.* **2008**, 114, (1-3), 93-102.
32. van Donk, S.; Janssen, A. H.; Bitter, J. H.; de Jong, K. P., Generation, characterization, and impact of mesopores in zeolite catalysts. *Catal. Rev. -Sci. Eng.* **2003**, 45, (2), 297-319.
33. Egeblad, K.; Christensen, C. H.; Kustova, M., Templating mesoporous zeolites. *Chem. Mater.* **2008**, 20, (3), 946-960.
34. Möller, K.; Yilmaz, B.; Jacubinas, R. M.; Muller, U.; Bein, T., One-Step Synthesis of Hierarchical Zeolite Beta via Network Formation of Uniform Nanocrystals. *J. Am. Chem. Soc.* **2011**, 133, (14), 5284-5295.
35. Tao, Y.; Kanoh, H.; Abrams, L.; Kaneko, K., Mesopore-modified zeolites: preparation, characterization, and applications. *Chem. Rev.* **2006**, 106, (3), 896-910.

36. Aguadoa, J.; Serrano, D. P.; Rodriguez, J. M., Zeolite Beta with hierarchical porosity prepared from organofunctionalized seeds. *Micropor. Mesopor. Mat.* **2008**, 115, (3), 504-513.
37. Choi, M.; Cho, H. S.; Srivastava, R.; Venkatesan, C.; Choi, D. H.; Ryoo, R., Amphiphilic organosilane-directed synthesis of crystalline zeolite with tunable mesoporosity. *Nat. Mater.* **2006**, 5, (9), 718-723.
38. Christensen, C. H.; Johannsen, K.; Schmidt, I.; Christensen, C. H., Catalytic benzene alkylation over mesoporous zeolite single crystals: Improving activity and selectivity with a new family of porous materials. *J. Am. Chem. Soc.* **2003**, 125, (44), 13370-13371.
39. Shetti, V. N.; Kim, J.; Srivastava, R.; Choi, M.; Ryoo, R., Assessment of the mesopore wall catalytic activities of MFI zeolite with mesoporous/microporous hierarchical structures. *J. Catal.* **2008**, 254, (2), 296-303.
40. Corma, A.; Diaz, U.; Fornes, V.; Jorda, J. L.; Domine, M.; Rey, F., Ti/ITQ-2, a new material highly active and selective for the epoxidation of olefins with organic hydroperoxides, *Chem. Commun.* **1999**, 779-780.
41. Cambor, M. A.; Corma, A.; Diaz-Cabanas, M. J.; Baerlocher, C., Synthesis and structural characterization of MWW type zeolite ITQ-1, the pure silica analog of MCM-22 and SSZ-25. *J. Phys. Chem. B* **1998**, 102, (1), 44-51.

42. Li, J. Z.; Wei, Y. X.; Liu, G. Y.; Qi, Y.; Tian, P.; Li, B.; He, Y. L.; Liu, Z. M., Comparative study of MTO conversion over SAPO-34, H-ZSM-5 and H-ZSM-22: Correlating catalytic performance and reaction mechanism to zeolite topology, *Catal. Today* 2011, 171, 221-228.
43. Celik, F. E.; Kim, T.-J.; Bell, A. T., Effect of zeolite framework type and Si/Al ratio on dimethoxymethane carbonylation. *J. Catal.* **2010**, 270, (1), 185-195.
44. Martinez, C.; Corma, A., Inorganic molecular sieves: Preparation, modification and industrial application in catalytic processes. *Coord. Chem. Rev.* **2011**, 255, (13-14), 1558-1580.
45. Milina, M.; Mitchell, S.; Michels, N.-L.; Kevlin, J.; Pérez-Ramírez, J., Interdependence between porosity, acidity, and catalytic performance in hierarchical ZSM-5 zeolites prepared by post-synthetic modification. *J. Catal.* **2013**, 308, (0), 398-407.
46. Martens, J. A.; Verboekend, D.; Thomas, K.; Vanbutsele, G.; Gilson, J. P.; Pérez Ramírez, J., Hydroisomerization of Emerging Renewable Hydrocarbons using Hierarchical Pt/H-ZSM-22 Catalyst, *ChemSusChem* **2013**, 6, 421-425.
47. Verboekend, D.; Keller, T. C.; Mitchell, S.; Pérez-Ramírez, J., Hierarchical FAU- and LTA-Type Zeolites by Post-Synthetic Design: A New Generation of Highly Efficient Base Catalysts. *Adv. Funct. Mater.* **2013**, 23, (15), 1923-1934.
48. Serrano, D. P.; Escola, J. M.; Pizarro, P., Synthesis strategies in the search for hierarchical zeolites. *Chem. Soc. Rev.* **2013**, 42, (9), 4004-4035.

49. Antoniou, M. K.; Diamanti, E. K.; Enotiadis, A.; Policicchio, A.; Dimos, K.; Ciuchi, F.; Maccallini, E.; Gournis, D.; Agostino, R. G., Methane storage in zeolite-like carbon materials. *Micropor. Mesopor.Mat.* **2014**, 188, 16-22.
50. R. Singh, P. K. D., MFI: a case study of zeolite synthesis. Scott M. Auerbach, Kathleen A. Carrado, Prabir K. Dutta (Eds.), *Handbook of Zeolite Science & Technology* (Ed.), Marcel Dekker, Inc. **2003**, Chapter 2.
51. Garcia, R.; Gomez-Hortiguela, L.; Diaz, I.; Sastre, E.; Perez-Pariente, J., Synthesis of materials containing ferrierite layers using quinuclidine and 1-benzyl-1-methylpyrrolidine as structure-directing agents. an experimental and computational study. *Chem. Mater.* **2008**, 20, (3), 1099-1107.
52. Pinar, A. B.; Márquez-Álvarez, C.; Grande-Casas, M.; Pérez-Pariente, J., Template-controlled acidity and catalytic activity of ferrierite crystals. *J. Catal.* **2009**, 263, (2), 258-265.
53. Pinar, A. B.; Gomez-Hortiguela, L.; Perez-Pariente, J., Cooperative Structure Directing Role of the Cage-Forming Tetramethylammonium Cation and the Bulkier Benzylmethylpyrrolidinium in the Synthesis of Zeolite Ferrierite. *Chem. Mater.* **2007**, 19, (23), 5617-5626.
54. Pérez-Pariente, J., García, R., Gómez-Hortiguela, L. and Pinar, A. B., Co-template in synthesis of zeolites. In *Zeolites and Catalysis: Synthesis, Reactions and Applications*, J. Čejka, A. C. a. S. Z., Ed. Wiley-VCH Verlag GmbH & Co. KGaA, Weinheim, Germany: 2010; pp 107-129.

55. Kresge, C. T.; Leonowicz, M. E.; Roth, W. J.; Vartuli, J. C.; Beck, J. S., Ordered mesoporous molecular sieves synthesized by a liquid-crystal template mechanism. *Nature* **1992**, 359, (6397), 710-712.
56. Guo, W.; Xiong, C.; Huang, L.; Li, Q., Synthesis and characterization of composite molecular sieves comprising zeolite Beta with MCM-41 structures. *J. Mater. Chem.* **2001**, 11, (7), 1886-1890.
57. Karlsson, A.; Stocker, M.; Schmidt, R., Composites of micro- and mesoporous materials: simultaneous syntheses of MFI/MCM-41 like phases by a mixed template approach. *Micropor. Mesopor. Mat.* **1999**, 27, (2-3), 181-192.
58. Wu, L. L.; Degirmenci, V.; Magusin, P.; Szyja, B. M.; Hensen, E. J. M., Dual template synthesis of a highly mesoporous SSZ-13 zeolite with improved stability in the methanol-to-olefins reaction. *Chem. Commun.* **2012**, 48, (76), 9492-9494.
59. Chal, R.; Gerardin, C.; Bulut, M.; van Donk, S., Overview and Industrial Assessment of Synthesis Strategies towards Zeolites with Mesopores. *Chemcatchem* **2011**, 3, (1), 67-81.
60. Huang, L.; Guo, W.; Deng, P.; Xue, Z.; Li, Q., Investigation of Synthesizing MCM-41/ZSM-5 Composites. *J. Phys. Chem. B* **2000**, 104, (13), 2817-2823.
61. Choi, M.; Na, K.; Kim, J.; Sakamoto, Y.; Terasaki, O.; Ryoo, R., Stable single-unit-cell nanosheets of zeolite MFI as active and long-lived catalysts. *Nature* **2009**, 461, (7265), 246-249.
62. Kim, J.; Choi, M.; Ryoo, R., Effect of mesoporosity against the deactivation of MFI zeolite catalyst during the methanol-to-hydrocarbon conversion process. *J. Catal.* **2010**, 269, (1), 219-228.

63. Park, W.; Yu, D.; Na, K.; Jelfs, K. E.; Slater, B.; Sakamoto, Y.; Ryoo, R., Hierarchically Structure-Directing Effect of Multi-Ammonium Surfactants for the Generation of MFI Zeolite Nanosheets. *Chem. Mater.* **2011**, 23, (23), 5131-5137.
64. Jung, J.; Jo, C.; Cho, K.; Ryoo, R., Zeolite nanosheet of a single-pore thickness generated by a zeolite-structure-directing surfactant. *J. Mater. Chem.* **2012**, 22, (11), 4637-4640.
65. Kim, W.-g.; Zhang, X.; Lee, J. S.; Tsapatsis, M.; Nair, S., Epitaxially Grown Layered MFI–Bulk MFI Hybrid Zeolitic Materials. *ACS Nano* **2012**, 6, (11), 9978-9988.
66. Shirazi, L.; Jamshidi, E.; Ghasemi, M. R., The effect of Si/Al ratio of ZSM-5 zeolite on its morphology, acidity and crystal size. *Cryst. Res. Technol.* **2008**, 43, (12), 1300-1306.
67. Smirniotis, P. G.; Zhang, W., Effect of the Si/Al Ratio and of the Zeolite Structure on the Performance of Dealuminated Zeolites for the Reforming of Hydrocarbon Mixtures. *Ind. Eng. Chem. Res.* **1996**, 35, (9), 3055-3066.
68. Xu, B.; Bordiga, S.; Prins, R.; van Bokhoven, J. A., Effect of framework Si/Al ratio and extra-framework aluminum on the catalytic activity of Y zeolite. *Appl. Catal. A: General* **2007**, 333, (2), 245-253.
69. Li, X. F.; Prins, R.; van Bokhoven, J. A., Synthesis and characterization of mesoporous mordenite. *J. Catal.* **2009**, 262, (2), 257-265.
70. Narender, N.; Krishna Mohan, K. V. V.; Kulkarni, S. J.; Ajit Kumar Reddy, I., Liquid phase benzylation of benzene and toluene with benzyl alcohol over modified zeolites. *Catal. Commun.* **2006**, 7, 583-588.

71. Sun, Y. Y.; Prins, R., Hydrodesulfurization of 4,6-Dimethyldibenzothiophene over Noble Metals Supported on Mesoporous Zeolites. *Angew. Chem. Int. Ed.* **2008**, 47, (44), 8478-8481.
72. Thibault-Starzyk, F.; Stan, I.; Abelló, S.; Bonilla, A.; Thomas, K.; Fernandez, C.; Gilson, J.-P.; Pérez-Ramírez, J., Quantification of enhanced acid site accessibility in hierarchical zeolites – The accessibility index. *J. Catal.* **2009**, 264, (1), 11-14.
73. Seo, Y.; Cho, K.; Jung, Y.; Ryoo, R., Characterization of the Surface Acidity of MFI Zeolite Nanosheets by ³¹P NMR of Adsorbed Phosphine Oxides and Catalytic Cracking of Decalin. *ACS Catal.* **2013**, 3, (4), 713-720.
74. Bouizi, Y.; Diaz, I.; Rouleau, L.; Valtchev, V. P., Core–Shell Zeolite Microcomposites. *Adv. Funct. Mater.* **2005**, 15, (12), 1955-1960.
75. Bouizi, Y.; Majano, G.; Mintova, S.; Valtchev, V., Beads Comprising a Hierarchical Porous Core and a Microporous Shell. *J. Phys. Chem. C* **2007**, 111, (12), 4535-4542.
76. Bouizi, Y.; Rouleau, L.; Valtchev, V. P., Factors Controlling the Formation of Core–Shell Zeolite–Zeolite Composites. *Chem. Mater.* **2006**, 18, (20), 4959-4966.
77. Song, Z.; Huang, Y.; Wang, L.; Li, S.; Yu, M., Composite 5A zeolite with ultrathin porous TiO₂ coating for selective gas adsorption. *Chem. Commun.* **2015**, 51, (2), 373-375.
78. Cavalcante, C. L., Jr.; Ruthven, D. M., Adsorption of Branched and Cyclic Paraffins in Silicalite. 2. Kinetics. *Ind. Eng. Chem. Res.* **1995**, 34, (1), 185-191.
79. Pirngruber, G. D.; Laroche, C.; Maricar-Pichon, M.; Rouleau, L.; Bouizi, Y.; Valtchev, V., Core–shell zeolite composite with enhanced selectivity for the

- separation of branched paraffin isomers. *Micropor. Mesopor. Mat.* **2013**, 169, 212-217.
80. Cejka, J., Perspectives of micro/mesoporous composites in catalysis. *Catal. Rev.* **2007**, 49, 457-509.
81. Xie, Z.; Liu, Z.; Wang, Y.; Yang, Q.; Xu, L.; Ding, W., An Overview of Recent Development in Composite Catalysts from Porous Materials for Various Reactions and Processes. *Int. J. Mol. Sci.* **2010**, 11, (5), 2152-2187.
82. Centi, G.; Perathoner, S., Creating and mastering nano-objects to design advanced catalytic materials. *Coord. Chem. Rev.* **2011**, 255, (13–14), 1480-1498.
83. Zheng, J.; Zeng, Q.; Yi, Y.; Wang, Y.; Ma, J.; Qin, B.; Zhang, X.; Sun, W.; Li, R., The hierarchical effects of zeolite composites in catalysis. *Catal. Today* **2011**, 168, (1), 124-132.
84. Kong, D.; Zheng, J.; Yuan, X.; Wang, Y.; Fang, D., Fabrication of core/shell structure via overgrowth of ZSM-5 layers on mordenite crystals. *Micropor. Mesopor. Mat.* **2009**, 119, (1–3), 91-96.
85. Lauridant, N.; Jean Daou, T.; Arnold, G.; Patarin, J.; Faye, D., MFI*BEA hybrid coating on aluminum alloys. *Micropor. Mesopor. Mat.* **2013**, 166, (0), 79-85.
86. Zheng, J.; Zhang, X.; Wang, Y.; Bai, Y.; Sun, W.; Li, R., Synthesis and catalytic performance of a bi-phase core-shell zeolite composite. *J. Porous Mat.* **2009**, 16, (6), 731-736.
87. Li, H.; Jin, J. J.; Wu, W.; Chen, C. C.; Li, L.; Li, Y. S.; Zhao, W. R.; Gu, J. L.; Chen, G. R.; Shi, J. L., Synthesis of a hierarchically macro-/mesoporous zeolite based on a micro-emulsion mechanism. *J. Mater. Chem.* **2011**, 21, (48), 19395-19401.

88. Liu, F. J.; Willhammar, T.; Wang, L.; Zhu, L. F.; Sun, Q.; Meng, X. J.; Carrillo-Cabrera, W.; Zou, X. D.; Xiao, F. S., ZSM-5 Zeolite Single Crystals with b-Axis-Aligned Mesoporous Channels as an Efficient Catalyst for Conversion of Bulky Organic Molecules. *J. Am. Chem. Soc.* **2012**, 134, (10), 4557-4560.
89. Na, K.; Choi, M.; Ryoo, R., Cyclic diquatery ammoniums for nanocrystalline BEA, MTW and MFI zeolites with intercrystalline mesoporosity. *J. Mater. Chem.* **2009**, 19, (37), 6713-6719.
90. Rinaldi, R.; Schuth, F., Design of solid catalysts for the conversion of biomass. *Energ. Environ. Sci.* **2009**, 2, (6), 610-626.
91. Sheldon, R. A.; Downing, R. S., Heterogeneous catalytic transformations for environmentally friendly production. *Appl. Catal. A: General* **1999**, 189, (2), 163-183.
92. Perez-Ramirez, J.; Christensen, C. H.; Egeblad, K.; Christensen, C. H.; Groen, J. C., Hierarchical zeolites: enhanced utilisation of microporous crystals in catalysis by advances in materials design. *Chem. Soc. Rev.* **2008**, 37, (11), 2530-2542.
93. Li, Y. N.; Liu, S. L.; Zhang, Z. K.; Me, S. J.; Zhu, X. X.; Xu, L. Y., Aromatization and isomerization of 1-hexene over alkali-treated HZSM-5 zeolites: Improved reaction stability. *Appl. Catal. A: General* **2008**, 338, (1-2), 100-113.
94. Srivastava, R.; Choi, M.; Ryoo, R., Mesoporous materials with zeolite framework: remarkable effect of the hierarchical structure for retardation of catalyst deactivation. *Chem. Commun.* **2006**, (43), 4489-4491.

95. Groen, J. C.; Sano, T.; Moulijn, J. A.; Perez-Ramirez, J., Alkaline-mediated mesoporous mordenite zeolites for acid-catalyzed conversions. *J. Catal.* **2007**, *251*, (1), 21-27.
96. Perez-Ramirez, J.; Abello, S.; Bonilla, A.; Groen, J. C., Tailored Mesoporosity Development in Zeolite Crystals by Partial Detemplation and Desilication. *Adv. Funct. Mater.* **2009**, *19*, (1), 164-172.
97. Corma, A.; Fornes, V.; Pergher, S. B.; Maesen, T. L. M.; Buglass, J. G., Delaminated zeolite precursors as selective acidic catalysts. *Nature* **1998**, *396*, (6709), 353-356.
98. Barth, J. O.; Jentys, A.; Kornatowski, J.; Lercher, J. A., Control of acid-base properties of new nanocomposite derivatives of MCM-36 by mixed oxide pillaring. *Chem. Mater.* **2004**, *16*, (4), 724-730.
99. Maheshwari, S.; Jordan, E.; Kumar, S.; Bates, F. S.; Penn, R. L.; Shantz, D. F.; Tsapatsis, M., Layer structure preservation during swelling, pillaring, and exfoliation of a zeolite precursor. *J. Am. Chem. Soc.* **2008**, *130*, (4), 1507-1516.
100. Fan, W.; Snyder, M. A.; Kumar, S.; Lee, P. S.; Yoo, W. C.; McCormick, A. V.; Penn, R. L.; Stein, A.; Tsapatsis, M., Hierarchical nanofabrication of microporous crystals with ordered mesoporosity. *Nat. Mater.* **2008**, *7*, (12), 984-991.
101. Jacobsen, C. J. H.; Madsen, C.; Houzvicka, J.; Schmidt, I.; Carlsson, A., Mesoporous zeolite single crystals. *J. Am. Chem. Soc.* **2000**, *122*, (29), 7116-7117.
102. Groen, J. C.; Bach, T.; Ziese, U.; Donk, A.; de Jong, K. P.; Moulijn, J. A.; Perez-Ramirez, J., Creation of hollow zeolite architectures by controlled desilication of Al-zoned ZSM-5 crystals. *J. Am. Chem. Soc.* **2005**, *127*, (31), 10792-10793.

103. Wang, Q. L.; Giannetto, G.; Guisnet, M., Dealumination of Y-zeolites with ammonium hexafluorosilicate-effect of washing on the hydrothermal stability. *Zeolites* **1990**, 10, (4), 301-303.
104. Jacobs, P. A. Martens., J. A., *Synthesis of high-silica aluminosilicate zeolites*. 1987; Vol. 2.
105. Bonilla, G.; Díaz, I.; Tsapatsis, M.; Jeong, H.-K.; Lee, Y.; Vlachos, D. G., Zeolite (MFI) Crystal Morphology Control Using Organic Structure-Directing Agents. *Chem. Mater.* **2004**, 16, (26), 5697-5705.
106. Chaikittisilp, W.; Davis, M. E.; Okubo, T., TPA⁺-Mediated Conversion of Silicon Wafer into Preferentially-Oriented MFI Zeolite Film under Steaming. *Chem. Mater.* **2007**, 19, (17), 4120-4122.
107. Cho, H. S.; Ryoo, R., Synthesis of ordered mesoporous MFI zeolite using CMK carbon templates. *Micropor. Mesopor. Mater.* **2012**, 151, (0), 107-112.
108. Agger, J. R.; Hanif, N.; Cundy, C. S.; Wade, A. P.; Dennison, S.; Rawlinson, P. A.; Anderson, M. W., Silicalite Crystal Growth Investigated by Atomic Force Microscopy. *J. Am. Chem. Soc.* **2002**, 125, (3), 830-839.
109. Pham, T. C. T.; Kim, H. S.; Yoon, K. B., Growth of Uniformly Oriented Silica MFI and BEA Zeolite Films on Substrates. *Science* **2011**, 334, (6062), 1533-1538.
110. Cheung, P.; Bhan, A.; Sunley, G.; Law, D.; Iglesia, E., Site requirements and elementary steps in dimethyl ether carbonylation catalyzed by acidic zeolites. *J. Catal.* **2007**, 245, (1), 110-123.

111. Cheung, P.; Bhan, A.; Sunley, G. J.; Iglesia, E., Selective carbonylation of dimethyl ether to methyl acetate catalyzed by acidic zeolites. *Angew. Chem. Int. Ed.* **2006**, 45, (10), 1617-1620.
112. Liu, D.; Bhan, A.; Tsapatsis, M.; Al Hashimi, S., Catalytic Behavior of Brønsted Acid Sites in MWW and MFI Zeolites with Dual Meso- and Microporosity. *ACS Catal.* **2011**, 1, (1), 7-17.
113. Na, K.; Choi, M.; Park, W.; Sakamoto, Y.; Terasaki, O.; Ryoo, R., Pillared MFI Zeolite Nanosheets of a Single-Unit-Cell Thickness. *J. Am. Chem. Soc.* **2010**, 132, (12), 4169-4177.
114. Na, K.; Choi, M.; Ryoo, R., Recent advances in the synthesis of hierarchically nanoporous zeolites. *Micropor. Mesopor. Mater.* **2013**, 166, (0), 3-19.
115. Sing, K. S. W.; Everett, D. H.; Haul, R. A. W.; Moscou, L.; Pierotti, R. A.; Rouquerol, J.; Siemieniewska, T., Reporting physisorption data for gas solid systems with special reference to the determination of surface-area and porosity (recommendations 1984). *Pure Appl. Chem.* **1985**, 57, (4), 603-619.
116. Thommes, M., Textural Characterization of Zeolite and Ordered Mesoporous Materials by Physical Adsorption. In *Introduction to Zeolite Science and Practice (3rd revised Edition)*, Cejka, J., van Bekkum, H., Corma, A., Schüth, F., Ed. Elsevier: 2007; pp 495-525.
117. Groen, J. C.; Peffer, L. A. A.; Pérez-Ramírez, J., Pore size determination in modified micro- and mesoporous materials. Pitfalls and limitations in gas adsorption data analysis. *Micropor. Mesopor. Mat.* **2003**, 60, (1-3), 1-17.

118. Mitchell, S.; Michels, N. L.; Kumze, K.; Pérez-Ramírez, J., Visualization of hierarchically structured zeolite bodies from macro to nano length scales. *Nature Chem.* **2012**, 861, (4), 825-831.
119. Pérez-Ramírez, J.; Verboekend, D.; Bonilla, A.; Abelló, S., Zeolite Catalysts with Tunable Hierarchy Factor by Pore-Growth Moderators. *Adv. Funct. Mater.* **2009**, 19, (24), 3972-3979.
120. Emeis, C. A., Determination of Integrated Molar Extinction Coefficient for Infrared Absorption Bands of Pyridine Adsorbed on Solid Acid Catalysts. *J. Catal.* **1993**, 141, 347-354.
121. Guisnet, M.; Ayrault, P.; Coutanceau, C.; Fernanda Alvarez, M.; Datka, J., Acid properties of dealuminated beta zeolites studied by IR spectroscopy. *J. Chem. Soc. Faraday Trans.* **1997**, 93, (8), 1661-1665.
122. Aiello, R.; Crea, F.; Testa, F.; Demortier, G.; Lentz, P.; Wiame, M.; Nagy, J. B., Synthesis and characterization of aluminosilicate MCM-22 in basic media in the presence of fluoride salts. *Micropor. Mesopor. Mat.* **2000**, 35-6, 585-595.
123. Burkett, S. L.; Davis, M. E., Mechanism of Structure Direction in the Synthesis of Si-ZSM-5: An Investigation by Intermolecular ^1H - ^{29}Si CP MAS NMR. *J. Phys. Chem.* **1994**, 98, (17), 4647-4653.
124. Kolodziejki, W.; Zicovich-Wilson, C.; Corell, C.; Perez-Pariente, J.; Corma, A., ^{27}Al and ^{29}Si MAS NMR Study of Zeolite MCM-22. *J. Phys. Chem.* **1995**, 99, (18), 7002-7008.

125. Maheshwari, S.; Martínez, C.; Teresa Portilla, M.; Llopis, F. J.; Corma, A.; Tsapatsis, M., Influence of layer structure preservation on the catalytic properties of the pillared zeolite MCM-36. *J. Catal.* **2010**, 272, (2), 298-308.
126. Chiang, H.; Bhan, A., Catalytic consequences of hydroxyl group location on the rate and mechanism of parallel dehydration reactions of ethanol over acidic zeolites. *J. Catal.* **2010**, 271, (2), 251-261.
127. Deng, J. F.; Zhang, G. R.; Dong, S. H.; Pan, H. S.; Wang, H. M., Acidic properties of ZSM-5 zeolite and conversion of ethanol to diethyl-ether. *Appl. Catal. A: General* **1988**, 41, (1-2), 13-22.
128. Kondo, J. N.; Ito, K.; Yoda, E.; Wakabayashi, F.; Domen, K., An ethoxy intermediate in ethanol dehydration on bronsted acid sites in zeolite. *J. Phys. Chem. B* **2005**, 109, (21), 10969-10972.
129. Pozas, C. d. I.; Lopez-Cordero, R.; Gonzalez-Morales, J. A.; Travieso, N.; Roque-Malherbe, R., Effect of pore diameter and acid strength in ethanol dehydration on molecular sieves. *J. Mol. Catal.* **1993**, 83 (1-2), 145-156.
130. Phillips, C. B.; Datta, R., Production of ethylene from hydrous ethanol on H-ZSM-5 under mild conditions. *Ind. Eng. Chem. Res.* **1997**, 36, (11), 4466-4475.
131. Bevilacqua, M.; Montanari, T.; Finocchio, E.; Busca, G., Are the active sites of protonic zeolites generated by the cavities? *Catal. Today* **2006**, 116, (2), 132-142.
132. Fărcașiu, D.; Leu, R.; Corma, A., Evaluation of Accessible Acid Sites on Solids by ^{15}N NMR Spectroscopy with Di-tert-butylpyridine as Base. *J. Phys. Chem. B* **2002**, 106, (5), 928-932.

133. Macht, J.; Baertsch, C. D.; May-Lozano, M.; Soled, S. L.; Wang, Y.; Iglesia, E., Support effects on Brønsted acid site densities and alcohol dehydration turnover rates on tungsten oxide domains. *J. Catal.* **2004**, 227, (2), 479-491.
134. Kim, J.-C.; Cho, K.; Ryoo, R., High catalytic performance of surfactant-directed nanocrystalline zeolites for liquid-phase Friedel–Crafts alkylation of benzene due to external surfaces. *Appl. Catal. A: General* **2014**, 470, (0), 420-426.
135. Verboekend, D.; Mitchell, S.; Pérez-Ramírez, J., Hierarchical Zeolites Overcome all Obstacles: Next Stop Industrial Implementation. *CHIMIA Int. J. Chem.* **2013**, 67, (5), 327-332.
136. Varoon, K.; Zhang, X.; Elyassi, B.; Brewer, D. D.; Gettel, M.; Kumar, S.; Lee, J. A.; Maheshwari, S.; Mittal, A.; Sung, C.-Y.; Cococcioni, M.; Francis, L. F.; McCormick, A. V.; Mkhoyan, K. A.; Tsapatsis, M., Dispersible Exfoliated Zeolite Nanosheets and Their Application as a Selective Membrane. *Science* **2011**, 334, (6052), 72-75.
137. Corma, A.; Fornés, V.; Martínez-Triguero, J.; Pergher, S. B., Delaminated zeolites: combining the benefits of zeolites and mesoporous materials for catalytic uses. *J. Catal.* **1999**, 186, (1), 57-63.
138. Ogino, I.; Nigra, M. M.; Hwang, S.-J.; Ha, J.-M.; Rea, T.; Zones, S. I.; Katz, A., Delamination of Layered Zeolite Precursors under Mild Conditions: Synthesis of UCB-1 via Fluoride/Chloride Anion-Promoted Exfoliation. *J. Am. Chem. Soc.* **2011**, 133, (10), 3288-3291.

139. Verboekend, D.; Milina, M.; Mitchell, S.; Pérez-Ramírez, J., Hierarchical Zeolites by Desilication: Occurrence and Catalytic Impact of Recrystallization and Restructuring. *Cryst. Growth Des.* **2013**, 13, (11), 5025-5035.
140. Verboekend, D.; Vilé, G.; Pérez-Ramírez, J., Hierarchical Y and USY Zeolites Designed by Post-Synthetic Strategies. *Adv. Funct. Mater.* **2012**, 22, (5), 916-928.
141. Chaikittisilp, W.; Suzuki, Y.; Mukti, R. R.; Suzuki, T.; Sugita, K.; Itabashi, K.; Shimojima, A.; Okubo, T., Formation of Hierarchically Organized Zeolites by Sequential Intergrowth. *Angew. Chem. Int. Ed.* **2013**, 52, (12), 3355-3359.
142. Inayat, A.; Knoke, I.; Spiecker, E.; Schwieger, W., Assemblies of Mesoporous FAU-Type Zeolite Nanosheets. *Angew. Chem. Int. Ed.* **2012**, 51, (8), 1962-1965.
143. Wang, Z.; Wan, W.; Sun, J.; Carrillo-Cabrera, W.; Gruner, D.; Yin, X.; Qiu, S.; Zhu, G.; Zou, X., Epitaxial growth of core-shell zeolite X-A composites. *CrystEngComm* **2012**, 14, (6), 2204-2212.
144. Lobo, R. F.; Zones, S. I.; Davis, M. E., Structure-direction in zeolite synthesis. *J. Inclusion Phenom.* **1995**, 21, 47-78.
145. Cundy, C. S.; Cox, P. A., The hydrothermal synthesis of zeolites: precursors, intermediates and reaction mechanism. *Micropor. Mesopor. Mat.* **2005**, 82, 1-78.
146. Wu, Y.; Emdadi, L.; Wang, Z.; Fan, W.; Liu, D., Textural and catalytic properties of Mo loaded hierarchical meso-/microporous lamellar MFI and MWW zeolites for direct methane conversion. *Appl. Catal. A: General* **2014**, 470, 344-354.

147. Kim, J.; Chun, J.; Ryoo, R., MFI zeolite nanosheets with post-synthetic Ti grafting for catalytic epoxidation of bulky olefins using H₂O₂. *Chem. Commun.* **2015**, 51, (66), 13102-13105.
148. Li, Y.; Sun, H. M.; Wang, Y. H.; Xu, B. J.; Yan, Z. F., Green Routes for Synthesis of Zeolites. *Prog. Chem.* **2015**, 27, (5), 503-510.
149. Sun, J. L.; Bonneau, C.; Cantin, A.; Corma, A.; Diaz-Cabanias, M. J.; Moliner, M.; Zhang, D. L.; Li, M. R.; Zou, X. D., The ITQ-37 mesoporous chiral zeolite. *Nature* **2009**, 458, (7242), 1154-1157.
150. Ngo, H. L.; Hoh, E.; Foglia, T. A., Improved synthesis and characterization of saturated branched-chain fatty acid isomers. *Eur. J. Lipid Sci. Technol.* **2012**, 114, (2), 213-221.
151. Hu, B.; Gay, I. D., Probing Surface Acidity by ³¹P Nuclear Magnetic Resonance Spectroscopy of Arylphosphines. *Langmuir* **1999**, 15, (2), 477-481.
152. Breck, D. W., Zeolite Molecular Sieves: Structure, Chemistry and Use. In John Wiley & Sons: New York.: 1974.
153. Thommes, M.; Mitchell, S.; Pérez-Ramírez, J., Surface and Pore Structure Assessment of Hierarchical MFI Zeolites by Advanced Water and Argon Sorption Studies. *J. Phys. Chem. C* **2012**, 116, (35), 18816-18823.
154. Kyungsu Na, M. C., Woojin Park, Yasuhiro Sakamoto, Osamu Terasaki, Ryong Ryoo, Pillared MFI zeolite nanosheets of a single-unit-cell thickness *J. Am. Chem. Soc.* **2010**, 132, (12), 4169-4177.
155. Deng, Y.-Q.; Zhou, W.-F.; Lv, H.-M.; Zhang, Y.-Y.; Au, C.-T.; Yin, S.-F., Synthesis of HZSM-5@silicalite-1 core-shell composite and its catalytic application

in the generation of p-xylene by methylation of toluene with methyl bromide. *RSC Adv.* **2014**, 4, (70), 37296-37301.

156. Wiedemann, S. C. C.; Muñoz-Murillo, A.; Oord, R.; van Bergen-Brenkman, T.; Wels, B.; Bruijninx, P. C. A.; Weckhuysen, B. M., Skeletal isomerisation of oleic acid over ferrierite: Influence of acid site number, accessibility and strength on activity and selectivity. *J. Catal.* **2015**, 329, 195-205.

157. Martins, J.; Birot, E.; Guillon, E.; Lemos, F.; Ribeiro, F. R.; Magnoux, P.; Laforge, S., Sodium exchange over H-EU-1 zeolite. Part II: Catalytic properties. *Micropor. Mesopor. Mat.* **2013**, 171, 238-245.

158. Ocakoglu, O.; Ustundag, C.; Koyluoglu, N.; Oguz, V.; Kendiroglu, G.; Ozkan, S., Long term follow-up of retinal nerve fiber layer thickness in eyes with optic nerve head drusen. *Curr. Eye Res.* 2003, 26, (5), 277-80.

159. Weber, R. W.; Möller, K. P.; Unger, M.; O'Conner, C. T., The chemical vapour and liquid deposition of tetraethoxysilane on the external surface of ZSM-5, *Micropor. Mesopor. Mat.* 1998, 23, 179-187.

160. Laforge, S.; Ayrault, P.; Manin, D.; Guisnet, M., Acidic and catalytic properties of MCM-22 and MCM-36 zeolites synthesized from the same precursors, *Appl. Catal., A* 2005, 279, 79-88.

161. Choudhary, V. R.; Nayak, V. S.; Choudhary, T. V., Single-Component Sorption/Diffusion of Cyclic Compounds from Their Bulk Liquid Phase in H-ZSM-5 Zeolite. *Ind. Eng. Chem. Res.* **1997**, 36, (5), 1812-1818.

162. Emdadi, L.; Liu, D., One-step dual template synthesis of hybrid lamellar-bulk MFI zeolite. *J. Mater. Chem. A* **2014**, 2, (33), 13388-13397.

163. Moliner, M.; Martínez, C.; Corma, A., Multipore Zeolites: Synthesis and Catalytic Applications. *Angew. Chem. Int. Ed.* **2015**, 54, (12), 3560-3579.
164. Rangnekar, N.; Mittal, N.; Elyassi, B.; Caro, J.; Tsapatsis, M., Zeolite membranes - a review and comparison with MOFs. *Chem. Soc. Rev.* **2015**, 44, (20), 7128-7154.
165. Vogt, E. T. C.; Whiting, G. T.; Dutta Chowdhury, A.; Weckhuysen, B. M., Chapter Two - Zeolites and Zeotypes for Oil and Gas Conversion. In *Advances in Catalysis*, Friederike, C. J., Ed. Academic Press: 2015; Vol. 58, pp 143-314.
166. Bouizi, Y.; Rouleau, L.; Valtchev, V. P., Bi-phase MOR/MFI-type zeolite core-shell composite. *Micropor. Mesopor. Mat.* **2006**, 91, (1-3), 70-77.
167. Emdadi, L.; Oh, S. C.; Wu, Y.; Oliaee, S. N.; Diao, Y.; Zhu, G.; Liu, D., The role of external acidity of meso-/microporous zeolites in determining selectivity for acid-catalyzed reactions of benzyl alcohol. *J. Catal.* **2016**, 335, 165-174.
168. Jin, F.; Chang, C.-C.; Yang, C.-W.; Lee, J.-F.; Jang, L.-Y.; Cheng, S., New mesoporous titanosilicate MCM-36 material synthesized by pillaring layered ERB-1 precursor. *J. Mater. Chem. A* **2015**, 3, (16), 8715-8724.
169. Zhang, K.; Ostraat, M. L., Innovations in hierarchical zeolite synthesis. *Catal. Today* **2016**, 264, 3-15.
170. Ghorbanpour, A.; Gumidyala, A.; Grabow, L. C.; Crossley, S. P.; Rimer, J. D., Epitaxial Growth of ZSM-5@Silicalite-1: A Core-Shell Zeolite Designed with Passivated Surface Acidity. *ACS Nano* **2015**, 9, (4), 4006-4016.

171. Chen, H. Y.; Wydra, J.; Zhang, X. Y.; Lee, P. S.; Wang, Z. P.; Fan, W.; Tsapatsis, M., Hydrothermal Synthesis of Zeolites with Three-Dimensionally Ordered Mesoporous-Imprinted Structure. *J. Am. Chem. Soc.* **2011**, 133, (32), 12390-12393.
172. Nair, S.; Tsapatsis, M.; A. Villaescusa, L.; A. Cambor, M., Zeolite-[small beta] grown epitaxially on SSZ-31 nanofibers. *Chem. Commun.* **1999**, (10), 921-922.
173. Okubo, T.; Wakihara, T.; Plévert, J.; Nair, S.; Tsapatsis, M.; Ogawa, Y.; Komiyama, H.; Yoshimura, M.; Davis, M. E., Heteroepitaxial Growth of a Zeolite. *Angew. Chem. Int. Ed.* **2001**, 40, (6), 1069-1071.
174. Goossens, A. M.; Wouters, B. H.; Buschmann, V.; Martens, J. A., Oriented FAU Zeolite Films on Micrometer-Sized EMT Crystals. *Adv. Mater.* **1999**, 11, (7), 561-564.
175. Okamoto, M.; Osafune, Y., MFI-type zeolite with a core-shell structure with minimal defects synthesized by crystal overgrowth of aluminum-free MFI-type zeolite on aluminum-containing zeolite and its catalytic performance. *Micropor. Mesopor. Mat.* **2011**, 143, (2-3), 413-418.
176. Kovo, A. S.; Opuoma, E.; Olu, S. C.; Edoga, M. O., Composite Zeolitic Material Synthesis And Its Functionality Synergism: A Review. *JMEST* **2015**, 2, (6), 1400-1407.
177. Qi, X.; Kong, D.; Yuan, X.; Xu, Z.; Wang, Y.; Zheng, J.; Xie, Z., Studies on the crystallization process of BEA/MOR co-crystalline zeolite. *J. Mater. Sci.* **2008**, 43, (16), 5626-5633.
178. Lei, Q.; Zhao, T.; Li, F.; Zhang, L.; Wang, Y., Catalytic cracking of large molecules over hierarchical zeolites. *Chem. Commun.* **2006**, (16), 1769-1771.

179. Higgins, J. B.; LaPierre, R. B.; Schlenker, J. L.; Rohrman, A. C.; Wood, J. D.; Kerr, G. T.; Rohrbaugh, W. J., The framework topology of zeolite beta. *Zeolites* **1988**, 8, (6), 446-452.
180. Newsam, J. M.; Treacy, M. M. J.; Koetsier, W. T.; Gruyter, C. B. D., Structural Characterization of Zeolite Beta. *P. Roy. Soc. Lond. A: Mat.* **1988**, 420, (1859), 375-405.
181. Liu, H.; Li, Y.; Shen, W.; Bao, X.; Xu, Y., Methane dehydroaromatization over Mo/HZSM-5 catalysts in the absence of oxygen: effects of silanation in HZSM-5 zeolite. *Catal. Today* **2004**, 93–95, 65-73.
182. Zhao, J. J.; Hua, Z. L.; Liu, Z. C.; Li, Y. S.; Guo, L. M.; Bu, W. B.; Cui, X. Z.; Ruan, M. L.; Chen, H. R.; Shi, J. L., Direct fabrication of mesoporous zeolite with a hollow capsular structure. *Chem. Commun.* **2009**, (48), 7578-7580.
183. Jung, J.; Jo, C.; Mota, F. M.; Cho, J.; Ryoo, R., Acid catalytic function of mesopore walls generated by MFI zeolite desilication in comparison with external surfaces of MFI zeolite nanosheet. *Appl. Catal. A: General* **2015**, 492, 68-75.
184. Jo, C.; Cho, K.; Kim, J.; Ryoo, R., MFI zeolite nanosponges possessing uniform mesopores generated by bulk crystal seeding in the hierarchical surfactant-directed synthesis. *Chem. Commun.* **2014**, 50, (32), 4175-4177.
185. Kim, W.; Kim, J. C.; Kim, J.; Seo, Y.; Ryoo, R., External Surface Catalytic Sites of Surfactant-Tailored Nanomorphous Zeolites for Benzene Isopropylation to Cumene, *ACS Catal.* **2013**, 3, 192-195.
186. Bhatia, S.; Beltramini, J.; Do, D. D., Deactivation of Zeolite Catalysts. *Catal. Rev.* **1989**, 31, (4), 431-480.

187. Mihindou-Koumba, P. C.; Cerqueira, H. S.; Magnoux, P.; Guisnet, M., Methylcyclohexane Transformation over HFAU, HBEA, and HMFI Zeolites: II. Deactivation and Coke Formation. *Ind. Eng. Chem. Res.* **2001**, 40, (4), 1042-1051.
188. Chiu, J. J.; Pine, D. J.; Bishop, S. T.; Chmelka, B. F., Friedel–Crafts alkylation properties of aluminosilica SBA-15 meso/macroporous monoliths and mesoporous powders. *J. Catal.* **2004**, 221, (2), 400-412.
189. Feller, A., Reaction mechanism and desactivation pathways in zeolithe catalysed : Isobuatne/2-butene alkylation. *PhD dissertation (Technischen Universität München)* **2003**.
190. Flego, C.; Pazzuconi, G.; Bencini, E.; Perego, C., Zeolite beta as a catalyst for alkylation of benzene with ethylene: a deactivation study. In *Studies in Surface Science and Catalysis*, Delmon, B.; Froment, G. F., Eds. Elsevier: 1999; Vol. 126, pp 461-464.
191. Tempelman, C. H. L.; Zhu, X.; Gudun, K.; Mezari, B.; Shen, B.; Hensen, E. J. M., Texture, acidity and fluid catalytic cracking performance of hierarchical faujasite zeolite prepared by an amphiphilic organosilane. *Fuel Process. Technol.* **2015**, 139, 248-258.
192. Zhu, J.; Meng, X.; Xiao, F., Mesoporous zeolites as efficient catalysts for oil refining and natural gas conversion. *Front. Chem. Sci. Eng.* **2013**, 7, (2), 233-248.
193. Nandiwale, K. Y.; Niphadkar, P. S.; Deshpande, S. S.; Bokade, V. V., Esterification of renewable levulinic acid to ethyl levulinate biodiesel catalyzed by highly active and reusable desilicated H-ZSM-5. *J. Chem. Technol. Biotechnol.* **2014**, 89, (10), 1507-1515.

194. Perego, C.; Bosetti, A., Biomass to fuels: The role of zeolite and mesoporous materials. *Micropor. Mesopor. Mat.* **2011**, 144, (1–3), 28-39.
195. Opanasenko, M. V.; Roth, W. J.; Cejka, J., Two-dimensional zeolites in catalysis: current status and perspectives. *Catal. Sci. Technol.* **2016**, 6, (8), 2467-2484.
196. Baerlocher, C.; McCusker, L. B.; Olson, D. H., *Atlas of Zeolite Framework Types*. 2007.
197. Szostak, R., *Molecular Sieves: Principles of Synthesis and Identification*. Blackie Academic and Professional: London **1998**.
198. Zones, S. I., Translating new materials discoveries in zeolite research to commercial manufacture. *Micropor. Mesopor. Mat.* **2011**, 144, (1–3), 1-8.
199. Lew, C. M.; Rajabbeigi, N.; Tsapatsis, M., One-Pot Synthesis of 5-(Ethoxymethyl)furfural from Glucose Using Sn-BEA and Amberlyst Catalysts. *Ind. Eng. Chem. Res.* **2012**, 51, (14), 5364-5366.
200. Mascal, M.; Nikitin, E. B., Towards the Efficient, Total Glycan Utilization of Biomass. *ChemSusChem* **2009**, 2, (5), 423-426.
201. Yi, Y.-B.; Lee, J.-W.; Chung, C.-H., Conversion of plant materials into hydroxymethylfurfural using ionic liquids. *EnviroN. Chem. Lett.* **2015**, 13, (2), 173-190.